URANIUM DIOXIDE SINTERING KINETICS AND MECHANISMS UNDER CONTROLLED OXYGEN POTENTIALS

Clauer Trench de Freitas

DISSERTAÇÃO E TESE IEA 141 IEA - DT - 141	JUNHO/1980

CONSELHO DELIBERATIVO

MEMBROS

Dr. Luiz Cintra do Prado – Presidente
Dr. Edgardo Azevedo Soares Júnior – Vice-Presidente

CONSELHEIROS

Dr. Hélcio Modesto da Costa
Dr. Ivano Humbert Marchesi
Dr. Admar Cervellini
Dr. Waldyr Muniz Olive

REPRESENTANTES

Dr. Jacob Charcot Pereira Rios
Dr. Paolo Enrico Maria Zaghen

SUPERINTENDENTE

Hernani Augusto Lopes de Amorim

DISSERTAÇÃO E TESE - IEA 141 JUNHO/1980
IEA - DT - 161
141

URANIUM DIOXIDE SINTERING KINETICS AND MECHANISMS UNDER CONTROLLED OXYGEN POTENTIALS

Clauer Trench de Freitas

A Thesis submitted in fulfillment of the requirements for the degree of Doctor of Philosophy in Ceramic Engineering, University of Illinois. Thesis Advisor Prof. Dr. D. R. O'Boyle. July 13, 1977

INSTITUTO DE ENERGIA ATÔMICA
SÃO PAULO – BRASIL

Série DISSERTAÇÃO E TESE IEA

INIS *Categories and Descriptors*

B23

URANIUM DIOXIDE: Chemical composition, Sintering
SINTERING: Controlled atmospheres, Reaction kinetics

TABLE OF CONTENTS

Page

LIST OF FIGURES

Figure | Page

Figure Page

LIST OF TABLES

URANIUM DIOXIDE SINTERING KINETICS AND MECHANISMS UNDER CONTROLLED OXYGEN POTENTIALS

Clauer Trench de Freitas

ABSTRACT

The initial, intermediate, and final sintering stages of uranium dioxide were investigated as a function of stoichiometry and temperature by following the kinetics of the sintering reaction. Stoichiometry was controlled by means of the oxygen potential of the sintering atmosphere, which was measured continuously by solid-state oxygen sensors. Included in the kinetic study were microspheres originated from UO_2 gels and UO_2 pellets produced by isostatic pressing ceramic grade powders.

The microspheres sintering behavior was examined using hot-stage microscopy and a specially designed high-temperature, controlled atmosphere furnace. This same furnace was employed as part of an optical dilatometer, which was utilized in the UO_2 pellet sintering investigations.

For controlling the deviations from stoichiometry during heat treatment, the oxygen partial pressure in the sintering atmosphere was varied by passing the gas through a Cu-Tl-Cu oxygen trap. The trap temperature determined the oxygen partial pressure of the outflowing mixture. Dry hydrogen was also used in some of the UO_{2+x} sintering experiments.

The determination of diametrial shrinkages and sintering indices was made utilizing high-speed microcinematography and ultra-microbalance techniques.

It was observed that the oxygen potential has a substantial influence on the kinetics of the three sintering stages. The control of the sintering atmosphere oxygen partial pressure led to very fast densification of UO_{2+x}. Values in the interval 95.0 to 99.6% of theoretical density were reached in less than one minute.

Uranium volume diffusion is the dominant mechanism in the initial and intermediate sintering stages. For the final stage, uranium grain boundary diffusion was found to be the main sintering mechanism.

1 – INTRODUCTION

1.1 – Objectives

Uranium dioxide* may exist over a considerable range of O/U ratios. This ratio in both the hypo and hyperstoichiometric composition ranges is significant in influencing the physical and chemical properties of UO_2 as well as its sintering behavior.

The objectives of this research are: (1) to measure the sintering kinetics of uranium dioxide as a function of temperature, particle size and furnace-atmosphere oxygen potencial for the initial,

Aproved for publication in May 1979.

Writing, orthography, concepts and final revision are of exclusive responsibility of the Author.

* Throughout this paper uranium dioxide refers to UO_{2+x} and is abbreviated as UO_2 for convenience. In this study the range of interest for x is $0.2 \leq x \leq 0.3$, that comprises the fluorite phase of the material, at temperatures less than 2000°C.

intermediate and final stages of sintering, (2) from the measurements and published data to determine the dominant sintering mechanism in each stage of sintering, (3) to correlate the measured sintering kinetics with defect structures in UO_2, (4) to establish the dependence of sintering mechanisms on temperature and on particle size using data from the experimental sintering studies and from published literature.

Emphasis will be given to the sintering characteristics of UO_2 gels*, due to peculiarities initial associated with extremely small initial crystallite size.

There are several reasons for investigating the sintering behavior of UO_2 under controlled oxygen potentials. (1) The phase diagram of the uranium-oxygen system at high temperatures has been extensively investigated, as well as the values of x in UO_{2+x} as a function of oxygen partial pressure and temperature. (2) The self-diffusion coefficients of the anion and cation species in UO_2 have been determined using different techniques, with consistent results. (3) Deviations from stoichiometry can be controlled by varying the oxygen partial pressure over a wide range, in which diffusion coefficients and sintering phenomena are measurably affected. (4) The conclusions of previous sintering studies are not in agreement. (5) The intermediate and final stages of sintering for UO_2 gels have not been investigated in a controlled oxygen potential atmosphere. (6) Early investigators of UO_2 sintering behavior did not have reliable theoretical models upon which they could base the analysis and interpretation of their kinetic data. (7) UO_2 is a material of considerable commercial importance, particularly in nuclear and magnetohydrodynamic energy production systems.

1.2 – Prior Work

The effects of atmospheres and deviations from stoichiometry on the sintering rate of UO_2 have been investigated in part by a number of workers[3,8,16,86,109,142,145]. These early studies stressed the effect of sintering atmosphere on sintering rate rather than the effect of oxygen partial pressure in the atmosphere. Lay and Carter[88] questioned their results, "since changes in the oxygen-to-uranium ratio during sintering have usually been ignored and since no adequate model exists for final stage sintering."

Lay and Carter, in their study of the role of the oxygen-to-uranium ratio on the sintering of UO_2, concluded that the initial stages of the phenomenon are controlled by volume diffusion of the uranium ions. This result does not agree with that presented by Bacmann and Cizeron[10], who attributed the initial sintering stage to grain boundary diffusion. Both data evaluations[14,88] were based on theoretical models proposed by Johnson[65,66].

Araoz[13] studied sintering mechanisms in stoichiometric and hyperstoichiometric UO_2, using a small high temperature vacuum dilatometer. He concluded that sintering of UO_2 is uranium diffusion controlled, without specifying the diffusion mode. His data and conclusions that sintering and uranium diffusion are equally affected by oxygen partial pressure, are only partially in agreement with the results of Lee and Alcock[90], who related uranium diffusion coefficients in UO_{2+x} with x.

Jakeshova[59], in a study similar to that of Lay and Carter, examined the initial stage of sintering to 1135°C under controlled oxygen potential, for UO_{2+x} ($2.002 \leq O/U \leq 2.010$), using an optical dilatometer. It was found that small deviations from stoichiometry strongly influenced the sintering rate. Differences in the initial microstructure of the compacts also had a significant effect on the sintering behavior.

According to Rothmann[124], work on the sintering of UO_2 may not directly shed light on the diffusion processes in the oxide. Rothmann considered it unlikely that UO_2 sinters generally by a

* Sol and gel forms consist of sub-micron colloidal particles dispersed in a liquid medium, the sol retaining the properties of a liquid, the gel having properties approaching those of a solid[1].

diffusion controlled process, since the diffusion coefficient of U in UO_2 is too small to account for the sintering rates observed.

Marin[96] judged that uranium grain-boundary diffusion may be the controlling mechanism in the sintering of hyperstoichiometric UO_2. This same investigation[97] noted that the lower activation energies that have been found for nonstoichiometric oxides in some sintering experiments[2], are not representative of volume uranium diffusion, as has been frequently inferred. Marin suggested that in these experiments either complex movements involving oxygen ions, or surface and grain-boundary diffusion may be operative.

The use of spherical particles, instead of irregularly shaped ones, has aided the interpretation of sintering kinetics and the evaluation of the controlling sintering mechanisms in both metallic and ceramic systems. Kumar and Johnson[82] have used microspheres in a study of the inital stage of cobaltous oxide sintering. After approximately 1% shrinkage, due to faceting of the microspheres, the model proposed by Johnson[61] used for data evaluation broke down, but the main sintering mechanisms could still be identified. A model proposed by Johnson[60] for intermediate stage sintering has been successfully applied to determine the sintering mechanisms in cobaltous oxide[83].

Burton and Reynolds[28] have recently investigated the final stage of sintering of UO_2 in an atmosphere of flowing hydrogen. They demonstrated that it is possible to predict the densification associated with the final stage of sintering if the porosity distribution is known, as well as predict the sintering rate of an individual pore, using the model proposed by Hull and Rimmer[57].

The contribution of dislocation motion for material transport during sintering is still subject to controversy in the literature. Morgan, in a recent review[105], concluded that in many cases there may be a substantial contribution to material transport by dislocation motion, as in the case of highly sinterable powder compacts. In an earlier paper he presented methods for evaluating the contribution of dislocation movement to the densification of various oxides[104]. Ashby[11] suggested that dislocation motion may be a dominant mechanism in the early stages of sintering. For later sintering stages he indicated that the predominant mechanism in the case of UO_2 is evaporation-condensation.

It has been recognized that many factors that are not susceptible to simple parametric analysis may influence sintering kinetics[35]. Some of these factors are: a) the formation of whisker bridges between particles; this phenomenon is a function of the sintering atmosphere[114]; b) faceting of grains during sintering due to surface effects or small amounts of water vapor in the sintering atmosphere[81]; c) the presence of dislocations introduced by grinding coarse material into fine grains before sintering[35]; d) adsorbates on the surfaces of the powder[40,113,133]. Considering the factors that may affect the validity of the parametric sintering models, Condit[11] suggested the application of nonparametric methods, using radioactive tracers, in sintering studies. The observation of the tracer motion, for instance in a system of two sintered microspheres, may lead to the identification of the dominant sintering mechanism. In this context the *ion microprobe* may be used to determine nonradioactive isotope concentration gradients[36,37], particularly for O^{18} in UO_2.

2 – THE SINTERING PROCESS

2.1 – Fundamental Aspects and the Different Sintering Stages

Several detailed reviews of the sintering process* are available[27,30,33,41,46,89,138,144]. Goetzel[44], Jones[67] and Schwartzkopf[128] presentd the older concepts of sintering in comprehensive and valuable general studies. More recently, the investigations of Frenkel[43], Kuczynski[79], Kingery[71], Johnson[61] and Coble[32], were responsible for substantial advances in

(*) A definition for sintering proposed by Thummler is presented in Appendix 1.

the whole field. Experimental and theoretical investigations of fundamental character, developed in the more recent past, are published in reference 80.

It is generally considered that the driving force for sintering originates from the tendency of a powder compact to reduce its solid-vapor surface area, therefore decreasing the total surface free energy. Burke[27] remarked that some investigators postulated the driving force to be due to the tendency of compacts to release energy, stored as dislocations and elastic stresses in its particles from prior deformation. Other researchers consider it possible that a driving force might result from gradients in chemical composition, created during sintering (for instance, in the reaction-sintering of gels).

The term sintering is often considered in ceramics as applying to pure oxide systems[51]; it is frequently differentiated from sintering in the presence of a liquid phase by terming the process solid state sintering.

In the ceramic and metallurgical literature, often the nomenclature associated with the various forms of the processes lacks uniformity and coherence. In this investigation, sintering shall be construed in the context of solid sintering; the related terminology is based on the nomenclature analysis presented in reference 54.

Certain geometric and physical changes are associated with the sintering process. They include neck formation between adjacent particles; rounding of the particles sharp corners; spheroidization, shrinkage and eventual disappearance of pores within the compact; and increase of the compact density, due to the decrease of total pore volume.

The total sintering process can be broken down into various stages. In this research, four stages described by Ashby[11] will be considered*.

Stage zero – necks between particles placed in contact form instantaneously due to interatomic forces.

Stage one – the necks grow, with the individual powder particles still distinguishable.

Stage two – (also designated "intermediate") – the necks have grown substantially, and the pores are roughly cylindrical.

Stage three – (also designed "final") – the pores have become isolated and spherical.

In order to simplify mathematical analysis, Ashby links stages 2 and 3 together, using a single set of rate equations to describe both. This is done considering the analysis level of precision as low, but meaningful for preliminary and broad determinations of sintering mechanisms and kinetics.

Other investigators[51,131] generally divide sintering in either three or four stages: initial, intermediate and final, adding sometimes grain-growth as the fourth stage. One of the first considerations of three different stages during sintering was associated with the work of Smothers and Reynolds[131] that divide the process in the following phases: (1) continuous pores present in the compact, (2) closed pores, and (3) isolated pores.

The mechanisms that have been proposed for stage 1 are: (1) evaporation-condensation, (2) lattice or volume diffusion; (3) grain-boundary diffusion; (4) surface diffusion; (5) viscous flow; (6) plastic flow. Theoretical applications of these different models of mechanisms for stage 1 are presented in summaries by Johnson and Cutler[66], Coble[30], Coble and Burke[33], and Wirth[148].

One of the first theoretical studies of stage 2 is due to Coble[32]. He assumed that diffusional

(*) The four sintering stages, as defined by Coble[32], are presented in Appendix 1.

mechanisms would be responsible for the mass transport leading to densification. He idealized the microstructure of a polycrystalline body as formed by grains of the same size and with the shape of a truncated octahedron. The pore phase was supposed to be formed by continuous cylindrical pores located at the intersections of three or four grains.

Coble modified his lattice diffusion model in a later publication[31], stating that he had erroneously equated grain size to grain edge length. This modification allowed him to determine the diffusion coefficient for Al^{+3} in Al_2O_3; the resulting value agreed with published data within a factor of about two.

Johnson[60] pointed out that attempts to solve certain problems of the Coble model had not succeeded completely; he presented a new approach to the intermediate stage of sintering, without any of Coble's assumptions relative to grain size, shape or size distribution. Johnson's model requires microstructural data for its application, including the mean separation between pores and the mean surface curvature of the pores. An utilization of this model is described in references 82 and 83.

Two approaches have been taken in the study of the final sintering stage (stage 3). One of them was presented by Coble[32] and involves the elimination of the final porosity (2 to 5%) from a sintering body. The other approach[59-63] takes into consideration the control of grain growth, but it does not have the fundamental character of Coble's investigation.

Coble[32] considered volume diffusion to govern mass transport in the final stage; the microstructure was imagined as being formed by tetrakaidecahedral grains packed ideally with spherical pores located at four grain corners. Diffusion between two concentric spherical shells was an approximation adopted for the determination of a flux equation. The time dependence for the porosity, P, in stage 3 was found to be:

$$P = \frac{6\pi}{2} \cdot \frac{D\gamma\Omega}{\ell^3 kT} (t_f - t) \qquad (2.1)$$

where:

D = self-diffusion coefficient

Ω = vacancy volume

ℓ = length of a grain edge

γ = surface free energy

k,T, as defined in Table II

t_f = time extrapolated to zero porosity

t = time elapsed during isothermal sintering.

Johnson[61] discussed the assumption that a single mass transport mechanism predominates during sintering, in such way as to make possible its determination by fitting experimental data to a certain model. The problems associated to this type of approach were also considered by Rockland[123] and led to the development of special models[61,63,64] and procedures[11] to allow the separation of the contributions of possible transport mechanisms.

Ashby[11] made it clear that "there is no single mechanism of sintering; the mechanism which appears as dominant depends on temperature, on size, and on time, taht is, on the stage that sintering

has reached." The application of Ashby's "sintering diagram" approach is discussed next and is used for the study of the mechanisms associated with the sintering of stoichiometric UO_2 produced from gels.

2.2 -- Sintering Diagrams

Sintering diagrams[11] show the dominant mechanism of sintering corresponding to a given homologous temperature, $\frac{T}{T_m}$, and normalized neck radius, $\frac{x}{a}$.

T_m = melting temperature of the material (°K)

T = sintering temperature (°K)

x = radius of disc of contact of two particles

a = particle radius.

The diagram is divided into fields, where a simple sintering mechanism is dominant.

In Figure 1 the field indicates that surface diffusion from a surface source is the dominant mechanism, during the initial sintering stage of stoichiometric UO_2. In Ashby's[11] work, superimposed on the different sintering diagram fields are "contours of constant neck growth" or of "constant time"; Figure 1 shows contours of constant time on the sintering diagram of UO_2.

The boundaries of the fields are obtained by equating pairs of rate equations corresponding to different sintering mechanisms and solving for neck size as function of temperature. Transitions between different sintering stages are marked by heavy lines.

Contours of constant neck growth-rate are determined by the sum of the contributions due to each of the sintering mechanisms involved. Contours of constant time are computed by a similar procedure , but require integrating the sum of the rate equations with respect to time. Ashby solved the integral and differential equations using numerical methods. He considered four sintering stages as described in the previous section.

Ashby's treatment links stage 2 and 3 together, describing both by a single set of rate equations. Figure 2 shows the geometries corresponding to this simplification. In this context, he remarks the level of precision attained with such an approximation is not high; nevertheless, many of the features of the sintering diagrams depend on the ratio of rates, not their absolute magnitudes, and consequently a substantial number of the approximations cancel. However, it must be observed that good judgement must be exercised in the evalution of results derived from such diagrams. This is particularly true in the cases for which considerable grain growth occurs during sintering or when there are reasons to suspect that parametric sintering models cannot be applied reliably (for instance when evaporation-condensation is dominant, with the formation of whisker bridges between particles[35,114]).

Table I lists the sintering mechanisms, transport paths and sources from which matter is drawn, important in Ashby's derivations for the relatively simple case of sintering in the absence of applied stress of a one-component system, formed by a pure stoichiometric compund.

The rate equations corresponding to adhesion and the mechanisms presented in Table I are given below. The symbols and nomenclature for the variables and parameters involved are listed in Table II, following the equations.

2.3 – Rate Equations for the Construction of Sintering Diagrams[11]

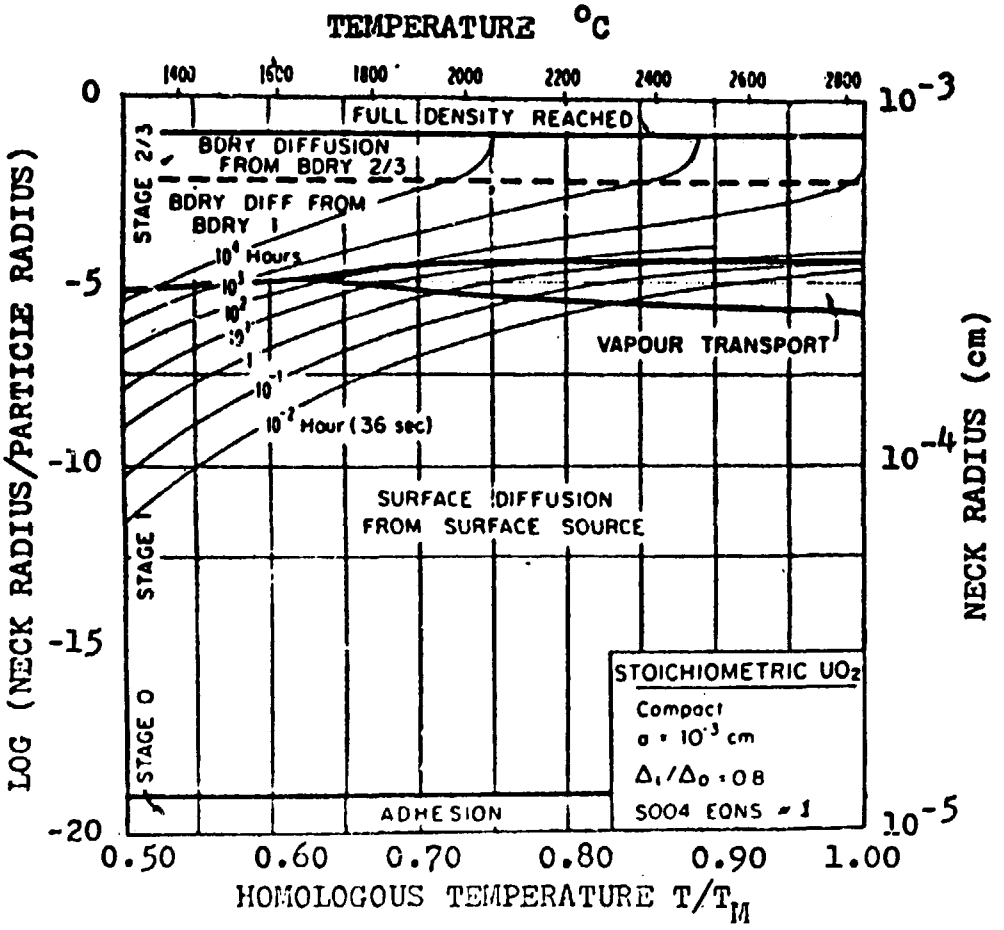

Figure 1 – Sintering diagram for stoichiometric UO_2; starting powder with particles of 10 μm radius (after ref. 28).

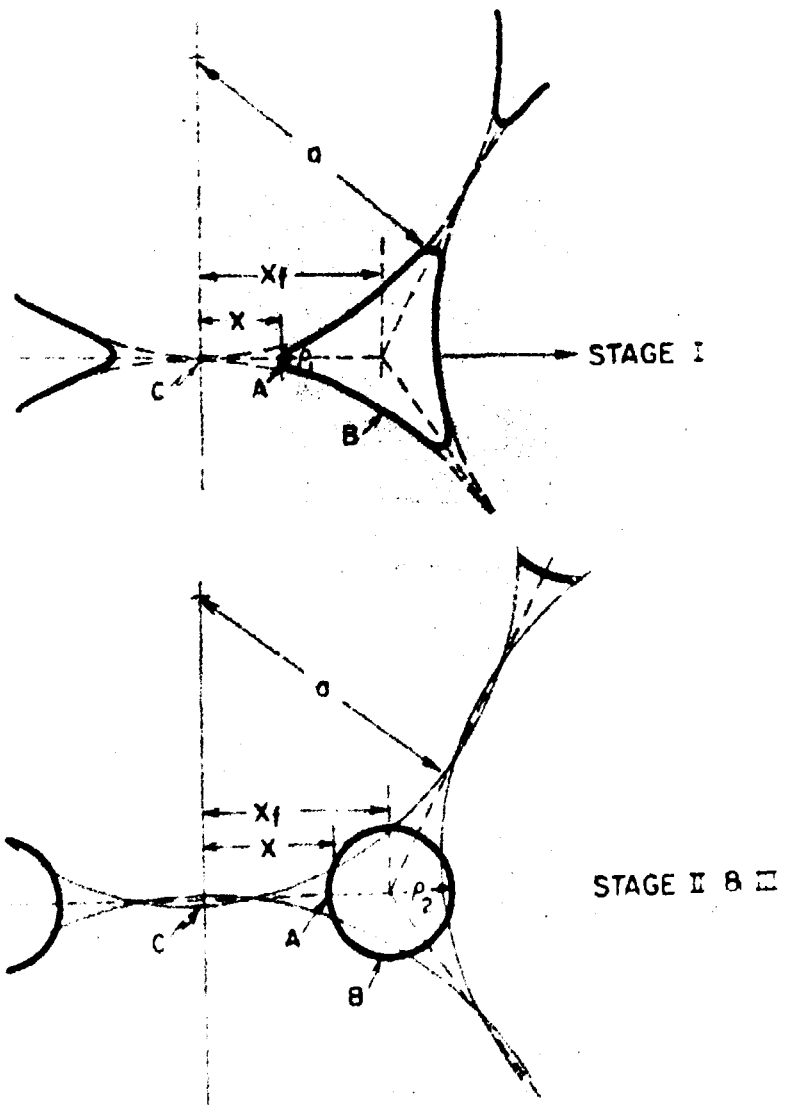

Figure 2 – Geometries during the different sintering stages. ρ_1 is the smallest radius of curvature during stage I. The pores have become cylindrical or spherical with radius ρ_2 in the stages II and III (after ref. 11).

Table I

Transport paths, sources and sinks* of matter corresponding to basic sintering mechanisms (after ref. 11)

Mechanism	Transport path	Source of matter
1	Surface diffusion	Surface
2	Lattice diffusion	Surface
3	Vapor transport	Surface
4	Boundary diffusion	Grain boundary
5	Lattice diffusion	Grain boundary
6	Lattice diffusion	Dislocations

* For all mechanisms the matter sink is considered to be the neck.

Stage 0 – Adhesion:

$$(\dot{x})_0 = \frac{ca^2}{x} \quad \text{for } x < \left(\frac{\gamma_s a^2}{10\mu}\right)^{1/3} \tag{2.2}$$

$$(\dot{x})_0 = 0 \quad \text{for } x \geq \left(\frac{\gamma_s a^2}{10\mu}\right)^{1/3} \tag{2.3}$$

Stage 1 – Diffusion controlled neck growth:

Mechanism 1.1 – Surface diffusion from a surface source:

$$\dot{x}_1 = 2D_s\delta_s FK_1^3 \tag{2.4}$$

$$\text{with } F = \frac{\gamma_s\Omega}{kT};\ K_1 = \left(\frac{1}{\rho_1} - \frac{1}{x} + \frac{2}{a}\right)\left[1 - \frac{x}{x_f - \left(\frac{f}{3}\right)^{1/3} a}\right] \tag{2.5),(2.6}$$

Mechanism 1.2 – Lattice diffusion from a surface source:

$$\dot{x}_2 = 2D_v FK_1^2 \tag{2.7}$$

Mechanism 1.3 – Vapor transport from a surface source:

$$\dot{x}_3 = P_v F\left(\frac{\Omega}{2\pi\Delta_0 kT}\right)^{1/2} K_1 \tag{2.8}$$

Table II

Symbols, nomenclature, units and observations relative to the variables and parameters involved in the construction of sintering diagrams[11]

a	particle radius
x	radius of disc of contact of two particles
x_f	the final value of x where 100 percent density has been reached
ρ, ρ_1, ρ_2	radius of curvature of the neck
K_1, K_2, K_3	curvature differences which drive diffusive fluxes
D_s	surface diffusion coefficient
D_v	lattice diffusion coefficient
D_B	grain boundary diffusion coefficient
D_G	diffusion coefficient in the gas phase
δ_s	effective surface thickness
δ_B	effective grain boundary thickness
P_v	vapor pressure [$P_v = P_0 \exp - (Q_{vap}/kT)$]
γ_s	surface free energy
γ_B	grain boundary free energy
Ω	atom or molecular volume
k	Boltzmann's constant (1.38×10^{-16} erg/°K)
T	absolute temperature (°K)
T_M	melting temperature (°K)
F	$\gamma_s \Omega/kT$ (typical magnitude = 10^{-6} cm)
f	volume fraction of pores
Δ_o	theoretical density
Δ_i	initial density of powder compact
μ	shear modulus
b	Burgers vector of dislocations, or the atomic or molecular diameter
N	dislocation density
c	velocity of sound (taken as 10^5 cm/sec)

Mechanism 1.4 – Grain boundary transport from sources in the grain boundary:

$$\dot{x}_4 = \frac{4D_B\delta_B F K_2^2}{x} \tag{2.9}$$

$$\text{with } K_2 = \left(\frac{1}{\rho_1} - \frac{1}{x} \right) \tag{2.10}$$

Mechanism 1.5 – Lattice diffusion from sources on the grain boundary:

$$\dot{x}_5 = 4D_v F K_2^2 \tag{2.11}$$

Mechanism 1.6 – Lattice diffusion from dislocation sources:

$$\dot{x}_6 = \frac{4}{9} K_2 N x^2 D_v F \left(K_2 - \frac{3}{2} \frac{\mu x}{\gamma_s a} \right) \tag{2.12}$$

The net sintering rate during stage 1 is then given by:

$$(\dot{x})_1 = \sum_{i=1}^{6} \dot{x}_i \tag{2.13}$$

Stages 2 and 3 – Diffusive flow of matter from points on the grain boundary separating two particles and the pore.

The following two mechanisms are important in stages 2 and 3.

Mechanism 7 – Boundary diffusion from sources on the boundary.

$$\dot{x}_7 = \frac{1}{16} D_B\delta_B F K_3^3 \left[\frac{1}{\log_e \left(\frac{x_f k_3}{2} \right) - \frac{3}{4}} \right] \text{ with } K_3 = \frac{2}{\rho_2} . \tag{2.14}$$

Mechanism 8 – Lattice diffusion from sources on the boundary:

$$\dot{x}_8 = \frac{1}{16} \cdot x \, D_v F K_3^3 \left[\frac{1}{\log_e \frac{x_f k_3}{2} - \frac{3}{4}} \right] \tag{2.15}$$

The net sintering rate during stages 2 and 3 is: $(\dot{x})_{2,3} = \dot{x}_7 + \dot{x}_8$

A sintering diagram for UO_2 produced from gels is presented in Fig. 3 and it will be discussed in Chapter 5 of this work. The initial particle radius of the starting material, determined by transmission electron microscopy, was 5.8 nm. For the determination of this diagram, the numerical values used in the preceding equations are given in Table III.

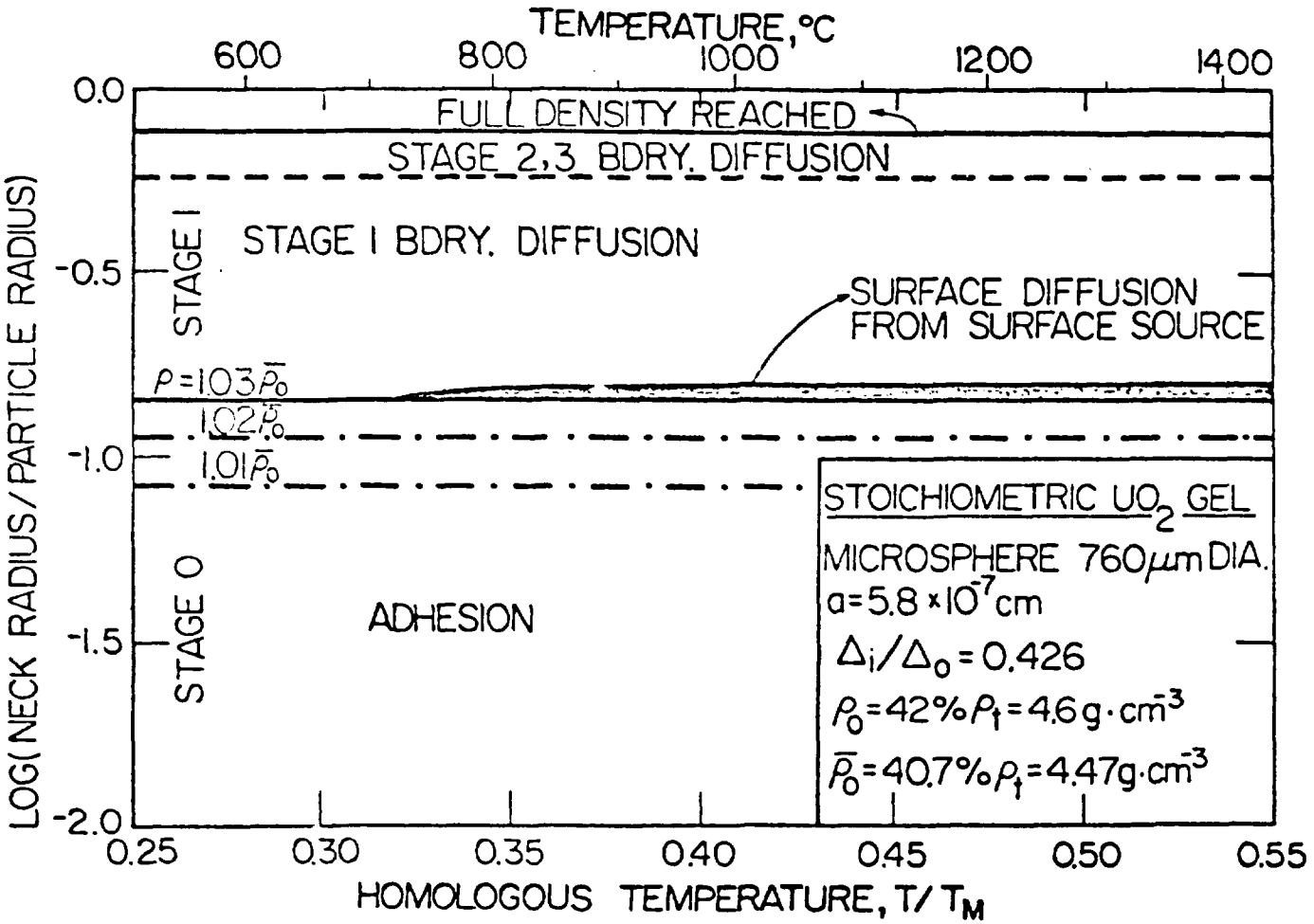

Figure 3 — Sintering diagram for stoichiometric UO_2 produced from gels

Table III

Properties needed for the construction of a sintering diagram; numerical values for stoichiometric UO_2 [11,54]

Atomic volume $\Omega(cm^3)$	4.1×10^{-23}
Burgers vector b(cm)	3.86×10^{-8}
Melting temperature T_M (°K)	3123
Shear modulus $\mu(dyn/cm^2)$	8.3×10^{11}
Temperature coefficient of $\mu(°K^{-1})$	1×10^{-4}
Dislocation density N	10^8
Theoretical Density Δ_o (g/cm^3)	10.94
Surface-energy γ_s (erg/cm^2)	1000
Grain boundary energy γ_B (erg/cm^2) *	700
Effective boundary thickness δ_B (cm)	5.54×10^{-8}
Effective surface thickness δ_S (cm)	5.54×10^{-8}
D_o for lattice diffusion (cm^2/sec)	6.8×10^{-5}
Activation energy for lattice diffusion Q_v (kcal/mole)	98.3
D_o for boundary diffusion (cm^2/sec)	4×10^{-2}
Activation energy for boundary diffusion Q_B (kcal/mole)	72.0
D_o for surface diffusion (cm^2/sec)	3.4×10^5
Activation energy for surface diffusion Q_s (kcal/mole)	108.0
Preexponential for vapor pressure P_o (dyn/cm^2)	4.11×10^{14}
Activation energy for evaporation Q_{vap} (kcal/mole)	143.9

* The value of γ_B is not given by Ashby in Ref. 11; the adopted γ_B value is an average (699 ± 194) erg/cm^2 of data tabulated by Hirth[67], corresponding to seven materials.

2.4 – Effects of Various Atmospheres on the Sintering of Uranium Oxides

Murray and Tackray[108] demonstrated that the oxide $UO_{2.13}$ (from British Springfields) sintered more radily in argon than the oxide $UO_{2.04}$ (from American Mallinkrodt). Densities of approximately 10.0 $g.cm^{-3}$ were obtained for the oxide $UO_{2.13}$, sintered at 1400°C. Under the same conditions, $UO_{2.04}$ sintered to approximately 8.0 $g.cm^{-3}$. The green densities of the corresponding compacts were respectively 4.7 and 6.2 $g.cm^{-3}$. When using hydrogen as the sintering atmosphere, the sintering bahavior of $UO_{2.04}$ was even less favorable. From these results it was first concluded that sintering of uranium dioxide was influenced by deviations from stoichiometry, but the reason was not understood.

Initial systematic experiments relating sinterability to the process atmosphere, were developed by Williams et al.[145], and Webster and Bright[142]. Their results will be analysed next.

2.4.1 – Investigations of Williams, Barnes, Scott and Hall

Williams et al.[145] sintered oxides in the composition range $2.00 < \frac{O}{U} < 2.67$ in hidrogen, carbon monoxide, carbon dioxide, nitrogen, argon and vacuum.

2.4.1.1. – Non-Dilatometric Experiments

Compacts were pressed at 1.4 ton/cm^2 and sintered for two hours. The following table presents the measured surface areas of the oxides before sintering. The surface areas were determined by the nitrogen adsorption method. All the oxides, with the exception of U_3O_8, were prepared by room temperature oxidation.

Table IV

Surface area of uranium oxides studied by Williams et al[145]

O:U ratio*	Surface area m^2/g
2.08	2
2.18	6
2.21	6
2.40	8
2.67 (U_3O_8)	15

* After oxidation.

Table IV shows considerable surface area variation with initial O/U ratio, for the powders prepared by room temperature oxidation. The atmospheres, final O:U ratios, densities, measured and calculated weight losses are given in Appendix 2 (Tables A-I to A-V). From the experimental data, the following conclusions were drawn:

a) Sintering in neutral atmospheres (argon, nitrogen and carbon dioxide)

The sintering atmosphere had little effect upon the final density (for initial O/U approximately constant). Variations in the initial oxigen content of the compacts also did not influence significantly

the sintering behavior in argon. Substantial composition took place while sintering in argon. The weight loss varied approximately 0.2 Wt% for $UO_{2.08}$ to about 1.2 Wt% for $UO_{2.4}$; oxygen loss alone was not enough to explain the total weight loss. For $UO_{2.4}$ volatilization of uranium must have taken place; for the other oxides the differences between weight losses and calculated oxygen losses are of the order of the experimental accuracy. Therefore no firm conclusion was possible about the volatilization of uranium. However, deposits of uranium dioxide were found on the apparatus, so that volatilization of uranium oxide must have taken place.

b) Sintering in vacuum

The densities were lower than those corresponding to sintering in argon. The weight losses were substantially larger than in argon. It was thought that the volatile bearing phase was UO_3.

c) Sintering in hydrogen and in CO

Temperatures substantially higher were needed to obtain the same densities reached in argon or in nitrogen. The data showed that there was a significant influence of the moisture content of the hydrogen. The densities decreased substantially for dry hydrogen. Reduction to the stoichiometric composition was not always reached. No uranium deposits were found; the oxygen and total weight losses agreed closely.

The sintering of U_3O_8 in hydrogen showed higher densities than those corresponding to the lower uranium oxides.

The sintering of $UO_{2.08}$ and $UO_{2.40}$ in CO demonstrated that this gas, as hydrogen, had a generally deleterious effect on the final densities.

d) Sintering in a mixed atmosphere involving hydrogen, vacuum and argon

The data showed that the sinterability of UO_{2+x} is better than that of $UO_{2.0}$ (obtained by heating UO_{2+x} in H_2 at 750°C).

2.4.1.2 – Dilatometric Experiments

Williams et al.[145] reported dilatometric data for UO_{2+x} at a heating rate of 10°C/min.. In the majority of the oxides analysed, most of the densification took place during the heating transient. Shrinkage in an argon or nitrogen atmosphere started at approximately 600°C; for hydrogen it began at about 900°C.

2.4.1.3 – Discussion

Williams et al.[145] suggested that oxygen in excess of stoichiometry influenced sintering in three ways:

a) Volatization processes occurred during sintering, involving losses of oxygen and uranium; the increased volatility of UO_{2+x} relative to that of $UO_{2.0}$ affected adversely the sinterability. The investigators[145] considered it unlikely that material transfer by an evaporation-condensation mechanism might aid sintering.

b) Hydrogen was chemisorbed or possibly absorbed in UO_{2+x}; this gas desorbed as water vapor at aboud 200°C, if the oxide powder was allowed to oxidize. If sintering behavior is adversely affected by chemisorbed or dissolved hydrogen, by reduction of surface free energy or by decreasing flow under stress, it is admissible to suppose that the beneficial

action of oxygen in excess of stoichiometry consists in the removal of that hydrogen. This explanation tends to be confirmed by the relatively poor sinterability of uranium oxides in hydrogen and by the higher densities reached in vacuum. However, sintering of hyperstoichiometric oxide in vacuum took place much more readily than for the stoichiometric material, suggesting a more complex action for the excess oxygen. Carbon monoxide had a similar effect on sintering as hydrogen, but since it is not chemisorbed, the action of excess cannot be the same as that proposed by Williams. Therefore, it is unlikely that the enhanced sinterability of hyperstoichiometric uranium oxides can be attributed to the action of excess oxygen in eliminating chemisorbed or absorbed gases.

c) It has been demonstrated by Scott et al.[129] that hyperstoichiometric oxide flows more easily, under stress at high temperatures, than the stoichiometric material. Since departure from stoichiometry affects to about the same degree flow processes in both creep and sintering, this suggests that a similar mechanism is operating in both cases. However, Scott et al.[129] were not able to identify a single mechanism as responsible for all the observed results. Their hypothesis, that the flow process was controlled by the diffusion of the uranium ion as the rate determining factor, was supported by the fact that the activation energies for uranium diffusion and plastic flow were about the same. For all the mechanism they proposed, one characteristic was: commen the diffusion of the uranium ions in the stoichiometric material should be slower than in nonstoichiometric oxides. It was also observed that for increasing departure from stoichiometry, the activation energy for flow decreased, but its value remained much greater than that for oxygen ion diffusion.

It is necessary to remark that deviation from stoichiometry need not be invoked to explain sintering behavior differences, reported for instance by Murray and Tackeray[108] in their studies of $UO_{2.04}$ and $UO_{2.14}$. The enhanced sinterability of the higher oxide might be due to an increase in powder surface area, resulting from particle break-up during oxidation, as shown in Table IV. However, in the work of Williams et al.[145], the authors did not believe their samples with $O/U \leq 2.04$ suffered significant particle break-up, since there is no phase change at least up to $O/U = 2.06$ at 900°C.

Williams et al[145] results on UO_2 sintering must be viewed with caution, since:

a) There was substantial change of composition during sintering. Such changes could have been avoided by equilibration of the samples with the sintering atmosphere.

b) The authors concluded plastic flow to be a dominant sintering mechanism for UO_2. This is not valid, considering more recent results[11].

c) A correlation between the defect crystalline structure of nonstoichiometric uranium oxides and their enhanced sinterability was not tried. In the next chapter this correlation is shown to have considerable importance.

The main value of Williams et al[145] work is in their systematic approach to the problem of atmosphere influence on sintering: well characterized uranium oxides were used, in a wide range of sintering atmospheres. The basic difficulty consisted in the lack of control over the oxygen potential of the neutral atmospheres (argon, nitrogen and CO_2), that implied compositional changes during the sintering process. Probably considerable variations in the O/U ratio also took place when vacuum or reducing atmosphere (H_2, CO) were employed. In this last case it is reasonable to suppose that equilibration, correponding to the stoichiometric composition, developed relatively fast, in a small fraction of the total sintering time.

It is possible to conclude that the smaller stoichiometric deviations associated with sintering in vacuum or in reducing atmospheres led to less favorable sintering kinetics, relative to that corresponding to neutral atmospheres.

2.4.2 – Work of Webster and Bright

Webster and Bright[142] also studied the influence of sintering atmospheres on the sinterability of uranium oxides; however, they gave some attention to the problem of controlling the oxygen potential of nonreducing atmospheres. Their careful sample preparation, characterization and sintering time-temperature cycles are summarily described in Appendix 2.

a) Sintering in reducing atmospheres*

Hydrogen sintering experiments were carried out from 1200 to 1500°C. The final density was considerably lower than at 1700°C (the temperature normally used in the industrial production of UO_2 pellets); there was no indication of an approach to a constant sintered density, for increasing temperatures. The final $\frac{O}{U}$ ratios generally descreased with increasing sintering temperatures.

The dilution of hydrogen with nitrogen did not improve the sintered densities.

From thermodynamic considerations, the $\frac{O}{U}$ ratio should be reduced well below 2.01 for sintering in reducing atmospheres with no substantial concentration of H_2O available. However this did not happen at temperatures lower than 1500°C; therefore equilibration sample-atmosphere was not attained.

(6) Sintering in neutral (argon and nitrogen) and slightly oxidizing atmospheres**

The final densities obtained in undiluted argon sintering are much higher than those attained in hydrogen atmospheres; however, the resulting $\frac{O}{U}$ ratios were also higher and a substantial proportion of U_4O_9 was found in the sintered material.

Lower densities were reached when about 0.6 vol. % of water vapor was added to argon (passing the gas through water at 0°C).

Firing in 76 vol. % argon + 24 vol. % O_2 also gave substantially higher densities than those obtained in reducing atmosphere sintering. However, the resulting $\frac{O}{U}$ values again indicated that equilibrium was not attained.

The use of undiluted nitrogen or N_2 + 0.6 vol. % water vapor sintering atmospheres, also was associated with higher final densities than those obtained with undiluted hydrogen sintering.

c) Sintering in steam

In this atmosphere, high final densities were reached, comparable with those obtained in argon. The x values of UO_{2+x}, in equilibrium with the dynamic steam atmospheres, were calculated from the equilibrium constant k corresponding to $H_2O \rightleftharpoons H_2 + \frac{1}{2} O_2$.

$$k = \frac{[p(H_2)]\,[p(O_2)]^{1/2}}{[p(H_2O)]} \quad \text{, with } p(H_2O) = 1 \text{ atm and } p(H_2) = 2[p(O_2)] \qquad (2.17)$$

---

* Data in Appendix 2, Tables A-6, 7

** Data in Appendix 2, Tables A 8 to A 12

The oxygen partial pressure $p(O_2)$ was determined from the following expression:

$$p(O_2)\ (\text{in atm}) = 76 \exp \frac{-33{,}000}{T} \exp \frac{31x}{1-x}, \qquad (2.18)$$

were T = absolute temperature in °K and $x = \frac{O}{U}$ ratio.

The observed values of x were lower than those calculated from the preceding formulas; therefore equilibrium was not reached.

2.4.2.1 – Correlation Between the Sintered Densities and the $\frac{O}{U}$ Ratios of Fired Compacts

Figure 4 shows the relationship between final oxygen-uranium atomic ratios and the corresponding densities of compacts sintered in nonreducing atmospheres.

It should be noted that if the excess oxygen were removed from the UO_{2+x} samples, for instance by reduction in hydrogen after sintering was completed, the densities of the fired compacts would be lowered due to two effects: a) weight loss originated from oxygen removal; b) enlargement of the fluorite-type lattice caused by the $U_4O_9 \rightarrow UO_{2.00}$ transformation. The dotted lines shown in Figure 4 were derived by correcting the observed density values (indicated by the dashed plots) for these two effects.

2.4.2.2 – Discussion

Considering that sample-atmosphere equilibrium was not attained during sintering, the poor correlation shown in Figure 4 is understandable. If the real $\frac{O}{U}$ ratios at the temperature of sintering were roughly equal to the measured final $\frac{O}{U}$ ratios, it appears that the final densities increased with increasing values of stoichiomety deviation.

The results of Webster and Bright[142] broadly agree with those of Williams et al.[145]. However, Webster and Bright clearly recognized the importance of the sintering atmosphere oxygen potential and really tried to control it with the somewhat unrefined means normally available at the time (1958). They indicated that the oxygen content of samples fired in argon and other neutral atmospheres, would depend on any small partial pressure of oxygen in the gaseous phase; a mole fraction as low as 10^{-7} could be significant. Therefore, the control of $\frac{O}{U}$ ratios by neutral atmospheres was considered extremely difficult experimentally; it was suggested that the use of a 100% steam atmosphere as probably the best method for controlling oxygen potential during sintering.

Webster and Bright[142] considered the study of the mechanism associated with UO_{2+x} sintering as being beyond the scope of their work but suggested two explanations for the enhanced sinterability of the hyperstoichiometric oxides: a) increased diffusion rates; b) substantial material transport by vapor phase transfer, since a certain volatility was apparent. In the context of sintering mechanisms determination, these suggestions are acceptable only as resulting from an investigation of preliminary character.

2.4.3 – Investigations of Müller

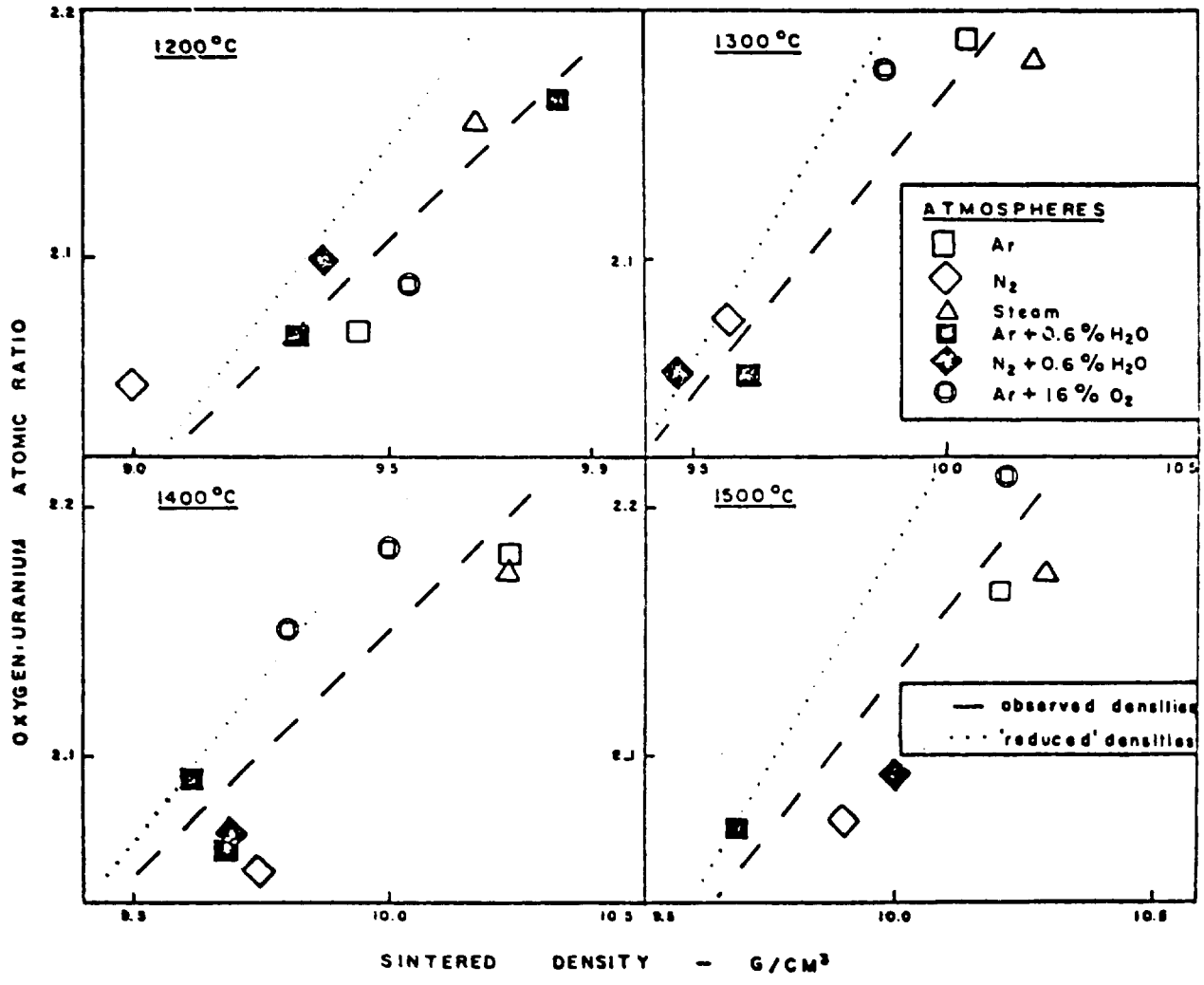

Figure 4 — Correlation between the sintered densities and the oxygen/uranium atomic ratios of UO_{2+x} fired compacts (after ref. 142)

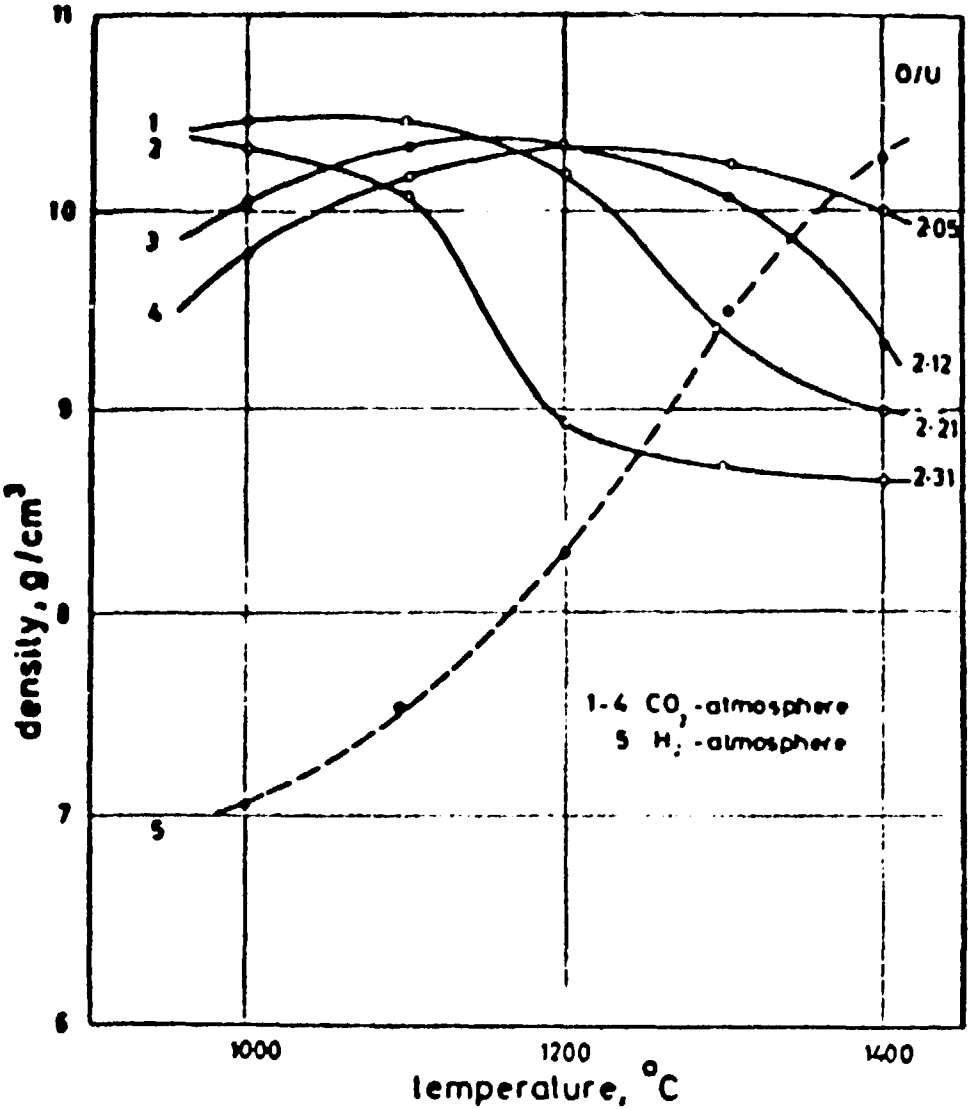

Figure 5 – The effect of deviations from stoichiometry in UO_{2+x} on the final sintered density. CO_2 and H_2 atmospheres were used the H_2 atmosphere corresponds to approximately stoichiometric UO_2 (after ref. 138).

Müller[107,138] studied the effect of UO_2 stoichiometry deviation on the sintering of UO_2 in CO_2 and hydrogen. His results, shown in Figure 5, do not show the same trends indicated in Figure 4. For increasing $\frac{O}{U}$ values the final densities decreased, for sintering at 1400°C; the overall variation trends are quite complex, in contrast with the results discussed before, suggesting that equilibrium sample-CO_2 atmosphere was not attained.

An unfavourable effect of hydrogen on sintering, when compared with CO_2, was not observed in the 1000-1400°C sintering temperature range.

2.5 – Williams' Experimental Correlation between $\frac{O}{U}$ Ratios and Compact Densities for the Final Stage of Sintering in Argon

Williams et al.[145] were able to obtain a very uniform correlation between $\frac{O}{U}$ ratios and compact final densities. Since this relationship approaches quite closely that obtained in the thesis research herein, it will be discussed in some detail.

The uranium oxide was prepared by pyrolysis of ammonium diuranate at 300°C and hydrogen reduction at 600°C. The resulting stoichiometric oxide was cooled in hydrogen and thereafter maintained in argon uninterrupted, until its compaction in an argon-filled glove box. Air was admitted to the oxide, samples of which were taken at intervals for sintering in argon. In this way, it was thought the particle size of the resulting material would be constant, independent of the variable oxygen content. It is convenient to remark here that room-temperature oxidation of fine uranium oxide powders could originate particle break-up, variable with the degree of oxidation (as shown in Table IV); by oxidizing compacts, it is reasonable to suppose particle break-up was eliminated or substantially reduced.

The experimental results showed that the density of the sintered compacts increased substantially with oxygen content up to about 2.02; the density increase was smaller in the 2.02-2.18 $\frac{O}{U}$ range.

The investigators did not describe exactly the sintering cycle used; the oxygen partial pressure of the sintering atmosphere was also not mentioned. However, if the soaking, heating and cooling times were small, it is possible the $\frac{O}{U}$ did not vary too much during sintering. With these restrictions, the Williams et al[145] correlation between $\frac{O}{U}$ and final density is the most uniform and reliable among all those discussed till now.

2.6 – Recent Investigations of the Intermediate and Final Stages* in UO_2 Sintering

Burton and Reynolds[28] (1972) studied the final stage sintering of uranium dioxide in the temperature range 1350-1700°C, for which the porosity is located mainly on grain boundaries. The initial porosity of the material was approximately 3.5% and sintering was performed in hydrogen to maintain stoichiometry. The sintering process was followed by measuring density changes using a density gradient column technique; density changes of 0.05% could be detected.

---

* Understood as stages 2 and 3, defined in item 2.1; more comprehensive definitions of the sintering stages are given in Appendix 1.

The observed reduction in the rate of sintering with time was considered to be due only to the progressive reduction of the number of pores. The distribution of pore sizes determined using scanning electron microscopy, with the knowlwdge of the volume change of an individual pore, allowed the derivation of shrinkage versus time relationships in agreement with experimental data.

The change in volume with time for a pore was derived using an equation given by Hull and Rimmer[57]:

$$\frac{dv}{dt} = \frac{-4\pi\ \gamma_B \Omega\ \delta_B D_B}{kT_x} \qquad (2.19)$$

v = pore volume

t = time

$\gamma_B, \Omega, \delta_B, k, T$ as defined in Table II

x = mean pore spacing on the grain boundary

The mean pore spacing was taken approximately euql to $1/\sqrt{n_A}$, where n_A is the number of pores per unit area of grain boundary. Since compacts fractured mainly along grain boundaries, n_A was taken as the number of pores per unit area on SEM fractographs.

It was concluded that the final stage of UO_2 sintering in hydrogen is controlled by grain boundary diffusion.

One of the most comprehensive phenomenological studies of the UO_2 sintering stages 2 and 3 was developed in 1975 by Coleman and Beere. Sintering was carried out in flowing hydrogen at 1250, 1400 and 1500°C. Their UO_2 compacts initially had a fractional volume of total porosity equal to 0.37, with open and closed porosity of 0.36 and 0.01 respectively.

The open porosity decreased continuously during sintering, and when it reached 0.15 the closed porosity began to increase, and thus indicated the transition from the intermediate to final stage; the closed porosity attained a maximum of 0.05 at 1600 minutes. It was observed that after 1600 minutes the grain growth during sintering followed a cubic law, but prior to this (in the intermediate sintering range) the rate of growth was significantly smaller.

Applying Beerés[21] equation for a volume diffusion mechanism, a self-diffusion coefficient for uranium was calculated, in good agreement with literature data. Beeré's equationis the following:

$$\frac{d}{dt}\left(\frac{\Delta V}{V}\right)_0 = \frac{-\pi D_v \gamma \Omega}{kT\ell^3}\left(K + \frac{L \sin\theta}{A}\right)\ell \qquad (2.20)$$

$$\left(\frac{\Delta V}{V}\right)_0 = \text{volume fraction of open porosity} \qquad (2.21)$$

D_v, γ, Ω, k as defined in Table II

K = surface curvature

L/A = ratio of the periphery to area of the boundary interfaces between grains

θ = dihedral angle

ℓ = distance between corners on the grain boundary faces

The term $(K + \frac{L \sin \theta}{A})$ takes on a value of 3.8 ± 0.4 for a dihedral angle of 45°, adequate for UO_2, and for volume fractions of porosity ranging from 0.05 to 0.25.

It was not possible to derive activation energy values in agreement with those typically associated with uranium volume diffusion.

For the final sintering stage Coleman and Beeré[34] applied their equation for grain boundary diffusion sintering mechanism; they calculated a grain boundary diffusion coefficient equal to that obtained by Burton and Reynolds[28].

Therefore the investigations of Burton, Reynolds[28] and Coleman-Beeré[34], indicated grain boundary uranium diffusion as the dominant mechanism for the final stage of UO_2, sintered in hydrogen. This result is in agreement with that obtained by Ashby (shown in Figure 1) and that reached in this thesis (cf. Figure 3) for UO_2 gels.

3 – NONSTOICHIOMETRY AND THE SINTERING OF DEFECT OXIDES

3.1 – Nonstoichiometry

Structural descriptions and thermodynamic treatments of nonstoichiometric compounds are the subject of detailed and comprehensive reviews by Kroger and Vink[78], Anderson[6] and Wadsley[139].

A compound chemical species with exact integral stoichiometry constitutes a concept based on Dalton's Law of Definite Proportions. Kurnakov[84,85] and co-workers discovered in the early 1900's that certain intermetallic compounds could contain elements in nonstoichiometric proportions. It is interesting to observe that Dalton's Law had been challenged at the time of its statement by Berthollet, who maintained that compounds had variable compositions. According to Kurnakov's classification, nonstoichiometric compounds belong to a general class of phases with variable composition called "Berthollides"; stoichiometric compounds form a special class he designated "Daltonide".*

Proust's principle is valid for molecular compounds[24], but Wagner and Schottky[141] showed theoretically that it cannot be extended to those crystalline solids formed by three-dimensional assemblies of atoms or ions to which statistical thermodynamics methods are applicable. It is now widely accepted that all crystalline inorganic compounds are inherently nonstoichiometric[92].

The ability of nonstoichiometric compounds to maintain a certain structure, practically without modification over a significant range of chemical composition, is often explained by the presence of vacancies or interstitial atoms, or by the replacement of a metal ion by a nonmetal ion. However, it is not satisfactory to consider these types of defects as the only possible alternatives. Certain features of some oxide phases, for instance, suggest that probably the correponding strutural defects are planar[83].

The analysis of the nature and significance of defects of all types is of utmost importance for relating physical and chemical properties of crystalline solids[45]. Considering that all solid state reactions take place by the movement of lattice imperfections, sintering and chemical reactivity are strongly affected by deviations from stoichiometry. Solid-gas reaction such as oxidation and reduction, that determine the equilibrium conditions prior to sintering, are also influenced by the degree of nonstoichiometry of the solid.

---

* In this work $UO_{2\pm x}$ will be considered "stoichiometric" when $0 < x < 0.0005$. The value $x = 0.0005$ corresponds approximately to the detection limit for stoichiometric deviations in analytical chemistry methods, such as that described by I. G. Jones, in AERE-R 6962 (1973).

3.2 – The Structure of Stoichiometric UO_2

The stoichiometric UO_2 fluorite structure is that expected for a typical MX_2 oxide with a large quadrivalent cation[47]. The eight-coordinate structure consists of a close-packed cubic array of cations in which all the tetrahedral sites are occupied by anions. Each anion is surrounded tetrahedrally by cations and each cation is surrounded by eight anions at the corners of a cube. This type of structure is the most prevalent MX_2 type. The fluorite structure of nonstoichiometric UO_2 is more complex, presenting irregularities such as Frenkel and Schottky defects.

3.3 – Frenkel Defects in Fluorite Structures

Due to their nature, Frenkel defects are generally important in crystals with a lattice structure which is open enough to accomodate interstitial ions without much distortion[47]. Such is the case of substances with low coordination number. For structures of high coordination number, there is less room for insterstitial ions, and consequently the energy for the formation of Frenkel defects reaches large values. In this cases the formation of Schttky defects is more probable.

In the fluorite-type structure, only the anion lattice is substantially subject to Frenkel defects[47]. This is due to the fact the anions, though larger than the cations, have a coordination number equal to 4, smaller than that corresponding to the cations (coordination number equal to 8). It is convenient to observe that more frequently the occurrence of Frenkel defects is limited to the sublattice of the smaller ion, usually the cation, clearly easier to displace than the larger ions; this does not happen in the fluorite-type structures as a consequence of the above mentioned peculiarity of the crystal lattice, related to the ion coordination numbers.

3.4 – Effect of Frenkel Defects on Densities

Small concentrations of Frenkel defects leave the density practically unchanged in stoichiometric crystals. This is due to the fact that the number of interstitial ions always match the number of Frenkel vacancies, within the volume of such crystals. However, in the case of nonstoichiometric crystals, if the supernumerary ions are located in interstitial sites without the corresponding number of vacant sites being created, the density may increase[47]. Such an increase is observed for hyperstoichometric UO_2.

3.5 – Equilibrium Concentration of Frenkel Defects

Even in stoichiometric uranium oxide, defects are present. These defects are originated from the general spontaneous tendency of all systems to increase their entropy. At any temperature the number of defects N_v will be such as to minimize the free energy of the crystal. Once an expression for the free energy of a crystal is known, minimizing it with respect to N_v permits the determination of the number of defects.

It can be shown that[47]:

$$n_f \simeq \sqrt{NN^*}\, e^{-w_f / 2RT} \tag{3.1}$$

where

n_f = number of ions that leave their lattice sites to go into interstitial positions = one half of the number of Frenkel defects

W_f = energy of formation of one mole of Frenkel defects

N = lattice sites per cm^3 in the sublattice affected by Frenkel defects

N^* = interstitial positions per cm^3

R = ideal gases constant; T = absolute temperature for UO_2, W_f = 79 Kcal/mole[47].

3.6 – Nonstoichiometric Phases

A stoichiometric compound MX corresponds to a point on the vapor pressure-composition curve at which the number of cations and anions in the solid phase are equal. When a crystal is in contact with the vapor of one of its constituents at high temperatures, nonstoichiometry might occur. The composition of the solid phase depends on the activity of that constituent in the vapor phase, in case thermodynamic equilibrium is reached[47].

Defect fluorite structures occur extensively among MX_2-type oxides and UO_{2+x} is among these. The defect structure may originate from the systematic substitution of either anion or cation by other ions of similar size, but with preservation of eletroneutrality. Another common defect structure arises when supernumerary anions occupy interstitial positions in the fluorite lattice. It is noteworthy that increasing oxygen content might correspond to a decrease in the lattice because the added ions merely fill vacant anion sites or large interstitial positions, while the cations become smaller and more highly polarizing. In UO_{2+x} the supernumerary anions occupy interstitial positions. The reduction of lattice constant a_o with increasing oxidation is due to the fact that the radius of U^{5+} is 10% smaller than the radius of U^{4+} (ref.(47)). The variation of the lattice constant with stoichiometry deviations x($0 < x < 0.25$) is given by[116]

$$a_o\,(\text{Å}) = 5.468 - 0.12x \tag{3.2}$$

Hockstra[90] shows an approximately linear variation of density with x, from 10.80 $g.cm^{-3}$ (x = 0) to 11.15 $g.cm^{-3}$ (x = 0.25).

For UO_{2+x}, if the activity of O_2 in contact with the solid is increased beyond the value adequate to maintain stoichiometry ($UO_{2.000}$), then the concentration of O^{2-} within the crystal must also increase to sustain equilibrium. The excess of O^{2-} goes into interstitial positions. Then in order to provide for electroneutrality, some U^{4+} ions are oxidized to U^{5+}. This reaction can be expressed in the following way[100]:

$$\frac{1}{2}\,X_2\,(g) + 2e^- = X_i^{2-} \tag{3.3}$$

$$M_\ell^{4+} = M_\ell^{5+} + e^- . \tag{3.4}$$

In the equations, MX_2 corresponds to UO_2, (g) indicates the gas phase, i and ℓ signify interstitial and lattice sites respectively.

In the uranium oxide fluorite lattice:

$$UO_2 + \frac{x}{2}\,O_2 = UO_{2+x} . \tag{3.5}$$

In the pressure of O_2 is decreased below the value appropriate for equilibrium, some U ions are reduced in order to maintain the charge balance. These ions go into interstitial positions. The associated reaction is:

$$M_{\ell}^{4+} + 2X_{\ell}^{2-} = X_2\,(g) + M_i^{4+} + 4e^-\,(\text{trapped near } M^{4+}) \tag{3.6}$$

It will be shown later that U ions in interstitial positions are particularly important for sintering in UO_{2+x}. Another way hypostoichiometric uranium oxide can be formed is by evaporating oxygen, leaving vacant anion sites and electrons trapped nearby; the corresponding equations are:

$$2X_{\ell}^{2-} = X\,(g) + 2\,\square_2 - + 4\,(\text{trapped } e^-) \tag{3.7}$$

$$M_{\ell}^{4+} + 4\,(\text{trapped } e^-) = M_{\ell} \tag{3.8}$$

The number of defects created in MX_{2+x} by a given oxygen pressure can be calculated. Let us consider the case of UO_{2+x}, in which the predominant anion defects are Frenkel-type, i.e. anion vacanies and interstitial oxygen atoms. Positive deviations from stoichiometry will occur by addition of oxygen to the crystal, the total number of vacant anion sites, N_{io} the number of interstitial anions, N the number of anion lattice sites and N^* the number of interstitial sites per cm^3. The value $\alpha = N^*/N$ is a constant for a given crystal structure; it depends only on the geometrical factors of such crystal structure[47].

The stoichiometric excess of oxygen in UO_{2+x} is given by:

$$x = \frac{N_{io} - N_{vo}}{N} \tag{3.9}$$

The value of x is positive when there are more interstitial anion sites than vacant anions. For $N_{io} = N_{vo}$ the crystal is stoichiometric.

If $N_{io} \ll N^*$ and $N_{vo} \ll N$, it is possible to write[47]:

$$N_{io} = N^* \sqrt{[p(x)]}\; K_x e^{-w_i / kT} \tag{3.10}$$

p(x) = oxygen pressure above the crystal of composition UO_{2+x}

w_i = energy required to place one anion on an interstitial site

K_x = normal partition function of an oxygen ion on a normal lattice site.*

From this equation it can be concluded that the greater the pressure p(x) and the smaller the energy w_i to create an anion interstitial, the greater will be the number of such interstitials, and therefore the greater the stoichiometry deviation.

It is also possible to determine the pressure required to achieve a given deviation from stoichiometry[47].

---

* K = is a function of the energy, w_x, liberated when 1/2 O_2 is dissociated, ionized, and placed on a lattice site proper to O^{2-}.

$$\frac{p(x)}{p(O_2)} = 1 + \frac{x^2 + x\sqrt{(x^2 + 4\delta^2)}}{2\delta^3} \qquad (3.11)$$

$\delta = \frac{N_F}{N}$ = intrinsic disorder of the stoichiometric crystal

N_F = number of Frenkel defects in a stoichiometric crystal

$p(O)$ = pressure of oxygen above a stoichiometric crystal.

The preceding equation gives the fundamental relation between the equilibrium pressure, intrinsic disorder, and deviation from stoichiometry. It is clear that the greater the intrinsic disorder, δ, of the stoichiometric crystal, the smaller is the relative pressure variation necessary to originate a certain deviation x from stoichiometry. When the stoichiometric crystal is well ordered, without being subjectd to a large number of inherent lattice defects, the values of x are relatively small. In the case of UO_{2+x}, the maximum deviation from stoichiometry is considered to be large[47].

A change in valence of some of the ions in a crystal takes place when a deviation from stoichiometry occurs. In general the deviation from stoichiometry happens in the direction of another stable oxidation state of the element involved.

For UO_{2+x}, $U^{4+} \rightarrow U^{5+}$. Another uranium stable oxidation state is U^{3+}, but the change $U^{4+} \rightarrow U^{3+}$ does not develop so favorably[91]. The increase in cation valence increases the lattice energy of the crystal and diminishes the cation radius; both effects contribute to the high stability and homogeneous range of the hyperstoichiometric composition.[47]

The analysis of small deviations from stoichiometry has been the object of many treatments[47,92,141], with results agreeing satisfactorily. However, for the fluorite phase UO_{2+x} the upper values of x is not small and the corresponding treatment is considerably more complicated.

Four types of large deviations from stoichiometry can be considered[87], but they are not always independent. Each type is a limiting description and a certain substance may present the characterisitics of more than one type, the main intervening factors being the magnitude of the defects interaction energies, temperature, and packing considerations. The four modes are the following: (i) submicroheterogeneity within a single phase; (ii) intermediate phases corresponding to shear structures; (iii) homogeneous array of defects of quasi-random character; (iv) intermediate phases structured on superlattice ordering of defects.

Greenwood[47] considers submicroheterogeneities within the fluorite phase as the main type of large deviation from stoichiometry in UO_{2+x}. It was Ariya[9] who indicated that it is possible for isolated microdomains to exist within a homogeneous phase. The local symmetry of such microdomains approximate that of a different crystal structure. It is considered that the submicroheterogeneous structure does not localize rigidly within the lattice, but migrates, continuously changing form and dimensions. The microdomains do not act as nuclei for growth of a second phase due to their small size. They do not originate superlattice lines in their x-ray patterns because they have a random distribution throughout the crystal.

Two structures occur in oxygen-rich uranium dioxide[47]: an oxygen-deficient U_4O_9 structure, $UO_{2.25-y}$, and a random nonstoichiometric phase UO_{2+x}. In both structures there are defect complexes consisting basically of two interstitial anions and a vacant anion site. A defect-complex of this type arise from the insertion of an interstitial anion into the fluorite structure of UO_2, with the displacement of a nearby anion from a regular anion site. There is one such defect-complex per unit cell in U_4O_9, and the orientation is such that a large superstructure cell is built.

For small values of x in UO_{2+x}, the same defect complexes are present, but they are orientated at random; for increasing values of x there is a tendency toward ordering, UO_{2+x} and U_4O_9 partaking the same type of structure. The entropy of UO_{2+x} is higher, but the difference decreases for increasing values of stoichiometry deviation and temperature. At approximately 1130°C the UO_{2+x} still has higher entropy than U_4O_9, but the entropy value is substantially smaller than that corresponding to a completely random distribution of the defect complexes. In these circumstances, when the positions and orientations of the defect complexes present a significant degree of order, the ordered U_4O_9 structure appears as submicrodomains within the UO_{2+x} phase[76].

The basic defect-complex can be indicated by $[(O_i^{2-})_2 \square_-]$.

Kofstad[94] presented a different description for the defect complex, that would consist of two displaced anions, the two corresponding vacancies and one or two interstitial anions. The so called 2:2:1 model has only one of the O', O'' sites occupied, in the UO_{2+x} defect structure shown in Figure 6. When both O' and O'' sites are occupied, two of the basic defect complexes $[(O_i^{2-})_2 \square_-]$, previously mentioned, can describe the structure that corresponds to the model designated 2:2:2 (two displaced anions, two interstitials and two vacancies).

Saito[95] considered the 2:2:2 model as satisfying the data from UO_{2+x} neutron diffraction better. He assumed that of four U^{5+} ions formed per interstitial pair O'-O'', two U^{5+} ions are trapped in the two uranium sites nearest to the O', O'' atoms, the other two U^{5+} ions being free to move in the lattice.

Kofstad[76] judged also the 2:2:2 model to describe better the available experimental data, particularly that obtained from electrical conductivity studies.

It is convenient to observe that the microdomains are not really different phases, since their extent and location fluctuate continuously, in dynamic equilibrium[47]. In this situation it is not possible to define two-phase boundaries. Only when the dynamic fluctuation substantially loses its intensity, it becomes possible to distinguish two-phase boundaries.

3.7 – The Phase Diagram and the Oxygen Partial Pressure of $UO_{2\pm x}$

Figure 7 shows the phase diagram for UO_{2+x}, with the corresponding equilibrium oxygen pressures indicated for different values of O/U. The pressure-composition curves reveal when a solid phase of variable composition is formed. According to the phase rule, a two-component system with one volatile component is univariant when two solid phases are present. The system is bivariant when only one nonstoichiometric phase corresponds to the composition being considered*.

The rectangular area indicated in Figure 7 by dashed lines, shows the region of the diagram where previous sintering studies of ceramic grade** UO_2 powders were carried out.

A more extended portion of the oxygen-uranium phase equilibrium diagram is presented in Figure 8. This diagram comprises the composition range usually most significant in the applications of

---

* $F + P = C + 2$, with F = number of degrees of freedom, P = number of phases, C = number of components = 2 for $UO_{2+x} + 1/2\ O_2$. The gas phase being always present, it is possible to write $F + P_S = C + 1$, where P_S is the number of coexisting solid phases; if F_T is the number of remaining degrees of freedom at a certain temperature T, $F_T + P_S = 2$ becomes valid. Then, when at a certain composition and temperatrue there are two nonstoichiometric phases present, $F_T = 0$ and the pressure is constant; if only one nonstoichiometric phase appears, the pressure can vary, since it is the remaining degree of freedom.

** UO_2 powder with surface areas between 1.0 and 6.0 m^2/gram.

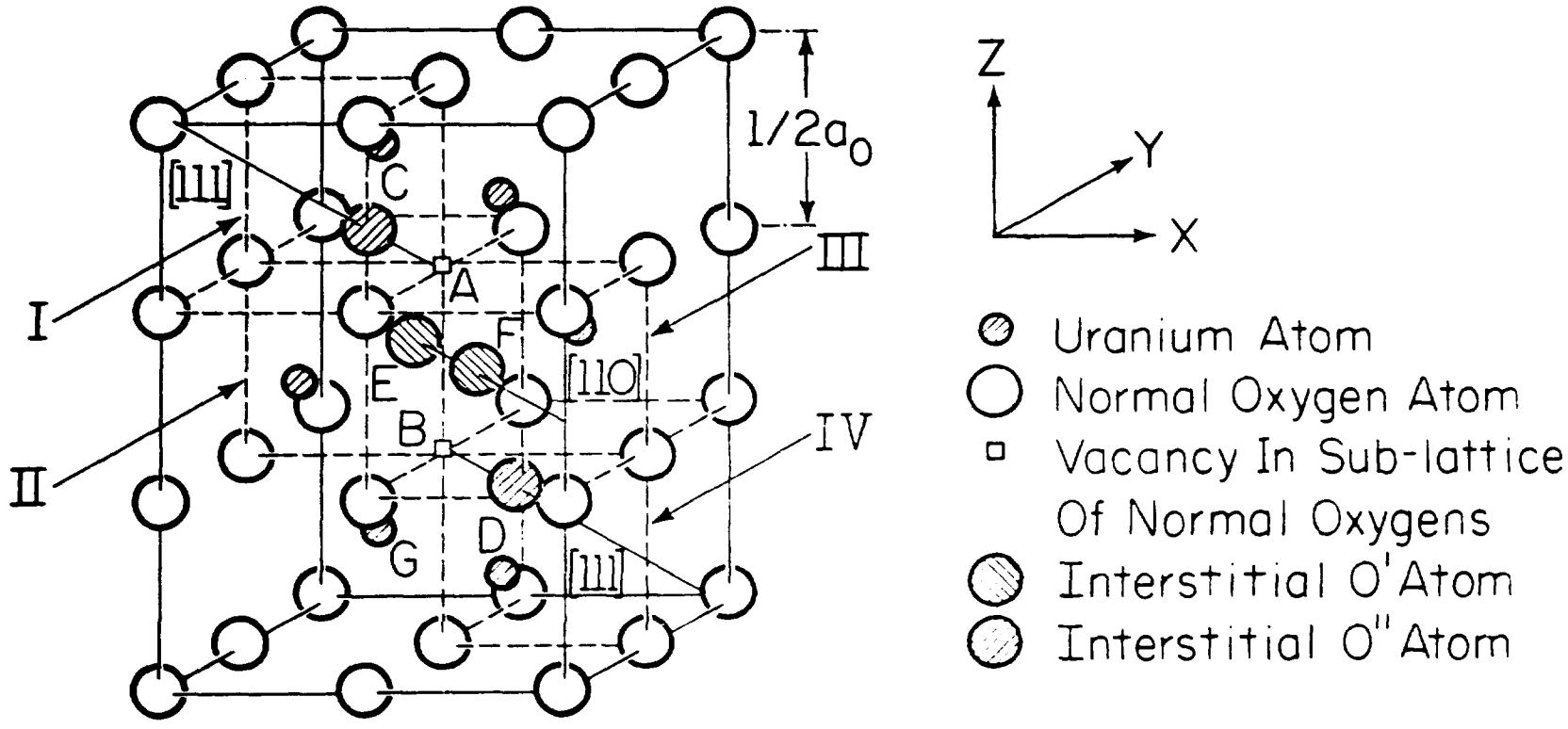

Figure 6 – Willis model for UO_{2+x} structure (after ref. 147). There are two kinds of interstitial sites O' and O'' that can be occupied by oxygen. The O' site marked E is approximately 1 Å along the $<110>$ direction from the center of the insterstitial hole in the fluorite lattice (the center of cube II). The O' site marked F is related to E by a 180° rotation about the line AB. When excess oxygen occupies the site O', they eject two nearest oxygen atoms from their normal positions at A and B, displacing them approximately 1 Å along the $<111>$ direction to the O'' sites marked C and D; in this process two normal oxygen vacancies V_o are created at A and B.

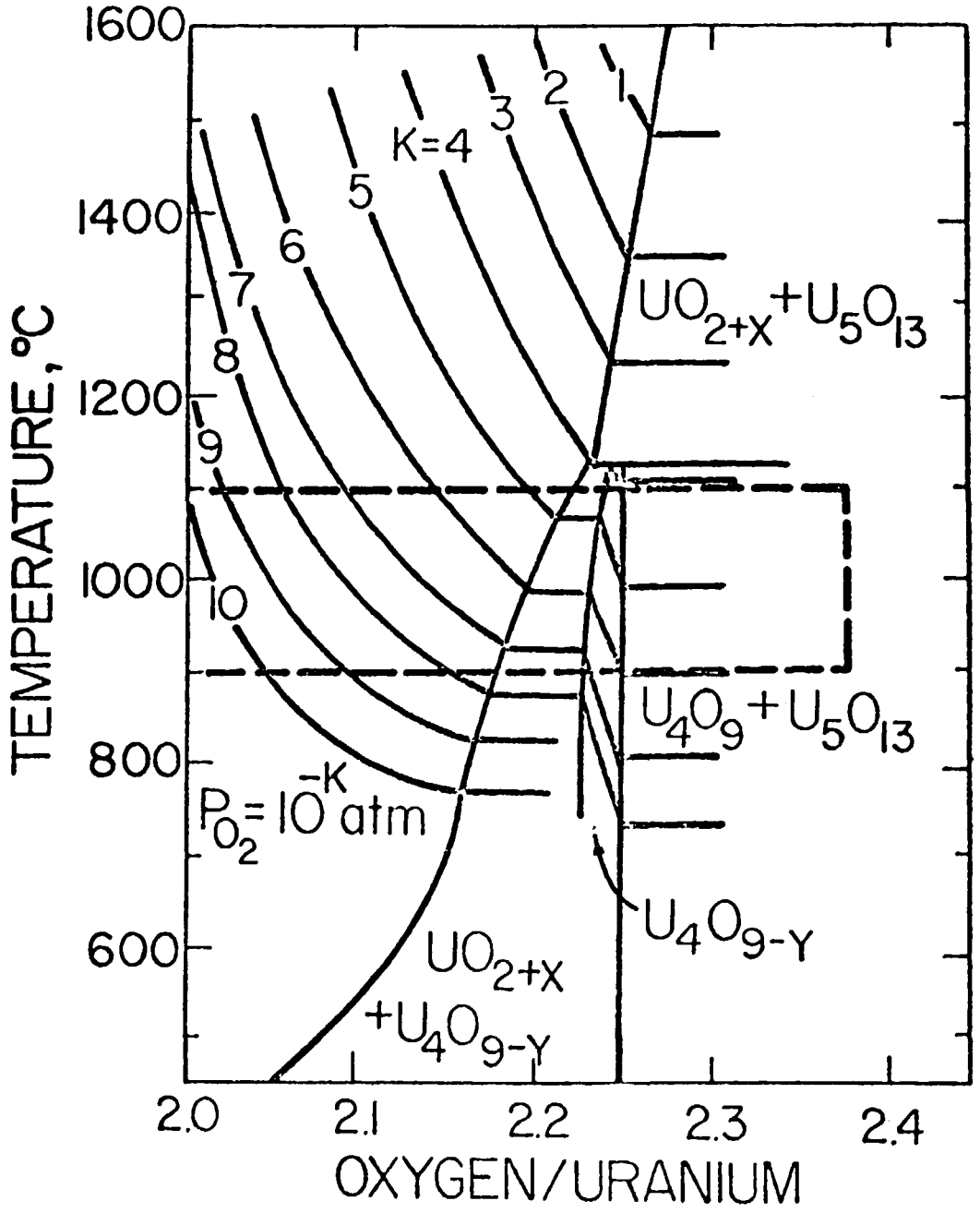

Figure 7 – Oxygen-uranium phase-equilibrium system with the equilibrium oxygen partial pressure in UO_{2+x} ($0 \leqslant x \leqslant 0.3$) indicated by $P_{O_2} = 10^{-K}$. The dashed lines show the region corresponding to most of the UO_{2+x} sintering studies under controlled oxygen potential developed until 1976 (in part after ref. 115).

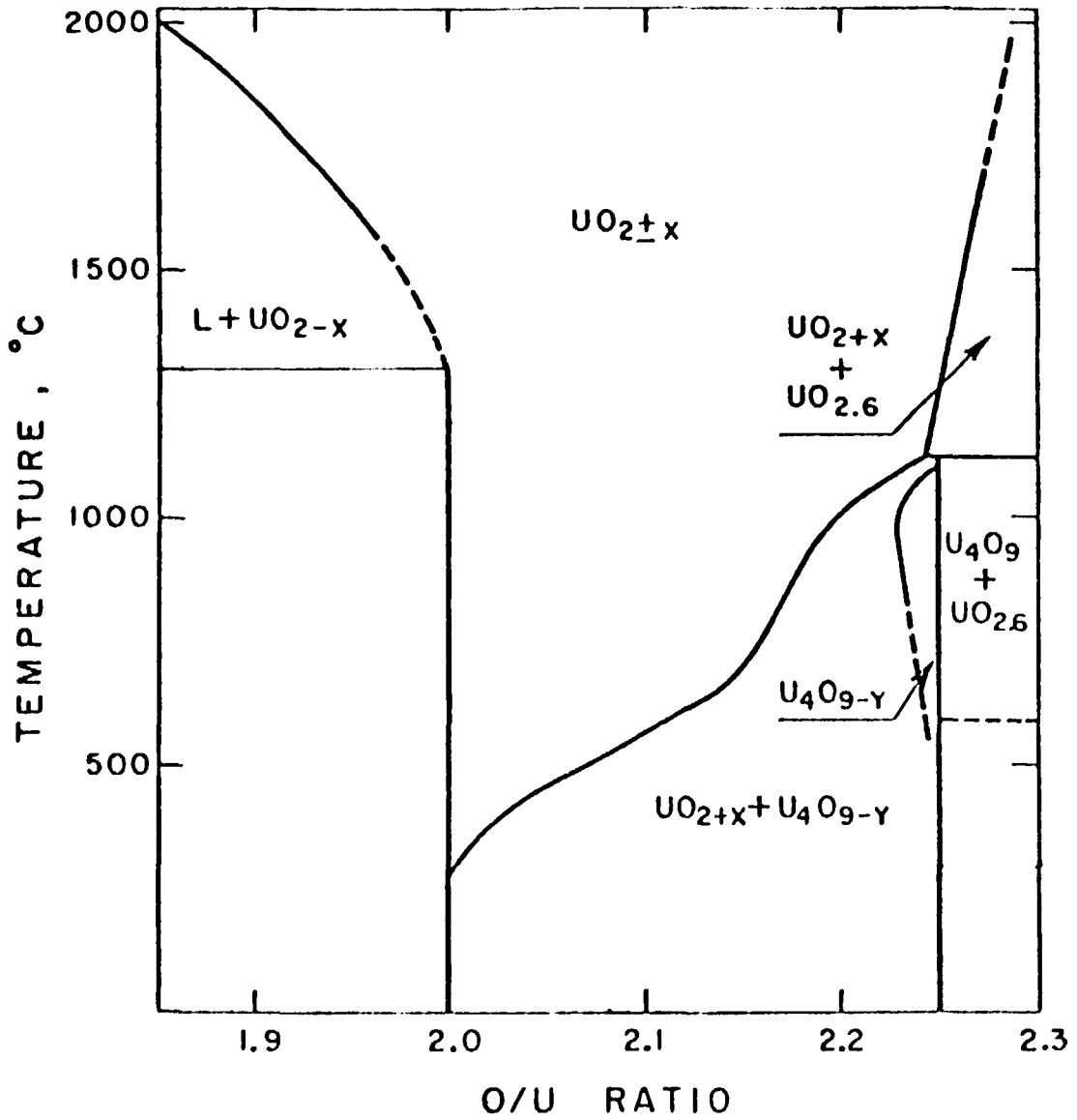

Figure 8 – Oxygen-uranium phase-equilibrium diagram comprising the composition range of more importance in the applications of uranium oxide (after ref. 117).

Table V

Thermodynamics of Oxygen in UO_{2+x} (after ref. 117)

	$\log P(O_2) = a + bT^{-1}$		$\bar{G}(O_2) = \bar{H}(O_2) - T\bar{S}(O_2)$	
O/U Ratio	a	- b	$-\bar{H}(O_2)$ cals mole^{-1}	$-\bar{S}(O_2)$ entropy units
2.0000	6.100	26,250	120,094	27.91
2.0010	4.563	22,848	104,528	20.877
2.0020	2.865	19,323	88,401	13.107
2.0030	1.800	17,196	78,667	8.233
2.0040	1.174	15,732	71,795	5.373
2.0050	0.664	14,684	67,179	3.037
2.0060	0.364	14,027	64,175	1.667
2.0070	0.391	13,788	63,080	1.790
2.0080	0.506	13,821	63,230	2.315
2.0090	0.526	13,656	62,476	2.406
2.0100	0.783	13,734	62,833	3.580
2.0110	0.629	13,517	61,841	2.877
2.0120	0.689	13,496	61,745	3.152
2.0130	0.775	13,509	61,807	3.547
2.0140	0.846	13,512	61,818	3.873
2.0150	1.035	13,619	62,307	4.734
2.0160	0.998	13,555	62,014	4.565
2.0170	1.097	13,613	62,280	5.018
2.0180	1.168	13,637	62,391	5.343
2.0190	1.230	13,652	62,456	5.627
2.0200	1.572	13,795	63,112	7.194
2.0250	1.397	13,606	62,249	6.392
2.0375	2.242	14,290	65,377	10.257
2.0500	2.800	14,702	67,267	12.812
2.0625	3.447	15,192	69,491	15.772
2.0750	3.892	15,494	70,885	17.808
2.0875	4.308	15,781	72,199	19.710
2.1000	5.046	16,544	75,687	23.087
2.1125	4.951	16,133	73,808	22.652
2.1250	5.375	16,422	75,129	24.592
2.1375	5.438	16,217	74,192	24.877
2.1500	5.806	16,417	75,107	26.563
2.1625	5.924	16,221	74,213	27.104
2.1750	5.720	15,600	71,370	26.171
2.1875	5.863	15,429	70,587	26.824
2.2000	6.609	16,159	73,916	30.238
2.2125	7.445	16,997	77,760	34.061
2.2250	8.222	17,720	81,071	37.616
2.2375	9.269	18,834	86,168	42.405
$UO_{2+x} + U_4O_{9-y}$	11.990	22,488	102,884	54.856

uranium oxide. Some of the phase limits are still subject to some doubt. It is known that UO_{2-x} exists at high temperatures. Upon cooling the hypostoichiometric oxide disproptionates into metallic uranium and stoichiometric UO_2, but the corresponding phase boundary is not well known. Apparently hypo-stoichiometric uranium dioxide does not exist at temperatures below about 1600°C[117].

The reaction involving the formation of $UO_{2\pm x}$ is[117]:

$$UO_2 \text{ (solid)} \pm \frac{x}{2} O_2 = UO_{2 \pm x} \qquad (3.12)$$

If $p(O_2)$ is the equilibrium oxygen pressure for this reaction, then:

$$\bar{G}(O_2) = RT \ln p(O_2) \qquad (3.13)$$

where

$\bar{G}(O_2)$ = partial molar free energy of oxygen

$p(O_2)$ = oxygen pressure

R,T as defined in Table II.

Expressing the free energy in terms of entropy $\bar{S}(O_2)$ and enthalpy $\bar{H}(O_2)$:

$$\bar{G}(O_2) = \bar{H}(O_2) - T\,\bar{S}(O_2) = R\,T \ln p(O_2), \text{ or} \qquad (3.14)$$

$$\log p(O_2) = a + b\,T^{-1} \qquad (3.15)$$

with $a = -\bar{S}(O_2)/4.575$ and $b = \bar{H}(O_2)/4.575$.

These equations are valid only for single-phase oxides; if a phase change occurs, there is a corresponding enthalpy change and an entropy of transformation. Table V presents the values of a, b, $\bar{H}(O_2)$ and $\bar{S}(O_2)$ utilized in this work.

It is important to observe that the errors in thermodynamic data of uranium dioxide are due, mainly, to the difficulty of precisely measuring oxygen to metal ratios[117]. The experimental obstacles are considerable. For instance, low temperature oxidation of samples might occur during cooling, even when cooling is done in hydrogen containing trace amounts of oxygen[117].

Due to the difficulty of controlling very low oxygen potentials[117], the thermodynamic data for uranium oxide with O/U < 2.003 present substantial variability in the literature. Figures 7 and 9, relating $p(O_2)$ with O/U, show data varying by about one order of magnitude for uranium oxides with composition close to $UO_{2.03}$, at approximately 1000°C; such discrepancies become more serious for smaller oxygen-uranium ratios [117].

As it was mentioned before, the uranium-oxygen system is bivariant when only one nonstoichiometric phase is present. Considering the equation $\log p(O_2) = a + b\,T^{-1}$, a hyperstoichiometric uranium oxide will have one set of coefficients a, b at temperatures above that at which UO_{2+x} disproportionates into $UO_{2+x} + U_4O_{9-y}$.

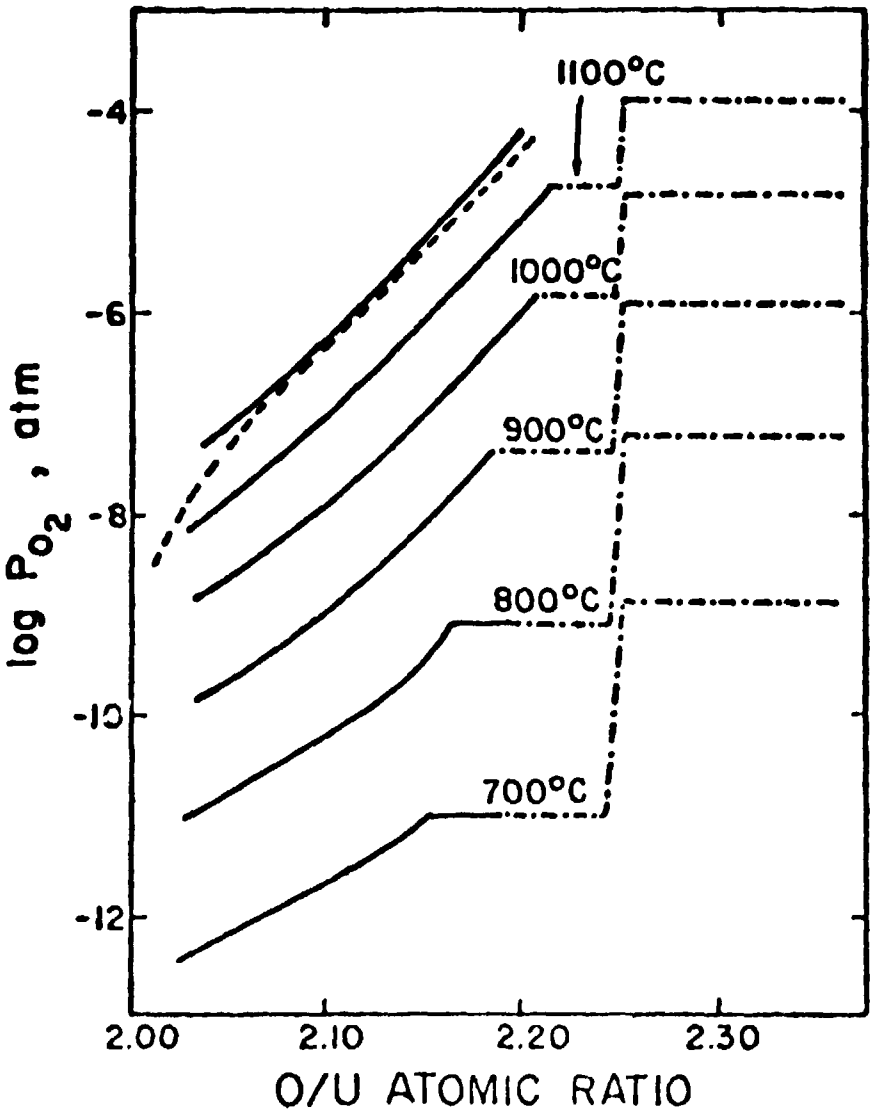

Figure 9 – Oxygen pressures at equilibrium for UO_{2+x}. The dashed line corresponds to data of Hagemark and Broli[99] (after ref. 125).

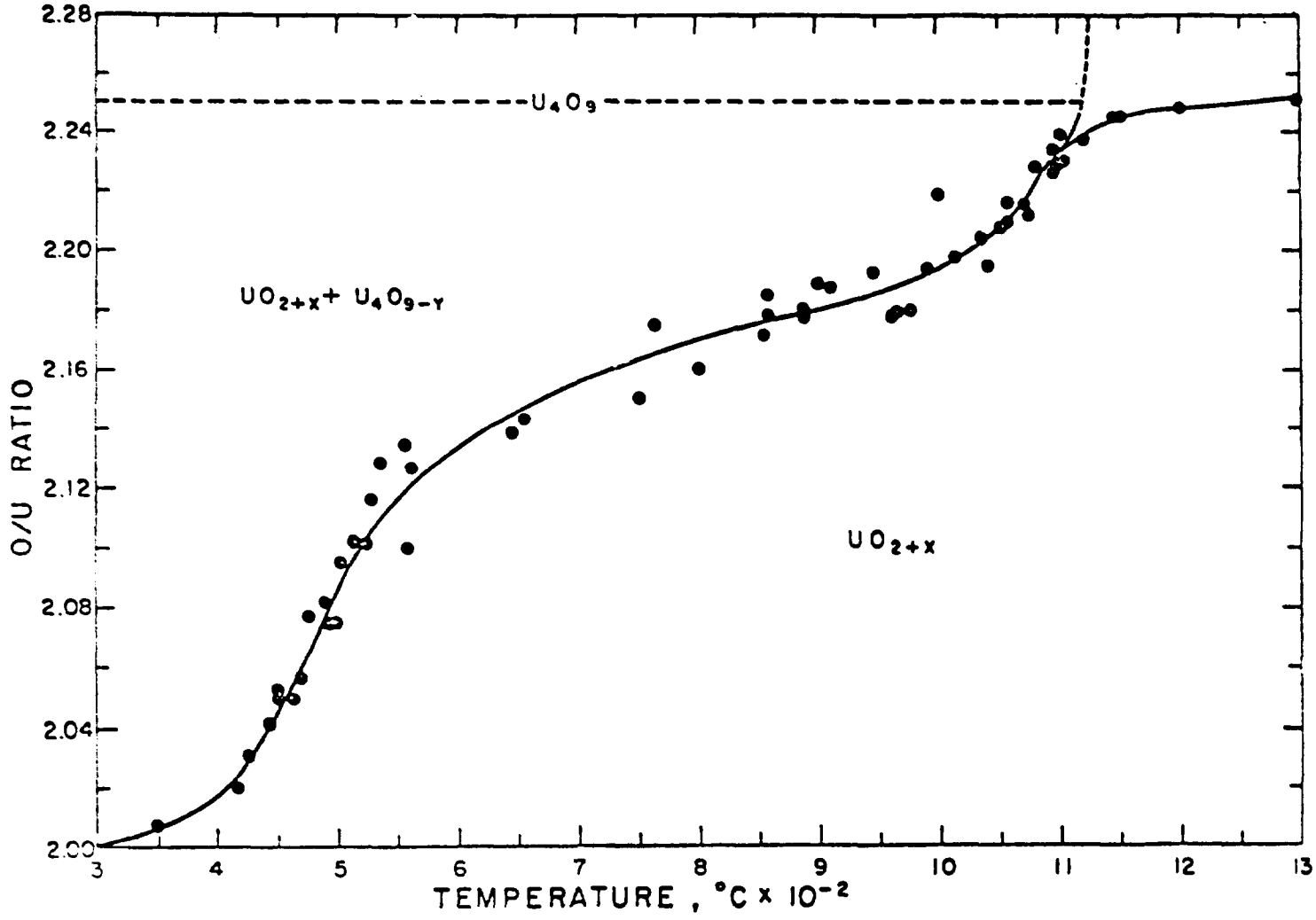

Figure 10 – The phase boudary $UO_{2+x}/UO_{2+x} + U_4O_{9-y}$ (after ref. 117)

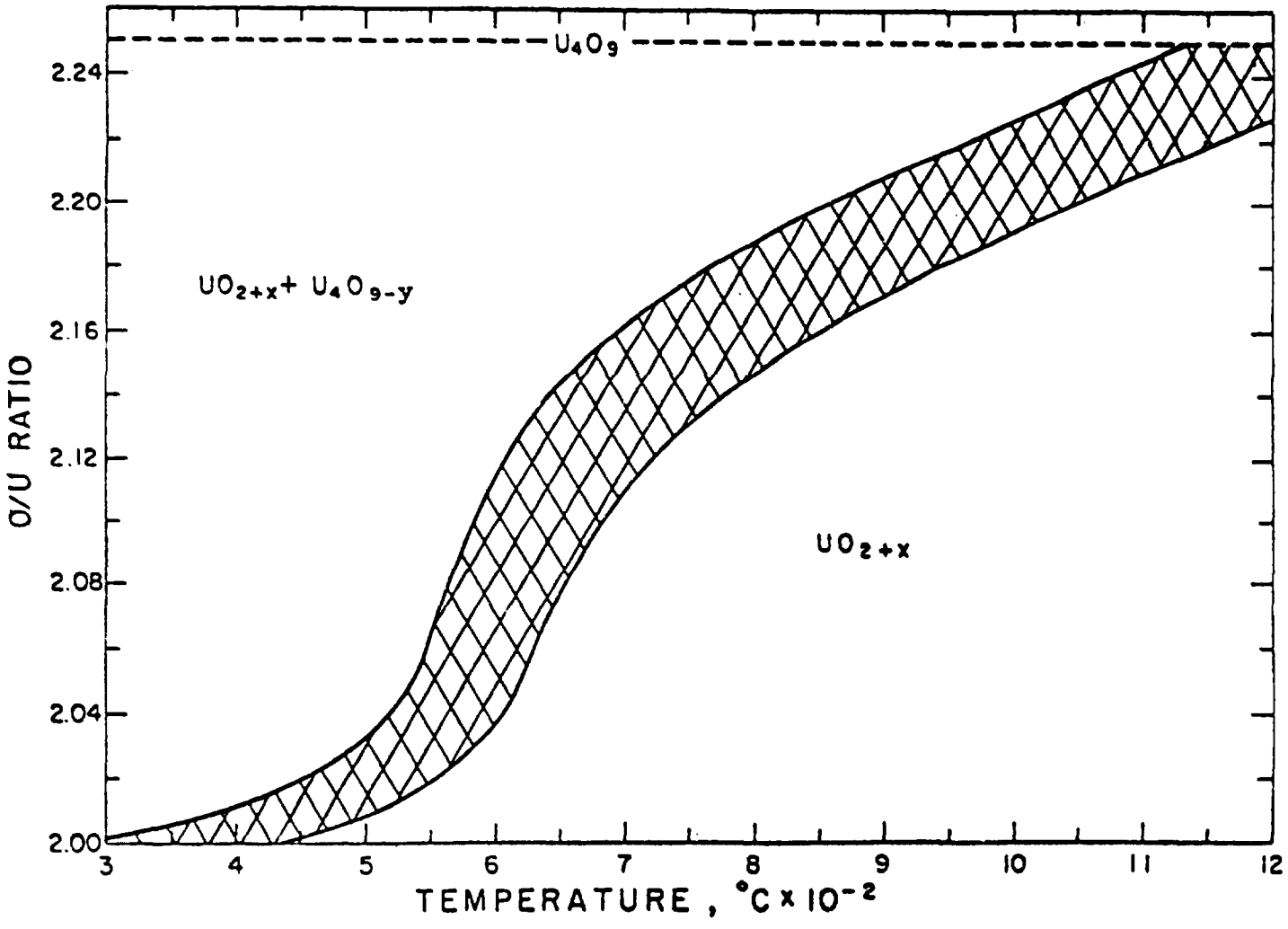

Figure 11 – $UO_{2+x}/UO_{2+x} + U_4O_{9-y}$ calculated phase boundary (after ref. 117)

The data available on the $UO_{2+x}/UO_{2+x} + U_4O_{9-y}$ phase boundary is plotted in Figure 10. Perron[98] calculated this phase boundary, obtaining the result indicated in Figure 11. There is good agreement only for ratios greater than about 2.12.

Figures 10 and 11 show that in the 750 to 1050°C range, the uncertainty of the O/U ratio corresponding to the $UO_{2+x}/UO_{2+x} + U_4O_{9-y}$ boundary may be as high as 0.03. The sintering experiments described here were planned considering this fact, since it was considered important to avoid the difficulties associated with sintering a material with a substantial amount of second phase present.

The variation of $p(O_2)$ of hypostoichiometric uranium oxide, as a function of temperature and of O/U, is presented in Figure 12. A statistically significant relation of the form $p(O_2) = f(T)$ has not been derived for the hypostoichiometric range, due to the limited data available[117].

3.8 – The Influence of Oxygen Partial Pressure on the Defect Structure of $UO_{2\pm x}$

The defect concentration in a compound is a function of temperature and partial pressure of their components[95]. For an oxide of the form MO_{2-x}, the nonstoichiometric reaction may be written:

$$MO_2 \rightleftharpoons MO_{2-x} + \frac{x}{2} O_2 \qquad (3.16)$$

It is seen qualitatively from this equation that on decreasing the oxygen pressure the oxygen deficit increases. For oxides with excess oxygen, the deviation from stoichiometry increases for increasing values of the oxygen pressure.

In the case of $UO_{2\pm x}$, the partial pressure of uranium is negligible in relation to the oxygen partial pressure for normal sintering conditions. Therefore, the nonstoichiometry in uranium dioxides results from the interaction of UO_2 with oxygen, in the surrounding gas atmosphere.

In UO_{2-x} an oxygen atom on a normal site is transferred to the gaseous state, forming an oxygen vacancy. There is no change in the number of lattice sites and the following defect reaction can be written:

$$O_o \rightleftharpoons V_o^x + 1/2\ O_2 \qquad (3.17)$$

For UO_{2+x} the formation of a neutral interstitial oxygen through reaction of oxygen with the oxide may be written:

$$1/2\ O_2 \rightleftharpoons O_i^x \qquad (3.18)$$

The neutral interstitial oxygen atoms ionize, yielding oxygen ions and electron holes with effective negative charges. The resulting structure is shown in Figure 6.

The defects in $UO_{2\pm x}$ are in equilibrium, at a given temperature and pressure, when the free energy of the system is at a minimum. The free energy G is given by:

$$G = H - TS \qquad (3.19)$$

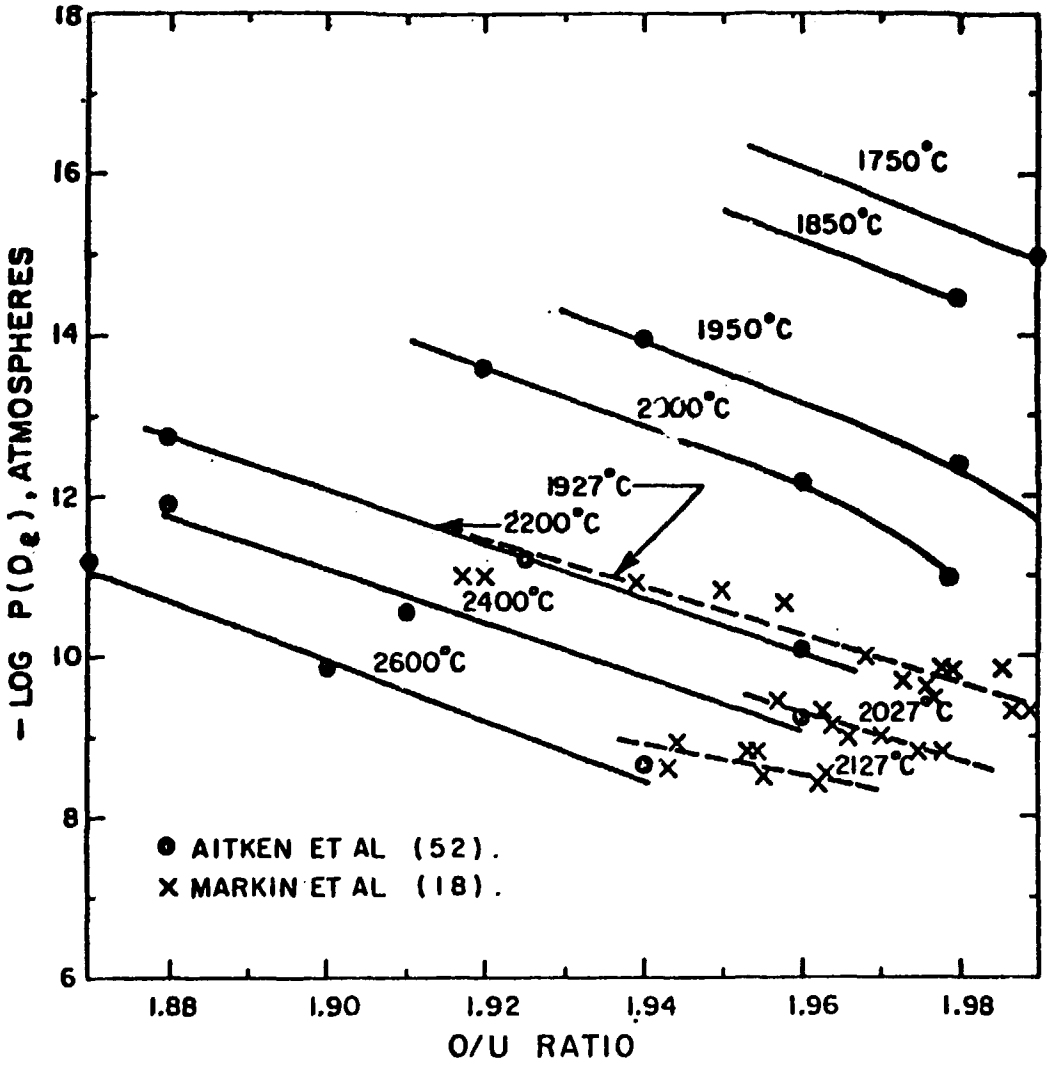

Figure 12 – The oxygen partial pressure of UO_{2-x} as a function of temperature and of oxygen-to-uranium ratio (after ref. 117).

T = absolute temperature

H = enthalpy

S = entropy

At equilibrium $dG_{T,p} = 0$.

Let us suppose a perfect crystal of UO_2 has N atoms. The total number of sites becomes N + n, if n vacancies are formed. In this situation the free energy change ΔG can be expressed as a function of the entropy change, ΔS, associated with the formation of the defects, and of the enthalpy of formation, ΔH, of the individual vacancies[74].

$$\Delta G = n\,\Delta H - T\,\Delta S \tag{3.20}$$

a) ΔS_{config}, a configurational entropy that arises from the distribution of n vacancies among the N + n sites;

b) ΔS_{vibr}, a vibrational entropy, originated by the change in vibrational modes of atoms close to each vacancy.

Therefore

$$\Delta G = n\,\Delta H - T\,\Delta S_{vibr} - T\,\Delta S_{config} \tag{3.21}$$

According to statistical thermodynamics $\Delta S_{config} = k \ln W$, where K is the Boltzmann's constant and $W = \frac{(N+n)!}{N!n!}$ (ref.(74)).

W is the number of distinct ways n vacancies may be placed on N + n lattice sites.

Using Stirling's approximation:*

$$\Delta S_{config} = k\left(N \ln \frac{N}{N+n} + n \ln \frac{n}{N+n}\right). \tag{3.22}$$

At equilibrium $\frac{\partial G}{\partial n} = 0$, or ΔG will be a minimum with respect to n.

From the previous equations:

$$\frac{\partial \Delta G}{\partial n} = \Delta H - T\,\Delta S_{vibr} + kT \ln \frac{n}{N+n} = 0 \text{ and}$$

$$\frac{n}{N+n} = \exp\left(\frac{\Delta S_{vibr}}{k}\right) \exp\left(\frac{\Delta H}{kT}\right) \tag{3.23}$$

In this equation ΔH and ΔS_{vibr} are respectively the enthalpy change and the vibrational entropy change per vacancy.

* $\ln x! = x \ln x - x$ for $x \gg 1$

Similar expressions for defect concentrations may be derived for other types of point defects.

In $UO_{2\pm x}$ it is *a priori* difficult to predict whether interstitial uranium ions or oxygen vacancies predominate. In fact, both types of defects may be important in certain regions of nonstoichiometry, and they must be considered simultaneously in the defect equilibria. It is also necessary to remark that in UO_2 sintering, the rate controlling ion is the cation. If the cation defects constitute a minority, it is important to know how the concentration of these vary with variations in the concentration of the major defect.

In order to determine the correct relationships betwenn defect concentrations and oxygen partial pressure for UO_{2+x}, it is useful to assume that interstitial U ions and charged oxygen vacancies are the most important point defects. The corresponding equations for the formation of these defects are:*

$$2O_O + U_U = U_i^{\cdot\cdot} + 2e' + O_2 \tag{3.24}$$

$$O_O = V_O^{\cdot\cdot} + 2e' + 1/2\ O_2 \tag{3.25}$$

Therefore:

$$K_{U_i^{\cdot\cdot}} [O_O]^2\ [U_U] = [U_i^{\cdot\cdot}] n^2\ p(O_2) \cong K_{U_i^{\cdot\cdot}} \tag{3.26}$$

$$K_{V_O^{\cdot\cdot}} [O_O] = [V_O^{\cdot\cdot}] n^2 (p(O_2))^{1/2} \cong K_{V_O^{\cdot\cdot}} \tag{3.27}$$

with $[e'] = n$, $[U_U] \cong [O_O] \cong 1$

From the electroneutrality condition:

$$n = 2\{[U_i^{\cdot\cdot}] + [V_O^{\cdot\cdot}]\} \tag{3.28}$$

It is possible to consider two limiting conditions: $[U_i^{\cdot\cdot}] >> [V_O^{\cdot\cdot}]$ and $[V_O^{\cdot\cdot}] >> [U_i^{\cdot\cdot}]$.

(i). $[U_i^{\cdot\cdot}] >> [V_O^{\cdot\cdot}]$

From equations (3.28) and (3.26):

$$n = 2[U_i^{\cdot\cdot}] \tag{3.29}$$

$$4[U_i^{\cdot\cdot}]^3\ p(O_2) = K_{U_i^{\cdot\cdot}} \tag{3.30}$$

Therefore:

$$[U_i^{\cdot\cdot}] = \frac{n}{2} = (K_{U_i^{\cdot\cdot}}/4)^{1/3}\ (p(O_2))^{-1/3} \tag{3.31}$$

* This deviation is based on the solution of a more general problem, presented in ref. 75.

From equations (3.29), (3.27) and (3.31):

$$4[V_O^{\cdot\cdot}]\,[U_i^{\cdot\cdot}]^2\,(p(O_2))^{1/2} = K_{V_O^{\cdot\cdot}} \tag{3.32}$$

$$4[V_O^{\cdot\cdot}]\,(K_{U_i^{\cdot\cdot}}/4)^{2/3}\,(p(O_2))^{-1/6} = K_{V_O^{\cdot\cdot}} \tag{3.33}$$

Therefore:

$$[V_O^{\cdot\cdot}] = K_{V_O^{\cdot\cdot}}\,(p(O_2))^{1/6}/2^{6/3}K_{U_i^{\cdot\cdot}}^{2/3}\,2^{-4/3}$$

$$[V_O^{\cdot\cdot}] = K_{V_O^{\cdot\cdot}}\,(p(O_2))^{1/6}\,/\,(2K_{U_i^{\cdot\cdot}})^{2/3} \tag{3.34}$$

(ii). $[V_O^{\cdot\cdot}] >> [U_i^{\cdot\cdot}]$

From equations (3.28) and (3.27)

$$n = 2[V_O^{\cdot\cdot}] \tag{3.35}$$

$$4[V_O^{\cdot\cdot}]^3\,(p(O_2))^{1/2} = K_{V_O^{\cdot\cdot}} \tag{3.36}$$

Therefore:

$$[V_O^{\cdot\cdot}] = \frac{n}{2} = (K_{V_O^{\cdot\cdot}}/4)^{1/3}\,(p(O_2))^{-1/6} \tag{3.37}$$

From equations (3.35), (3.26) and (3.37):

$$4[U_i^{\cdot\cdot}]\,[V_O^{\cdot\cdot}]^2\,p(O_2) = K_{U_i^{\cdot\cdot}} \tag{3.38}$$

$$4[U_i^{\cdot\cdot}]\,(K_{V_O^{\cdot\cdot}}/4)^{2/3}\,(p(O_2))^{2/3} = K_{U_i^{\cdot\cdot}} \tag{3.39}$$

Therefore:

$$[U_i^{\cdot\cdot}] = K_{U_i^{\cdot\cdot}}\,(p(O_2))^{-2/3}/2^{6/3}K_{V_O^{\cdot\cdot}}^{2/3}\,2^{-4/3}$$

$$[U_i^{\cdot\cdot}] = K_{U_i^{\cdot\cdot}}\,(p(O_2))^{-2/3}/(2K_{V_O^{\cdot\cdot}})^{2/3} \tag{3.4}$$

Markin[98], Tetenhaum and Hunt[135] determined the oxygen deficiency in UO_{2-x} as a function of the partial pressure of oxygen $p(O_2)$. The relationship has the form $x \alpha (p(O_2))^{-1/3}$, for $x \geq 0.04$.

If interstitial uranium ions with two effective charges predominate in UO_{2-x}, expression (3.31) is valid. This expression agrees with the $(p(O_2))^{-1/3}$ pressure dependence found experimentally.

Thorn and Winslow[136] assumed that oxygen defects are predominant in UO_{2-x}. However, expression (3.37) shows that if this were the case the experimental data should yield a pressure dependence of $(p(O_2))^{1/6}$.

Assuming a $(p(O_2))^{-1/3}$ pressure dependence given by equation (3.31) and that $y = [U_i^{\cdot\cdot}]$ in $U_{1+y}O_2$, Kofstad presented an expression for $K_{U_i^{\cdot\cdot}}$ as a function of absolute temperature, based on the data of Tetenbaum and Hunt[105].

$$K_{U_i^{\cdot\cdot}} = \exp(47.5/R)\ \exp(-305{,}000/RT) \tag{3.41}$$

Considering that[75]

$$K = \exp \Delta S^{O}/R\ \exp(-\Delta H^{O}/RT) \tag{3.42}$$

with ΔS° and ΔH° being respectively standard entropy and enthalpy changes, it is possible to conclude that for the formation of doubly charged uranium interstitials in UO_{2-x}, $\Delta S_{U_i^{\cdot\cdot}} = 47.5$ kcal/mole °K and $H_{U_i^{\cdot\cdot}} = 305$ kcal/mole.

For $x \leqslant 0.04$, the data of Markin, Tetenbaum and Hunt mentioned before indicate a deviation from the $(p(O_2))^{-1/3}$ dependence to a large oxygen pressure dependence. Kofstad[76] suggests that at and close to stoichiometry intrinsic electronic conductivity predominates, considering the results of electrical conductivity investigations. In this case*, the concentrations of electrons and holes that predominate in UO_{2-x} are related by $np = K_i$, and the electroneutrality condition is given approximately by:

$$n = p = K_i^{1/2} \tag{3.43}$$

From Eq. 3.31:

$$K_i = 4(K_{U_i^{\cdot\cdot}}/4)^{2/3}\ (p(O_2))^{-2/3}$$

$$[U_i^{\cdot\cdot}]K_i = 4(K_{U_i^{\cdot\cdot}}/4)^{3/3}\ (p(O_2))^{-3/3} \tag{3.44}$$

$$[U_i^{\cdot\cdot}] = \frac{K_{U_i^{\cdot\cdot}}}{K_i}\ (p(O_2))^{-1}$$

Assuming $y = [U_i^{\cdot\cdot}]$ in $U_{1+y}O_2$, y is proportional to $(p(O_2))^{-1}$, as shown in Figure 13, where the relationship $y \alpha (p(O_2))^{-1/3}$ is also indicated.

Figure 14 shows how x in UO_{2+x} varies with $p(O_2)$, at temperatures between 600 and 1730°C. For $x < 0.05$ and above approximately 1000°C, $x \alpha p(O_2)^{1/2}$. There is a decrease of the $p(O_2)$ dependence in x, for larger values of x. For $x < 0.01$ and under 1000°C, the $p(O_2)$ dependence becomes larger and approaches $x \alpha p(O_2)$.

From electrical conductivity studies which show that UO_{2+x} is a p-conductor, with conductivity approximately proportional to x for small values of x, it is concluded that the oxide complex defects consist of two $(O_i^1 V_O O_i^2)$ defects or $(O_i^1 V_O O_i^2 O_i^2 V_O O_i^1)$, each having one negative effective charge[94]. Designating O_c as this defect, its formation may be written[76]

---

* The equilibrium corresponding to the intrinsic ionization of electrons from the valence to the conduction band can be written $np = K_i$, where $n = [e']$ and $p = [k']$ denotes respectively the concentrations of electrons and holes[75].

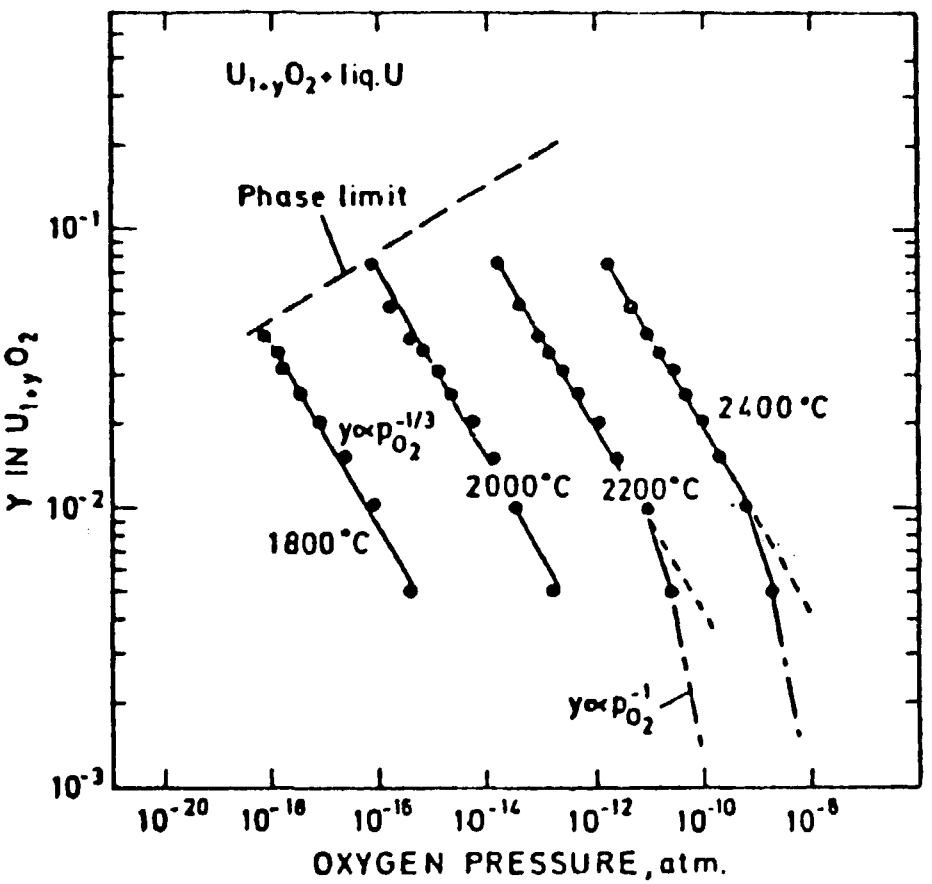

Figure 13 – The variation of y in $U_{1+y}O_2$ as a function of the partial pressure of oxygen in the 1800 – 2400°C temperature range, according to Tetenbaum and Hunt[135] (after ref. 76).

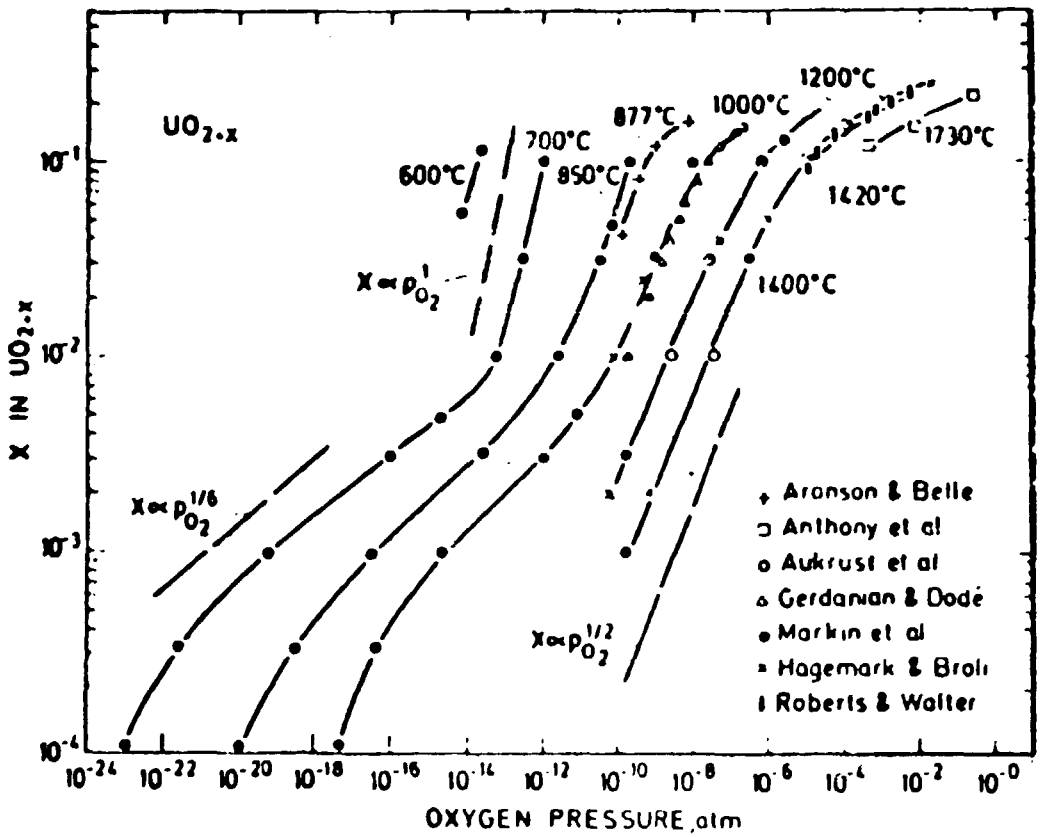

Figure 14 – The variation of x in UO_{2+x} as a function of the oxygen partial pressure in the 600 - 1730°C temperature range (after ref. 76).

$$U_U + 2V_i^1 + 2V_i^2 + 2O_O + O_2 = O_C^{\cdot} + U_U^{\cdot} \tag{3.45}$$

with the electron hole localized at normal U_U atoms; therefore the valence of the uranium atoms is changed from +4 to +5.

The electroneutrality condition is:

$$[O_C^{\cdot}] = [U_U^{\cdot}] \tag{3.46}$$

Therefore, considering expression (3.45)

$$\bar{K}_{O_C^{\cdot}} = K^2_{O_C^{\cdot}} \tag{3.47}$$

$$[O_C^{\cdot}] = K_{O_C^{\cdot}} [U_U]^{1/2} [V_i^1] [V_i^2] [O_O] (p(O_2))^{1/2}$$

$$x = 2[O_C^{\cdot}] \tag{3.48}$$

When the defect concentrations are small, $[U_U]$, $[V_i^1]$,$[V_i^2]$, $[O_O]$ may be considered equal to unity, and

$$\frac{x}{2} = [O_C^{\cdot}] \alpha (p(O_2))^{1/2} \tag{3.49}$$

in agreement with the experimental results mentioned before for $x < 0.05$ and temperatures above 1000°C. For $x > \sim 0.05$, Figure 14 shows that $x \alpha (p(O_2))^{1/2}$ is not valid, and the preceding approach for calculating $[O_C^{\cdot}]$ must be refined. Kofstad[76] suggests the following refinements:

(i) to consider the real concentrations of the sites involved in the expression (3.45), since some sites are not available for the defect reaction.

(ii) to take in account "blocking effects", originated by the fact that complex defects do not allow neighbor interstitial sites to be occupied by other complex defects.

From the data presented in Figure 14, considering expressions (3.47) and (3.48), it follows:

$$K_{O_C^{\cdot}} = \frac{x}{2} (p(O_2))^{-1/2} = 4 \times 10^{-3} \exp(30{,}500/RT) \tag{3.50}$$

Therefore the enthalpy of defect formation, $\Delta H_{O_C^{\cdot}}$, is negative and the process is exothermic. Such behavior is not frequent in nonstoichiometric oxides[94].

For $0.01 < x < 0.1$ and below 800°C, Figure 14 shows that x is approximately proportional to $p(O_2)$. Pairing or further association of defects with decreasing temperature can explain such proportionality. Different effective charges on the defects, and presence of impurities are two reasons that can explain the variability of $p(O_2)$ with x, for $x < 0.01$.

The concentration of neutral uranium vacancies in UO_{2+x} can be calculated taking into account the fact that the oxygen type defect predominates. The formation of neutral uranium vacancies may be expressed by

$$O_2 = V_U^X + 2O_O \tag{3.51}$$

Therefore

$$[V_U^X] = K_{V_U^X}\, p(O_2) \tag{3.52}$$

For expressions (3.49) and (3.51)

$$K_{O_C^{\cdot\cdot}}^2 = \frac{x^2}{4}\,\frac{K_{V_U^X}}{[V_U^X]} \tag{3.53}$$

or

$$[V_U^X] = \frac{K_{V_U^X}}{4K_{O_C^{\cdot\cdot}}^2}\, x^2$$

In the case of approximately stoichiometric UO_2, the nature of the defects depends on the relative value of the thermodynamic properties for the formation of possible alternatives. These alternative point defects at very high temperatures are complex oxygen interstitials and interstitial uranium ions. The same defects may exist at lower temperatures, but complex interstitial defects and oxygen vacancies may be dominant[76].

Let us admit that oxygen and uranium interstitials are dominant at high temperature. In this situation, the formula $U_{1+y}O_{2+x}$ is valid. Figures 13 and 14 show that at constant partial pressure of oxygen, y decreases and x increases with decreasing temperature. For the stoichiometric composition

$$\frac{2+x}{1+y} = 2 \tag{3.54}$$

Therefore, if a stoichiometric sample at high temperature is cooled at constant partial pressure of oxygen, allowing equilibrium to be reached, $\frac{2+x}{1+y} > 2$ and the oxide will be changed to a hyperstoichiometric composition. Considering expression (3.53) and the data in Figures 13 and 14, ti is possible to conclude that the values of $p(O_2)$ at which stoichiometric composition exists will increase, with increasing temperature. These observations are important in the analysis of sintering transient temperature data, which generally do not correspond to conditions of constant oxygen-uranium ratios.

3.9 – Lidiard and Matske Models for Nonstoichiometric UO_2.

Lidiard[93] considers anion Frenkel defects (O^{2-}vacancies and O^{2-}interstitials) as the dominant point defects in stoichiometric UO_2. In UO_{2+x} there is excess oxygen in the form of O^{2-} interstitials together with 2x electron holes, that at normal sintering temperatures are not substantially trapped at the O^{2-}interstitials. The existence of a significant association between the electron holes and U^{4+} vacancies is not probable.

The Frenkel and Schottky products for UO_{2+x} are the following:

$$u_i u_v = F_u(T) = \exp\left(-\frac{\Delta G_{F_u}}{kT}\right) \tag{3.55}$$

$$o_i o_v = F_o(T) = \exp\left(-\frac{\Delta G_{F_o}}{kT}\right) \tag{3.56}$$

$$u_v o_v^2 = S(T) = \exp\left(-\frac{\Delta G_S}{kT}\right) \tag{3.57}$$

where o_i, o_v, u_i, u_v are O^{2-} and U^{4+} interstitials and vacancies, respectively.*

Based on the preceding equation (3.55) – (3.57), the electroneutrality equation $2u_v + o_i = o_v + x + 2u_i$, and $F_o \simeq \exp(-71\ \text{kcal/RT})$, Lidiard reached the following conclusions, valid for temperatures less than about 1700°C:

(i) for $x > 0$

$$o_i \simeq x \qquad u_v \simeq Sx^2/F_o^2 \tag{3.58),(3.59}$$

$$o_v \simeq F_o/x \qquad u_i \simeq F_u F_o^2/Sx^2 \tag{3.60),(3.61}$$

(ii) for $x < 0$

$$o_v \simeq -x \qquad o_i \simeq F_u x^2/S \tag{3.62),(3.63}$$

$$o_i \simeq F_o/x \qquad u_v \simeq S/x^2 \tag{3.64),(3.65}$$

(iii) for stoichiometric UO_2

$$o_i^o = o_v^o \simeq F_o^{1/2} \qquad u_v^o = S/F_o \tag{3.66),(3.67}$$

$$u_i^o = F_u F_o/S \tag{3.68}$$

In case the UO_2 is surrounded by an atmosphere in which the oxygen partial pressure is not sufficiently low, $x > 0$ and Lidiard[93] conclued that

$$x^6 = \frac{1}{16}\exp[(\mu O_2 - \Delta G)/(kT)] \tag{3.69}$$

μO_2 = chemical potential of the O_2 molecule in the gas

ΔG = free energy on adding one O_2 molecule* to a stoichiometric and perfect crystal.

Taking into account that ΔG does not vary substantially with temperature and that $\mu O_2/(kT)$ depends logarithmically on the partial pressure and on T, Lidiard state that for $x > 0$, x is proportional to $(p(O_2))^{1/6}$, the temperature dependence being largely through the factor $\exp[-\Delta G/(kT)]$. The self-diffusion of U in the extrinsic region was expected to be via U^{4+} interstitials for $x < 0$ and via U^{4+} vacancies when $x > 0$. It is necessary to remark here that Kofstad[94] derived a relation $x \alpha (p(O_2))^{1/2}$, as shown by Eq. (3.49), valid for $x < 0.05$ and temperatures above 1000°C.

* Considered to be in its lowest quantum state at rest, initially

The following expression for the uranium self-diffusion coefficient were presented by Lidiard[107]:

a) $x < 0$ (interstitial diffusion)

$$D = \frac{1}{6} S_i^2 f_i w_i (F_u/S) x^2 \quad (3.70)$$

b) $x > 0$ (vacancy diffusion)

$$D = \frac{1}{12} a^2 f_v w_v (S/F_o^2) x^2 \quad (3.71)$$

where

S_i = interstitial jump distance

f_i = interstitial correlation factor

w_i = interstitial jump frequency

a = edge length of the face-centered cube

f_v = correlation factor = 0.7815

w_v = vacancy jump frequency

The same author showed that in the expression $D = D_o e^{-Q/RT}$, Q will depend on the heats of formation of both Frenkel and Schottky defects, and on the heat of activation for defect movement. In the case where x is governed by equilibrium with oxygen in the vapor phase, one third the enthalpy ΔH corresponding to ΔG should be included in Q. The values of D_o are much smaller than those most frequently found,* due to the factor x^2 in (3.70) and (3.71); this factor is introduced due to the composition MX_2 of the fluorite structure, and implies a large effect of nonstoichiometry on diffussion dependent properties of UO_2. The factor would be simply x for an MX composition (for instance, a NaCl-type structure).

Lidiard suggested more two diffusion mechanisms for $x < 0$:

(i) diffusion via vancancy triplets formed from one U^{4+} vacancy and two O^{2-} vacancies;

(ii) diffusion via dislocations, that can correspond to kinetics similar to those of volume diffusion. Matzke[99] developed a model for nonstoichiometry in UO_2 applying the usual theory of disorder, in a way similar to that of Lidiard. It was assumed that

a) the dominant defects in UO_2 are oxygen vacancies and interstitials;

b) no association of defects occurs;

c) associations of impurities and defects do not occur.

Matzke[109] observed that a more general approach would be extremely complex, mathematically. If both Frenkel and Schottky disorders were considered, as well as changes in

* Normally in the range 10^{-2} to 1.

stoichiometry, 49 electroneutrality conditions would have to be used in a simultaneous solution of 18 equations.

The following equations were obtained using Matzke's simplified approach:

(i) stoichiometric UO_2

$$o_i^o \simeq 2o_v^o = \sqrt{2}\exp\left(-\frac{\Delta G_{F_o}}{2kT}\right) \tag{3.72}$$

$$u_v^o \simeq 2\exp\left(-\frac{\Delta G_S - \Delta G_{F_o}}{kT}\right) \tag{3.73}$$

$$u_i^o \simeq \frac{1}{2}\exp\left(-\frac{\Delta G_{F_u} + \Delta G_{F_o} - \Delta G_S}{kT}\right) \tag{3.74}$$

(ii) UO_{2+x} $(x > 0)$

$$o_i \simeq x^* \tag{3.75}$$

$$o_v \simeq \frac{1}{x}\exp\left(-\frac{\Delta G_{F_o}}{kT}\right) \tag{3.76}$$

$$u_v \simeq x^2\exp\left(-\frac{\Delta G_S - 2\Delta G_{F_o}}{kT}\right) \tag{3.77}$$

$$u_i \simeq \frac{1}{x^2}\exp\left(-\frac{\Delta G_{F_u} + 2\Delta G_{F_o} - \Delta G_S}{kT}\right) \tag{3.78}$$

(iii) UO_{2-y} $(y > 0)$

$$o_v \simeq \frac{y^{**}}{2} \tag{3.79}$$

$$o_i \simeq \frac{2}{y}\exp\left(-\frac{\Delta G_{F_o}}{kT}\right) \tag{3.80}$$

$$u_v \simeq \frac{4}{y^2}\exp\left(-\frac{\Delta G_S}{kT}\right) \tag{3.81}$$

$$u_i \simeq \frac{y^2}{4}\exp\left(-\frac{\Delta G_{F_u} - \Delta G_S}{kT}\right) \tag{3.82}$$

Because of the anion prevailing type of disorder

---

* It is assumed $x \gg (o_i)$ thermal.

** It is assumed $\frac{Y}{2} \gg (o_v)$ thermal.

$$\Delta G_{F_u} > \Delta G_{F_o} \text{ and } \Delta G_S > \Delta G_{F_o} \tag{3.83}$$

Matzke's model permits the calculation of approximate values for certain UO_2 thermodynamic functions. He derived the following expressions[99]:

$$\Delta G_{F_o} \simeq 3\,eV$$

$$\Delta H \simeq 4.5\,eV \text{ to } 4.7\,eV \text{ for stoichiometric } UO_2$$

$$\Delta H \simeq 2.8\,eV \text{ for } UO_{2+x}$$

$$\Delta H \simeq 5.9\,eV \text{ for } UO_{2-x}$$

Assuming that the movement of single uranium defects is the rate controlling process (for instance for sintering, grain growth, uranium self-diffusion and creep), ΔH contains both the enthalpy for the formation of a defect, and enthalpy needed for its movement, H_m. If it is considered that ΔH_m does not change appreciably with stoichiometry, a comparison of equations (3.73), (3.77) and (3.81) shows that the changes in ΔH, on adding or subtracting oxygen to stoichiometric UO_2, should be approximately equal to ΔH_{F_o}. The agreement with experimental results is not very satisfactory, which could be explained by the considerable scatter in experimental data or by a change in ΔH_m with stoichiometry. ΔH_m could vary in such circumstances due to changed valence of some uranium atoms, with alteration of their ionic size. Matzke[106] took $H_m = 2.4 \pm 0.4$ eV for $UO_{2.005}$ considering measurements on the recovery of the electrical conductivity of irradiated or quenched specimens. Using equations (3.77), he concluded

$$\Delta G_S - 2\Delta G_{F_o} + \Delta H_m \simeq 2.8\,eV \tag{3.84}$$

With $\Delta G_{F_o} \simeq 3$ eV and $\Delta H_m = 2.4$ eV, $\Delta G_s \simeq 6.4$ eV.

Matzke[109] stated that a vacancy diffusion mechanism is still operative in UO_{2-y} with $y = 2 \times 10^{-3}$, but an interstitial mechanism becomes dominant, when y exceeds some value that depends on the unknown ratio of t the mobilities of interstitial uranium and uranium vacancies. Assuming that $u_i^o < u_v^o$, from equations (3.73) and (3.74):

$$\Delta G_S - \Delta G_{F_o} < \Delta G_{F_u} + \Delta G_{F_o} - \Delta G_S$$

or

$$\Delta G_{F_u} > 6.8\,eV$$

Considering the preceding results and equations (3.72) to (3.82), the approximate concentrations of point defects in UO_2, $UO_{2.002}$ and $UO_{1.998}$ can be calculated. Table VI presents these values at 1400°C.

Table VI

Concentration of point defects in
UO_2, $UO_{2.002}$ and $UO_{1.998}$ at 1400°C (ref. 99)

	o_v	o_i	u_v	u_i
UO_2	2×10^{-5}	4×10^{-5}	1.2×10^{-10}	$< 3 \times 10^{-11}$
$UO_{2.002}$	5×10^{-7}	2×10^{-3}	2.4×10^{-7}	$< 1.5 \times 10^{-14}$
$UO_{1.998}$	10^{-13}	10^{-6}	6×10^{-14}	$< 6 \times 10^{-8}$

3.10 – Uranium and Oxygen Diffusion Coefficients for UO_2

The usual Arrhenius equation for self-diffusion

$$D = D_o \exp(-Q/kT) \tag{3.85}$$

can be written[109]

$$D = \left[a_o^2 V \exp\left(\frac{\Delta S_f + \Delta S_m}{k}\right)\right] \exp - \frac{\Delta H_f + \Delta H_m}{kT} \tag{3.86}$$

The subscripts f and m, in the entropy and enthalpy terms, correspond respectively to the formation of a defect and to its motion.

a_o = lattice constant

V = mean vibration frequency of an atom about its equilibrium site

All the parameters involved in (3.86) can be determined experimentally or theoretically.

Usually V is considered equal to the Debye frequency V_D, that is related to the Debye temperature θ_D by[99]

$$k\,\theta_D = h\,V_D \tag{3.87}$$

With h being the Planck's constant

θ_D for UO_2 varies between 154 and 870°K[23].

For high temperatures θ_D can be taken as 650°K[38]. Then

$$V_D \simeq V \simeq 1.6 \times 10^{13}\ sec^{-1}$$

For uranium self-diffusion[112] $D_o \simeq 0.2\ cm^2\ sec^{-1}$ and $D_o \simeq 10^3\ cm^2\ sec^{-1}$ for oxygen[130]. Therefore, considering (3.85) and (3.86)

$\Delta S = \Delta S_f + \Delta S_m \simeq 2.8$ e.u for uranium.*

$\Delta S \simeq 19.4$ e.U. for oxygen diffusion

ΔS_m can be given by

$$\Delta S_m \simeq \beta \frac{\Delta H_m}{T_{mp}} \tag{3.88}$$

where $\beta \simeq 0.35$ for many materials

T_{mp} = melting point

---

* e.u. = entropy unit = kcal/mole°K = 4.32×10^{-5} eV/mole°K or kcal/°K for a system corresponding to one mole.

$\Delta H_f \simeq 3$ eV (ref. 12) and since $\Delta H = \Delta H_f + \Delta H_m$, the value of ΔH_m can be approximately evaluated, considering the values of ΔH corresponding to $x \lesssim 0$ presented in item 3.9.

The values of ΔH_m for uranium and oxygen diffusion in UO_2 are respectively 2.4 and 1.3 eV[5].

Consequently, $\Delta S_m \simeq 2.7 \times 10^{-4}$ eV $^\circ k^{-1}$ and $\Delta S_f \simeq -1.5 \times 10^{-4}$ eV $^\circ k^{-1}$ for uranium. For oxygen $\Delta S_m \simeq 1.5 \times 10^{-4}$ eV $^\circ k^{-1}$ and $\Delta S_f \simeq 6.9 \times 10^{-4}$ eV $^\circ k^{-1}$.

The experimental results of uranium and oxygen self-diffusion studies show poor agreement. Kofstad[76] judges it is difficult to give a detailed interpretation of the diffusion mechanisms, considering the available data.

Figure 15 shows the variation of oxygen self-diffusion with temperature, for nearly stoichiometric UO_2. The theoretical plots for $x = 0$, $x = 0.01$ and $x = 0.002$ were calculated using the equation

$$D = 0.02016 \{ x + [x^2 + 500 \exp(-40900/RT)]^{1/2} \} \exp(-35100/RT) \quad (3.89)$$

derived from a model developed by Thorn and Winslow[136,137]. This model is based on a quantitative description of the thermodynamic properties of UO_{2+x}, as functions of the energies associated with oxygen vacancies and interstitials.

Figure 16 and 17 indicate the variation of the oxygen self-diffusion in UO_{2+x}. It appears that the model of Thorn and Winslow[136,137] is not in full agreement with the data presented in Figures 15, 16 and 17.

Marin and Contamin[96] by means of mass spectrometry, proton bombardment activation analysis and by the application of an ionic mass analyzer, obtained oxygen self-diffusion coefficients for stoichiometric UO_2 samples, both small and large grained, annealed in the 780-1250°C temperature range. His results can be fitted by

$$D = 0.26 \exp(-59300/RT) \text{ cm}^2/\text{sec} \quad (3.90)$$

In Figure 16, there is clearly a very large enhancement of the self-diffusion coefficient near the stoichiometric composition. In the same figure, equation (3.89) was plotted for comparison.

There is very substantial variability in the values reported for the uranium self-diffusion coefficient in near-stoichiometric UO_2, as shown in Figure 18. The large divergencies are probably due to the following reasons[76]:

(i) Both grain boundary and volume diffusion occur.

(ii) The ambient partial pressure of oxygen may differ for the different investigations. For instance, if the amount of water is not controlled in hydrogen atmospheres, the partial pressure of oxygen might vary, affecting the degree of nonstoichiometry and the diffusion coefficient.

For near stoichiometric UO_2, some of the expressions obtained for the uranium self-diffusion coefficient are given next.

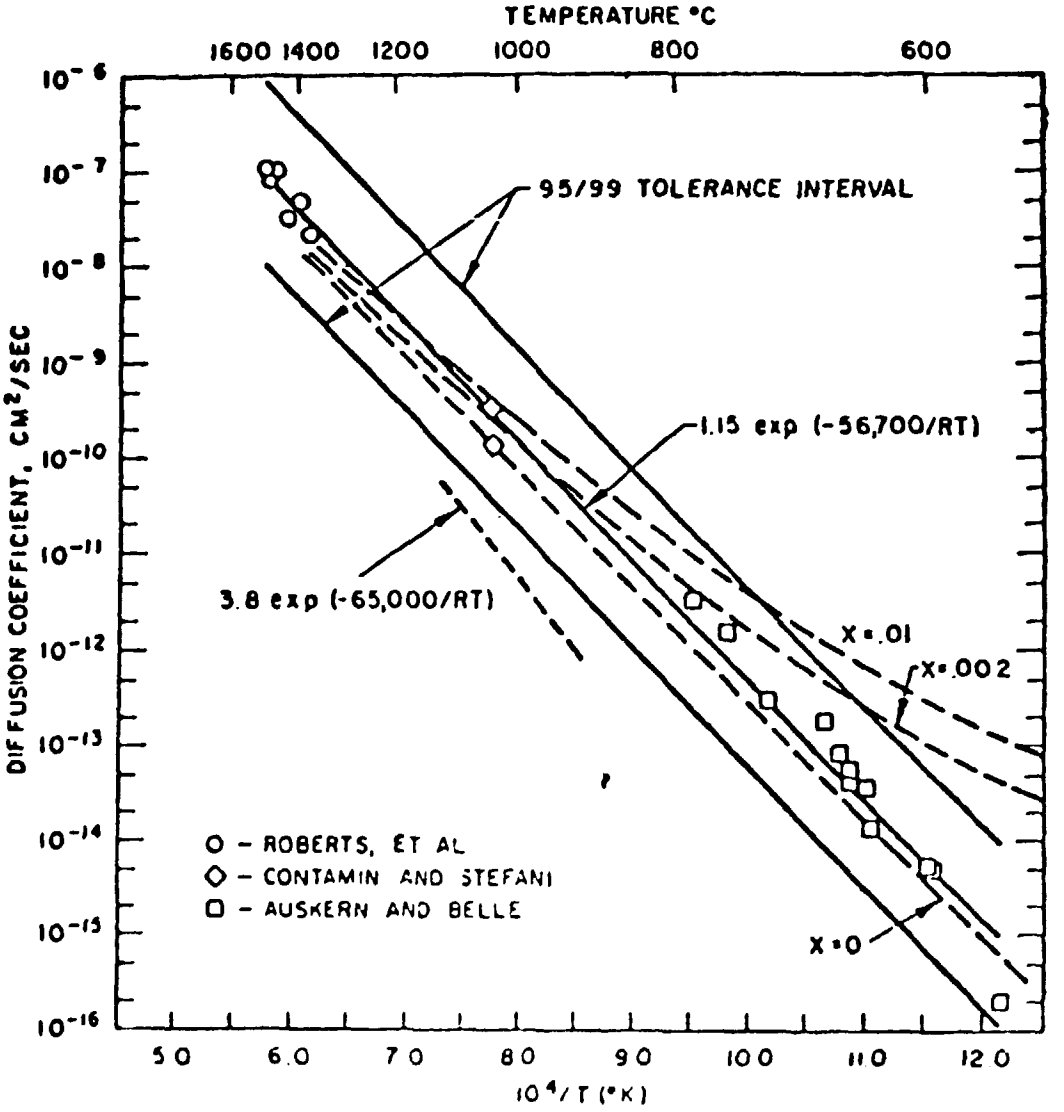

Figure 15 – The oxygen self-diffusion in nearly stoichiometric UO_2. The values indicated by dashed lines for $x = 0$, $x = 0.002$, and $x = 0.01$ were calculated from equation (3.89). The diffusion equation $D = 3.8 \exp(-65000/RT)$ cm^2-sec, derived in ref. 39, falls outside the 95/99 tolerance interval (after ref. 22).

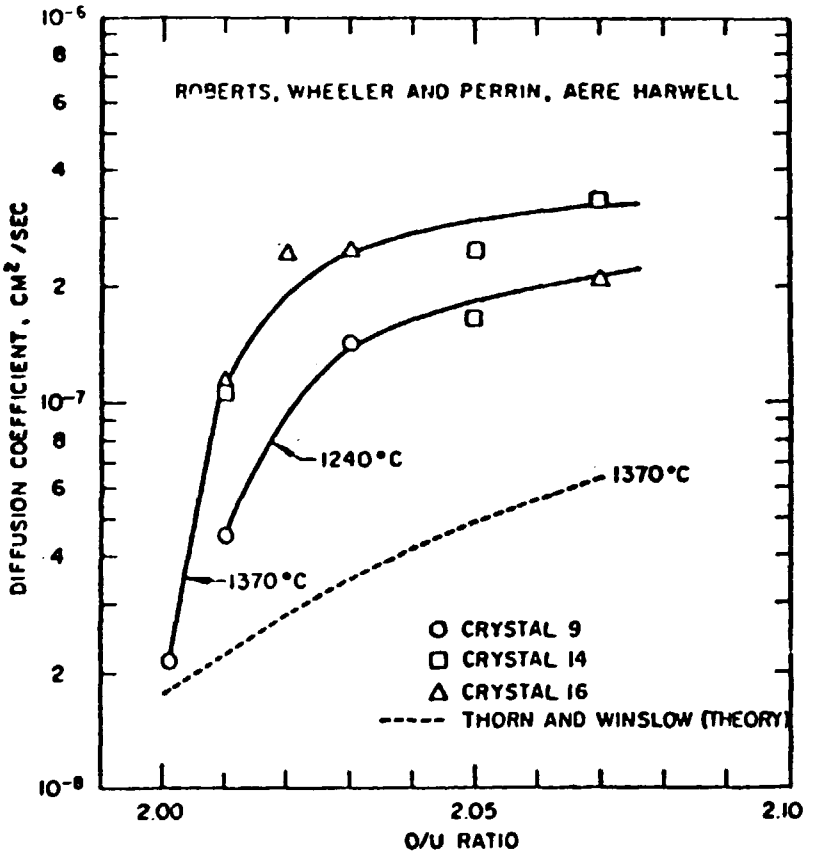

Figure 16 – The influence of the $\frac{O}{U}$ ratio on oxygen self-diffusion in UO_{2+x} (after ref. 22)

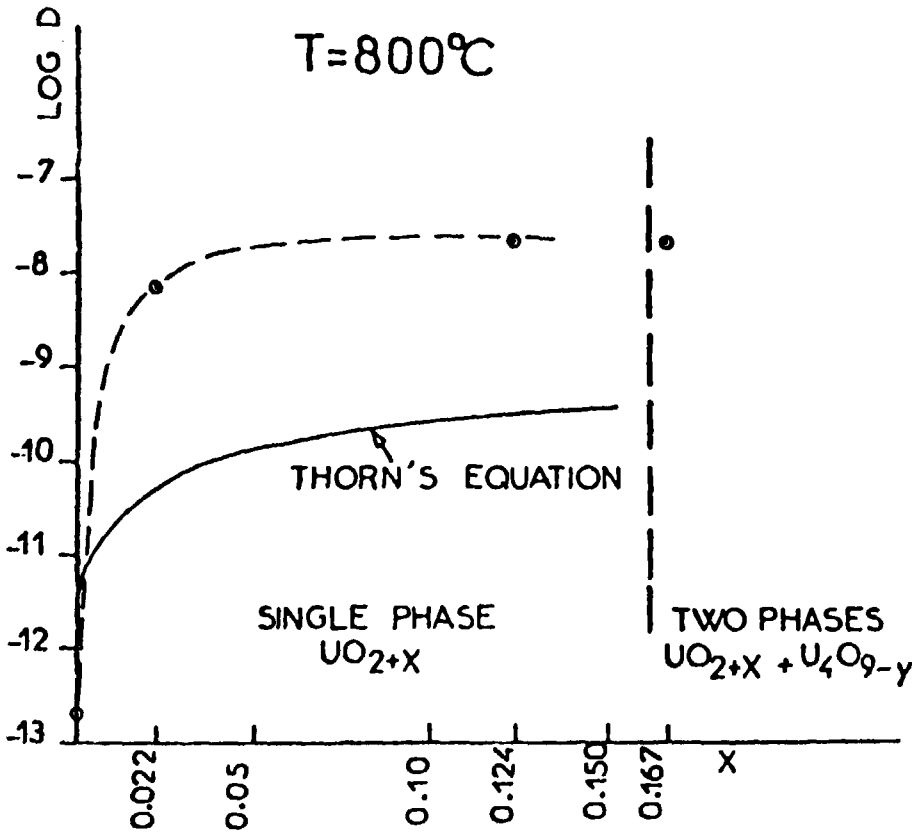

Figure 17 – The ^{18}O self-diffusion coefficient in UO_{2+x} at 800°C. Thorn's equation (3.89) is plotted for comparison (after ref. 97).

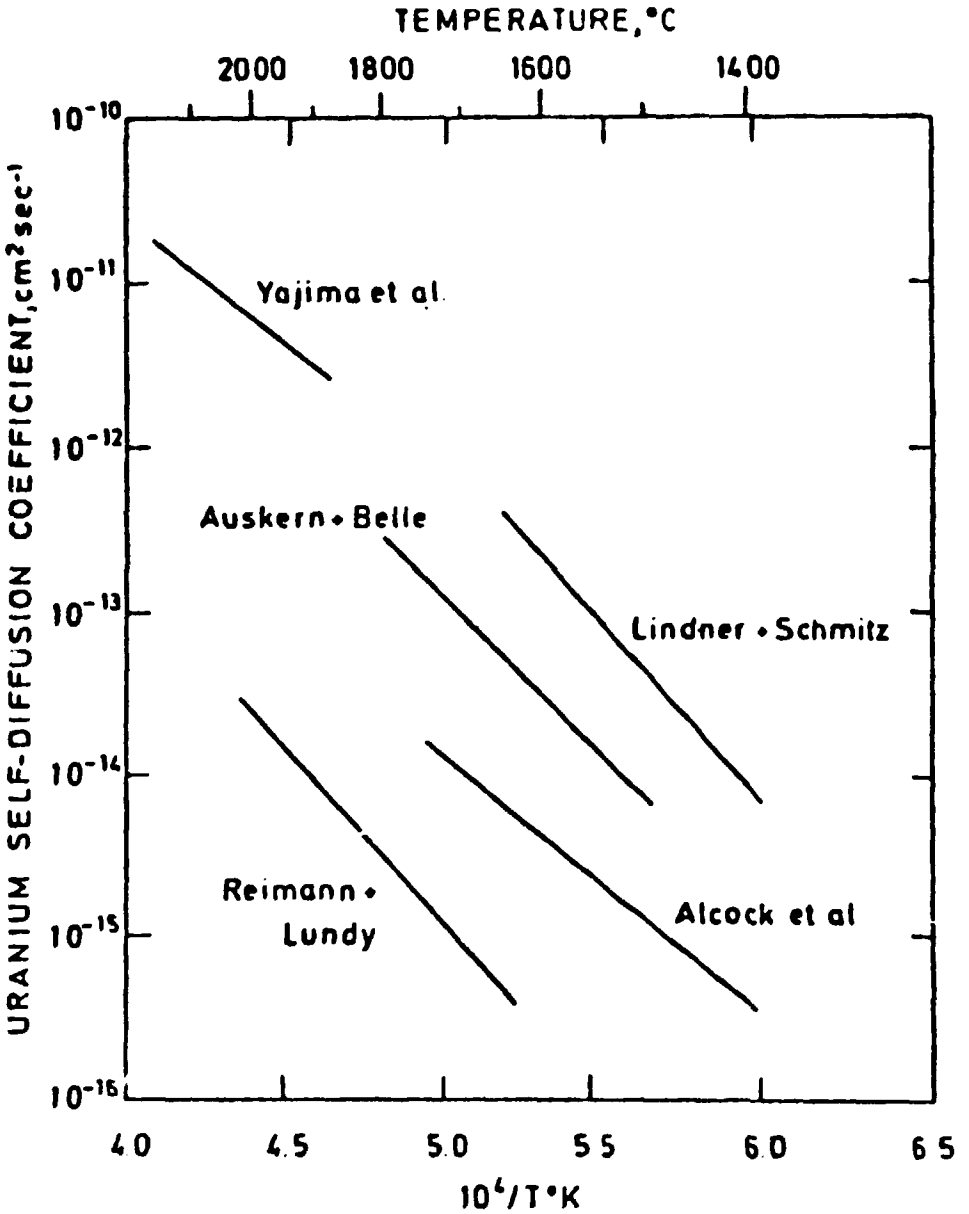

Figure 18 – The uranium self-diffusion coefficient in near stoichiometric UO_2 (after ref. 76)

Lindner and Schmitz[94], for temperatures between 1300 and 1600°C, in flowing hydrogen:

$$D = 0.23 \exp(-104{,}600 / RT) \tag{3.91}$$

Reimann and Lundy[120], for single crystals in the 1620-2010°C temperature range:

$$D = (6.8 \pm 2.0) \times 10^{-5} \exp(-98{,}300 \pm 9{,}700 / RT) \tag{3.92}$$

Alcock, Hawkins, et al.[1,52], for temperatures between 1450 and 1700°C:

$$D = 1.2 \exp(-108{,}000 / RT) \tag{3.93}$$

obtained using the surface activity method, and

$$D = 4 \times 10^{-7} \exp(-70{,}000 / RT) \tag{3.94}$$

obtained by analyzing concentration profiles.

Auskern and Belle[13], for temperatures between 1450 and 1785°C, using sintered UO_2 samples diffusion annealed in flowing hydrogen:

$$D = 4.3 \times 10^{-4} \exp(-88{,}000 / RT) \tag{3.95}$$

Yajima et al.[149] studied U^{237} tracer diffusion using the sectioning method, in the temperature range 1900-2150°C, and obtained

$$D = 5.82 \times 10^{-5} \exp(-72{,}700 / RT) \tag{3.96}$$

Matzke[101], for temperatures between 1500 and 2000°C:

$$D = 0.5 \exp(-110{,}000 / RT) \tag{3.97}$$

The average value of the activation energies in equations (3.91) and (3.97) is 93±17 kcal/mol. The variability of the pre-exponential factor is such that precludes a meaningful average.

Matzke[102] suggested that discrepancies in the values of D, shown in Figure 18, might be due to small differences in impurity concentration. Iron and calcium, two major impurities in UO_2, create oxygen vacancies and reduce both the uranium vacancy concentration and the uranium ion diffusion rates. The effect of only 200 to 400 ppm of impurity is sufficient to yield drastic changes in uranium vacancy concentration. The effect of impurities is in general most likely to lead to too low diffusion coefficients.

Matzke[102] observed also that for UO_2 (sinters and single crystals) annealed in H_2, the apparent diffusion coefficients deduced from α-spectrometry decreased with time. The decrease in D, under such reducing conditions, was attributed to an ordered reduction of the samples near surface layers to about $UO_{1.98}$[101]; the resulting shear structures consisted of layers of UO_2 separated by lamellae of very low O/M ratios, approximately equal to unity. Therefore, for UO_2 near the stoichiometric composition and in equilibrium with a given atmosphere, at a given temperature, structural and compositional differences are possible[102]. These remarks are an additional explanation for the previously mentioned scatter in D-values, measured in reducing atmospheres.

The diffusion coefficient D for uranium in UO_{2+x} ($x > 0$) can be given by an equation of the form[102]

$$D = \gamma\, a_o^2\, u_v\, w \tag{3.98}$$

with

a_o = lattice constant

w = total jump frequency of the uranium atom next to a vacant site

u_v = concentration of uranium vacancies

γ = constant ≃ 1

It is possible to consider[102] that w does not change appreciably with small changes in x. Therefore, since uranium diffusion proceeds via a vacancy mechanism in UO_{2+x}, UO_2 and UO_{2-x} (for $x > 0.02$)[101], expressions (3.73), (3.77) (3.81) and (3.98) give the variation of D with temperature and UO_2 thermodynamic properties, discussed and presented in the previous item 3.9. Therefore, for UO_{2+x}

$$D = \gamma a_o^2 w x^2 \exp\left(-\frac{\Delta G_s - 2\Delta G_{Fo}}{kT}\right) \tag{3.99}$$

For UO_{2-x} ($x > 0.02$), admitting uranium diffusion proceeds via an interstitialcy mechanism:

$$D = \gamma a_o^2 w \frac{x^2}{4} \exp\left(-\frac{\Delta G_{Fu} - \Delta G_s}{kT}\right) \tag{3.100}$$

For stoichiometric UO_2:

$$D = 2\gamma a_o^2 w \exp\left(-\frac{\Delta G_s - \Delta G_{Fo}}{kT}\right) \tag{3.101}$$

with $\Delta G_s = 6.4$ eV and $\Delta G_{Fo} = 3.0$ eV.

The data for uranium diffusion, as a function of nonstoichiometry, is not so abundant as for stoichiometric or near stoichiometric UO_2.

Figure 19 shows the diffusion coefficients obtained by Marin and Contamin[97], for compositions varying between 2.043 and 2.217. Their values for the activation energy Q and frequency

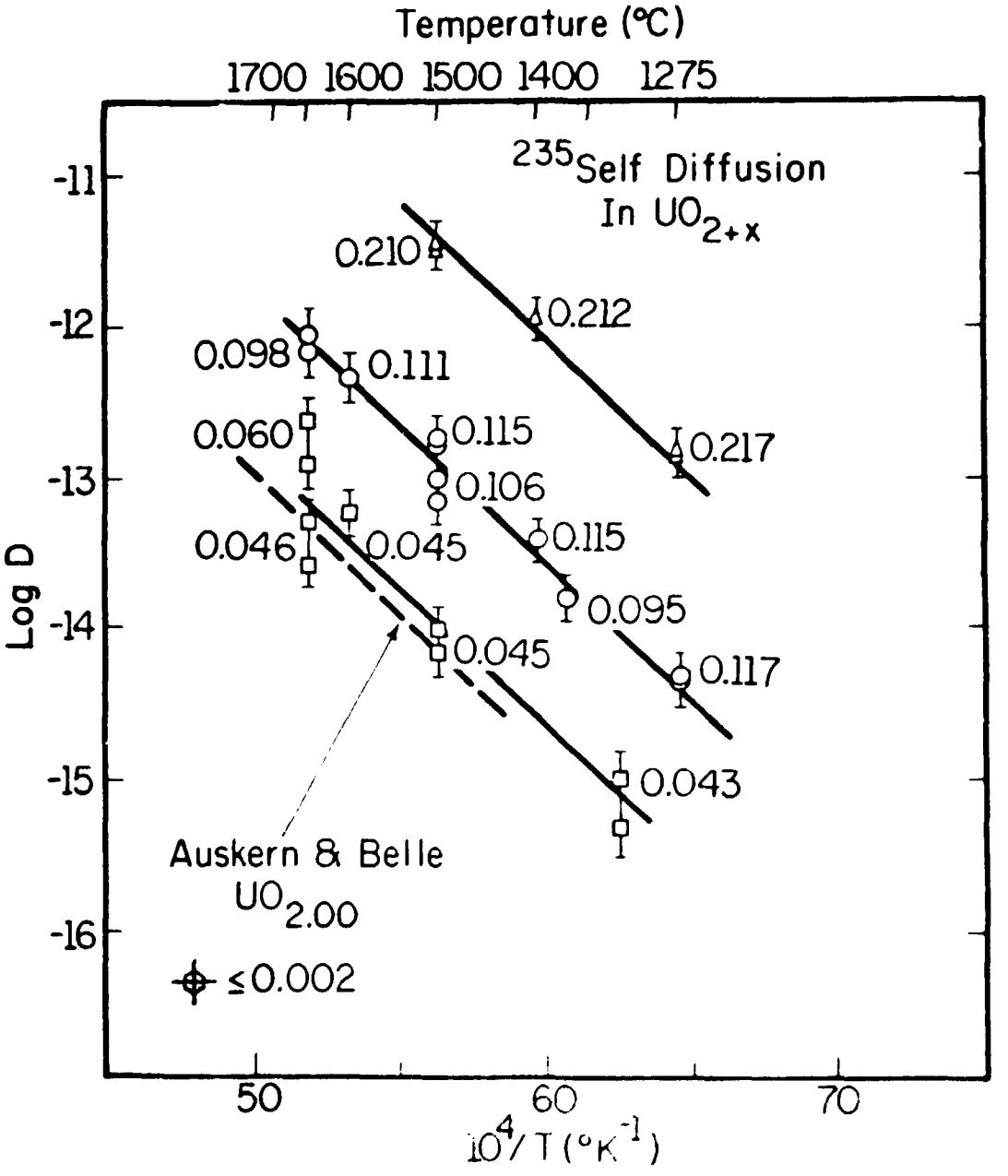

Figure 19 — Uranium self-diffusion in UO_{2+x} (after ref. 97)

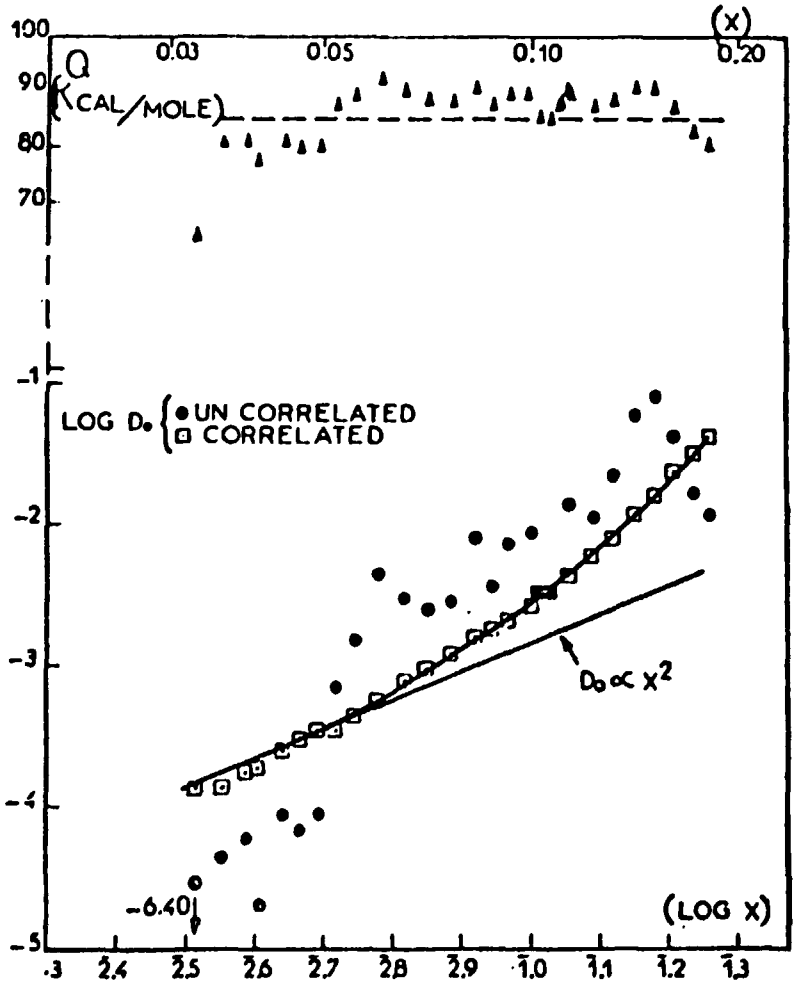

Figure 20 – Activation energies and frequency factors for uranium self-diffusion in UO_{2+x} as a function of x (after ref. 97).

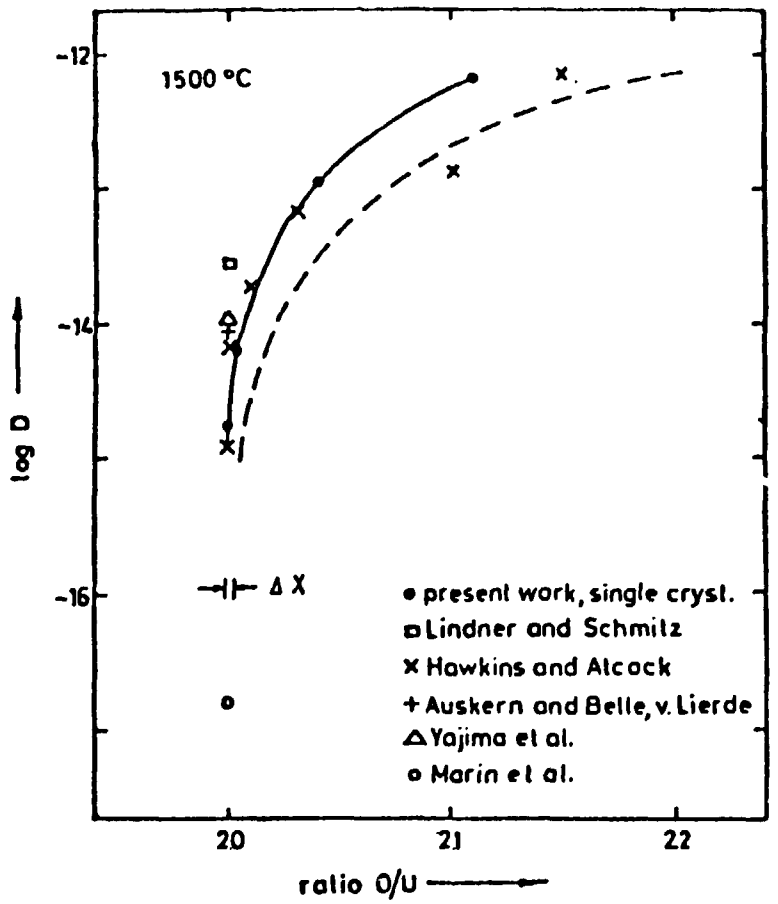

Figure 21 — The influence of stoichiometry deviations on the uranium self-diffusion coefficient for UO_{2+x} (after ref. 102).

factor D_o, as a function of the stoichiometry deviations, are presented in Figure 20; the "correlated" log D_o values were obtained considering Q equal to its mean value, over the whole range of x, from 0.03 to 0.20. In this range the experimental points may be represented by the following empirical equation:

$$D = 0.13x^2 \ (1 + 10^3 x^3) \exp(-85{,}000/RT) \ cm^2/s \qquad (3.102)$$

For low values of x, equation (3.102) gives a dependence on x^2 predicted by equation (3.71), derived by Lidiard. For values of D corresponding to $x < 0.03$, Marin and Contamin indicate the dearth of data is due to experimental difficulties.

Figure 21 shows the dependence of D on x at 1500°C, as presented by Matzke[102].

Close to the stoichiometric composition, a small increase in x yields a significant increase in D. Within the region indicated by Δx in Figure 21, the expected variation of D is of several orders of magnitude. The increase in D with x is roughly proportional to x^2 (ref. 101).

Matzke[101] has shown that at 1600°C the dependence of the uranium diffusion in UO_{2+x}, with $x > 0$, is similar to that presented in Figure 21. However, for $x < 0$, more negative x-values correspond to decreasing values of D; a minimum is attained at $x \simeq -0.02$ to -0.03. For smaller values of x the diffusion coefficient increases. The diffusion is via vacancies for $x \gtrsim -0.02$, and via interstitials for $x \lesssim -0.02$. Matzke explains the increase in D, for $x \lesssim -0.02$, by an increase in the concentration of uranium interstitials and an interstitialcy mechanism of diffusion. He stated also that the activation energy attains a maximum value in the hypostoichiometric range.

3.11 – UO_2 Grain-Boundary and Surface Diffusion Coefficients

Atomic diffusivity is higher along grain boundaries and on free surfaces, when compared with that in the bulk of a crystalline specimen[12]. These high-diffusivity paths are important in phenomena such as sintering.

Table VII lists values for D_o and Q the equation $D_{gb} = D_o \exp(-Q/RT)$, where D_{gb} is the grain-boundary diffusion. These values correspond to uranium diffusion in stoichiometric UO_2.

Table VII

Uranium grain-boundary
Diffusion Terms in Stoichiometric UO_2

Temperature range (°C)	D_o (cm^2/s)	Q (kcal/mole)	Reference
1470 – 1720	4×10^{-2}	70	120
1900 – 2100	1.04×10^{-1}	47.2	123
727 – 1314	214	103	10*
1350 – 1700	3	70	24**

* This result was calculated from data in ref. 62, taking the average data points obtained in initial stage sintering experiments.

** Obtained in final stage sintering experiments.

Coleman and Beere[34] studying the UO_2 final sintering stage, determined that $D_{gb} = 2.3 \times 10^{-9}$ cm^2/s. This result agrees with that metioned in reference 133, also obtained from sintering experiments. Ashby, in his work on sintering diagrams, took $D_o = 4 \times 10^{-2}$ cm^2/s and Q = 70 kcal/mole (data from Alcoock, Hawkins, Hills and McNamara[1]).

From data of Marin[96] it is possible to derive $D_{gb} = 50 \exp(-66.4/RT)$ cm^2/s, for $UO_{2.10}$. In the same reference, the activation energies for $UO_{2.045}$ and $UO_{2.106}$ are given as 46±17 and 68±11 kcal/mole, respectively.

Shewmon[12] stated that, except for low angle boundaries, there is no accepted model of a grain boundary. For low angle boundaries a dislocation model is generally accepted but even for this situation no quantitative theory is available to explain why, and by how much D_{gb} is greater than the volume diffusion coefficient. For metals there is an indication that the activation energy for grain boundary diffusion is considerably less than that for volume diffusion. It is reasonable to assume relatively open regions in a grain boundary, in which the energy to form a vacancy or move an atom into a vacancy will be less than in the bulk of the material.

According to ref.(118) diffusivities, measured with polycrystalline samples, probably are more representative of volume diffusion if the determinations are made at high temperature. At lower temperatures there may be a marked influence of grain-boundary diffusion, particularly if the grain size is small. On increasing the grain size, the contribution of the grain boundaries to diffusivity decreases.

It is useful to remark that randomly oriented dislocations also contribute to the increase of apparent diffusivities[12]. While grain boundaries increase the apparent diffusivities in their own planes, bulk dislocations increase the diffusivity in all directions. For metals at temperatures below half the absolute melting point, the apparent volume diffusion coefficient is determined entirely by the dislocation density[12].

The dislocation model for grain boundaries is not valid for disorientations greater than about 10°[56]. Higher angle boundaries are described as narrow regions in which the atoms are substantially disordered. Ion microscope studies show that high angle boundaries correspond to large regions of good atomic fit, interrupted by regions of bad fit which are associated with ledges.

Systematic studies of the oxygen partial pressure influence on the disorder of atoms at UO_{2+x} grain boundaries, were not found in the literature, However, from the above considerations, it is expected that grain boundary diffusion in UO_{2+x} equilibrated with an atmosphere containing oxygen, varies with the oxygen partial pressure.

Robertson[122] indicated that mass transfer measurements, on UO_2, showed surface diffusion to be dominant over volume diffusion, at high temperatures. Stoichiometry deviations could influence the mechanisms of material transport, by changing the surface diffusion coefficient and its value relative to the volume diffusion coefficient.

Figure 22 presents the surface diffusion coefficients for stoichiometric or nearly stoichiometric UO_2. The data of Henney and Jones[53] indicate an influence of stoichiometry, since the experiments in argon atmosphere gave an oxide with excess oxygen, $UO_{2.005}$, while the oxide specimen tested in hydrogen was stoichiometric. The activation energies were the same; however, the argon atmosphere gave a pre-exponential factor D_o one order of magnitude higher. The activation energy experimental results for surface diffusion vary between 110 and 125 kcal/mole, and therefore are greater than those corresponding to volume diffusion (93±17 kcal/mole, for stoichiometric composition*). The pre-exponential factors are much greater, approximately 10^7 against about 10^{-1}. Consequently, the values of the surface diffusion coefficients are substantially higher than those corresponding to volume diffusion.

* Value presented in Section 3.10.

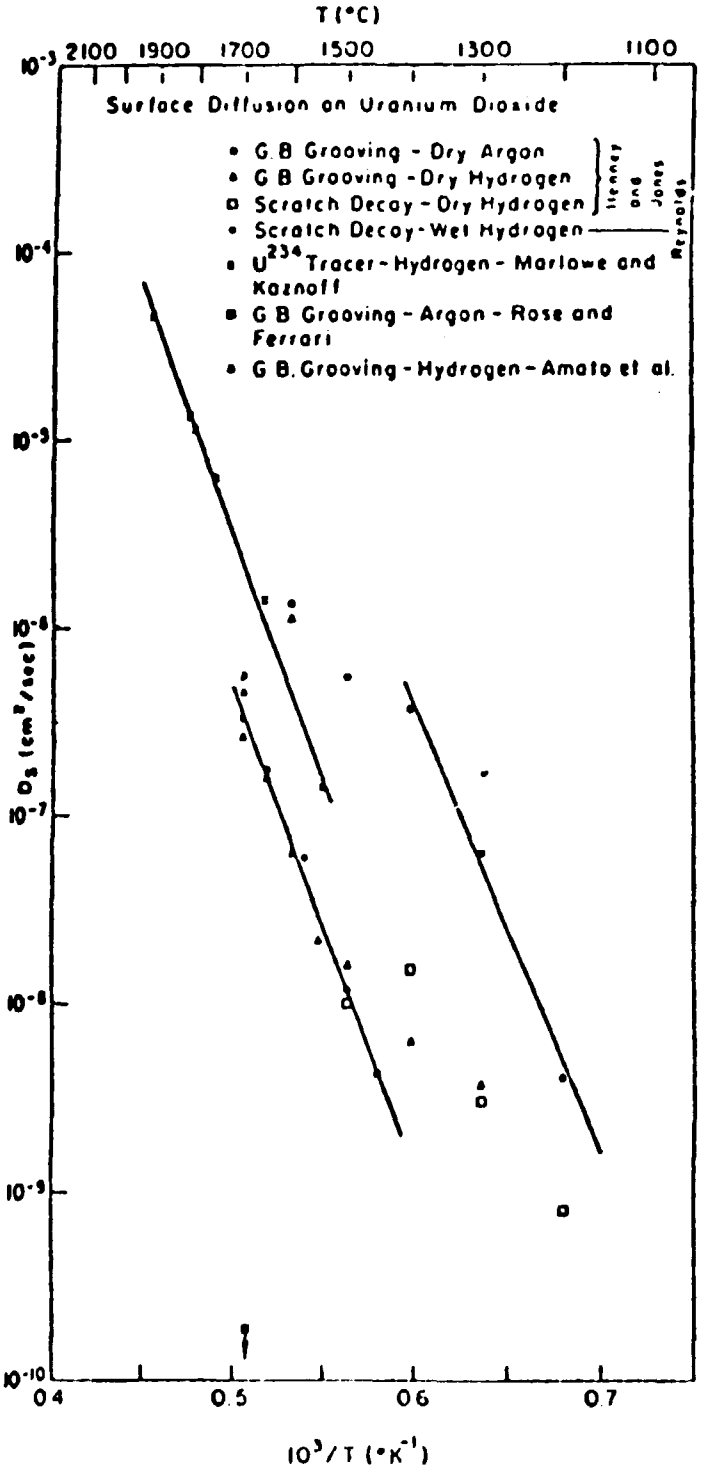

Figure 22 – Surface diffusion coefficients on stoichiometric or nearly stoichiometric uranium dioxide (after ref. 122).

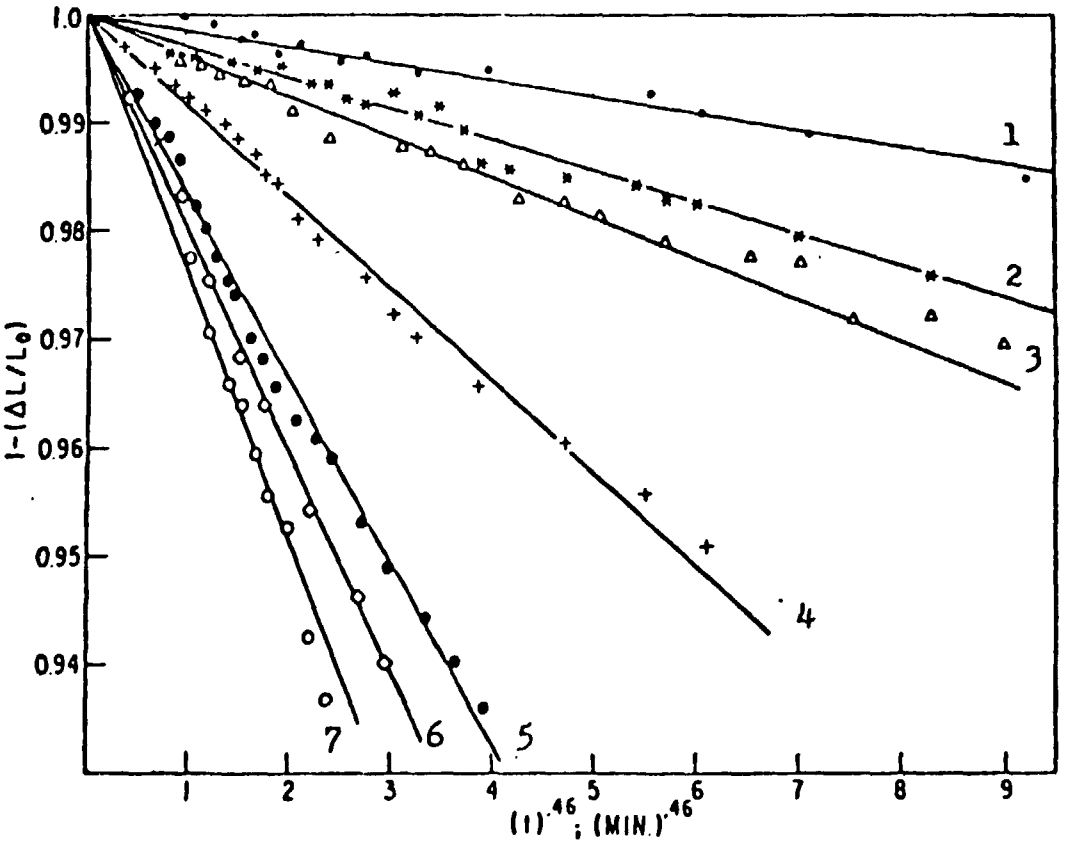

Figure 23 – Shrinkage isotherms for UO_{2+x} sintered in atmospheres with different oxygen potentials (after ref. 88). 1 – H_2, 1155°C; 2 – CO_2/CO, O/U = 2.01, 745°C; 3 CO_2/CO, O/U = 2.01, 700°C; 4 – CO_2/CO, O/U = 2.015, 750°C; 5 – CO_2/CO, O/U = 2.03, 775°C; 6 – CO_2/CO, O/U = 2.03, 790°C; 7 – H_2, 1355°C.

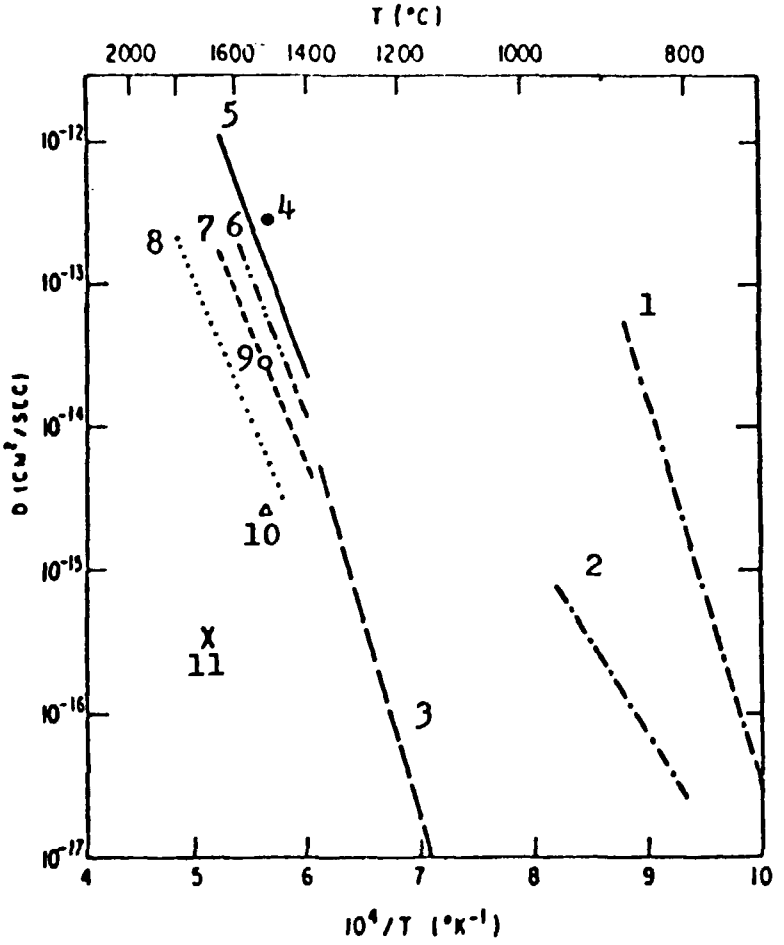

Figure 24 – Uranium self-diffusion coefficients for UO_2, obtained from sintering experiments and from direct determinations (after ref. 88). Line 1 – sintering in CO_2/CO, O/U = 2.02 + 0.01; line 2 – sintering in argon, O/U = 2.06; line 3 – sintering in H_2, O/U ≃ 2.00. The following data were derived from direct determinations: point 4 – O/U = 2.10; line 5 – O/U = 2.10; line 6 – O/U = 2.03; line 7 – O/U ≃ 2.01; line 8 – O/U ≃ 2.00 (H_2); point 9 – O/U = 2.03; point 10 – O/U = 2.01; point 11 – O/U = 2.002 (H_2).

3.12 – Grain Growth in UO_2 and Nonstoichiometry

Brook[25] showed that oxygen activity during processing of oxides can influence grain growth. In oxides the oxygen activity is related to defect concentration, that influences pore movement and boundary migration, therefore affecting grain growth.

The following expression is valid for the grain growth in UO_2[95]:

$$d^m - d_o^m = \frac{k_o t}{m} \exp(Q/RT) \tag{3.103}$$

d = grain size at time t

d_o = initial grain size

m = constant

k_o = constant

Q = activation energy

T = temperature

R = ideal gases constant

At constant temperature

$$d^m - d_o^m = kt \tag{3.104}$$

where k = growth constant

For stoichiometric UO_2 and UO_{2+x} with $0.016 < x < 0.13$, MacEwan and Hayashi[95] showed that $m = 2.5$. However, varying x from zero to 0.23 increased the growth constant by nearly four orders of magnitude, at 1325°C. The activation energy was found to be 66±10 kcal/mole for $UO_{2.02}$ and 109 kcal/mole for stoichiometric UO_2. From the results of MacEwan and Hayashi[95] the following expression can be derived for the growth constant at $T = 1598$°K, as function of stoichiometry:

$$k = 936\ x^{1.47},\ \text{in (micron)}^{2.5}/\text{hour} \tag{3.105}$$

Amato et al.[4] confirmed enhanced grain growth in UO_{2+x}. The growth developed following equation (3.104), with m in the range 2.2 to 2.6.

3.13 – Nonstoichiometry and Sintering of Uranium Dioxide

The influence of nonstoichiometry on sintering was analyzed comprehensively by Reijnen[119] and Johnson[62].

Considering the models for sintering discussed in Chapter 2, it is clear the process kinetics is related to diffusion coefficients. From expression (3.99), (3.100) and the discussion on the variation of

D with x in Section 3.10, a substantial dependence of sintering kinetics on nonstoichiometry is expected. For the initial stage of sintering, this influence has been demonstrated by various investigators, as indicated in Chapter 1.

Figure 23 presents the results obtained by Lay and Carter[88], for sintering of UO_2 in the 700-1355°C temperature range.

It is seen that hyperstoichiometric UO_2 sintering in CO_2/CO, has shrinkages considerably greater than those corresponding to material sintered in H_2 (O/U ratio approximately 2.00). The data can be represented with a time exponent of 0.46, corresponding to a volume diffusion mechanism[9].

Figure 24 shows the uranium self-diffusion coefficients obtained from sintering and from direct experiments. The influence of the O/U ratios is very substantial. The self-diffusion coefficients increase with O/U, for constant temperatures. From this figure, the effective uranium self-diffusion coefficient is 107±11 kcal/mole, 50% confidence limit, for stoichiometric and hyperstoichiometric UO_2. The agreement between the hydrogen sintering diffusion coefficients, and self-diffusion coefficients determined directly, is very satisfactory. However, the apparent diffusion coefficients for $UO_{2.02}$ are about 10^8 greater than for $UO_{2.00}$, sintered in hydrogen. This difference far exceeds that corresponding to directly measured diffusion coefficients.

Lay and Carter[88] observed that UO_2 approaches equilibrium with furnace atmospheres within 2-4 minutes, so that its initial stoichiometry does not influence sintering rates. This is valid particularly for small specimens plunged directly into a hot furnace. Bacmann and Cizeron[15] also indicated a rapid equilibration of UO_2 with furnace atmospheres. Lay[87] indicated also that since the uranium diffusion rate is much smaller than that of oxygen, it seems reasonable to suppose that UO_{2+x} equilibrate with respect to oxygen concentration before shrinkage occurs.

The preceding observations are important for the development of the investigation described herein, since it demanded that the deviation from stoichiometry, at the sintering temperature, be independent of the initial stoichiometry of the powder, depending only upon the oxygen activity of the furnace atmosphere.

Lay[87] studied the sintering kinetics for UO_{2+x} ($2.03 < O/U < 2.16$, $800 < T < 1050$°C). For $UO_{2.08}$ he determined the following expression for the uranium diffusion coefficient:

$$D = 1.3 \times 10^{-6} \exp(-55{,}000/RT) \ cm^2/s \qquad (3.103)$$

Lay observed that the results did not agree with those presented in one of his previous papers (Lay and Carter, ref. 9); the new data were approximately in agreement with that obtained by Amato et al[2]. Two possible reasons were given for the discrepancy.

(i) In the work described in ref. 88, it is possible the initial O/U value of 2.20 was not reduced to the desired value of 2.01, before shrinkage occured. Oxygen was supposed to be removed from the samples during the heating up transient, by reaction with CO gas. For the desired O/U ratio, the CO_2/CO mixtures were very low in CO at the temperatures of the experiment. Consequently, the CO available might not have been sufficient to reduce the material before shrinkage started. Without this previous reduction, the uranium coefficients for UO_{2+x} would be too high.

(ii) Bannister and Woolfrey[18] pointed out that in the sintering model utilized for the derivation of the initial equation, used by Lay and Carter, it is assumed that the neck radius is greater than $\gamma\Omega/kt$. This condition was not satisfied in the experiment, and therefore the sintering model applied was not valid for shrinkage values smaller than about 2.2%.

Lay[87] avoided the first difficulty by the utilization of UO_{2+x} powders having the desired level of x, prior to sintering. The stoichiometry deviation was maintained during sintering with a flowing CO_2/CO atmosphere, mixed in the proper ratio. Some of the O/U values were obtained by mixing oxidized or reduced powder with the starting powder (O/U = 2.08).*

The second difficulty was circumvented by the use of a relatively coarse powder, with a BET surface area of 1.40 m^2/g, for which the sintering model was applicable to shrinkages greater than 1%.

Lay's experimental diffusion coefficients, up to $x = 0.08$, agreed reasonably well with the x^2 dependence expected from Lidiard's model, discussed in Section 3.9. For $x > 0.08$ the coefficients are higher than those predicted by Lidiard. It was suggested that such deviation could result from the breakdown of Lidiard's model for high defect concentrations; in this case the use of defect concentration, instead of activities, in expressions for the equilibrium constants is invalidated due to defect interactions. Assuming the oxygen interstitial activity to be a function of the oxygen partial pressure, the uranium vacancy concentration could be calculated as a function of the stoichiometry deviation. The concentrations of uranium and oxygen vacancies could be considered equal to the corresponding activities, since these concentrations are small. However the concentrations of oxygen interstitials is not small in an oxide with a high O/U ratio, and therefore the oxygen activity must be taken into account. Using an approach similar to that developed by Lidiard in the presentation of his nonstoichiometry model, it is possible to demonstrate that the uranium vacancy concentration is proportional to $a_{O_i}^2$, the square of the oxygen interstitial activity. Assuming that the main oxygen defects are uncharged interstitials, the chemical activity of the oxygen interstitial is proportional to $(p(O_2))^{1/2}$. The values of the oxygen interstitial activity a_{O_i} can be determined from a plot of log x versus log $p(O_2)$, and therefore the change in uranium diffusion can be calculated, since D is proportional to $a_{O_i}^2$. Beyond about $x = 0.05$, a_{O_i} increases rapidly with x; this corresponds approximately to the range in which D deviates from the x^2 dependence, predicted theoretically by Lidiard.

Jakeshova[59] in her investigations of the sintering behavior of UO_{2+x}, under controlled oxygen potential, demonstrated the shrinkage kinetics were substantially influenced by the substructure and agglomerate structure of the starting powders. The shrinkage curve, corresponding to a certain powder, could not be represented by one straight line in $\log \frac{\Delta \ell}{\ell}$ vs. log t coordinates ($\frac{\Delta \ell}{\ell}$ = shrinkage, t = time). Each curve was divided in regions of approximately linear variation, of the form $\log \frac{\Delta \ell}{\ell} = \text{cte} + n \log t$. According to the review of Thümmler[5], some investigators derive the nature of the sintering mechanism from the value of n. This would be impossible with Jaeshova's results, due to the very large variations of n, that in one case was in the 0.07 to 0.15 range. Both samples of uranium dioxide utilized had very large surface area, 31.6 and 8.0 m^2/g respectively. The free crystallite size, determined by electron microscopy, was about 250-300 Å for the two powders.

The microstructure evolution during sintering, associated with the very high surface area powders of different initial characteristics utilized by Jakeshova, probably contributed for the considerable variability of n. However it was possible to conclude that small deviations from stoichiometry in UO_{2+x}, with $0 < x \leq 0.01$, drastically influenced the sintering rate, up to 75-85% of the total linear shrinkage.

Figure 28 shows results obtained by Stuart and Adams[132] for sintering of UO_2, in hydrogen containing water vapor. There is a significant influence of the ratio R = partial pressure H_2O/partial pressure H_2, on the density of UO_2 pellets sintered for three hours at 1300 °C. The densities indicated in Figure 29 correspond to the intermediate and final stages of the sintering process. Therefore, if the

* We observe that under such conditions the average particle size of the powder may vary as a function of O/U (cf. Chapter 2 of this work).

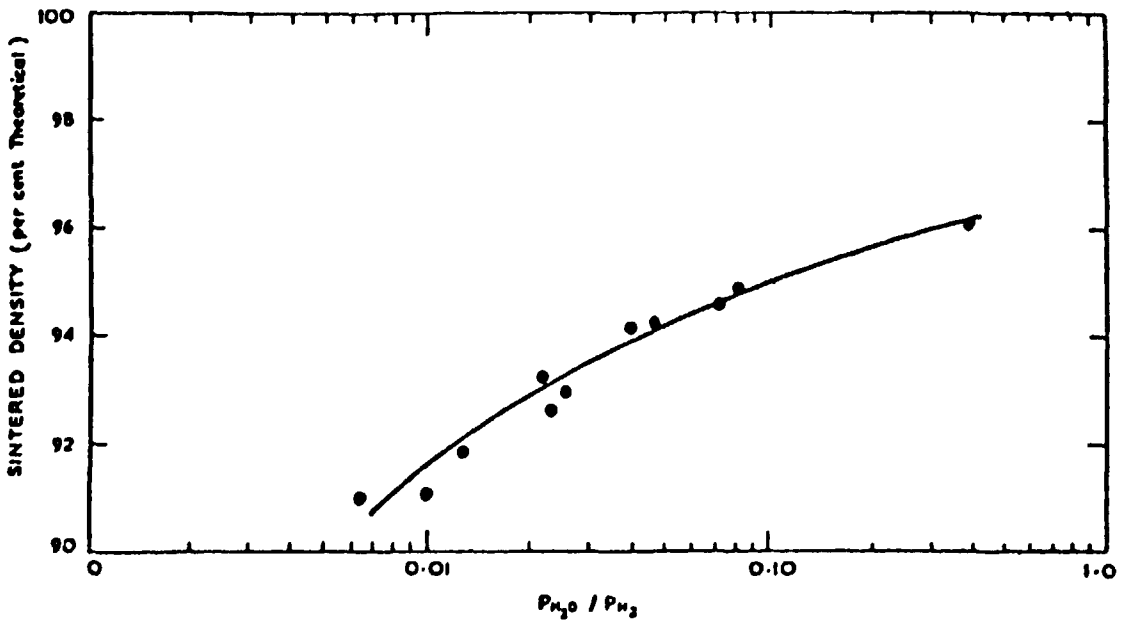

Figure 25 – The combined effect of H_2O and H_2 on the sintered density of UO_2; p_{H_2O} and p_{H_2} are the partial pressures of H_2O and H_2 respectively (after ref. 132).

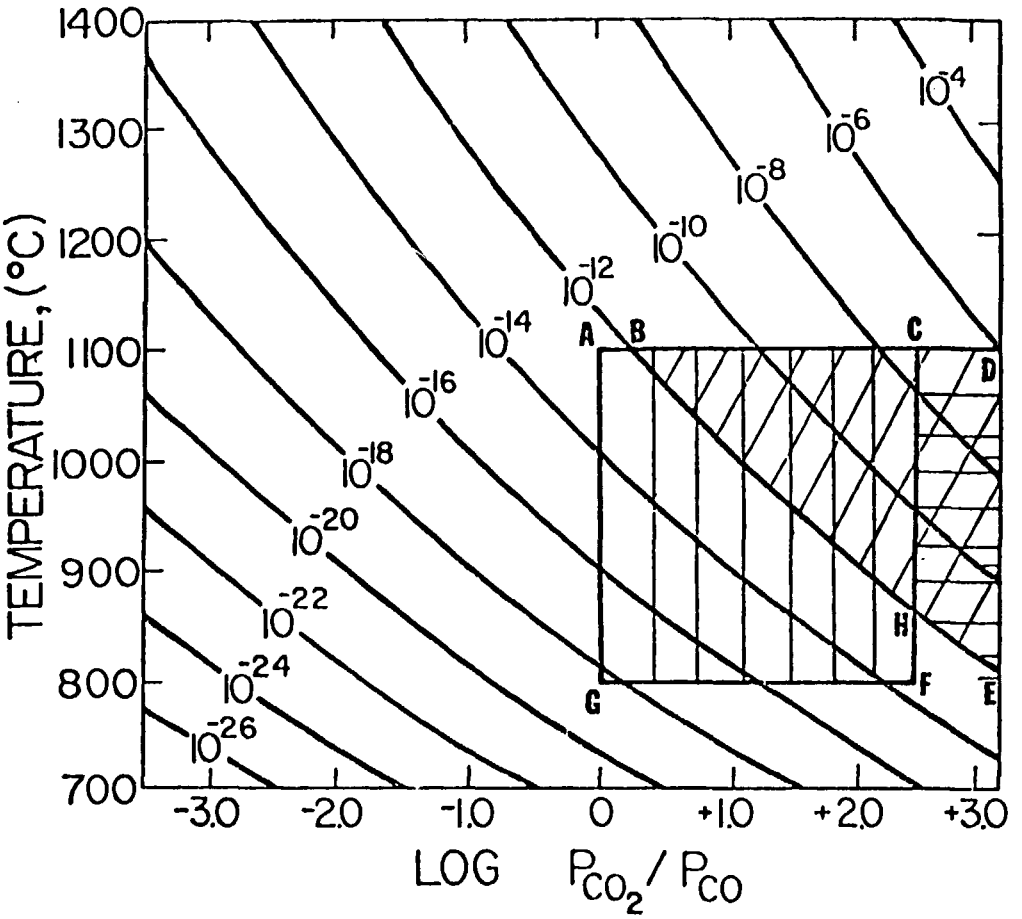

Figure 26 – Equilibrium oxygen partial pressure in mixtures CO_2 + CO, as a function of temperature and partial pressure ratio of CO_2 and CO. The marked areas indicate regions of main interest for equilibration of UO_{2+x} (after ref. 106).

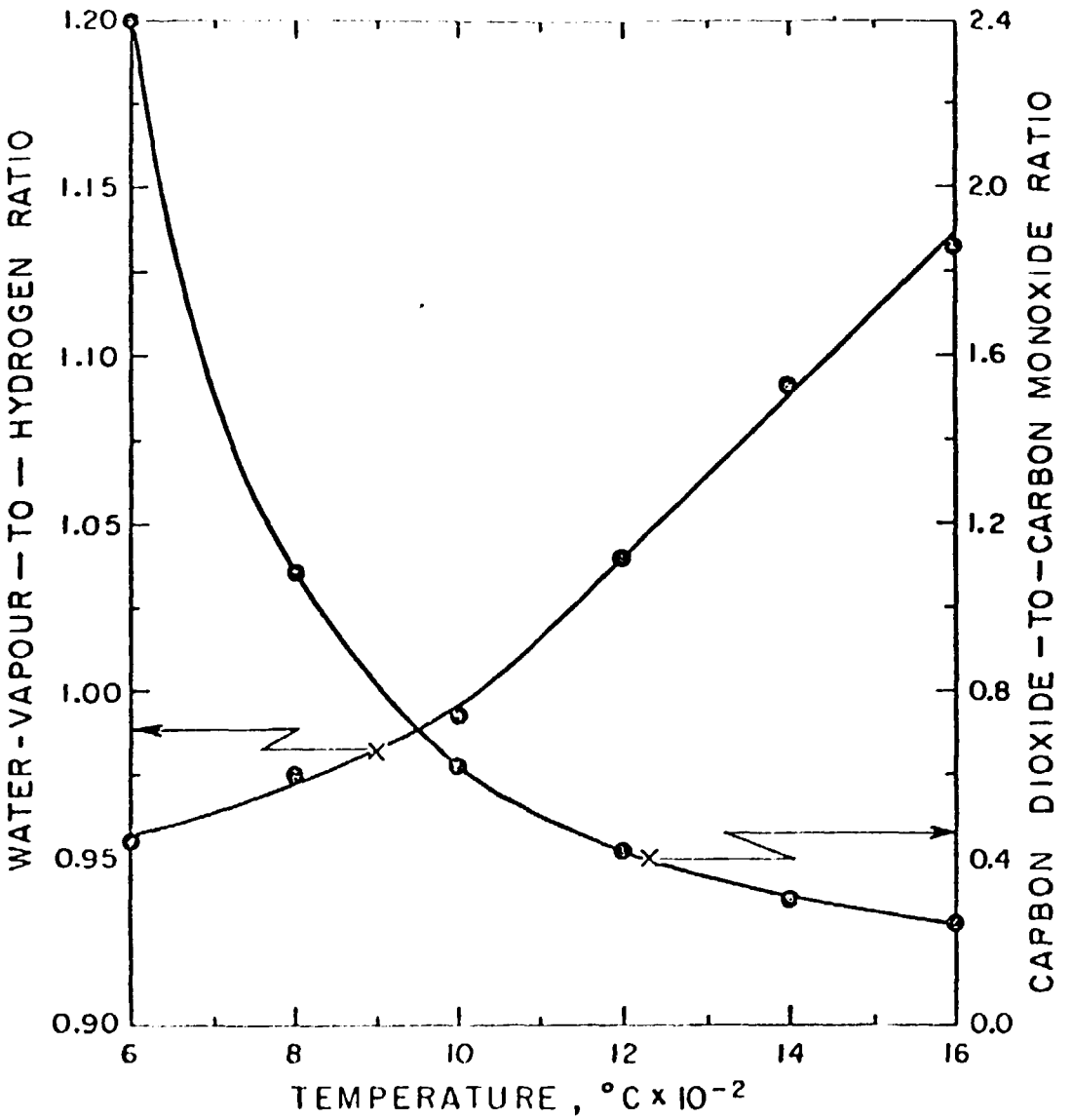

Figure 27 – Influence of temperature on the mixture ratio corresponding to equilibrium with stoichiometric UO_2, for CO_2 + CO and H_2O + H_2 (after ref. 117).

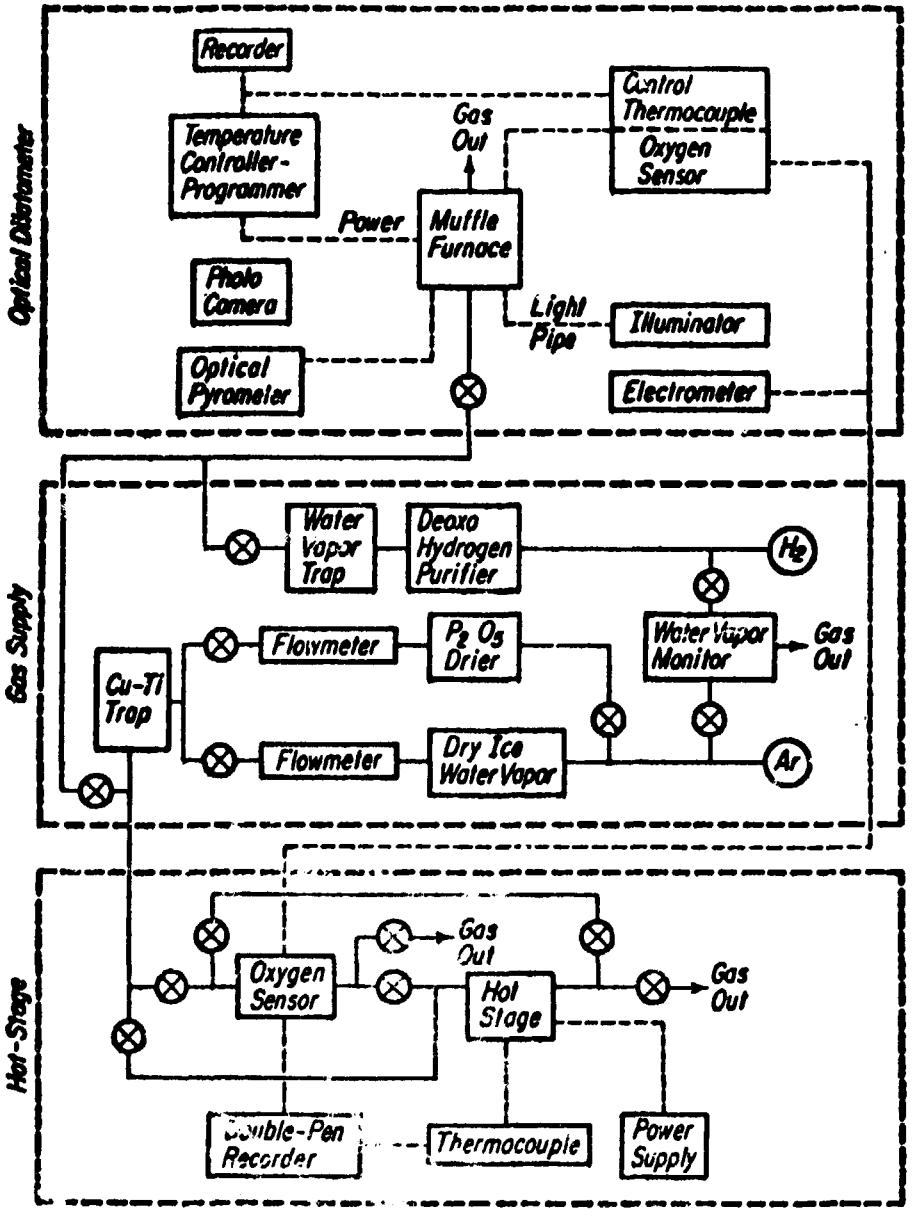

Figure 28 – Diagram of sintering system. The continuous lines indicate the overall arrangement of the gas ducts.

Figure 29 – General view of the controlled atmosphere high temperature sintering system

influence of the pressure ratio R is related to the oxygen potential of the gas mixture, Stuart and Adams data demonstrate that the intermediate and final stages of sintering can be influenced by the sintering atmosphere oxygen partial pressure. However it is necessary to remark the above investigators do not agree with this interpretation. They attribute the enhanced sinterability to surface effects, involving competitive absorption of H_2 and H_2O; they recognize the controlling adsorption mechanisms are not clear.

4 – EXPERIMENTAL WORK

4.1 – General Experimental Approach

Mixtures of $CO_2 + CO$ or $H_2 + H_2O$ (vapor) have been utilized to control the oxygen potential of sintering atmospheres. Lay and Carter[88], Jakeshova[59], Webster and Bright[142], Kumar and Johnson[61,82], Stuart and Adams[132] have used this approach in investigations of sintering, under controlled oxygen potential.

The reaction involved and respective equilibrium constant k were given in Section 2.4.2 for $H_2 + H_2O$ (vapor)*. For $CO_2 + CO$:

$$CO_2 \rightleftharpoons CO + \frac{1}{2} O_2 \tag{4.1}$$

$$k = \frac{[p(CO)]\,[p(O_2)]^{1/2}}{[p(CO_2)]} \tag{4.2}$$

For both gas mixtures the equilibrium conditions are substantially dependent on temperature, as shown in Figures 26 and 27.

For the study of UO_{2+x} initial stage of sintering, in the 800-1100°C range, oxygen partial pressures $p(O_2) \lesssim 10^{-5}$, atm are required, as indicated in Figures 7 and 14. Figure 26 (area ADEG) indicates that using $CO_2 + CO$ mixtures for $0 \leq \log [p(CO_2)/p(CO)] \leq 3.2$, it is possible to control $p(O_2)$ in the range 10^{-18} to 10^{-6} atm.. Mixtures with $0 \leq \log [p(CO_2)/p(CO)] \leq 2.5$ are readily available; they can be prepared by measuring the proportions of the components with regular gas flowmeters (area ACFG in Figure 26). The complete coverage of the area BDE in Figure 26 can be attained using flowmeters for area BCH, and solid-electrolyte oxygen sensors for CDEH.

Richardson and Alcock[121] discussed the general principles for obtaining adequate equilibrium. For electric tube-furnaces, they suggested the heated length should be at least fifteen diameters. They noted also that even in flowing atmospheres consisting of mixtures of two gases, segregation of one component might occur due to thermal diffusion. The extent of this phenomenon becomes progressively less important, the faster the rate of flow.

Reactions of $CO + CO_2$ mixtures with UO_2 are possible, originating uranium carbides and/or oxycarbides[19]. The situation is complex, since CO rich mixtures of $CO+CO_2$ on cooling may deposit carbon, that can contribute to carbide formation. In such circumstances the amount of carbon (as part of a compound) can become significant, in UO_{2+x} samples equilibrated in $CO + CO_2$, with free carbon eventually present[19,143].

Nafziger, et al.[110] reviewed most of the procedures to obtain controlled oxygen fugacities**, at

---

* Eq. 2.17

** When the perfect gas law cannot be applied to the gas mixture, the term fugacity is used instead of partial pressure[134].

high temperature and at one atmosphere total pressure. Among the most used methods are those dependent on the high-temperature dissociation equilibria of suitable gases. Variable oxygen fugacity from dilution of oxygen by inert gases has been used, with a practical lower limit of approximately 10^{-3} atm $f(O_2)$. Lower oxygen fugacities would demand excessively large volumes of gas. An important characteristic of dilution methods is that temperature can be varied independently of oxygen fugacity.

Partially based on a suggestion given by S. D. Brown[26], a method for controlling $f(O_2)$ in argon was developed in the course of this research investigation. It was derived from the fact that commercial argon, for commom industrial applications*, has traces of oxygen. Measurements with a solid electrolyte oxygen sensor indicated $f(O_2) \simeq 10^{-5}$ atm. Flowing the gas through a copper-titanium trap, at temperatures between 25 and 900°C, it was possible to vary $f(O_2)$ in the interval 10^{-5} to 10^{-18} atm.

After leaving the oxygen trap, the oxygen fugacity of the argon + O_2 was independent of temperature, similar to the situation of the previously mentioned dilution methods. However, the practical lower $f(O_2)$ limit could be reduced from 10^{-3} to 10^{-18} atm. Thermal diffusion effects in the sintering atmosphere were minimized by high flows, as suggested by Richardson and Alcock[121].

It is necessary to observe that the need to vary the CO to CO_2 or H_2O to H_2 ratios, when controlling $f(O_2)$ by the utilization of the corresponding gas mixtures, introduces a serious experimental difficulty, in the case of sintering investigations. In Chapter 1 it was mentioned the nature of the atmosphere can influence the sintering process, possibly due to surface effects, in which gas adsorption may have a major role. The differential adsorbate sintering effects, when using widely different CO/CO_2 or H_2O/H_2 ratios, introduce the need to account for them. This could be avoided in the work here described, using instead argon with traces of oxygen, or highly purified hydrogen. It is thought the relatively very small, variable concentrations of O_2, would not create significant adsorbate differential effects.

The $f(O_2)$ of the argon + O_2 mixtures being independent of temperature gradients in sintering furnaces, for high flows, allowed the utilization of regular equipment in this investigation, without the need for the very long furnaces mentioned before, suggested by Richard and Alcock[121]. In particular, it was possible to use a hot-stage microscope furnace, where temperature gradients are extremely severe.

The utilization of hot-stage microscopy for sintering studies of UO_2 microspheres, obtained from gels, was expected to be very effective for the following reasons:

(i) Possibility of determining sintering kinetics for single microspheres.

(ii) The furnace's very high specific power** should permit extremely short heating-up and cooling down times, minimizing shrinkage during transients.

(iii) Direct observation of the microspheres would lead to the identification of critical points during the gel reduction to UO_2.

The microsphere's geometry and size was considered favorable for high thermal shock resistence, making possible very fast heating and cooling rates. The absence of microstructural effects introduced by binders and pressing was thought also to favor the sintering development.

A special optical dilatometer was built for determining the sintering kinetics of UO_2 pellets. It was able to accept a solid-electrolyte sensor in its hot-zone, close to the specimen, and could be operated in reducing or oxidizing atmospheres, at temperatures up to 1950°C.

---

* For instance, argon grade PG-2 from Linde.

** Power dissipated per unit-volume of the hot-zone.

The sintering atmosphere oxygen fugacities were determined using solid-electrolyte oxygen sensors, specially designed for work above 1000°C, up to 1650°C. The sensors were basically similar to that described by Williams, in refence 146, for work up to about 1400°C; however, the sensor electrodes were redesigned, for improved emf stability over all the temperature range of interest (750-1650°C).

The gas flows were controlled by flowmeters with 3% full scale accuracy. The readings were corrected for temperature, pressure and gas type using formulas presented in reference 111.

A diagram of all the sintering system is presented in Figure 28. A general photographic view is shown in Figure 29.

4.2 – Materials

Microspheres and pellets were utilized in this investigation.

Two types of microspheres were used. They will be designated M-1 and M-2.

The starting material for the preparation of M-1 was a gel produced in the course of other work, using a sol-gel process* described in reference 112. A chemical analysis of this gel is in Appendix 3.

Microspheres M-2 were also produced by a sol-gel procedure, developed at Oak Ridge, by Haas[48,49].

The pellets were prepared from a commercial ceramic grade UO_2 powder, of nuclear purity.**

4.3 – Procedures and Apparatus

The basic procedures in the sintering investigation, described herein, were hot-stage microscopy of UO_2 microspheres and optical dilatometry of UO_2 pellets.

$Ar + O_2$, $Ar + H_2$ and dry H_2 permitted variation of the oxygen activity of the sintering atmosphere over more than 13 orders of magnitude.

In $Ar + O_2$ mixtures, $p(O_2)$ was controlled by means of an oxygen trap and measured by a solid-electrolyte sensor.

The optical dilatometer, the oxygen sensor and the oxygen trap were built or assembled at the University of Illinois.

A very substantial part of this work was dedicated to the development of the above equipment.

Even in the case of the hot-stage microscopy, based on a Leitz instrument, it proved necessary to change radically the orignal power control system, in order to attain satisfactory temperature stability during sintering. Electron microscopy was employed extensively to characterize the materials and samples involved. Optical microscopy had less importance as a microstructure evaluation method, but it was basic for the determination of the UO_2 microspheres sintering kinetics.

---

* A colloidal liquid solution of a material is dropped through a nozzle into a liquid, practically immiscible with water; the resulting spherical droplets are solidified by a gelation process[112].

** From NUMEC, BET surface area approximately 5 m^2/g.

The reduction of the gel microspheres to UO_2 samples, with low densities (5.3 ± 0.1 g.cm^{-3}), proved to be exceptionally delicate. A special heat treatment involving processing in vacuum, air, and $Ar + H_2$ had to be developed, in order to avoid inadmissible loss of microspheres, due to breakage.

The unexpected, extraordinarily fast sintering rates of the UO_{2+x} microspheres in $Ar + O_2$ made imperative the application of microcinematography techniques, in order to follow most of the shrinkage. Film speeds as high as 54 frames per second had to be employed.

It was possible to grow necks between UO_2 microspheres, by sintering in H_2 + 10 V/O He at 1750-1950°C, in a specially modified tungsten-heater furnace.*

Due to the very small grain size of the microspheres structure, the disintegrated samples exhibited very high activity, even after sintering. They oxidized in extremely short times when not protected by suitable atmospheres. This introduced severe difficulties for the effective application of characterization methods such as TGA and X-ray diffractometry.

For the determination of the densities of the microspheres, their weights were measured using ultramicrobalance techniques[91]; the diameters were determined by optical microscopy. The resulting average fractional standard deviation was 0.013 for the densities of microspheres weighing (520 ± 30) μg after sintering.

4.3.1 – Measurement and Control of the Sintering Atmosphere Oxygen Potential

The oxygen partial pressure in $Ar + O_2$ was controlled using a copper-titanium trap, through which the gas mixture flowed. The variation of the trap temperature permitted the control of $p(O_2)$ in the range 10^{-5} to 10^{-18} atm. The pressure measurements were made with zirconia-yttria (or calcia) oxygen sensors.

No oxygen had to be added to the argon. The commercial gas used** had initial 5-10 ppm O_2. It was dried by flowing through phosphorous pentoxide or a dry-ice vapor trap.

The hydrogen utilized*** previously passed through an oxygen trap**** and a liquid nitrogen drier. In some experiments the liquid nitrogen was changed for dry-ice, in order to allow a measurable quantity of water vapor in the sintering atmosphere.

Only metal (stainless steel, copper and brass) or teflon tubing was used in the gas system, between the driers and the sintering furnace.

4.3.1.1 – Oxygen Trap

The oxygen trap is schematically depicted in Figures 30, 31 and 32. It consisted of a 460 mm long, 25 mm diameter quartz tube, filled with copper turnings and titanium sponge in three layers, each one being approximately 80 mm long. The gas was injected in the trap through a 430 mm long, 6 mm diameter quartz tube located in the longitudinal axis of the apparatus, in such a way the mixture had to pass through the three layers of oxygen getters, before outflowing.

The trap was closed by an O-ringed, clamped pyrex-cover, with two exits controlled by stopcocks, one of which permitted the evacuation of the system prior to operation.

---

* Centorr model 15-2x3T-22.

** Linde PG-2.

*** Linde Pre-Purified grade.

**** Engelhardt Deoxo.

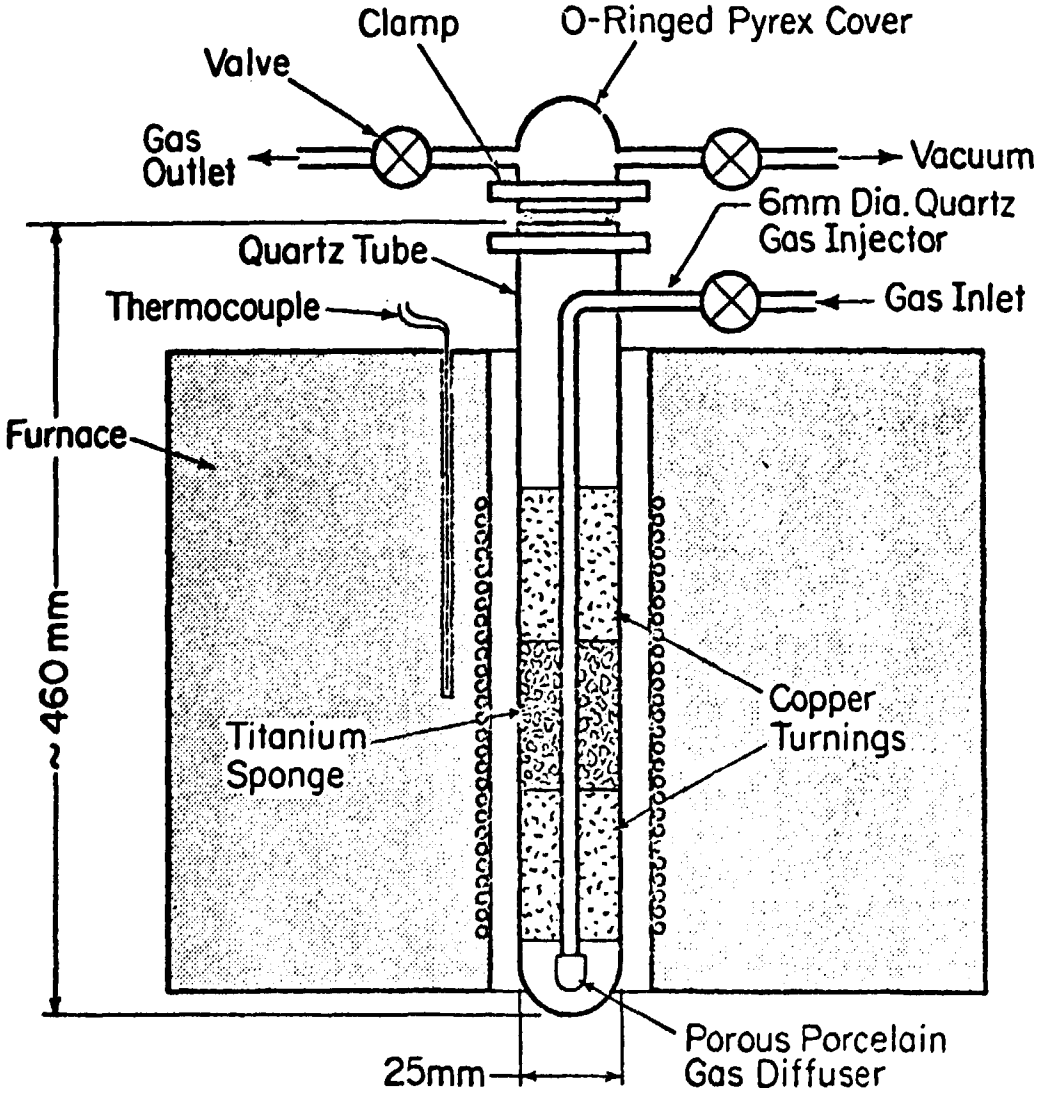

Figure 30 – Schematic view of Cu-Ti-Cu trap

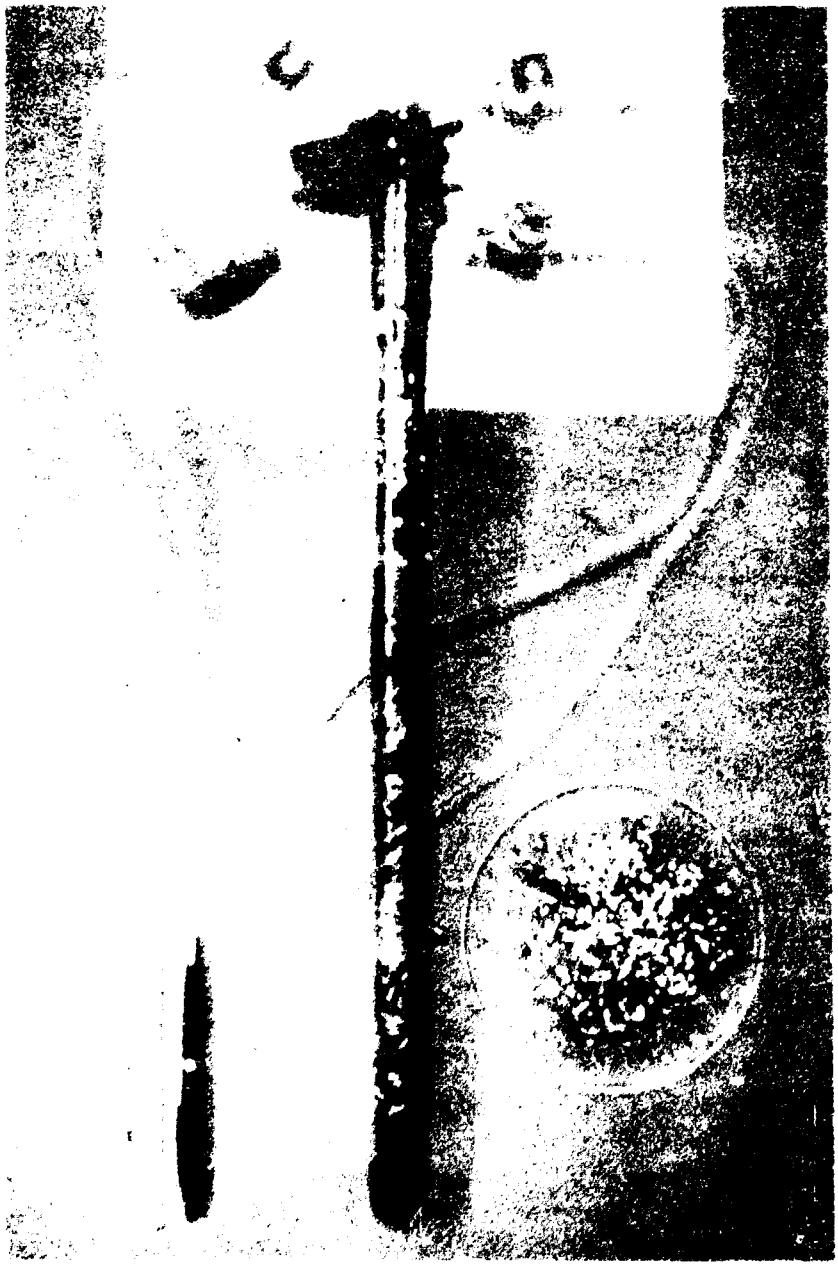

Figure 31 – Components of the copper-titanium-copper trap. In the center is the quartz tubular chamber containing copper turnings and titanium sponge.

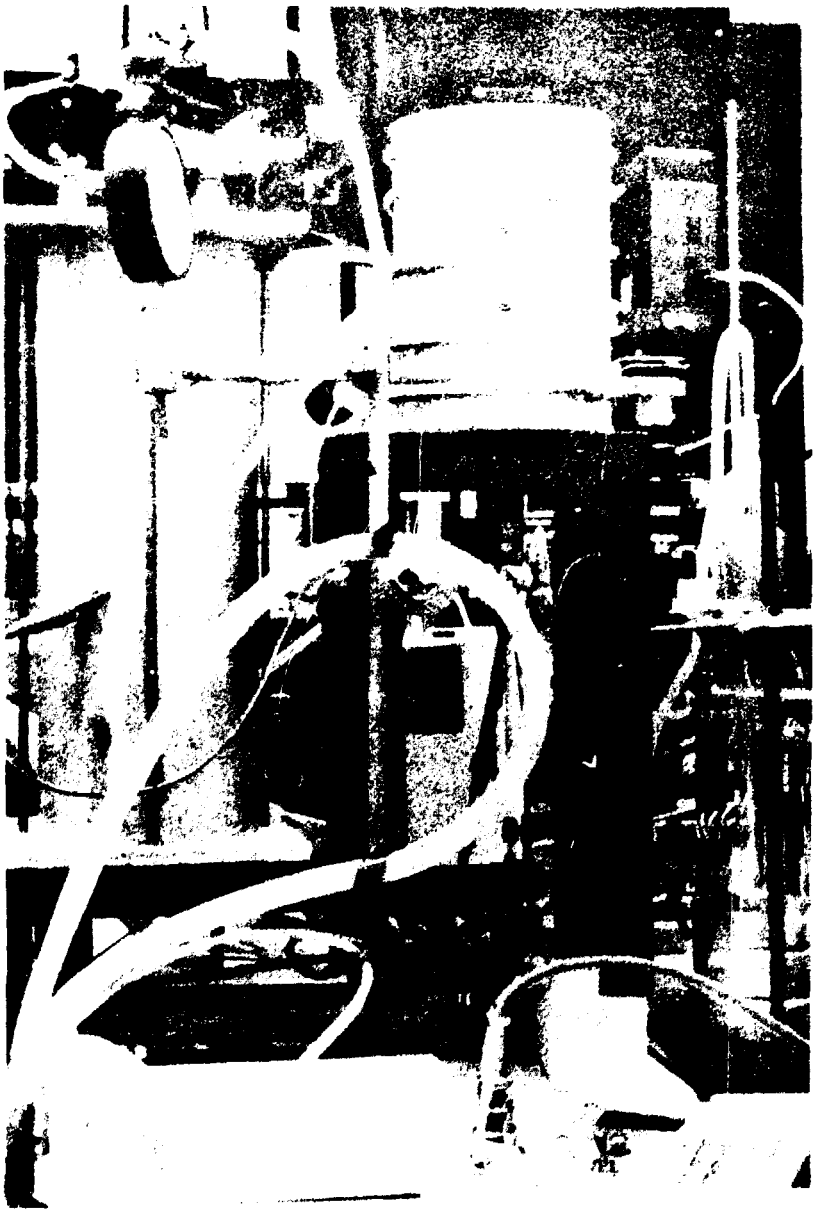

Figure 32 – General view of the apparatuses for controlling the oxygen potential of sintering atmospheres. At left is shown the Cu-Ti-Cu oxygen trap. To its right is the oxygen sensor furnace assembly.

The trap furnace had a power control similar to that used for the hot-stage microscopy system, described in Appendix 4. In this way it was possible to control the furnace temperature fluctuations within about 1°C, and at the same time to vary rapidly the power level, so as to compensate for variations of the trap oxygen-adsorption characteristics.

The lifetime of the trap getters was about 200 hours, thereafter their response to the power control was not adequate, with excessive variations in the desired level of $p(O_2)$.

Table VIII indicates the variability of log $p(O_2)$ during typical sintering experiments.

Table VIII

Standard deviation σ of log $p(O_2)$ = k for sintering experiments at different oxygen potentials

k (log atm)	σ (log atm)
- 4.84	0.02
- 7.20	0.20
- 8.10	0.10
- 8.80	0.10
- 9.74	0.07
- 11.62	0.07
- 12.36	0.06
- 13.02	0.02
- 14.65	0.03
- 15.71	0.03
- 17.95	0.02

The average fractional standard deviation of k was 0.0073, adequate for the development of sintering investigations for which k varied between - 18 and - 5.

It is necessary to observe that $p(O_2)$ varied not only with temperature, but also with gas flow Q and the time the trap had been previously utilized. No systematic study of the $p(O_2) = f$ (temperature, Q, time) relationship was made. For $p(O_2) \simeq 10^{-12}$ atm and $Q = 600\,cm^3/min$, the trap temperature had to be 340°C, with new oxygen getters; after approximately 150 hours operation, it was necessary to increase the trap temperature to about 600°C, in order to reach the same $p(O_2)$ (Q maintained constant).

Many trap configurations were tried, one of them utilizing only titanium sponge. The configuration adopted, shown in Figure 30, permitted satisfactory control of $p(O_2)$, but it is felt there is considerable margin for optimizing the design.

For $Ar + O_2$ flow in the range 400 to 600 cm^3/min, the time required to establish trap-equilibrium, at a certain $p(O_2)$, was approximately 3 hours.

4.3.1.2 – Oxygen Sensor

A schematic view of one of the oxygen sensors used in this investigation is shown in Figure 33. The quartz chamber 9 is inserted in a furnace, as depicted in Figure 32. This sensor configuation was

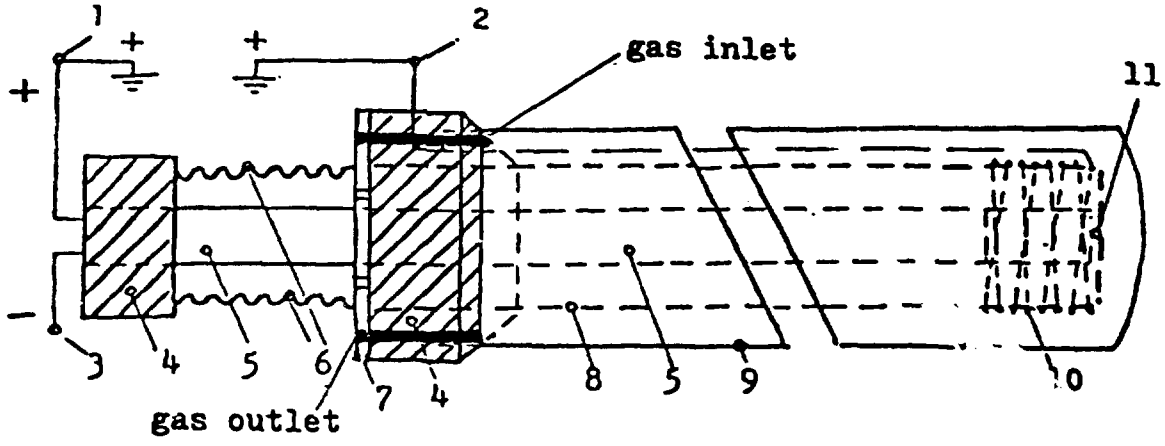

1-Thermocouple Pt leg
2-Solid electrolyte external contact, Pt-wire connection
3-Thermocouple Pt-Rh leg
4-Molded epoxy support for springs 6
5-Thermocouple tube
6-Springs for spring-loading thermocouple tube
7-Vented supporting disc for thermocouple tube
8-Solid electrolyte tube
9-Quartz chamber
10-Solid electrolyte external contact
11-Thermocouple tip in contact with the closed-end of the solid electrolyte tube

Figure 33 – Schematic view of solid-electrolyte oxygen sensor for operation in the 700 – 1150°C range. Its furnace is not shown.

adequate up to a temperature of about 1150°C, measuring the oxygen potential of the sintering furnace inflowing or outflowing atmosphere. For higher temperatures the quartz chamber did not provide the necessary separation, between the internal and external atmospheres.

For temperatures higher than 1150°C another sensor configuration was developed. It is presented in Figure 34. In this case the extremity of the sensor is located close to the sample being sintered, measuring the oxygen potential of the sintering atmosphere in the furnace hot-zone.

Initially both sensor types presented very severe instabilities in the readings of electromotive forces, when operating over 1100°C or under 750°C. This problem is avoived, in current solid-electrolyte oxygen sensor technology, by operating the instrument in the interval 750 to 1100°C. Such a solution could not be applied to a sensor located in the hot-zone of the sintering furnace utilized in this work, since it was supposed to have reliable response in a wider range of temperatures.

The emf instabilities were eliminated by the use of a specially designed platinum electrode. It consisted of a cruciform platinum foil, with its equal-length arms folded along the tip of the solid electrolyte. The foil was maintained in place by platinum wire, passing over and under the arms of the cross, around the extremity of the solid electrolyte, in an extension of about 13 mm.

The sensors were checked using mixtures of CO_2 and CO, in different ratios and temperatures.* The calculations were based on the following formula, presented in reference 127 by Sato:**

$$\log f(O_2)\ (CO_2 - CO) = 2\left(1.505 - \frac{14700}{T} + \log\left[\frac{p(CO_2)}{p(CO)}\right]\right) \pm 0.005 \qquad (4.3)$$

with

$fO_2(CO_2\text{-}CO)$ = oxygen fugacity of the CO_2-CO mixture.

$p(CO_2)$ = partial pressure of CO

$p(CO)$ = partial pressure of CO

The emf E was calculated using the following formula[127], derived from the Nernst relationship:***

$$E = 0.04960\ T \log\left[fO_2(CO_2 - CO)/fO_2\ (air)\right]\ (mV) \qquad (4.4)$$

with fO_2 = oxygen fugacity of air ≈ 0.21.

For $p(CO_2)/p(CO)$ varying from 0.07 to 14, and temperatures between 869 and 958°C, the average difference between the experimental and calculated emf values was 1.3%, for 9 determinations. This result was judged satisfactory, considering the 3% full scale accuracy of the flowmeters utilized in the preparation of the CO_2-CO mixtures.

---

* The gases were from Linde, Research Grade; the flows were measured by means of Matherson flowmeters, series 620.

** The formula is not correct in reference 127. The factor 2 in the right member was not printed.

*** $\Delta G^o = Z_i F E$, where ΔG^o = standard free energy change, Z_i = valence of ions i, F = Faraday constant, E = voltage[72].

It can be shown that $E = \frac{RT}{4F} \ln\left[\frac{p(O_2)_I}{p(O_2)_{II}}\right]$ for solid electrolytes such as calcia-stabilized zirconia, with $p(O_2)_I$ and $p(O_2)_{II}$ corresponding to oxygen partial pressure ion opposite sides of the electrolyte. The relationship applies only if there is no appreciable current drain during the voltage measurement, and if the electrolyte has only negligible eletronic conductions.

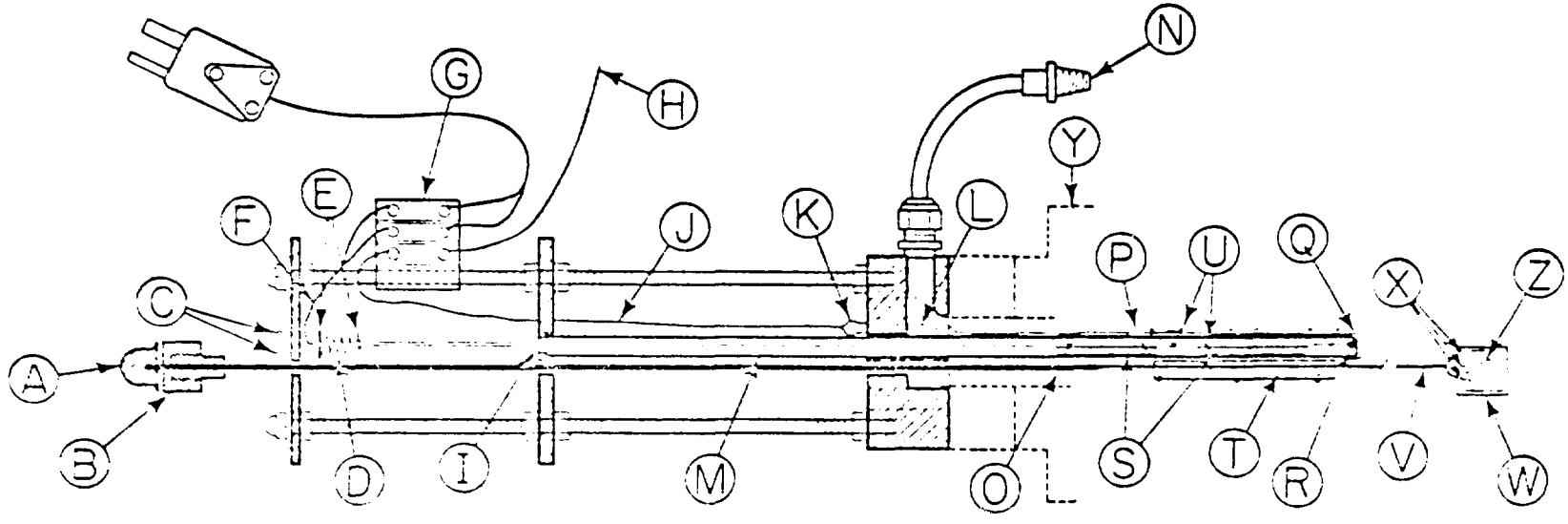

Figure 34 – Oxygen sensor for dilatometry work. A – Handling knob for push rod; B – WITT seal; C – Spring tension adjusting screws; D – Spring; E – Bakelite discs; F – Thermocouple Pt 6% Rh – Pt 30% Rh (type B); G – Thermocouple and solid electrolyte wiring connector; H – To high imp. electrometer; I – Vent; J – External Pt electrode wire; K – Ampnenol connector; L – Al_2O_3 insulator tubing; M – Zirconia – Yttria tube (closed one end); N – Gas inlet; O – Inconel rod; P – Electrical insulator tubing; Q – External Platinum electrode; R – Thermocouple tip in contact with solid electrolyte wall; S – $ZrO_2 - Y_2O_3$ rod for support of thermocouple tube; T – Zirconia – Yttria support; U – Pt wire; V – Pt – Rh wire; W – Pt – Rh crucible; X – Cavities for microspheres; Y – Furnace; Z – Position of cylindrical sample.

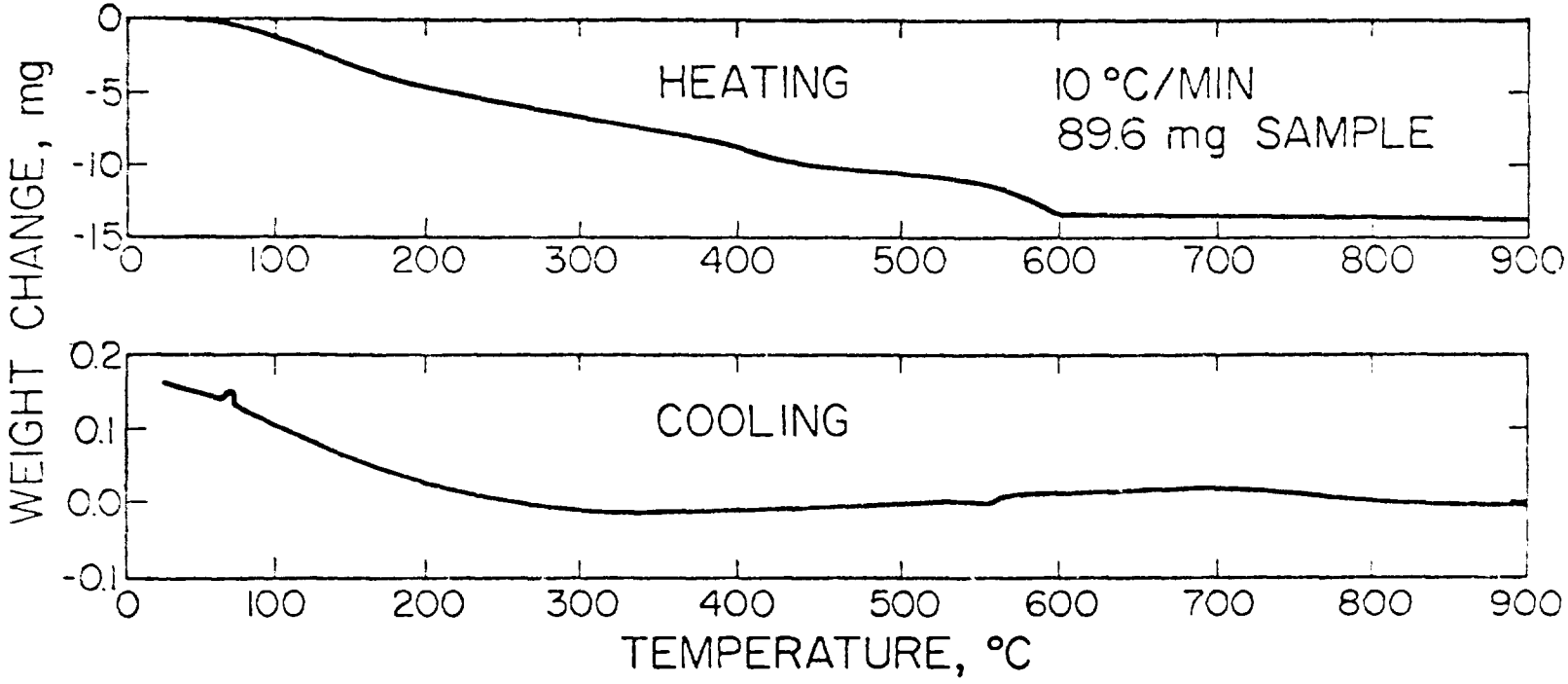

Figure 35 – Thermogravimetric analysis of gel type M-1

For the calculation of $p(O_2)$ in mixtures of argon and oxygen, another formula derived from the Nernst relationship was utilized:

$$E = 2.1517 \quad 10^{-2} \; T \; \ln \frac{p(O_2)}{0.2095} \; (mV) \qquad (4.5)$$

4.3.2 – Thermogravimetric Analysis

A DuPont 950 Thermogravimetric Analyzer was used to obtain the analysis of the gels M-1, presented in Figure 35. The atmosphere was reducing and consisted of N_2 + 10 v/o H_2. The weight loss became constant after 600°C, and was interpreted as reduction of the gel to UO_2 at that temperature. On cooling from 900°C at 10°C/min, the sample weight started to increase significantly again, for temperatures under 300°C; this increase was attributed to oxidation. It was seen in Chapter 3 that to maintain stoichiometry at low temperature, the atmosphere must have a very small oxygen potential relatively to that at higher temperatures. Traces of oxygen in the N_2 + 10 v/o N_2 mixture were thought to be responsible for that oxidation. Considering this interpretation, it was decided to use dry hydrogen for the preparation of stoichiometric uranium dioxide microspheres.

4.3.3 – Vacuum Drying

The gel microspheres M-1 were dried at 130°C for three hours, in a vacuum oven* at a pressure of approximately 50 mm Hg. This drying proved useful to decrease the breaking of the microspheres, during the subsequent reduction operation.

4.3.4 – Reduction

The main problem for the preparation of M-1 microspheres was their rupture, during reduction to UO_2. The heating cycles shown in Figure 36 permitted the elimination of considerable breakage.

It was desirable to reduce the gel to UO_2 in the smallest time and temperature possible, in order to avoid significant sintering during reduction.

Figure 37 shows that the weight loss became constant at about 500°C, for a heating cycle described by the line A-H-I in Figure 36. Figure 37 indicates that the shrinkage decreased substantially after 500°C. In order to assure the reduction of all the gels to UO_2, 600°C was chosen as the maximum reducing temperature, maintained for 30 minutes. The heating cycle corresponded to the line A-H in Figure 36; after H, the temperature was increased by 10°C/min, up to 600°C. A 1-inch diameter quartz-muffle in a Ni-Cr wounded furnace was utilized for this operation.

The total weight loss and the diametral shrinkage during reduction were 15 and 20% respectively.

4.3.5 – Hot-Stage Microscopy

A Leitz model 1750 microscope heating-stage, shown in Figure 38, was used for the sintering kinetics studies.

Figure 39 shows the hot-stage positioned under a microscope. Figure 40 indicates the position of light pipes used to direct the illumination at such angles that back-reflection, into the microscope

* Thelco model 19, from Precision Scientific, Chicago, Illinois.

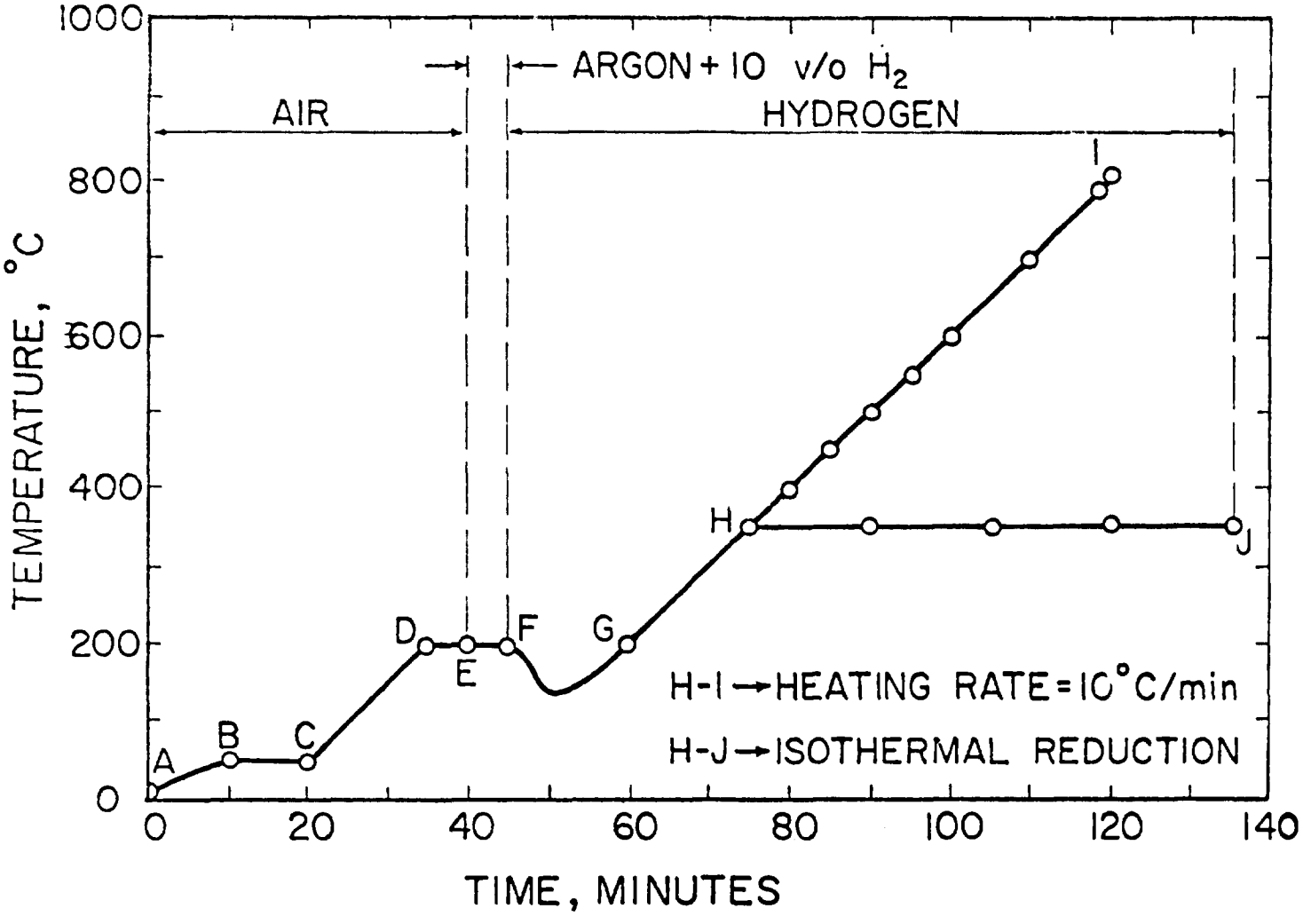

Figure 36 — Heating cycle for the reduction of gel M-1 to UO_2

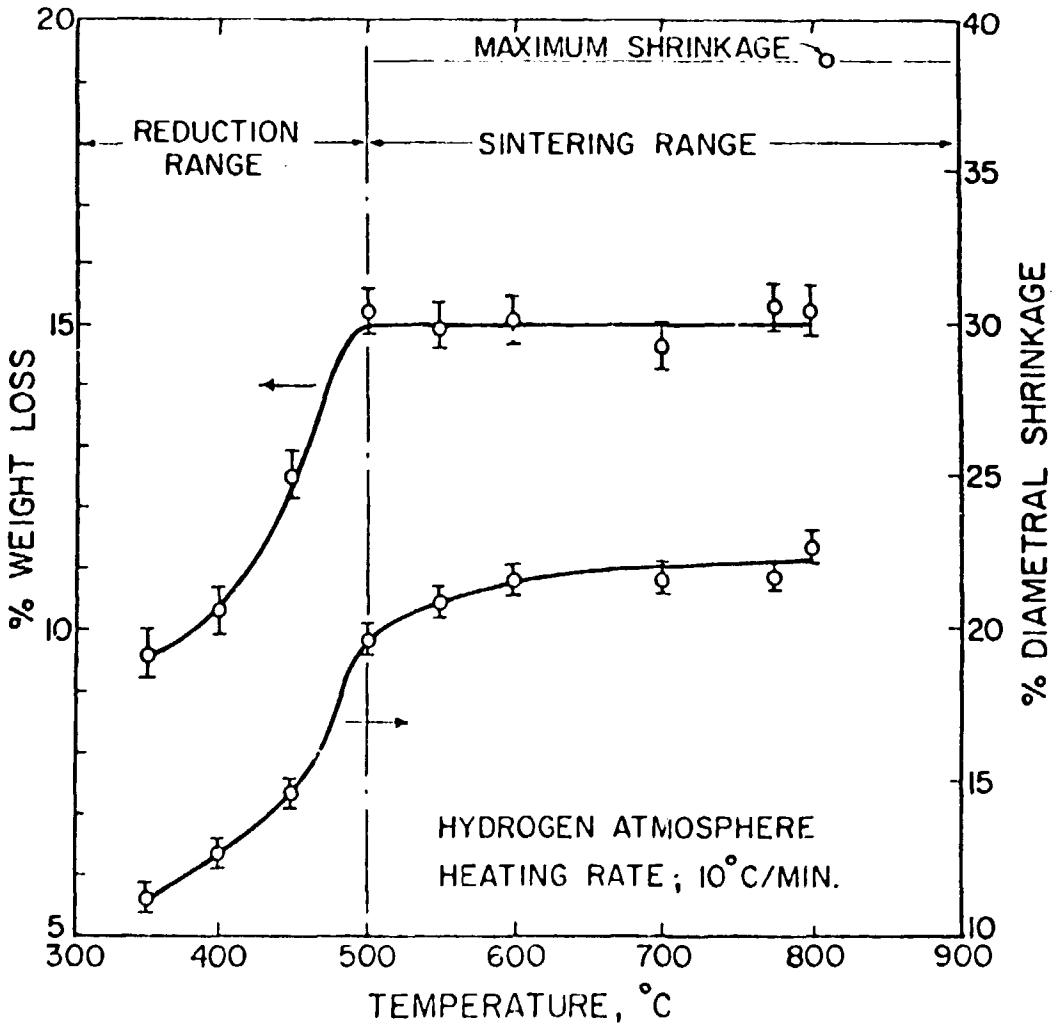

Figure 37 – Weight-loss and shrinkage variation with temperature for gels type M-1, treated in H_2

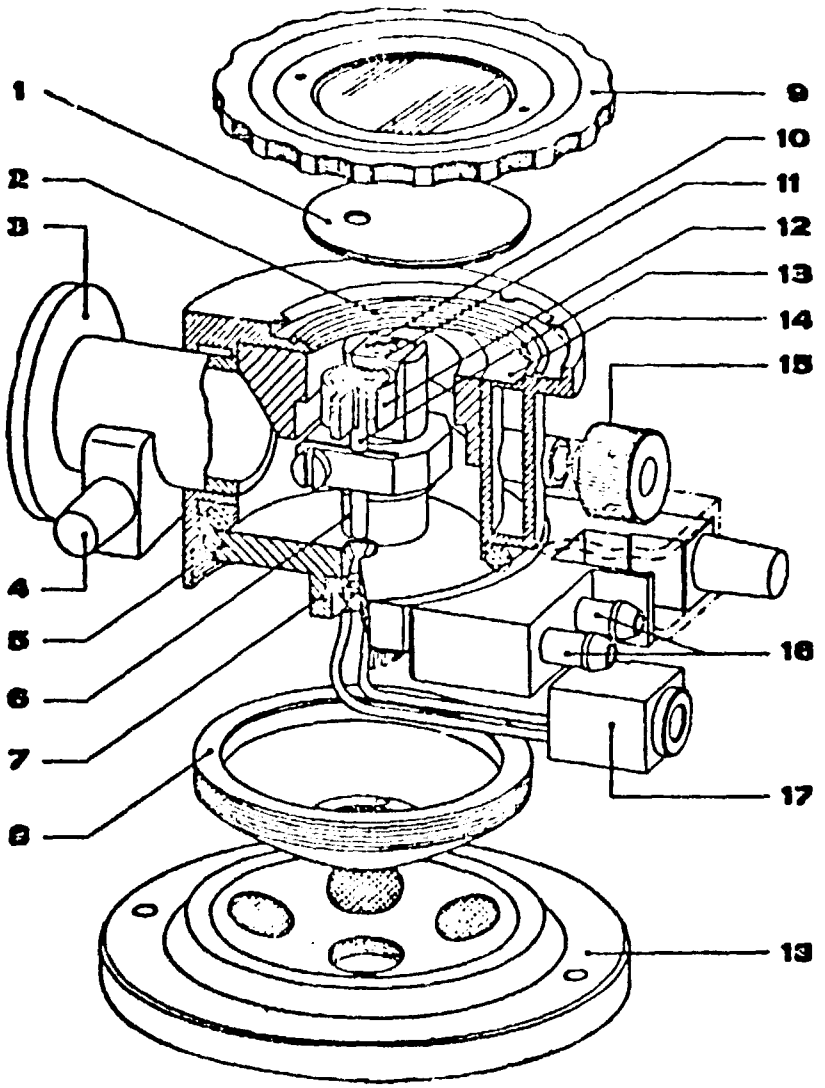

Figure 38 – View of high-temperature hot-stage (after ref. 72). 1 – radiation screen; 2 – gasket; 3 – suction tube; 4 – heating current connection; 5 – base plate; 6 – electrode column with clamp; 7 – thermocouple clamp; 8 – screw cup; 9 – cover with quartz window; 10 – clamping wedges; 11 – sample; 12 – heating and screening plates; 13 – cappilary tube with thermocouple; 14 – double-walled vacuum tank; 15 – flooding valve, inert gas flushing; 16 – cooling-water connections; 17 – thermocouple bush; 18 – base with spherical bearings and magnets

Figure 39 – Hot-stage positioned for operation

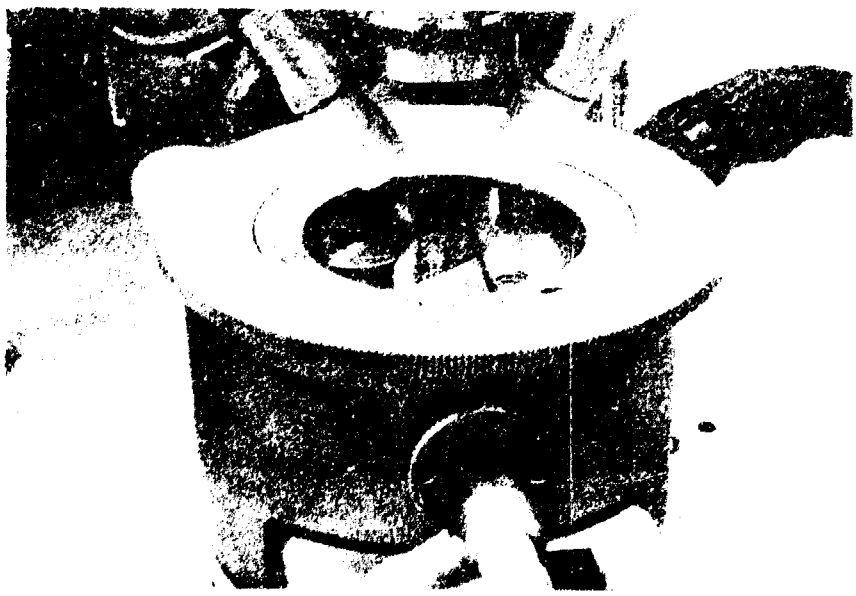

Figure 40 – Light-pipes used for illumination and contrast optimization. In the center, a platinum gauze heater can be seen.

objective, could be avoided. The variability of the light pipes position allowed also for optimization of image contrast; a platinum gauze heater is also shown in the center of the hot-stage.

Figure 41 presents a general view of the hot-stage microscopy system, including the oxygen trap and sensor, utilized for controlling atmosphere oxygen activity. A Nikon microscope, Microflex PFM * viewer and 35 mm camera are also shown. Both still and movie cameras were used to record shrinkage.

The hot-stage had to operate either in argon + O_2 or in dry hydrogen. For temperatures up to about 600°C, a platinum gauze heater worked satisfactorily in both atmospheres. However, at higher temperatures the lifetime of platinum heaters was unacceptably short. In these conditions molybdenum heaters demonstrated satisfactory performance.

The platinum heaters were made from 52 mesh gauze, in two rectangular pieces of approximately 16 x 9 mm. Each piece was positioned as indicated in Figure 38.

Molybdenum heaters had the same dimensions given above; they were formed from foils 30 μm thick.

For both heaters the electrical resistance was low, of about 0.025 Ω. In order to dissipate adequate power, the heaters were connected to a high-current transformer. The original Leitz electric power system proved unsuited to maintain the necessary current stability (± 0.3 A). A special power source had to be built; it is described in Appendix 5.

One microsphere was sintered in each hot-stage run. The microsphere was placed over an alumina powder layer, in a 2 mm diameter quartz crucible, mounted atop the thermocouple (type B) indicated in Figure 38. The alumina layer precluded direct contact between the sample and the crucible, at the same time enhancing the contrast microsphere-background, for photographic purposes. For temperatures over 1200°C, in hydrogen, the quartz crucible had to be substituted by a molybdenum one.

As observed before, in order to minimize thermal diffusion segregation effects in the argon + O_2 atmospheres, high flows had to be used. These tended to cool the crucible and the thermocouple, whose readings without special calibration were not indicative of the true temperatures.

The correct temperatures were determined by melting high-purity substances in the crucible, at the same position to be occupied by the microsphere. Calibration graphs, relating true temperature with heater current or thermocouple output, are presented in Figure 42 to 45.

For the gas flows utilized during sintering, oxygen activity measurements of the inflowing and outflowing atmospheres demonstrated that $p(O_2)$ did not vary significantly, with the passage through the hot stage. Consequently, only the inflowing gas was monitored for its oxygen activity.

The heating cycle adopted for equilibration of UO_{2+x} with argon + O_2 atmosphers, in the hot-stage, is shown in Figure 46. In the first 20 minutes the microspheres were reduced in hydrogen to the stoichiometric composition. Argon + O_2 at the desired oxygen potential was introduced after 24 minutes, mixing with hydrogen. The hydrogen flow was interrupted on the 26th minute.

This heating cycle was critical for the equilibration of UO_{2+x} with the sintering atmosphere. In Chapter 3 it was metioned that to maintain x constant, for decreasing temperatures, $p(O_2)$ had also to be decreased. This corresponds to more reducing conditions at low temperatures. The above heating cycle provided an atmosphere with the very low oxygen potential, necessary to prevent sample oxidation during the heating-up transient.

It is necessary to observe that for hot-stage operation in hydrogen (flow 470 cm^3/sec), the electric power necessary to maintain a certain temperature is substantially higher than that needed when

* Nikon auxiliary focusing device.

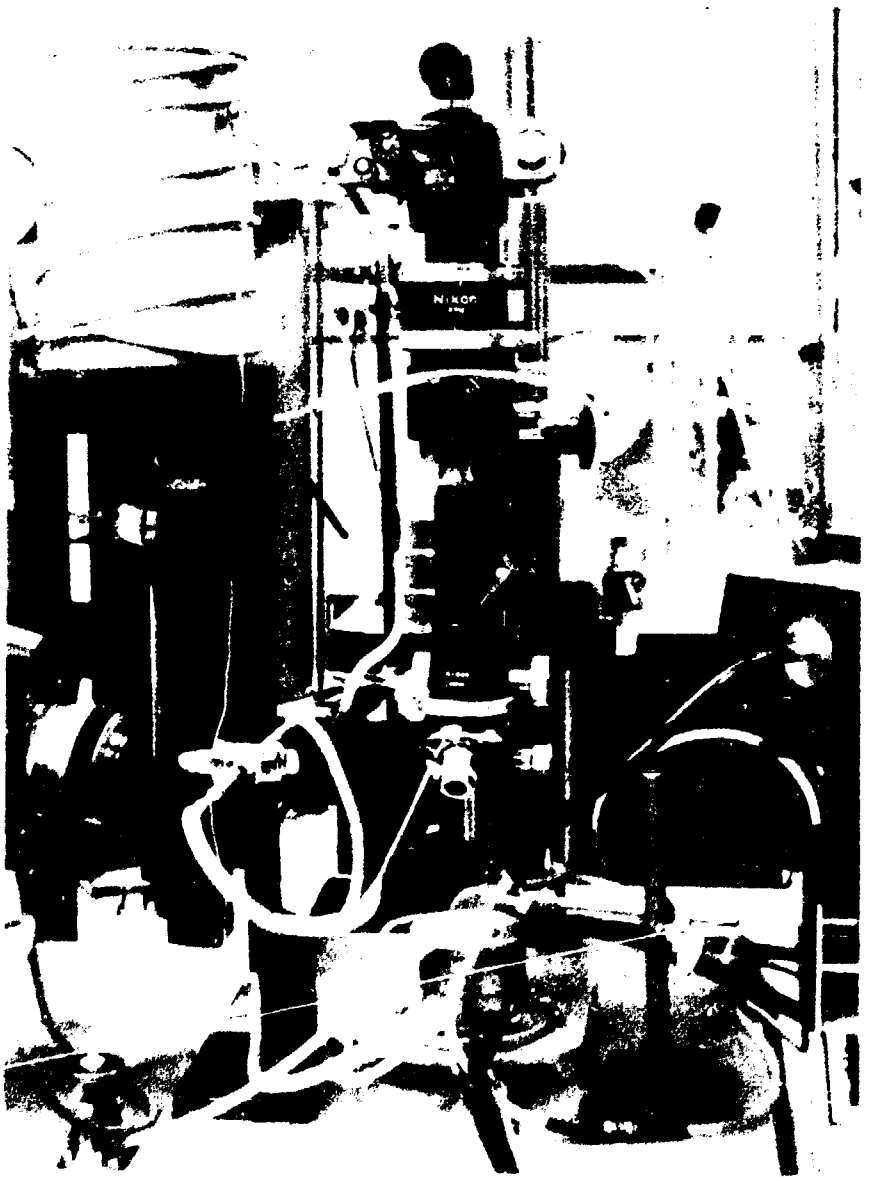

Figure 41 - Overal view of the system for hot-stage microscopy

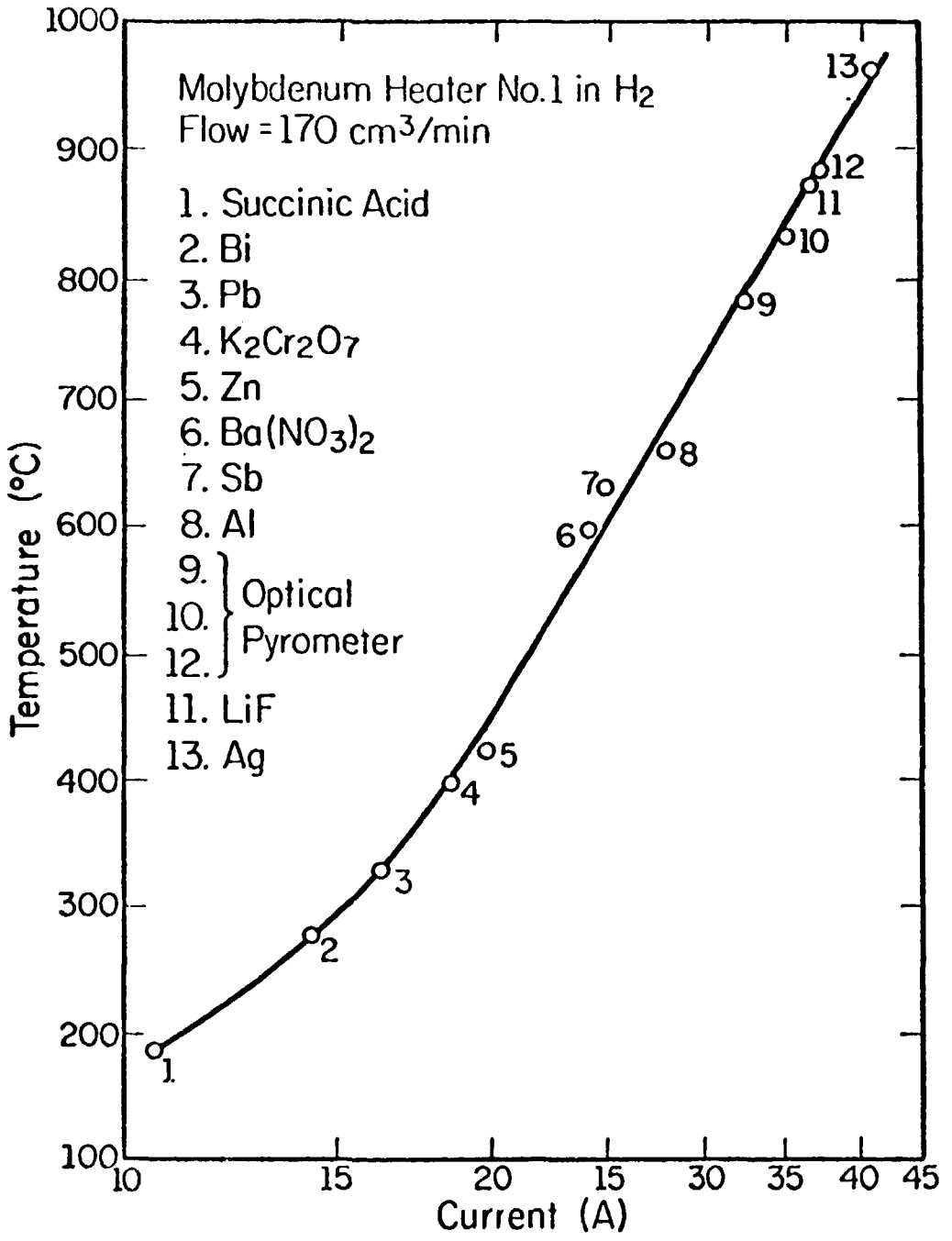

Figure 42 – Temperature calibration for hot-stage operating with molybdenum heater, in H_2

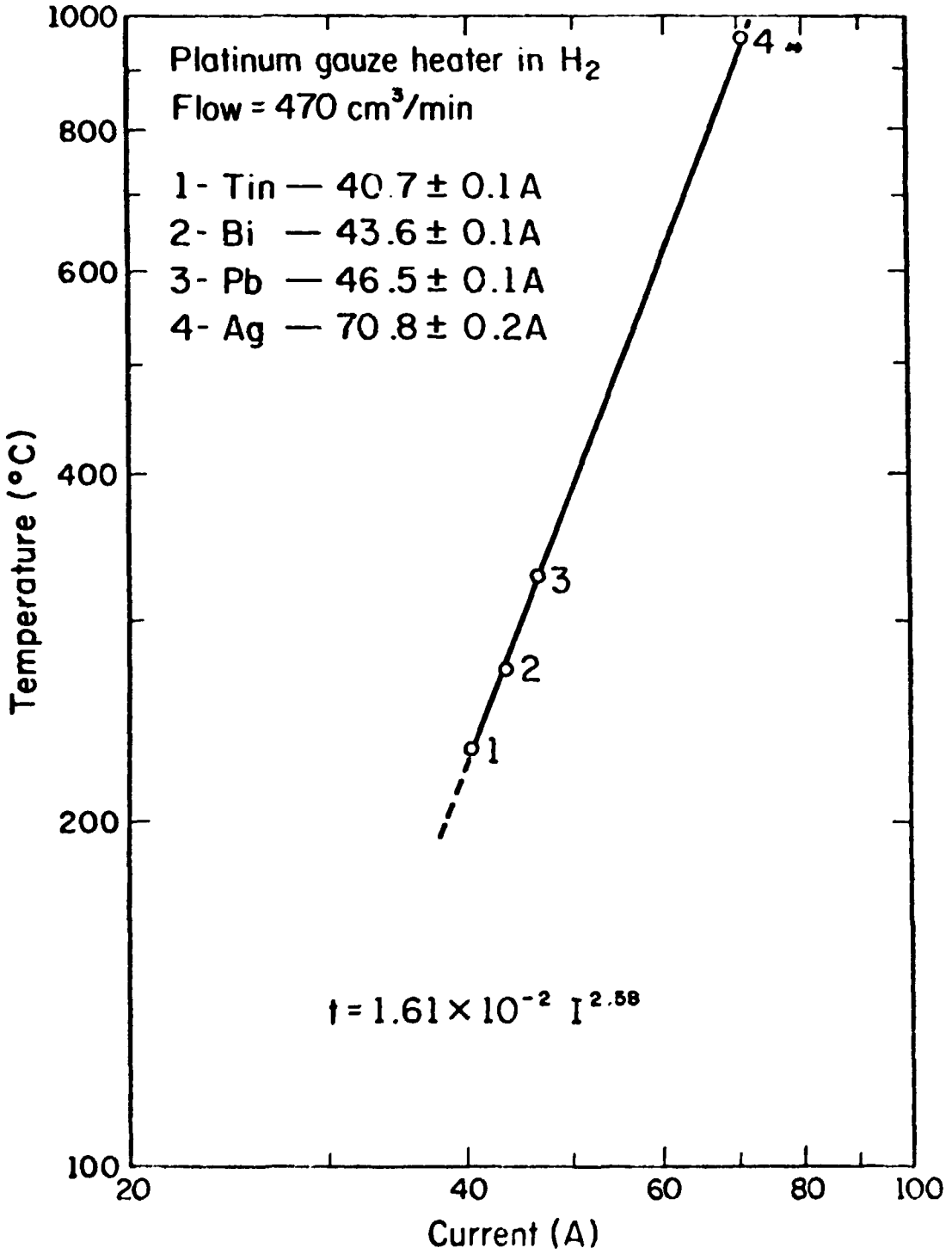

Figure 43 -- Temperature calibration for hot-stage operating with platinum heater, in H_2

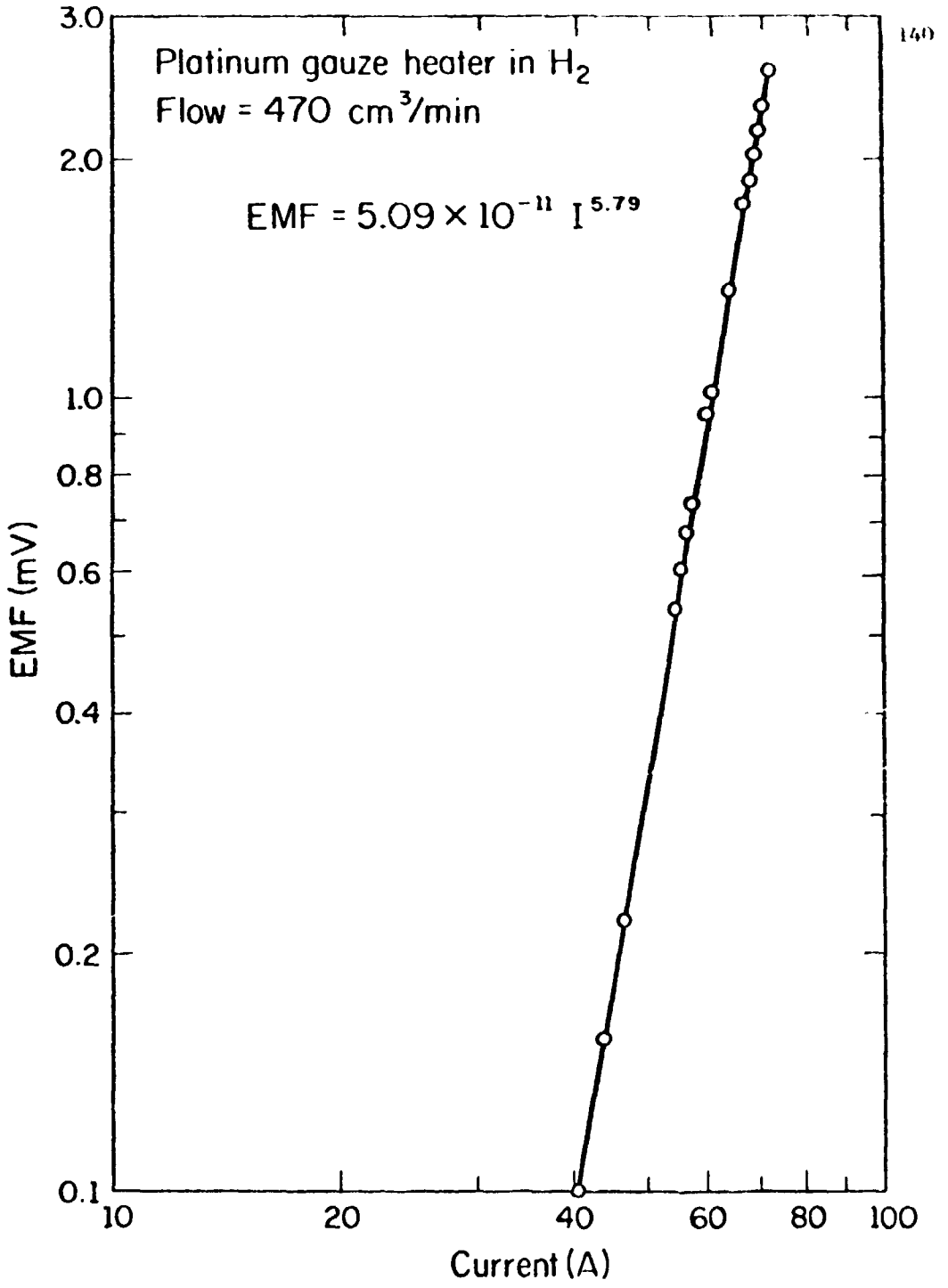

Figure 44 – Relation between thermocouple reading and current, for hot-stage operation in H_2, with platinum heater.

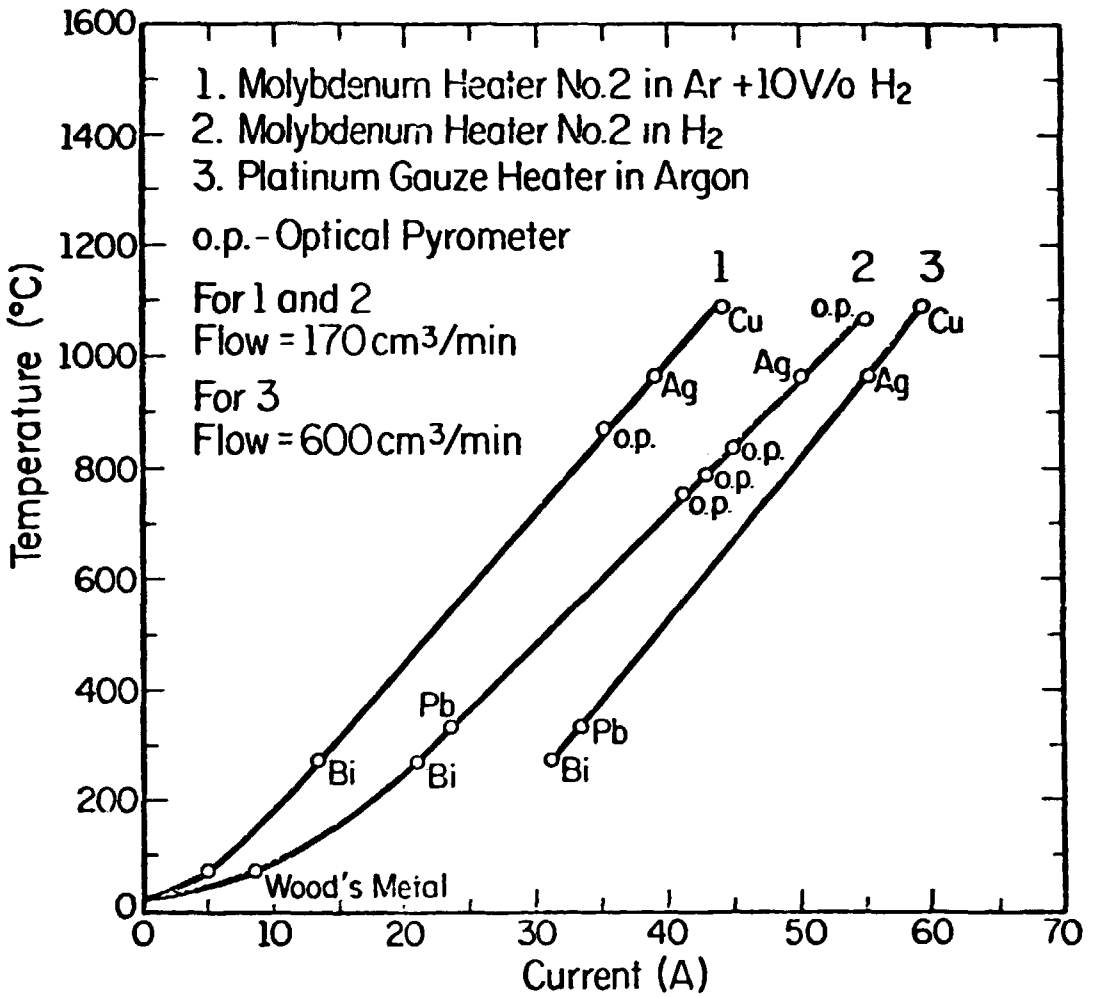

Figure 45 – Temperature vs. current for different operation modes of the hot stage

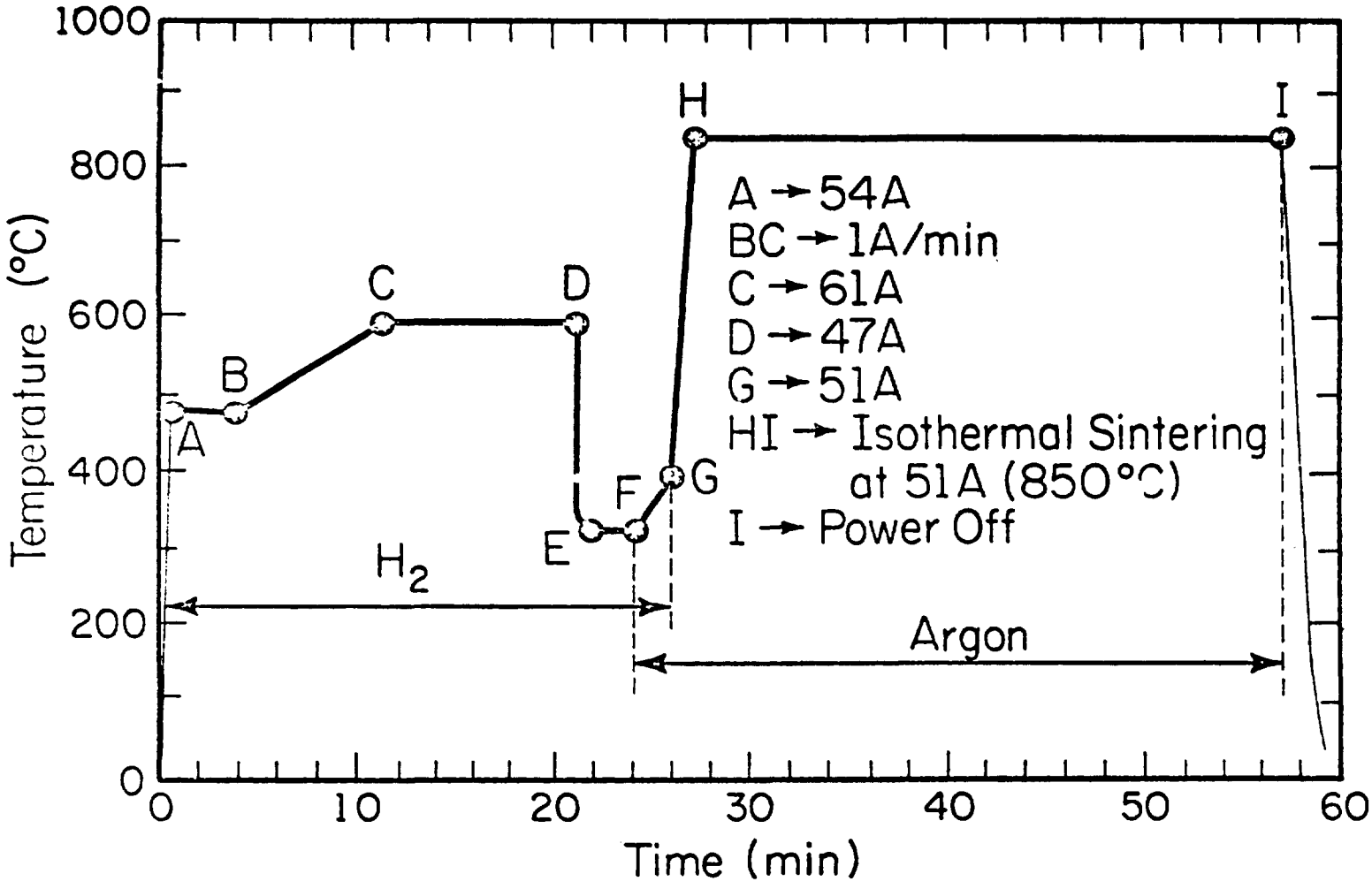

Figure 46 – Typical sintering cycle for UO_2 type M-1. Line HI corresponds to the particular case of isothermal sintering at 850°C. The hot-stage current is indicated at transition points.

operating with argon,* flowing at 600 cm^3/sec. Figure 46 shows that at the 20th minute the hot-stage current was reduced from 61 to 47 A.** The dilution of H_2 with argon + O_2, after the 24th minute, increased the hot-stage temeprature, the current being maintained at 47 A till the 26th minute, when it was increased to a value corresponding to the desired sintering temperature. Therefore, there was a gradual increase of the sintering atmosphere oxygen potential up to the desired level, obtained when all the hydrogen had been carried away by argon+ O_2. Equilibration between argon + O_2 and the UO_{2+x}, initially at a lower oxygen potential, takes place rapidly, as observed in Chapter 3. It is thought that equilibration occurs before significant sintering shrinkage develops, since the two processes are controlled respectively by oxygen and uranium diffusion.***

In this context, it would be more complex to maintain the desired atmosphere oxygen potential, during the heating-up transient, if only $CO + CO_2$ or $H_2 + H_2O$ mixtures were to be used. If this were the case, the ratios of the gas mixture components would have to be adjusted during the fast transient. It is doubful adequate equilibrium could be attained in a short time, for the system sample-gas mixture.

Most of the hot-stage microscopy data was obtained using a 8 mm movie camera**** operating at 1.5 frames per second. The microsphere diameters were measured over a back-projection screen. A special movie projector***** allowing automatic single frame projection, permitted convenient data collection.

The average fractional standard deviation in the measurement of the microsphere diameters was 0.39%. In the following section it will be seen that this value is satisfactory for the analysis of sintering kinetics data.

4.3.6 – Optical Dilatometry

The optical dilatometry system consisted basically of a high-temperature furnace, an oxygen sensor-thermocouple assembly and an optical system, as shown in Figure 47.

The optical system is detailed in Figure 48. Its main components are:

(i) a Leeds & Northrup optical pyrometer model 8643, comprising a microscope;

(ii) a Nikon filar eyepiece micrometer;

(iii) a photographic system consisting of a Nikon Microflex viewer model PFM, to which it was possible to attach photographic cameras (for movies or motorized 35 mm photography).

The furnace, shown in Figure 49, was a substantially modified Centorr unit model 15-2 x 3T-22 with a Honeywell controller-programmer able to reach up to 1950°C using an alumina muffle.****** The tungsten-mesh heater, around the muffle, operated in argon. The furnace was water-cooled. The maximum power could reach 10 kW. The main modifications of the original design consisted in the introduction of new water cooled flanges, allowing furnace operation with an open both-ends horizontal muffle. Two smaller flanges, close to the muffle extremities, permitted the assembly of a quartz double window and of a thermocouple-oxygen sensor system. The double window was cooled by nitrogen

---

* Due to the different heat-transfer characteristics of the two gases.

** 47A corresponding to 750°C in Ar + O_2, the lowest sintering temperature.

*** It is shown in Chapter 3 that oxygen diffuses in UO_{2+x} many orders of magnitude faster than uranium.

**** Leicina Special, from Leitz.

***** KODAK EKTAGRAPHIC MSF-8

****** The furnace could also operate with ThO_2 muffle, at temperatures higher than 1950°C.

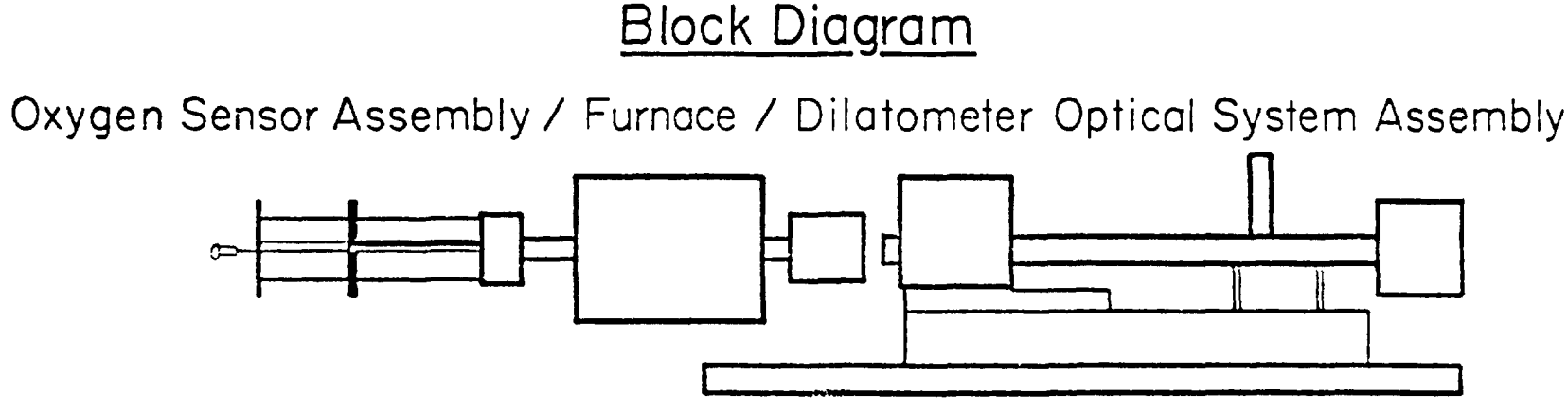

Figure 47 – Optical dilatometer block-diagram

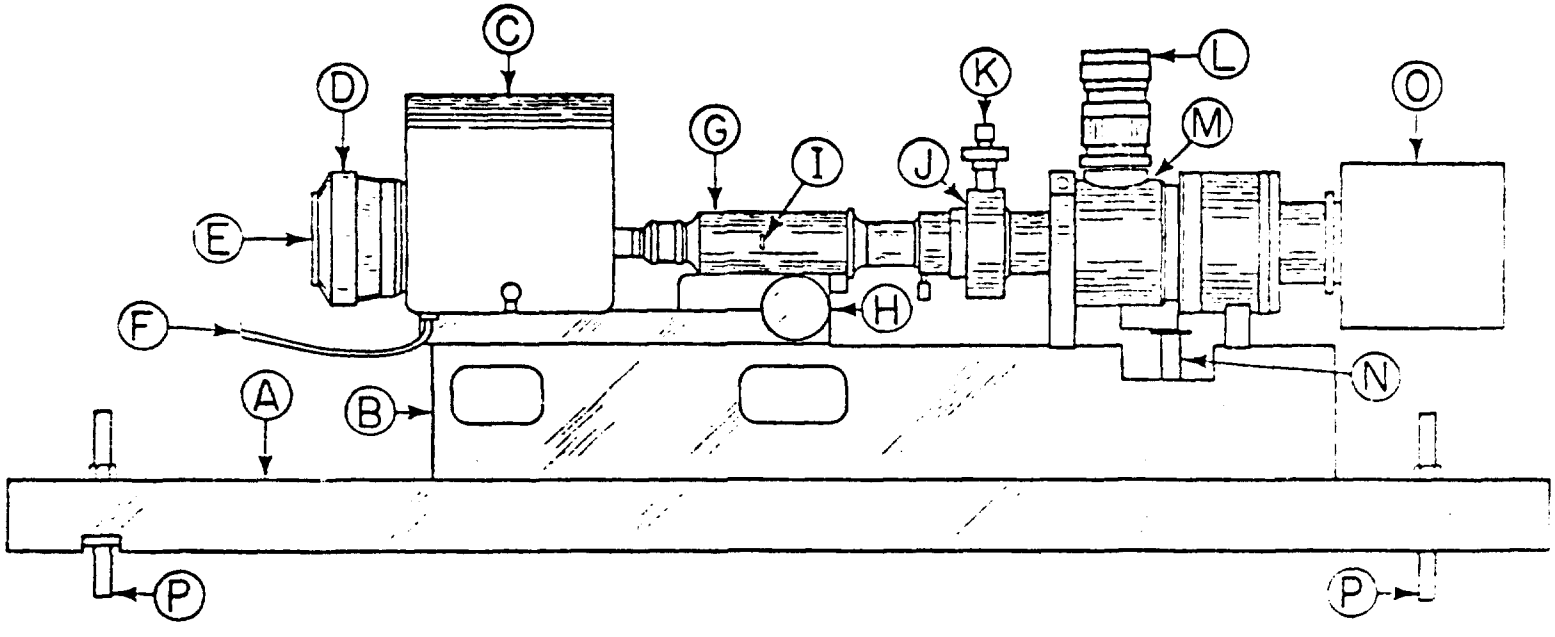

Figure 48 – Dilatometer optical system assembly. A – Channel support for optical dilatometer assembly; B – Alignment support; C – 8634 Leeds & Northrup Precision Optical Pyrometer; D – Objective lens; E – Focusing extension tube; F – To null balance measuring circuit; G – Microscope assembly; H – Microscope focus; I – Variable beta stop; J – Filar eyepiece micrometer; K – Filar micrometer knob; M – Nikon microflex model PFM; N – Height adjustment screw; O – Camera; P – Leveling screw.

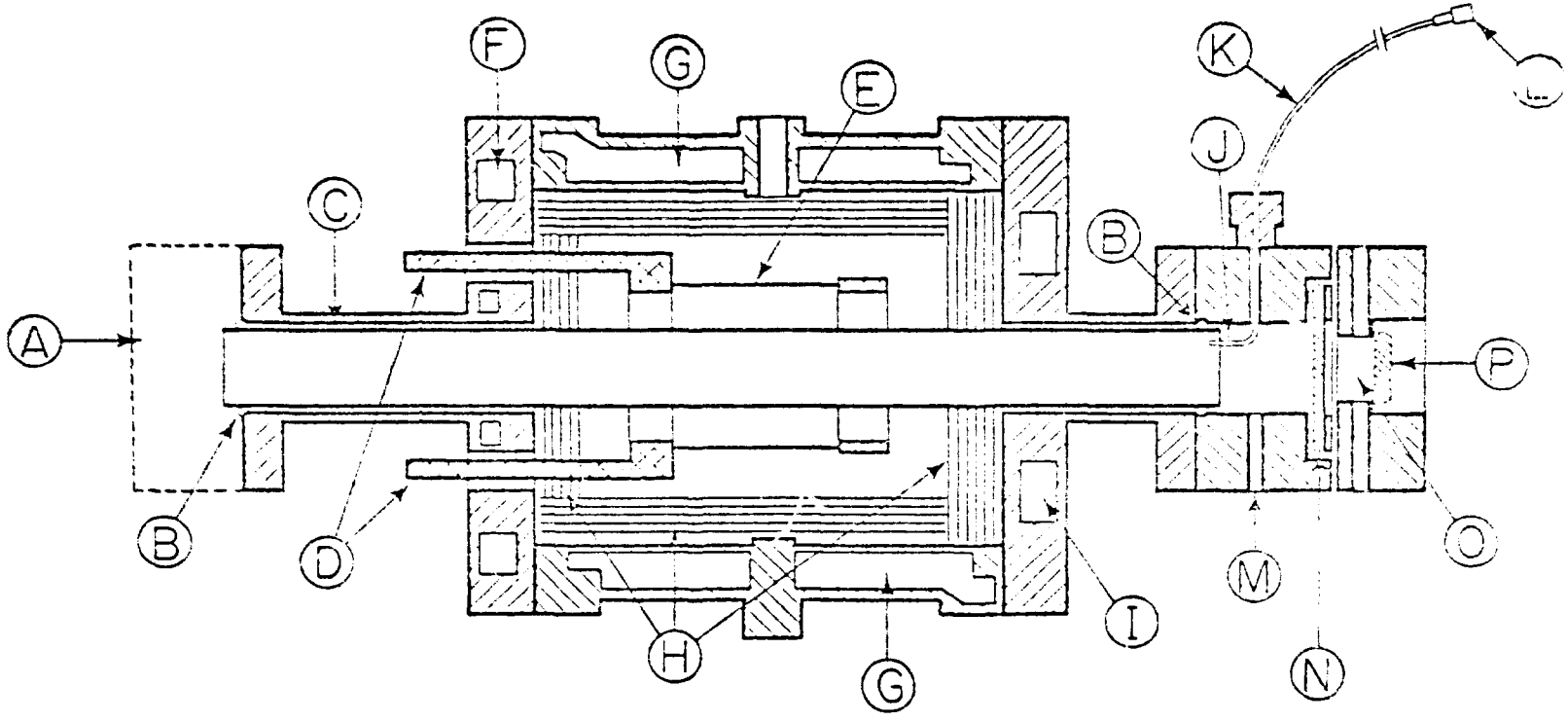

Figure 49 – Cross-section of dilatometer furnace. A – Attached to O/P/S Assembly; B – High Temperature O-ring; C – Muffle (Al_2O_3, ThO_2, ZrO – CaO or refractory metal); D – Electric Terminals for Heating Element; E – Tungsten Mesh Heating Element; F – Cooled Flange; G – Cooled Jacket; H – Thermal Shields; I – Cooled Flange; J – Glass Light Pipe; K – Plastic Fiber Optics Light Pipe; L – To Light Source; M – Furnace Atmosphere Gas Inlet; N – Primary Quartz Window; O – Protective Double–Window Observation Chamber; P – Secondary Quartz Window

insuring operator's protection in case the quartz component in contact with the sintering atmosphere ruptured. This precaution was specially important during operations in dry hydrogen, were rupture of the double window could orignate a serious explosion.

The sample was illuminated by light pipes, as indicated in Figure 49.

Figure 34 shows the thermocouple-sensor assembly, set for operation in slightly oxidizing atmospheres. The samples were placed in the crucible W, that could slide along the furnace, pulled by the rigid Pt-Rh wire V. In this way the samples could be moved from the cooler part of the furnace to the hot-zone, in less than one second. The internal electrode was the tip of a type B thermocouple. The external electrode was made of Pt-30% Rh and connected to point H by a wire of the same composition. The sensor emf was measured between point H and the extremity of the Pt-30% Rh thermocouple leg. A Keithley 610-C high-impedance electrometer was utilized for the emf measurements.

Figure 50 and 51 show the modified thermocouple-sensor assembly, for operation in hidrogen. This proved to be necessary due to possible damage to the Pt-Rh electrodes and thermocouple, if used in hydrogen. A W5%Re-W26%Re thermocouple, molybdenum crucible and connections of the same material were used in the zones in contact with hydrogen.

A general view of the optical dilatometer system is shown in Figure 52.

For optical dilatometry, pellets were prepared by compacting UO_2 powder, without binder, in a 1.25 cm diameter die at 800 kg. cm^{-2}, and subsequent isostatic pressing at 1750 kg. cm^{-2}. The resulting average green density was 5.589 ± 0.004 $g.cm^{-3}$ (51% of the theoretical value); the height was 1.3 cm and 1.2 cm the diameter.

In each sintering run, one pellet was positioned in the crucibles shown in Figures 34 and 50, with its longitudinal axis approximately parallel to that of the furnace. Adjustment of the optical system permitted alignment of pellet-dilatometer axes, allowing for adequate measurement of the pellet diameter Using 35 mm film it was possible to determine relative diameters of the pellets, with an average percent fractional standard deviation (% fr σ_ϕ) equal to 0.13%.

In Appendix 5 it is shown that

$$(\%\ \text{fr}\ \sigma_{S\%}) = \left(\frac{100}{S\%} - 1\right)(\%\ \text{fr}\ \sigma_\phi)\sqrt{2}$$

with % fr $\sigma_{S\%}$ = percent fractional standard deviation of shrinkage S%.

$$S\% = 100\left(1 - \frac{\phi_S}{\phi_G}\right) = \text{percent diametral shrinkage} \qquad (4.6)$$

Figure 53 shows the variation of (% fr $\sigma_{S\%}$) with S% and (% fr σ_ϕ). The line corresponding to (% fr σ_ϕ) = 0.13% characterize the precision of the optical dilatometer.* Even for the low shrinkage between 1 and 3%, corresponding to the initial sintering stage, the average (% fr $\sigma_{S\%}$) is about 13%, satisfactory for the study of sintering kinetics.

Microspheres were also sintered in the optical dilatometer, then operating as a regular furnace. They were loaded in two layers, in a small molybdenum crucible. Necks formed between adjacent microspheres, while sintering in H_2 + He mixture, at temperatures between 1850 and 1950°C.

* The line corresponding to (% fr σ_ϕ) = 0.39% characterize the precision of the hot-stage microscopy.

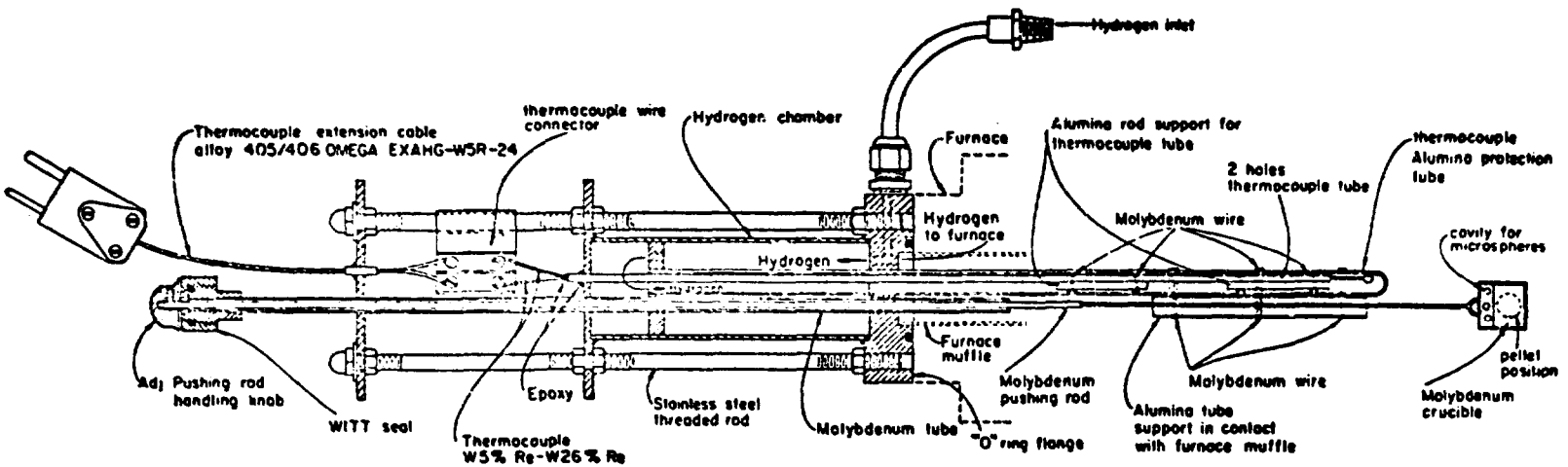

Figure 50 – Thermocouple and push-rod assembly for dilatometer operation in hydrogen

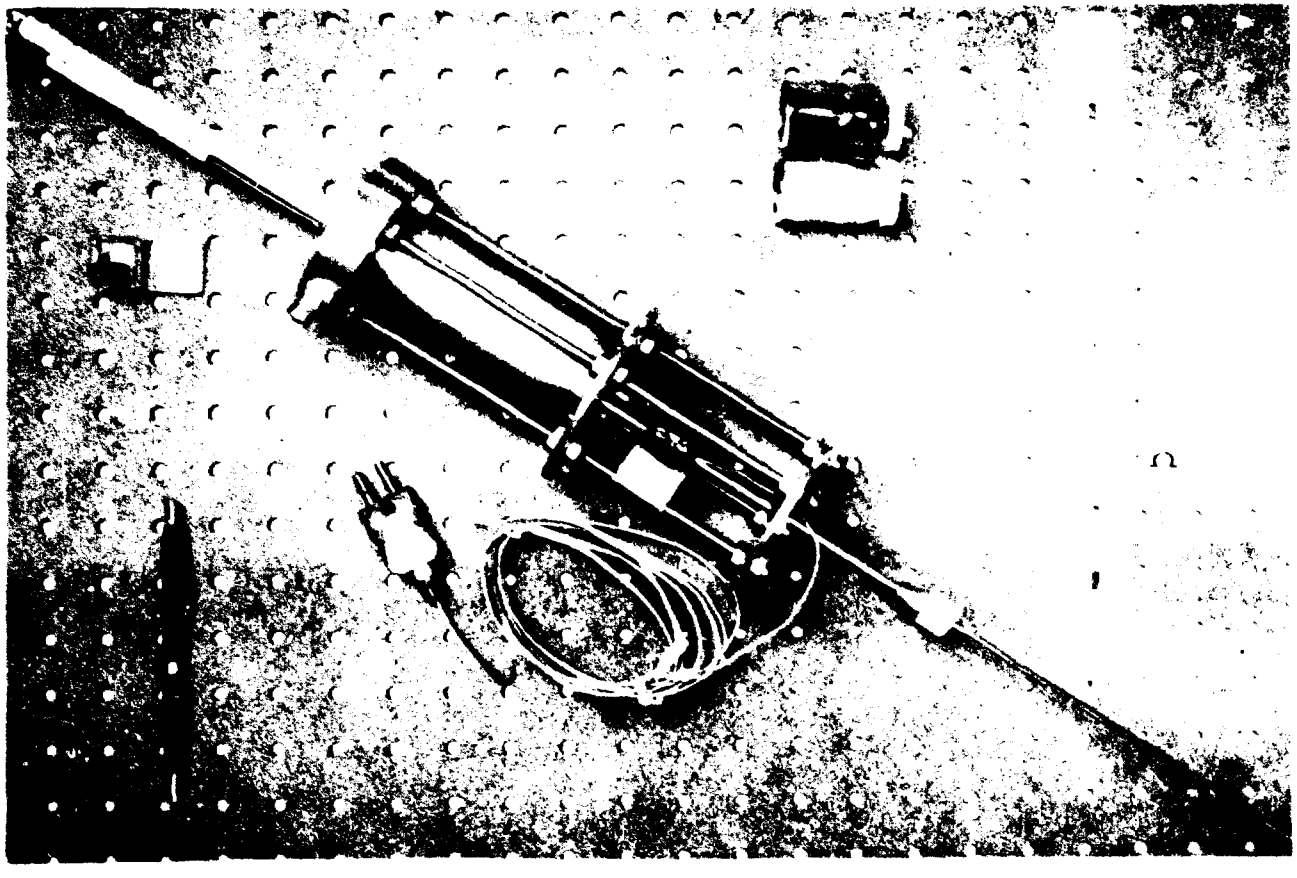

Figure 51 – View of the dilatometer thermocouple-mount and rod for crucible movement

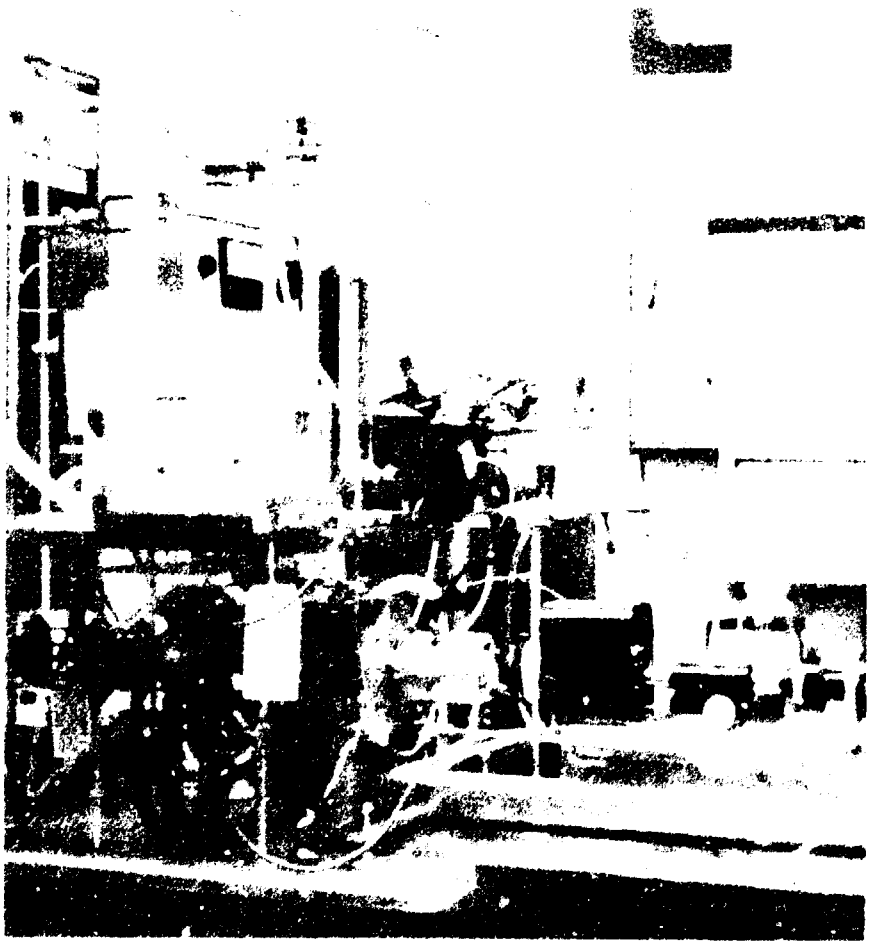

Figure 52 – Overall view of optical dilatometer

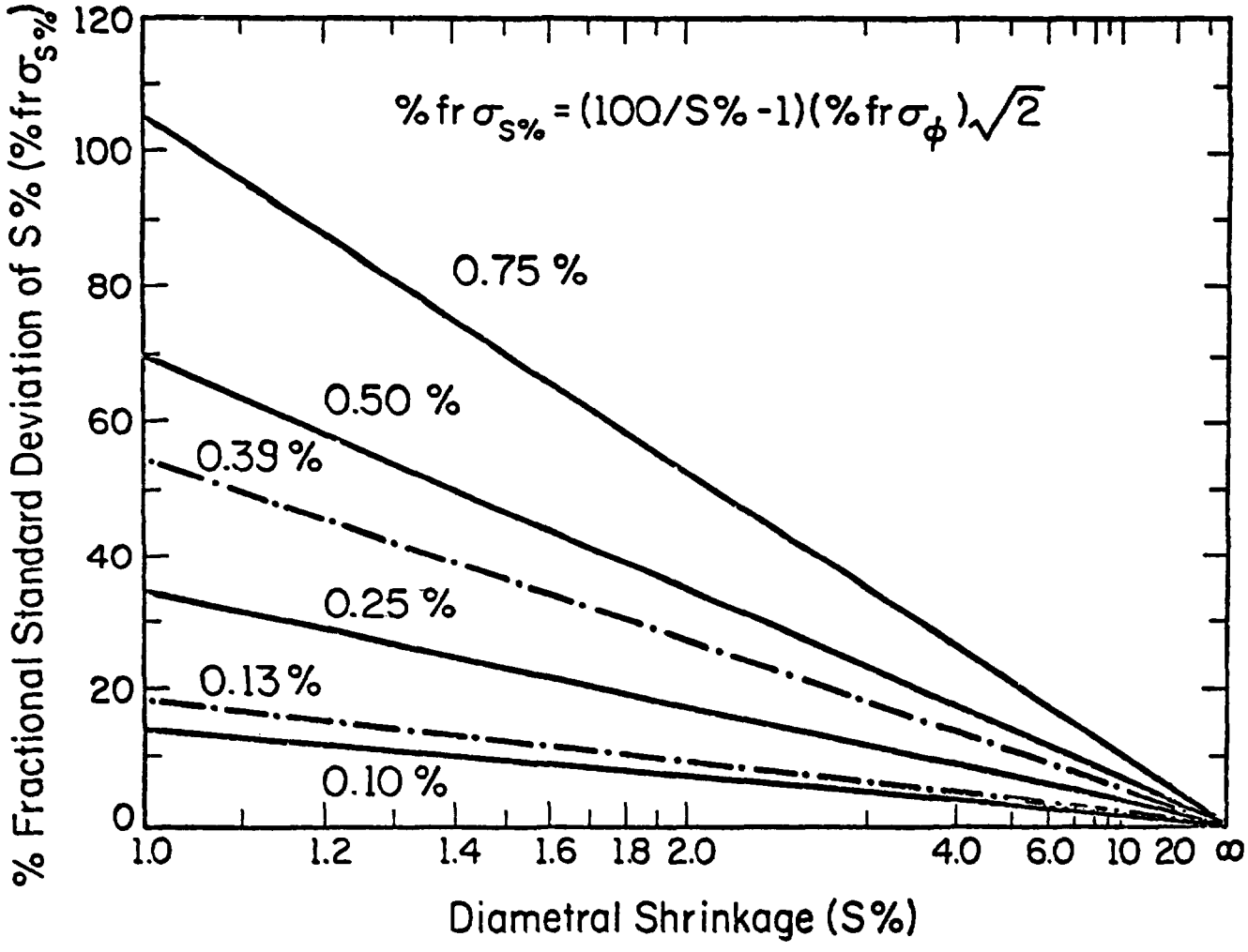

Figure 53 — Relation between errors in the measurements of diameter, (% fr σ_ϕ), and shrinkage, (% fr $\sigma_{S\%}$), where ϕ = diameter and S% = shrinkage, (% fr σ_ϕ) is equal to 0.39% and 0.13%, respectively for microspheres and pellets.

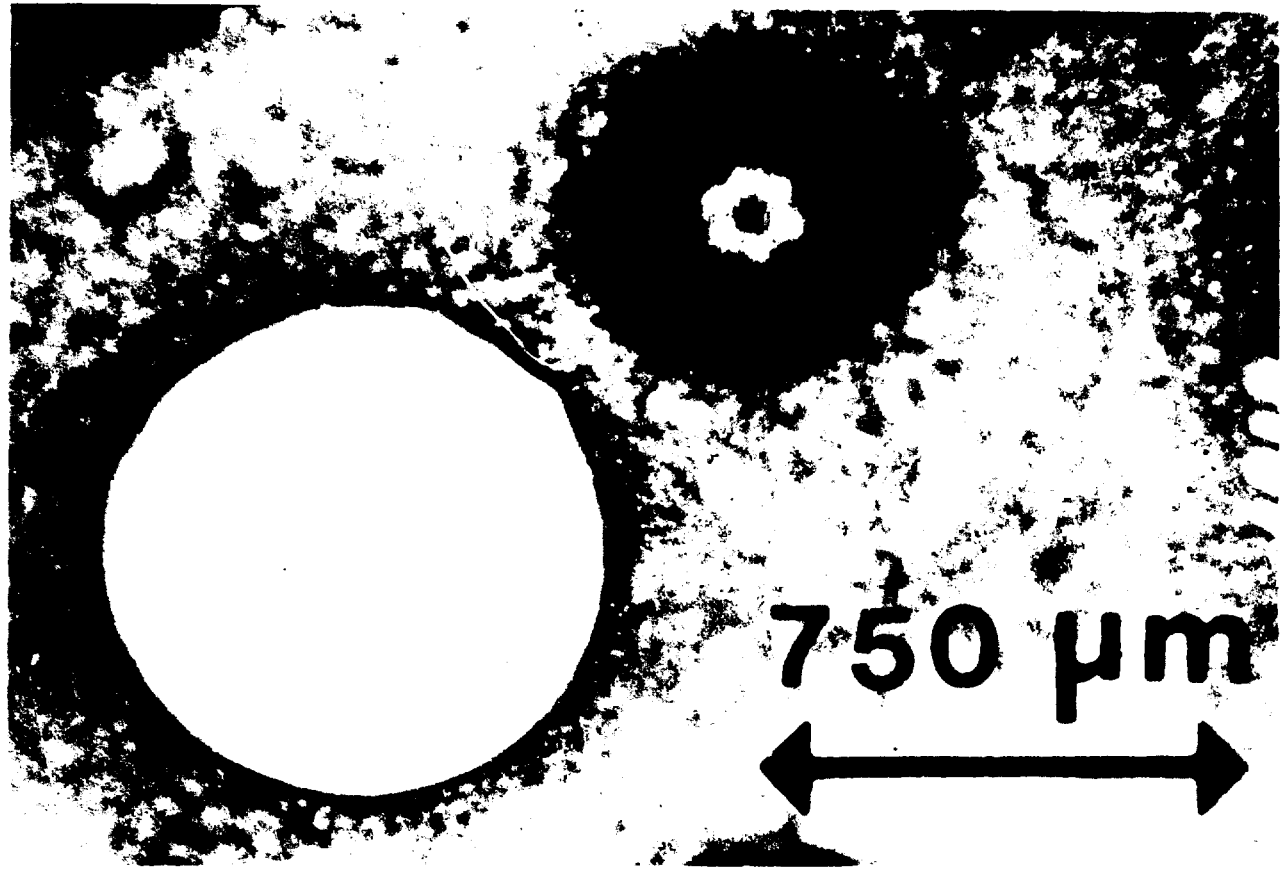

Figure 54 — Microspheres type M-1, as a gel (left) and after sintering

4.3.7 – Methods for the Evaluation of Microstructure, Paticle Size and Sample Geometric Characteristics

Standard optical and scanning electron microspy procedures were used for the study of the samples microstructure. Due to the very small grain-size ($< 0.3\,\mu m$) in the microstructure of the sintered microspheres, most of the investigation was developed using a JEOL U-3 scanning electron microscope.

Figure 54 is an optical micrograph, reflected light, showing a dried gel microsphere and a sintered UO_2 sample (material M-1). The microsphere diameters were determined by transmitted light microscopy.

Pellet diameters and heights were determined by means of a caliper, with a reading accuracy of $10\,\mu m$.

The particle size of gels M-1 were determined using a method similar to that described by Bannister[17], for the measurement of crystallite sizes on thoria gel. About 0.1 mg of gel was dispersed in 10 ml of dilute, warm nitric acid. A droplet of the resulting sol, placed on a carbon film over copper grid, was examined in a Hitachi HU-11 transmission electron microscope, at magnifications up to 55,000 X.

CHAPTER 5

RESULTS AND DISCUSSION

5.1 – Sintering in a Reducing Atmosphere

The measured kinetics of sintering in a reducing atmosphere are substantially different than those obtained in experiments carried out in $Ar + O_2$. The diametral shrinkage rates obtained for samples sintered under reducing conditions were those expected, considering the particle size of the starting material and the data presented in the literature*, which was discussed in Chapter 2.

5.1.1 – Microspheres

The data presented in Figures 55 to 85 were obtained using M-1 type gel microspheres. Figure 55 shows the diametral shrinkage evolution as a function of time, for the reactive sintering of a M-1 type gel microsphere in $Ar + H_2$ at 1000°C, with concomitant reduction to UO_2. Heating rates lower than 70°C/min were necessary to avoid microsphere rupture, which generally occurred in the 400 to 600°C temperature range. In the temperature range in which microsphere rupture occured, hot-stage microscopy was very effective for optimization of the reactive sintering process.

Figure 56 presents kinetic data for sintering of a UO_2 microsphere in dry hydrogen. The results can be described by a power curve $S\% = At^n$, with $n = 0.135$.

It was possible to grow necks between $500\,\mu m$ diameter microspheres, during sintering in H_2 + 10v/O He, in the 1850 to 1950°C temperature range. Details of the development of the neck regions are shown in Figures 57, 58 and 59, for microspheres sintered at 1850°C for 2 hours.

The apparent uranium volume diffusion coefficient can be calculated once the neck radius and the diameter of the connected microspheres are known[50]:

* Some of the most significant data are tabulated in Appendix 2.

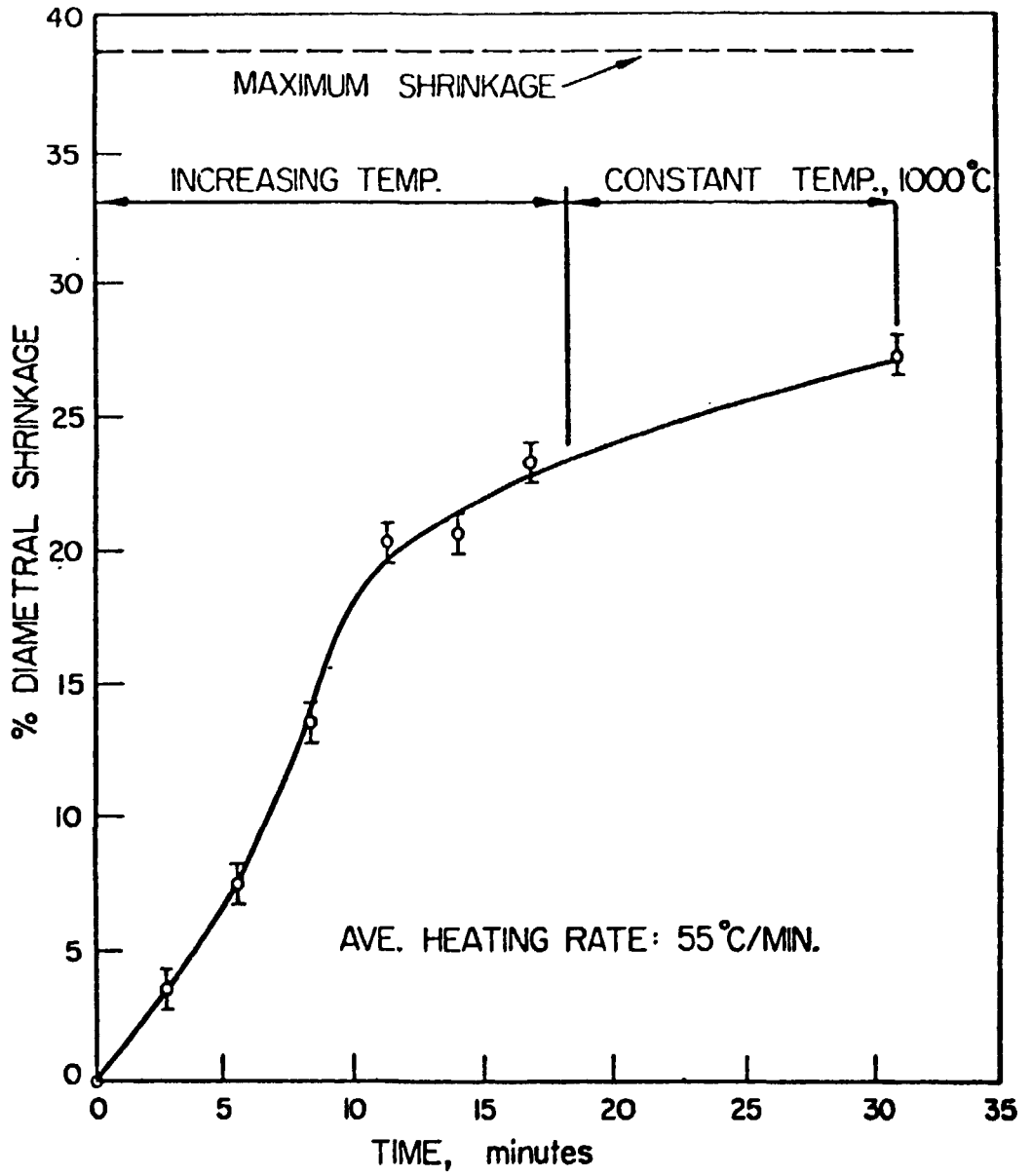

Figure 55 – Direct reactive sintering of gel M-1 to UO_2 in argon + 10 v/o H_2

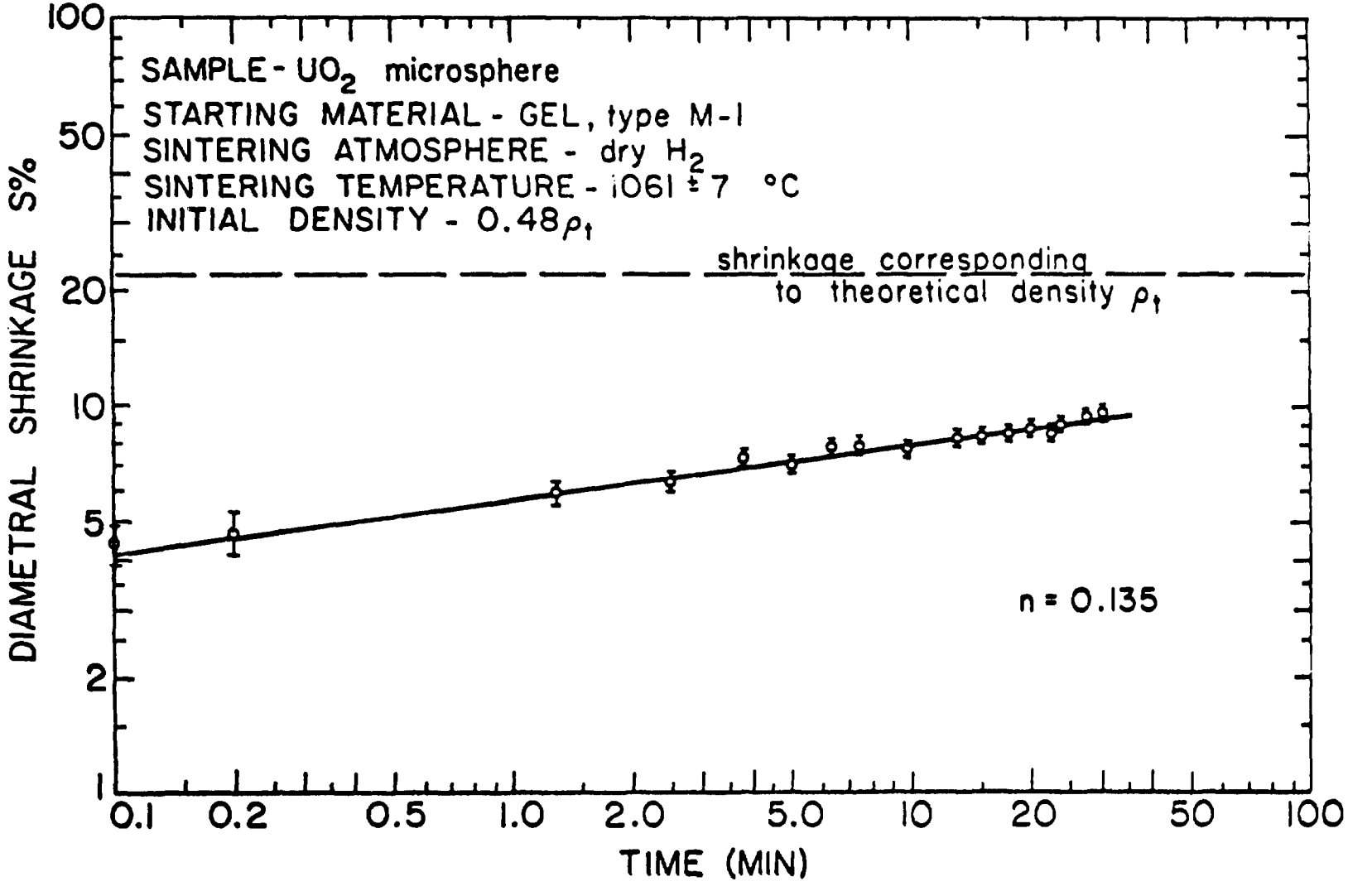

Figure 56 — Sintering of UO_2 microsphere in H_2

Figure 57 — Triple-neck formed during sintering of microspheres

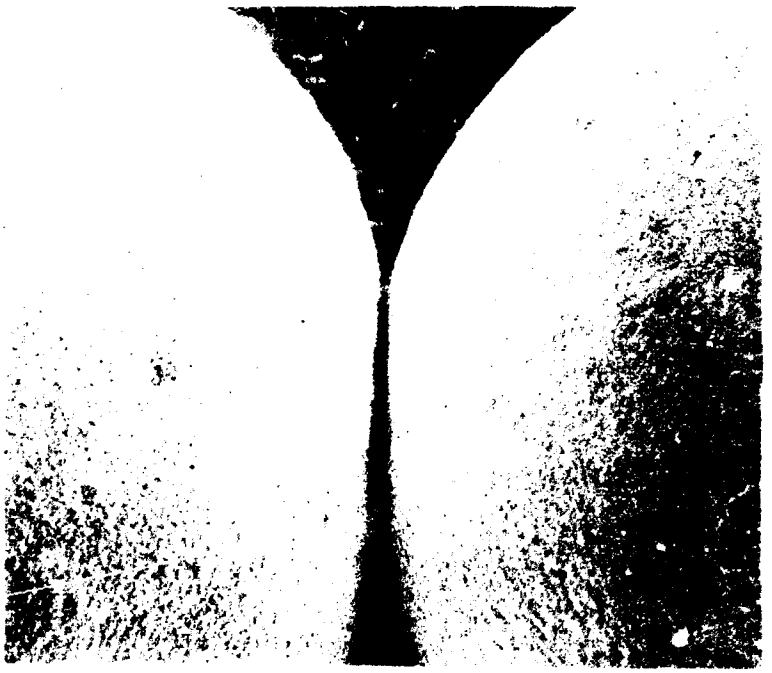

Figure 58 – Neck between microspheres sintered in H_2 + He

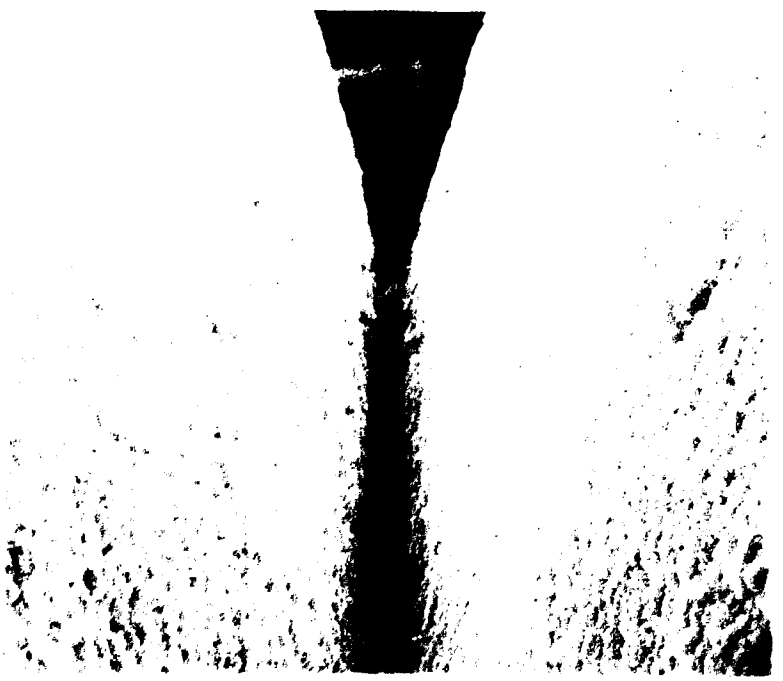

Figure 59 – The same neck shown in Figure 58, at high magnification. The average grain size is approximately 2 μm.

$$\frac{x}{a} = \left(\frac{40\gamma\Omega^3 Dv}{kT} \right)^{1/5} a^{-3/5} t^{1/5} \qquad (5.1)$$

with the symbols as defined in Table II.

Therefore:

$$D_v = \frac{kTx^5}{40\gamma\Omega^3 a^2 t} \qquad (5.2)$$

From Table III:

$\gamma = 1000\ \text{erg/cm}^2$

$\Omega = 4.1 \times 10^{-23}\ \text{cm}^3$

From direct measurements of scanning electron micrographs, it was found that for T = 2123°K and t = 7200 sec:

$x = 7.6 \times 10^{-3}$ cm

$a = 2.5 \times 10^{-2}$ c,

D_v was found to be $4.8 \times 10^{-7}\ \text{cm}^2/\text{sec}$.

5.1.2 – Pellets

The sintering kinetics results for pellets sintered in H_2 at 1300 and 1600°C are shown in Figures 60 and 61. The value of n in the power curve fit corresponding to the linear range A-B, in Figure 61, was found to be 0.20 ± 0.01, at 1300 and 1600°C.

5.2 – Sintering under Controlled Oxygen Potential

The sintering kinetics varied markedly with the sample-atmosphere equilibration procedure and the oxygen potential of the sintering atmosphere. Figure 62 indicates the results obtained when $p(O_2)$ was maintained constant during the entire run. Under these conditions, it was expected the initially stoichiometric UO_2 would oxidize at 600°C, with subsequent reduction to the desired O/U value. The densification rate and the final density corresponding to $p(O_2) = 8 \times 10^{-16}$ atm is much higher than at $p(O_2) = 4 \times 10^{-10}$ atm. The effect of oxygen potential was such that at a constant temperature, it was possible for sintering to develop either up to the final stage or to be maintained in the initial stage by varying $p(O_2)$ between 4×10^{-10} and 8×10^{-16} atm. For a heating rate of 10°C/min, most of the densification occurred during the heating transient, in approximately 7 minutes. A final density of 99% theoretical was reached in about 20 minutes at $p_{O_2} = 8 \times 10^{-16}$ atm.

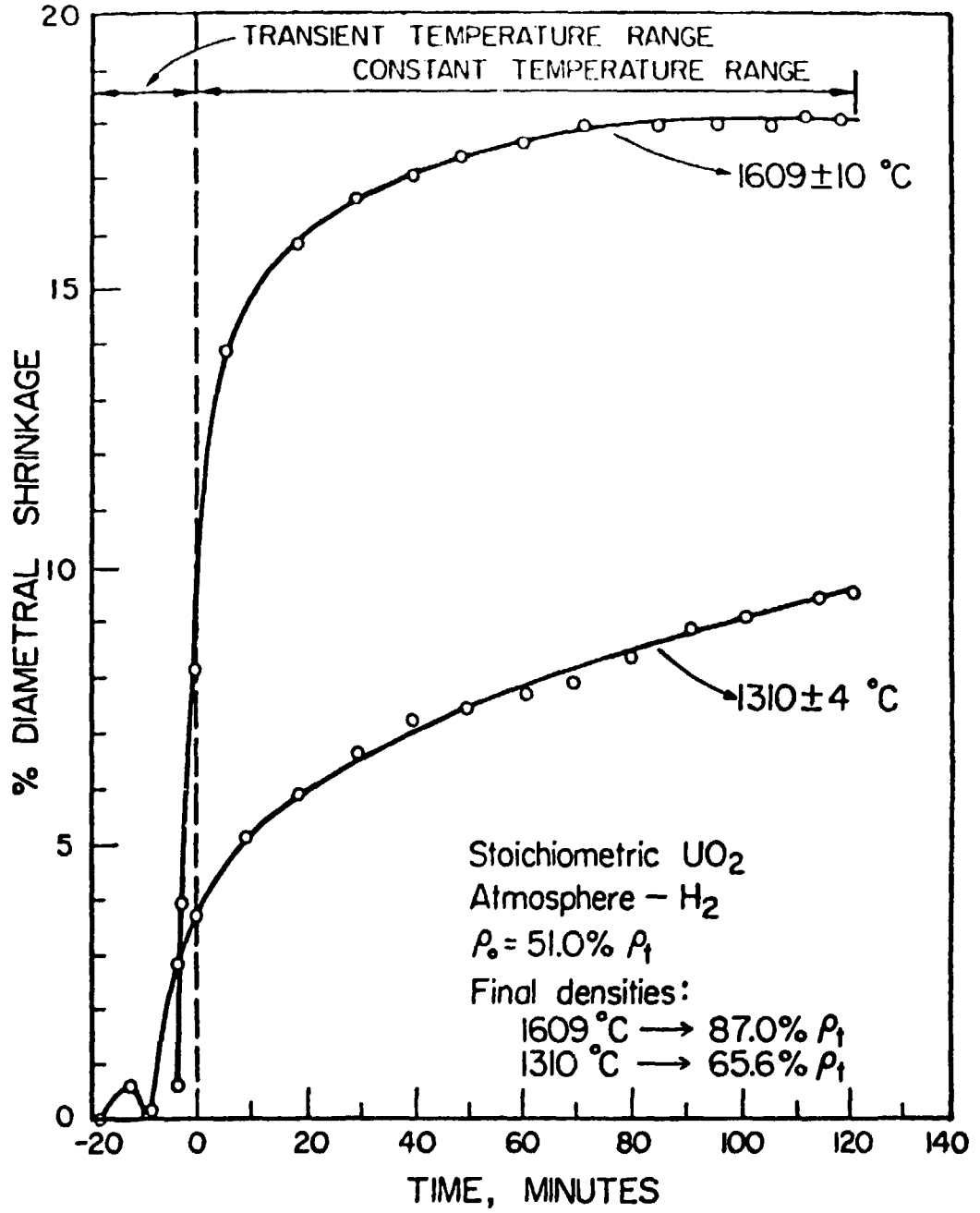

Figure 60 – Sintering of UO_2 pellets in hydrogen

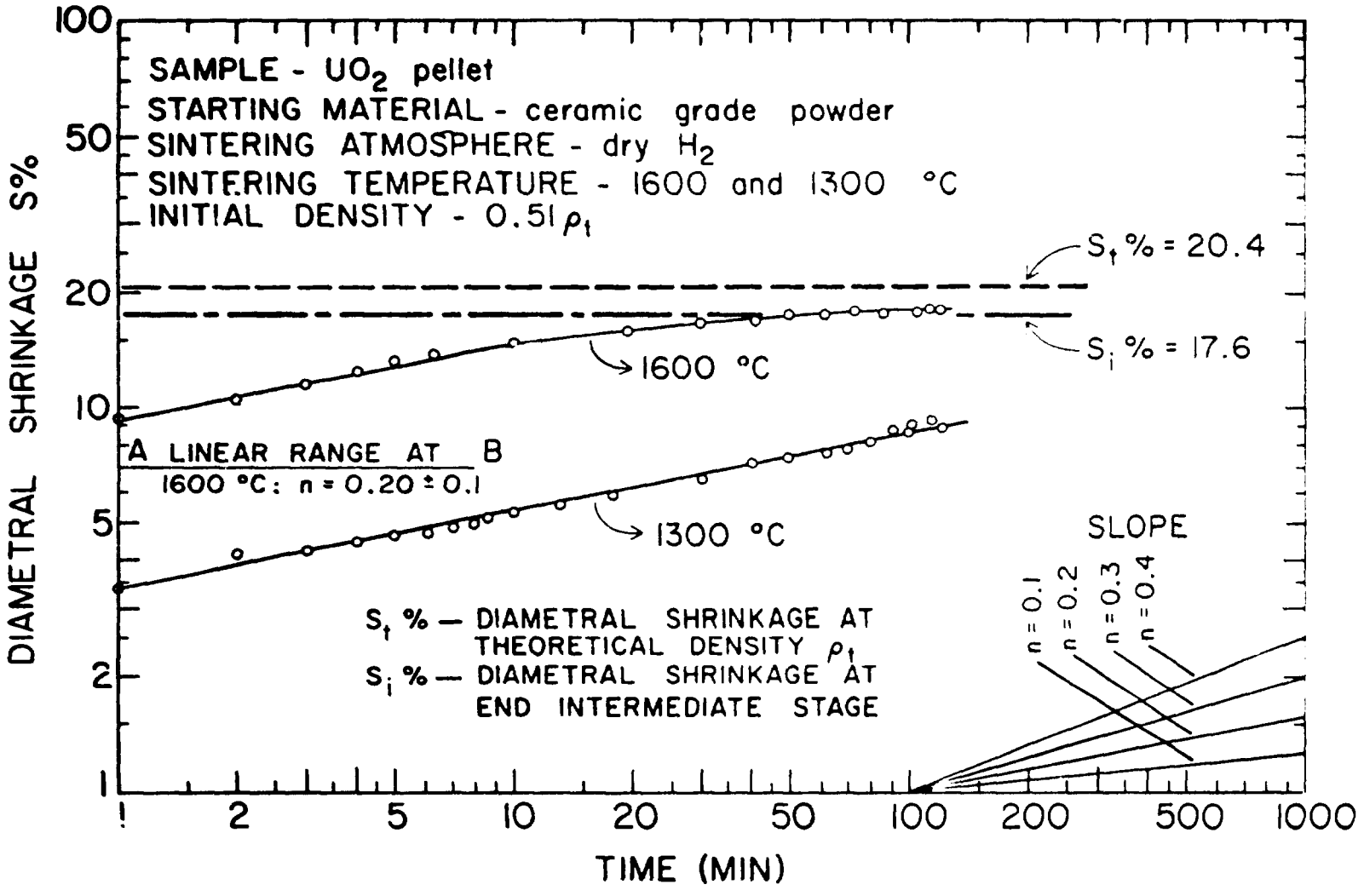

Figure 61 — Linear ranges in log S% = f(t) for hydrogen sintering. n = 0.20 ± 0.1 in the linear ranges, both at 1300 and 1600°C

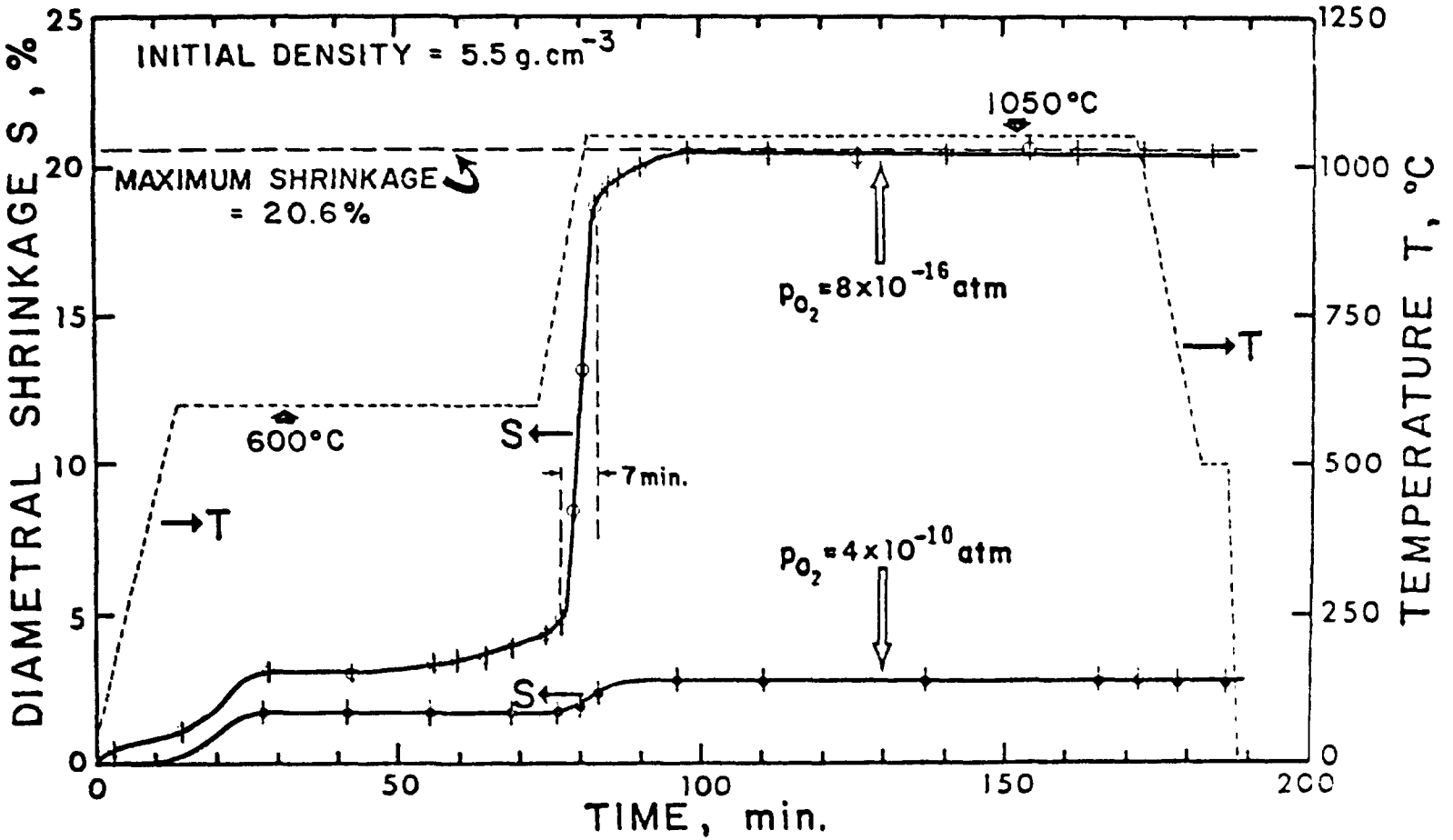

Figure 62 — Sintering of UO_2 microspheres in argon + O_2 for two values of p_{O_2}

Equilibrium using the sintering cycle described in section 4.3.5 (Figure 46) led to different kinetic behavior, the densification increasing for increasing values of $p(O_2)$. Most of the sintering runs in this investigation were carried out following this cycle. Figure 63 shows the results for sintering at 1150°C with $p(O_2) = 1.5 \times 10^{-8}$ atm. As shown in the figure, full densification was reached in 36 seconds.

For the equilibration cycle indicate in Figure 62, the kinetic data can fit a power curve very similar to that corresponding to hydrogen sintering. In both cases the average value of n in the expression $S\% = At^n$, is the same ($n = 0.13$). The final density is only slightly higher for argon + O_2 sintering, as shown by a comparison of the 1050°C results indicated in Figures 56 and 64.

The relation between equilibrium temperature and $p(O_2)$ for UO_{2+x}, indicated in Figure 65, was calculated using the data shown in Table V and thermodynamic data presented by Perron[117]. The line corresponding to hydrogen was determined using gas dried in a dry ice moisture trap at -78.5°C. From expressions given by Nelson[111] and Perron[117] we obtained the formula:

$$p(O_2) = \text{antilog}\left[2\log\left(\frac{H_2O}{H_2}\right) - \frac{25{,}749}{T} + 5.727\right] \qquad (5.3)$$

with $\log\left(\frac{H_2O}{H_2}\right) = -6.16$, for hydrogen at dry ice temperature.

Most of the values of x as a function of $p(O_2)$, in this work, are based on Figure 65.

Sintering kinetic data for Ar + O_2 sintering at different temperatures and equilibrium oxygen partial pressures are shown in Figure 66 and 67. The values of x in these and in the following figures were taken from Figure 65.

The influence of oxygen partial pressure on sintering, over a range of approximately 10 orders of magnitude and for $750 \leq T \leq 1150$°C, is shown in Figures 68, 69 and 70. The solid lines corresponding to Ar + O_2 sintering data were extended to the hydrogen sintering data points, conforming approximately with the theoretical predictions presented in chapter 3 and discussed in section 5.6.

5.3 – Microstructure

The crystallite size in sol-gel M-1 type gel microspheres was calculated from direct measurements of images in transmission electron microscopy photographic plates similar to that shown in Figure 71. The average crystallite size of the original microspheres was found to be (116 ± 18)Å.

The preparation of the specimen for transmission electron microscopy proved to be very sensitive to minor variations in procedure. The material had to be examined within a few hours after preparation, as described in section 4.3.7, otherwise relatively large crystals formed in the sol, as shown in Figure 72. The transmission electron microscopy results are similar to those obtined in other investigations, as indicated by micrographs shown in Figures 73 and 74.

The direct microscopic observation of a gel microsphere by scanning electron microscopy was difficult due to volatile evolution in the SEM high-vacuum. Figure 75 shows parts of the surface of a gel microsphere not ruptured due to this loss of volatile material.

The grain size of the microspheres sintered in hydrogen was under 0.3 μm as shown in Figures 76 and 77. This explains the failure in the use of optical ceramography methods, for microstructure evaluation. SEM fractography had to be used, at magnifications up to 20,000 X in order

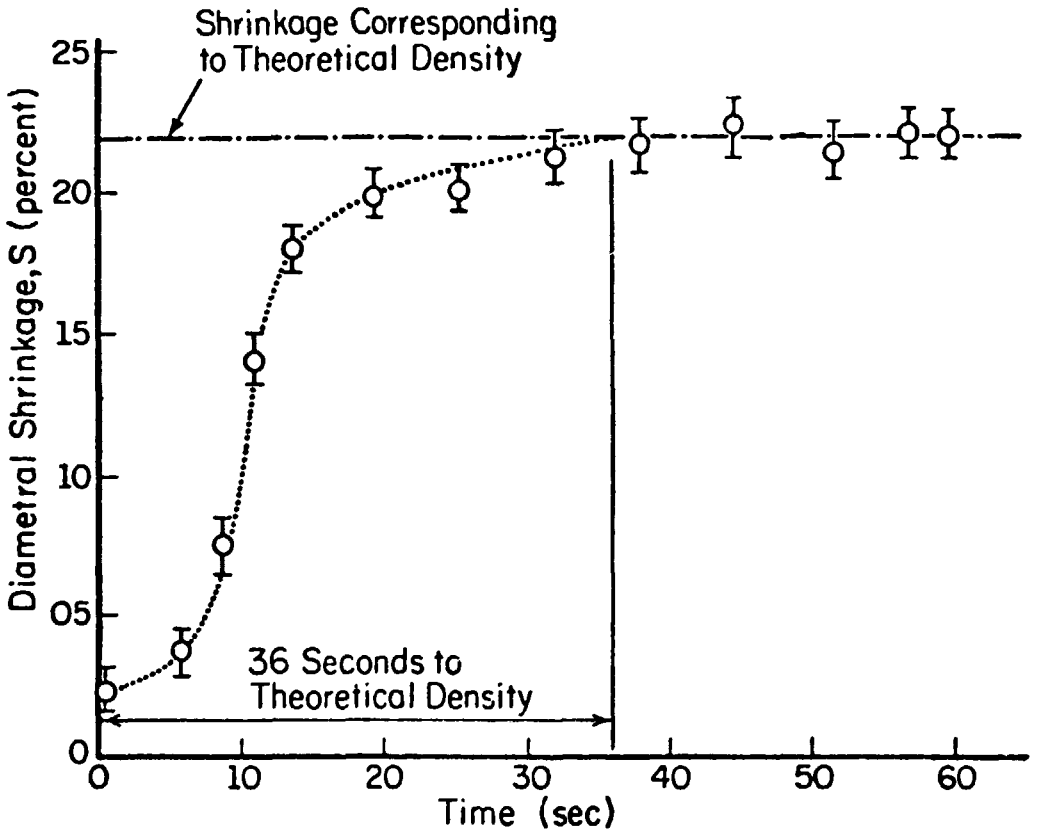

Figure 63 – Diametral shrinkage vs. time for UO_2 microsphere type M-1 sintered in Ar + O_2 at 1150°C for 60 minutes, with $p(O_2) = 10^{-16}$ atm.

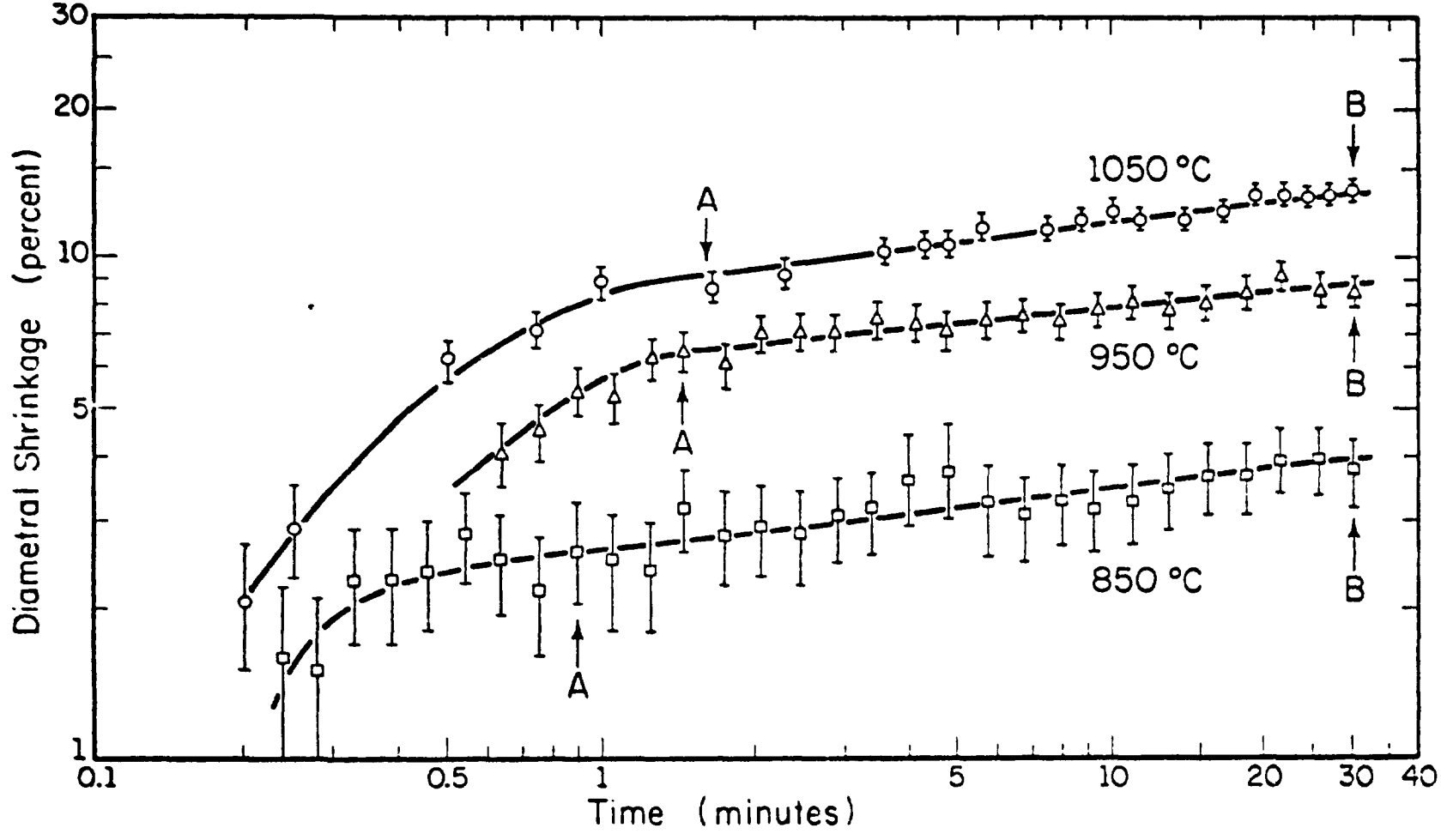

Figure 64 — Sintering of UO_2 microspheres type M-1 in argon + O_2, $p_{O_2} = 10^{-16}$ atm

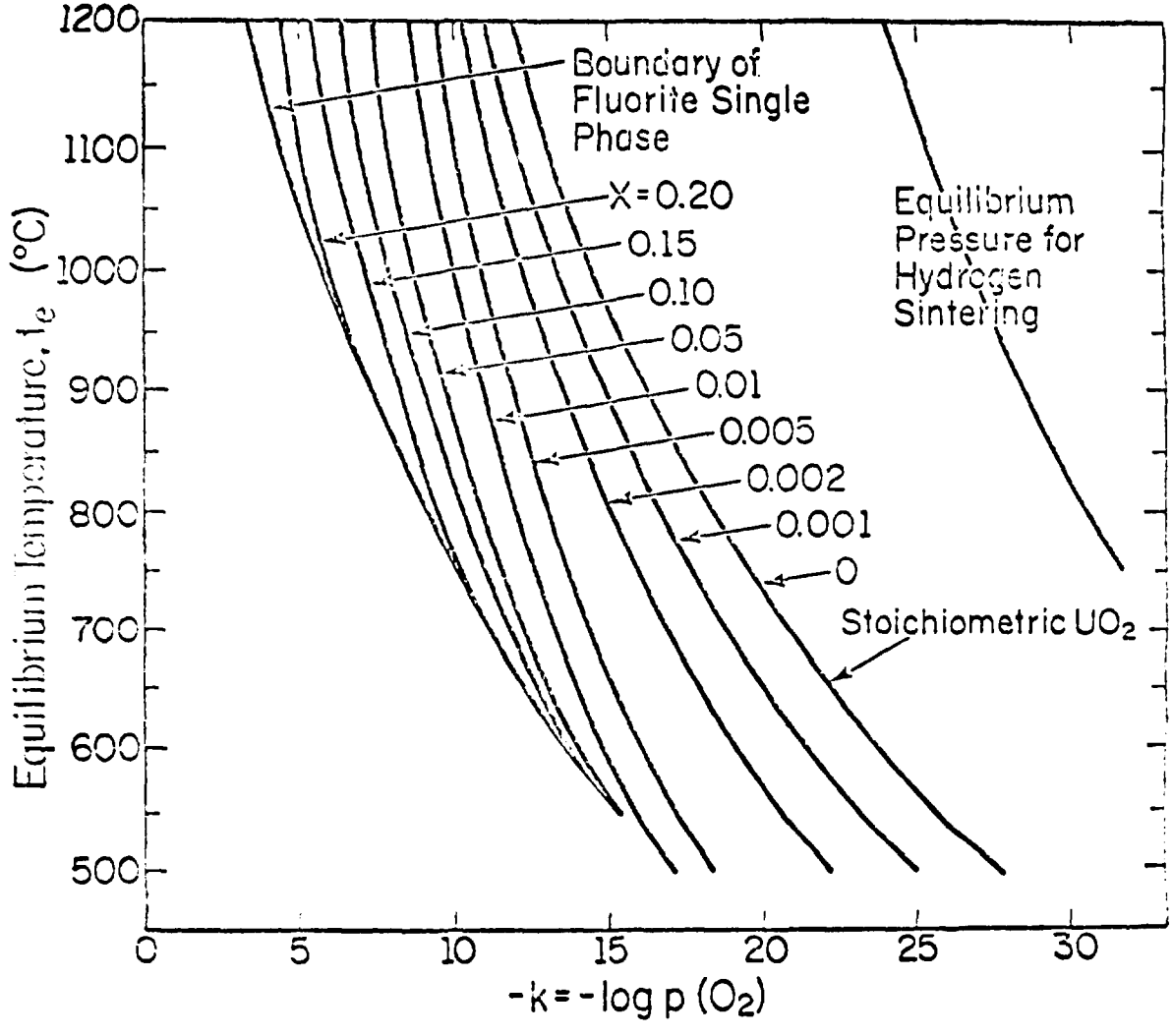

Figure 65 — Relation between equilibrium temperature and $p(O_2)$ for UO_{2+x}

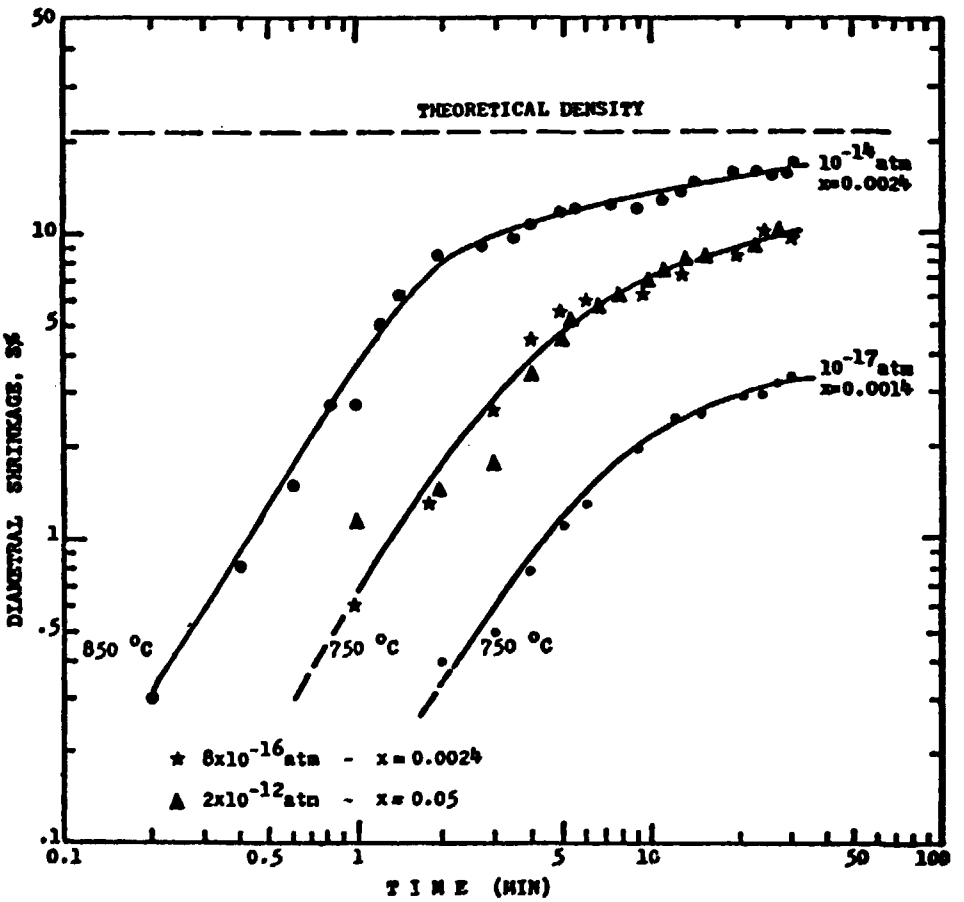

Figure 66 — Diametral shrinkage as a function of time for UO_{2+x} sintered in argon + O_2 at 750 and 850°C.

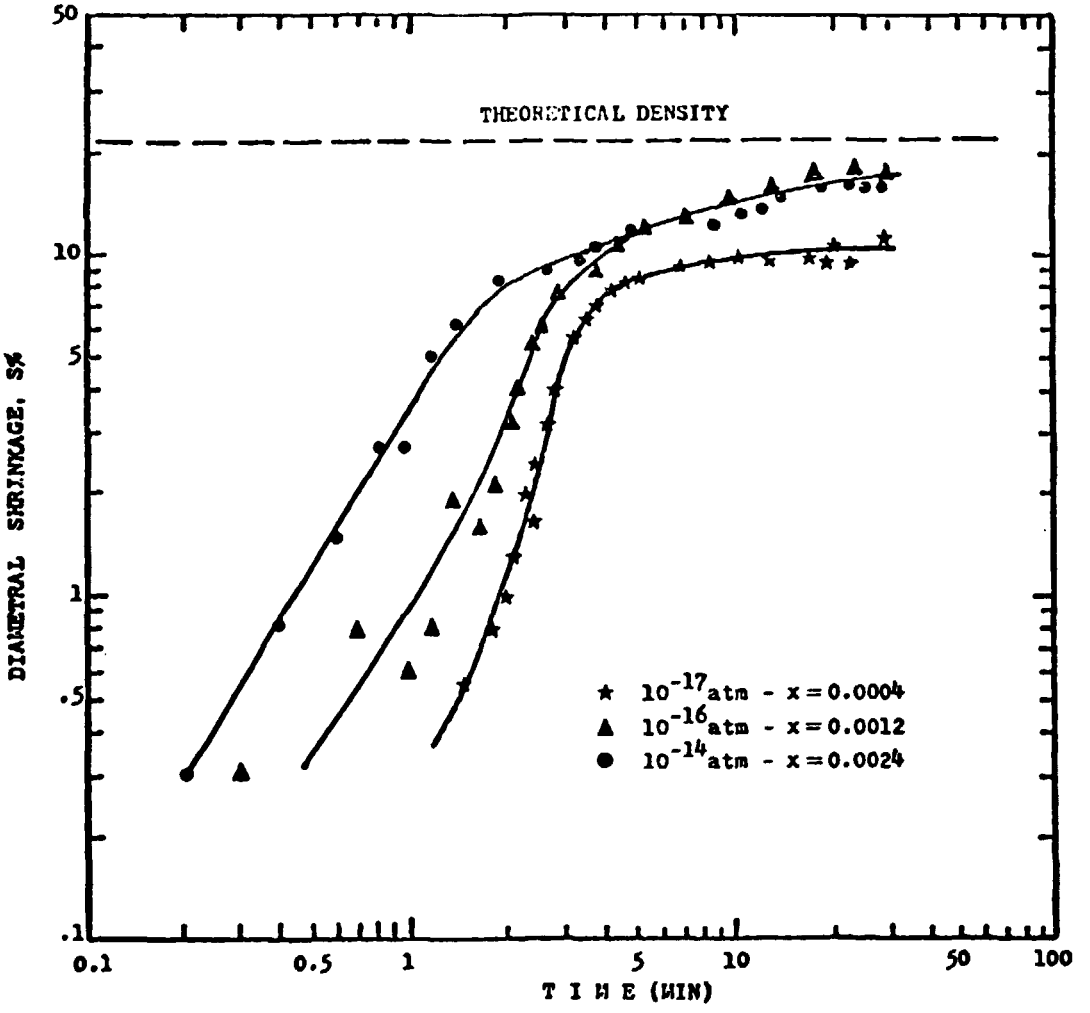

Figure 67 – Diametral shrinkage as a function of time for UO_{2+x} sintered in argon + O_2 at 850°C.

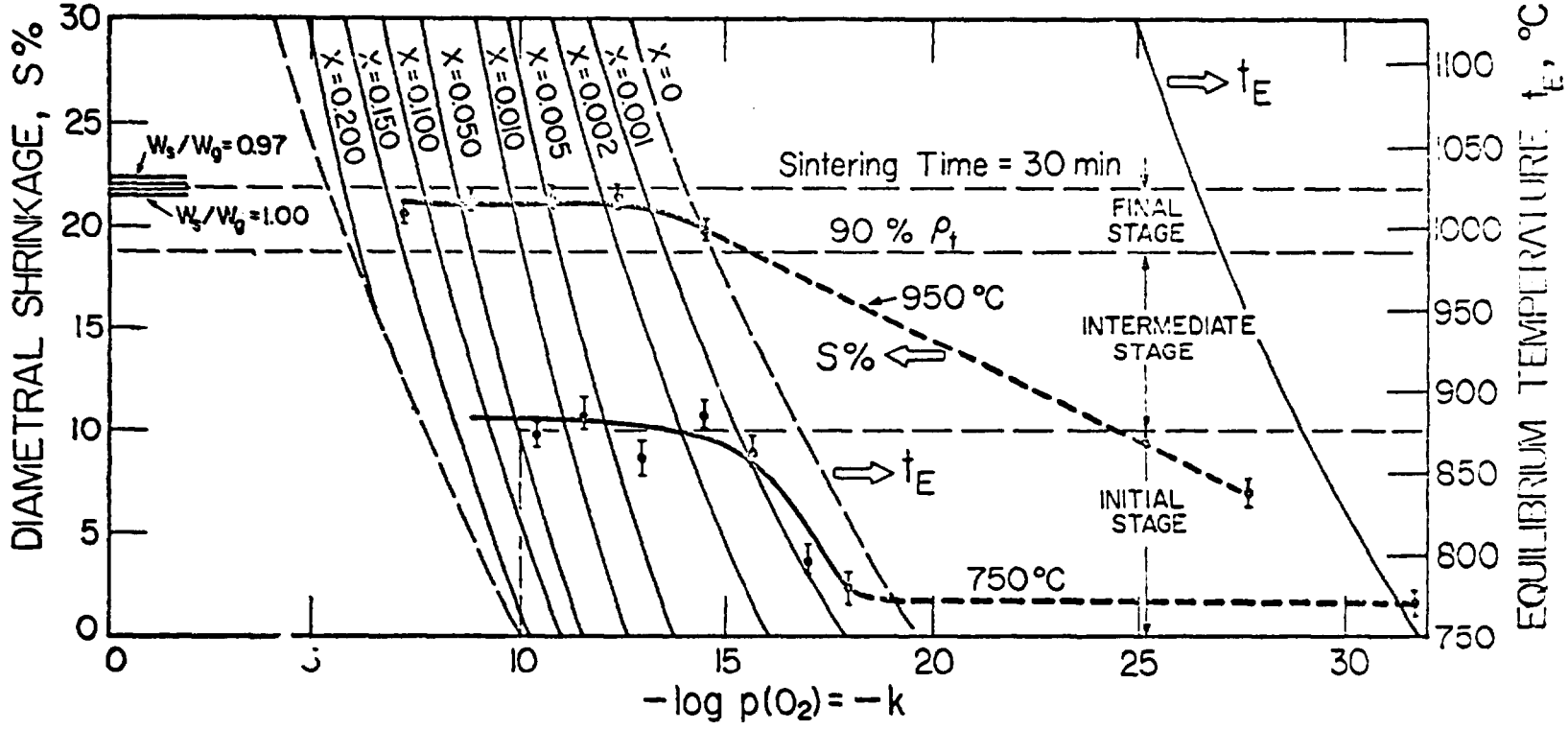

Figure 68 — Sintering of UO_{2+x} microspheres in argon + O_2 and in hydrogen for 30 minutes at 750 and 950°C

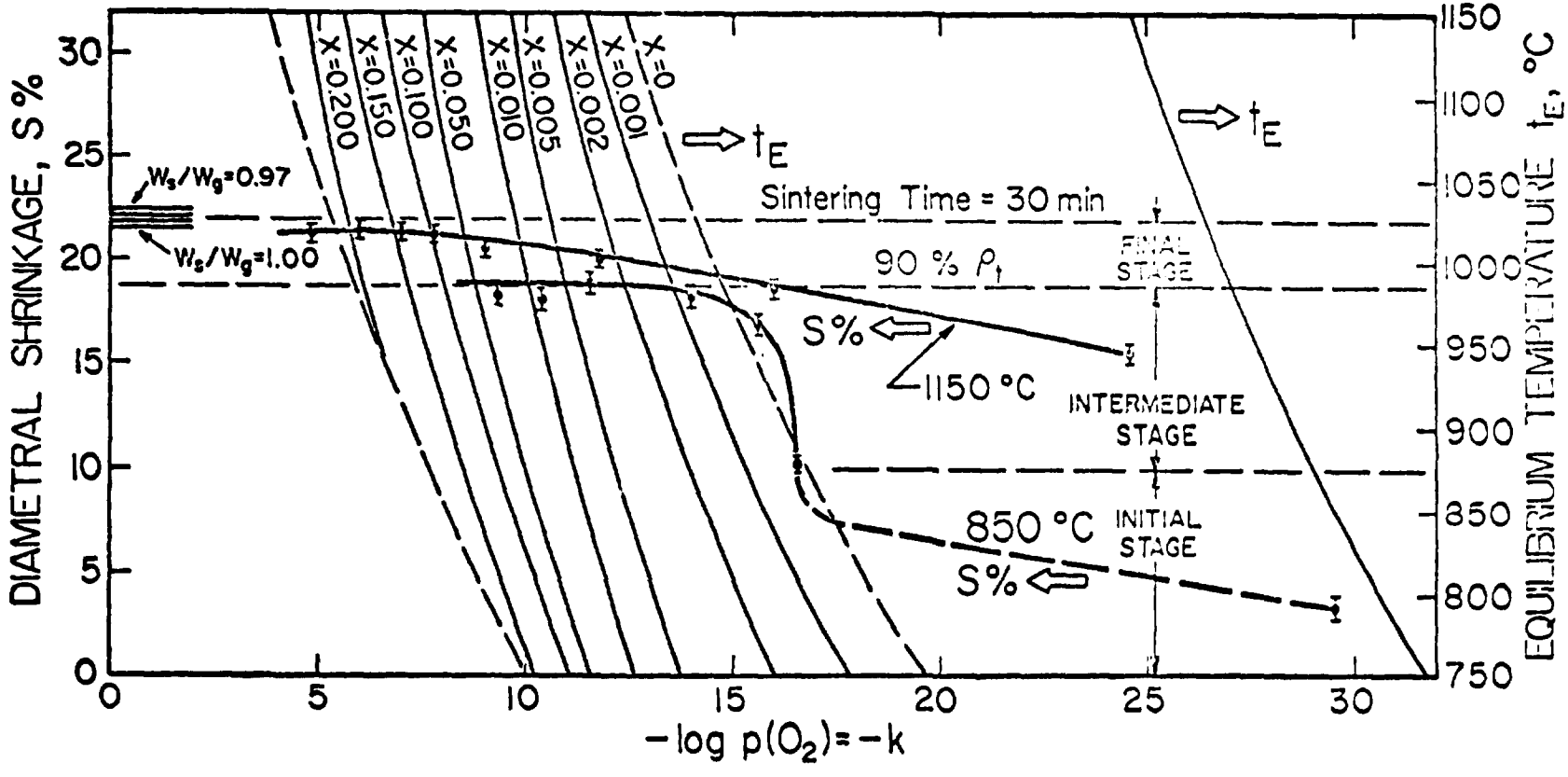

Figure 69 – Sintering of UO_{2+x} microspheres in argon + O_2 and in hydrogen for 30 minutes at 850 and 1150°C

Figure 70 – Influence of oxygen potential on sintering of UO_{2+x}

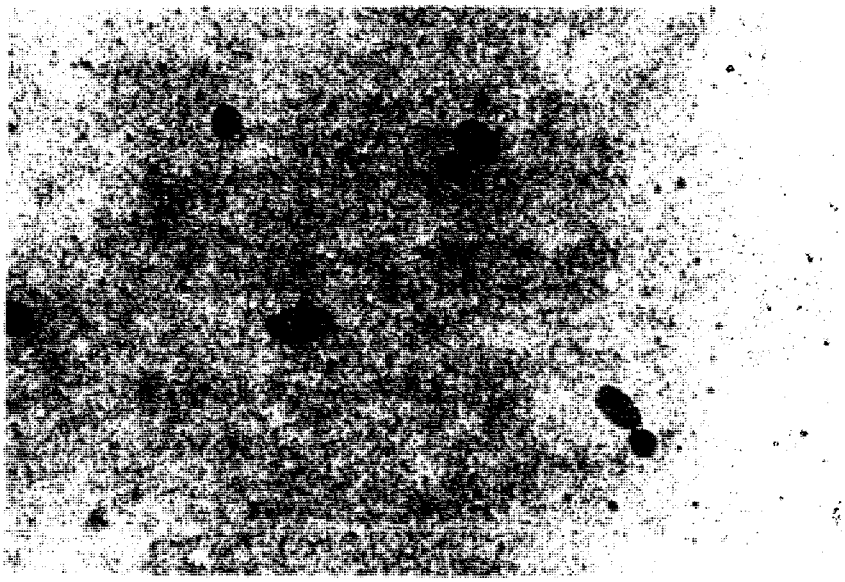

Figure 71 – Isolated crystallites and agglomerations in transmission electron microscopy specimen prepared with gel M-1.

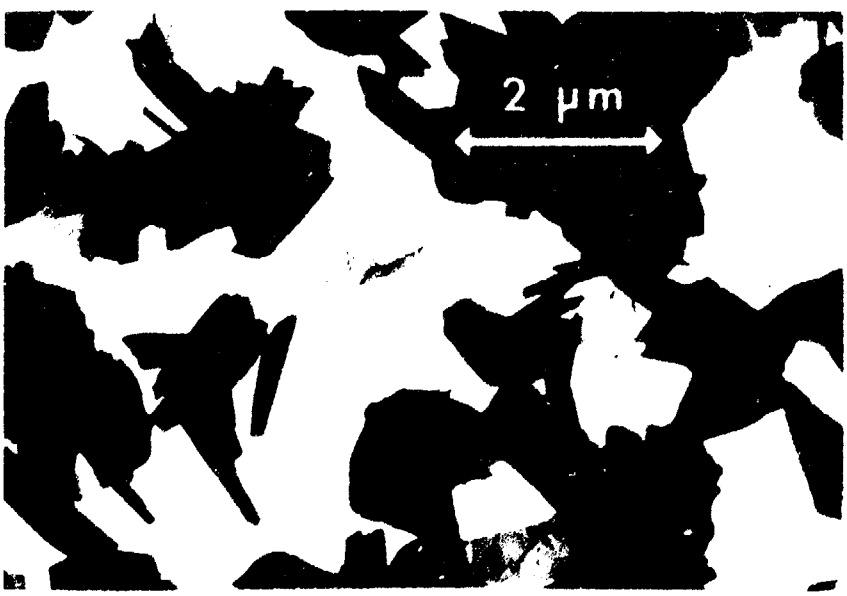

Figure 72 – Crystals formed after 96 hours in a solution of gel M-1 in diluted nitric acid

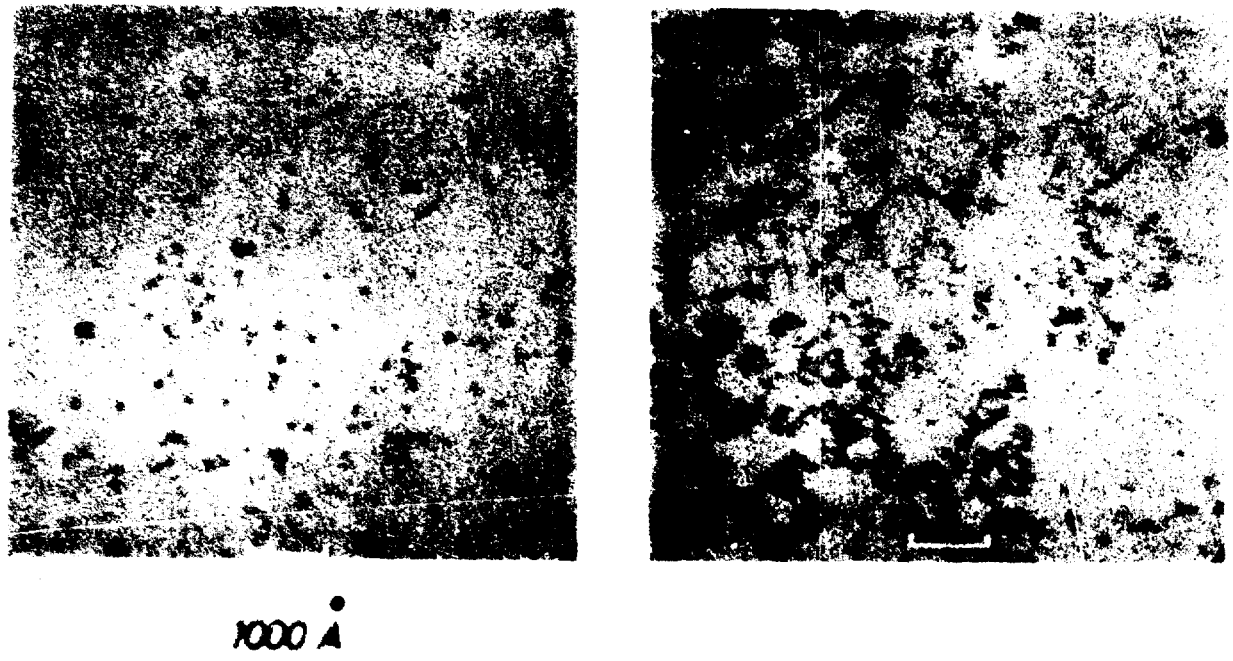

Figure 73 – Crystallites in gel (right) and sol (left) produced by the KFA sol-gel process (after ref. 112)

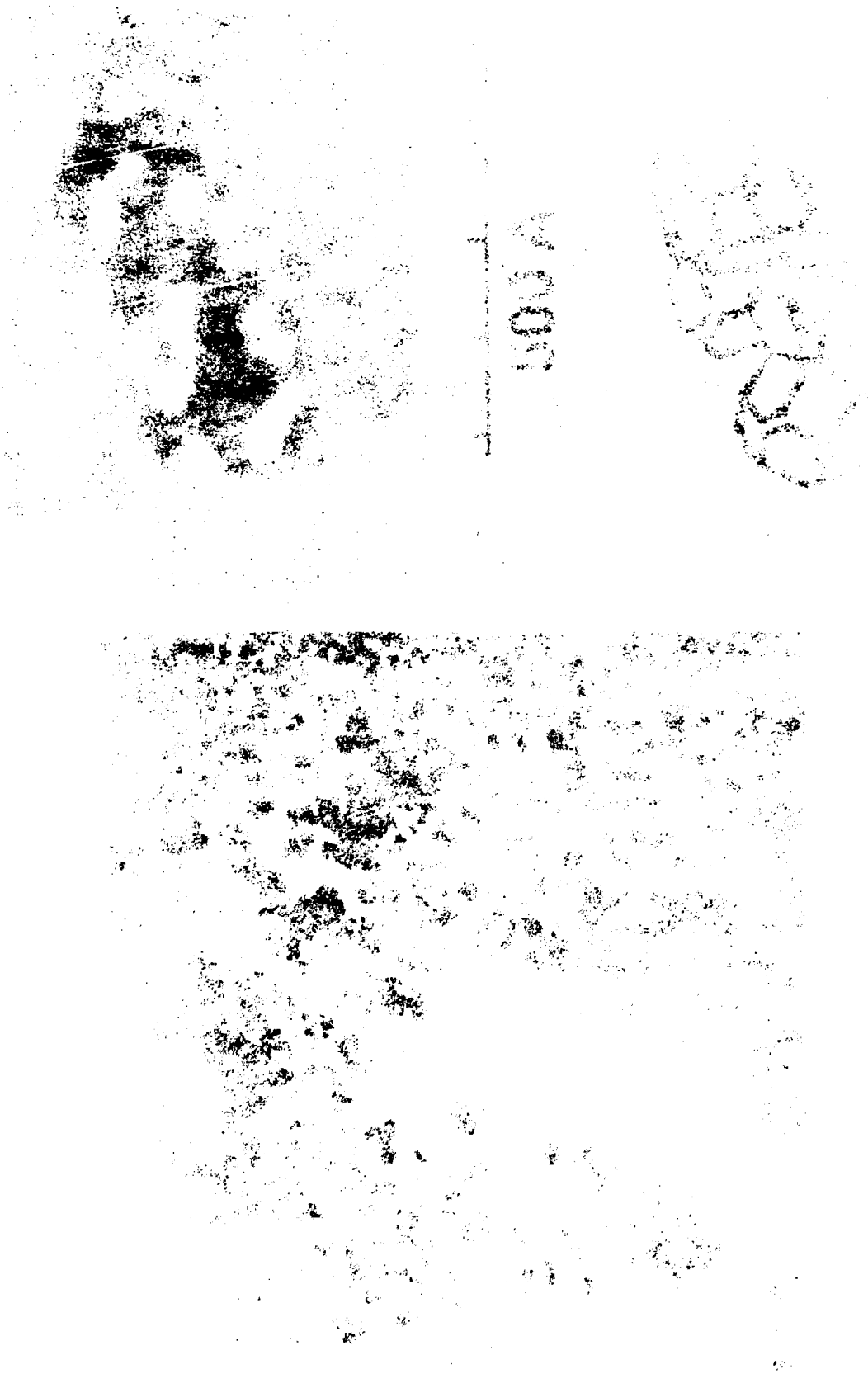

Figure 74 (A,B,C) -- Crystallites in thoria sol (after ref. 17)

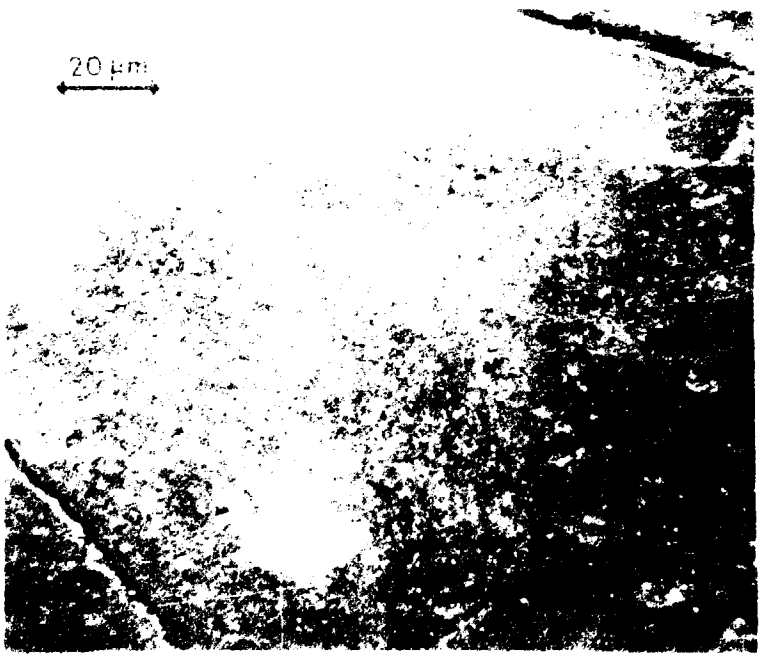

Figure 75 – Surface of gel microsphere type M-1

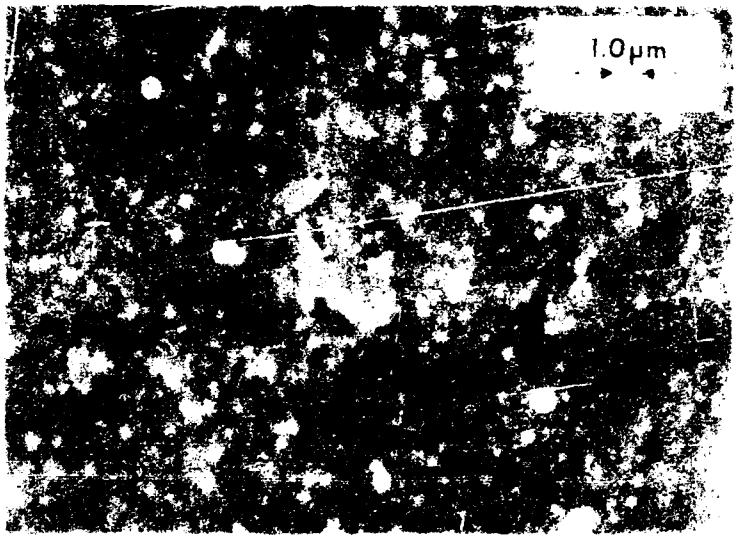

Figure 76 – Surface of UO_2 microsphere sintered in H_2. A grain of average size is indicated by arrow

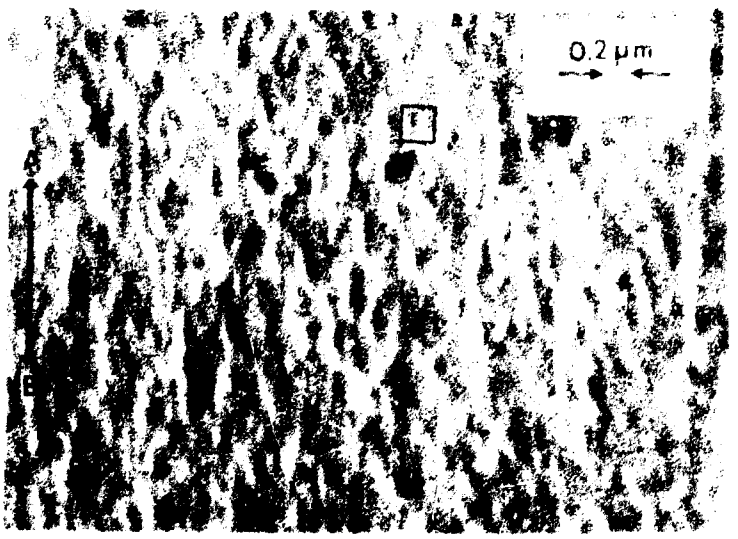

Figure 77 – Fractograph of UO_2 microsphere sintered in H_2. A grain representative of the microstructure is marked by arrow. Grain sizes were measured in direction A-B.

to obtain statistically meaningful results. The grain size after gel reduction to UO_2 at 600°C was found to be 760Å. After sintering at 1150°C the grains had increased in size to 2100Å.

The microstructure shown in Figure 78, corresponding to UO_2 microspheres sintered in H_2 + 10v/o He for two hours at 1850°C, indicate appreciable secondary recrystallization. The average grain size is approximately 4 μm, determined by the grain boundary intercept method.

Columnar grain growth is shown in the neck regions depicted in Figure 79, forming grains with dimensions significantly larger than 5 μm.

5.4 – Sintering Diagram for Microspheres

A sintering diagram that shows regions of dominant mechanisms was constructed for UO_2 microspheres sintered in hydrogen. It was presented in Figure 3, in chapter 2, with a discussion of the necessary material constants and assumptions. The initial particle size was that as determined in section 5.3.

5.5 – Activation Energies

The activation energies for sintering were derived from the data presented in Figures 61, 80 and 81 and the values of n presented in the preceding sections.

For hydrogen sintering the activation energy was found to be 101 ± 2 kcal/mole for both microspheres and pellets. However, for microspheres sintered in argon + O_2, the activation energies were smaller, varying between 61 and 96 kcal/mole.

5.6 – Defect Concentrations, Diffusion Coefficients and Sintering Kinetics

From the theoretical considerations presented in Chapter 3, a significant effect of defect concentration was expected on the uranium lattice and grain-boundary diffusion coefficients, and consequently on sintering kinetics. Figure 82 shows the variation of the uranium lattice diffusion coefficient with stoichiometry deviation, obtained by extrapolation of Marin and Contamin[97] data to values of x under 0.03, with the assumptions that activation enthalpy does not vary with x. The frequency factor was considered proportional to x^2, in agreement with Lidiard's model for the description of nonstoichiometry in UO_2.

Considering Figure 82, a very substantial effect of stoichiometry on shrinkage was expected for values of x under 0.005. This expectation was confirmed by the results shown in the insert of Figure 83, particularly for the sintering experiments carried out at 750°C for 30 minutes. This same figure indicates the variation of uranium vacancy concentration (N_{vu}) with stoichiometry deviation, derived from the Matzke model for the quantitative relationships in the structure of UO_{2+x}. The slope of the lines does not vary appreciably with stoichiometry deviations for temperatures under 1050°C and corresponds to a relationship of the form $(N_{vu}) = kx^2$, with k = constant. The graph in the insert suggests that for temperatures ≤ 850°C the diametral shrinkage has the form $S\% = \bar{k}\, x^n$, with $n \simeq 2$, for $x < 0.002$ and $\bar{k}$ = constant. Therefore, for low sintering temperatures and $x < 0.002$ there is a clear relationship between the concentration of uranium vacancies and sintering kinetics. This conclusion received additional confirmation from the data shown in Figure 84 insert. In this figure the concentration of uranium defects (N_u) as a function of stoichiometry deviation, was also determined using Matzke's model, (N_{iu}) and (N_v) being respectively the concentrations of uranium interstitials and uranium vacancies.

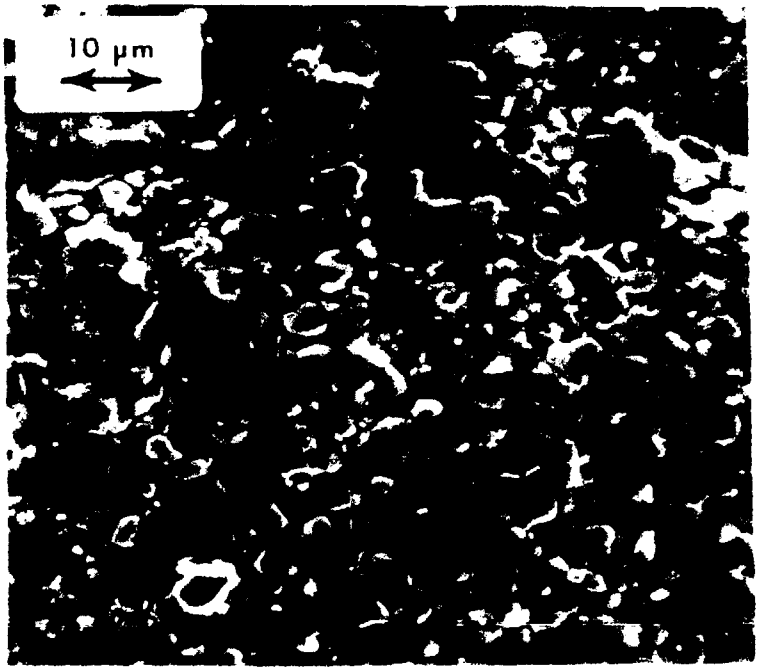

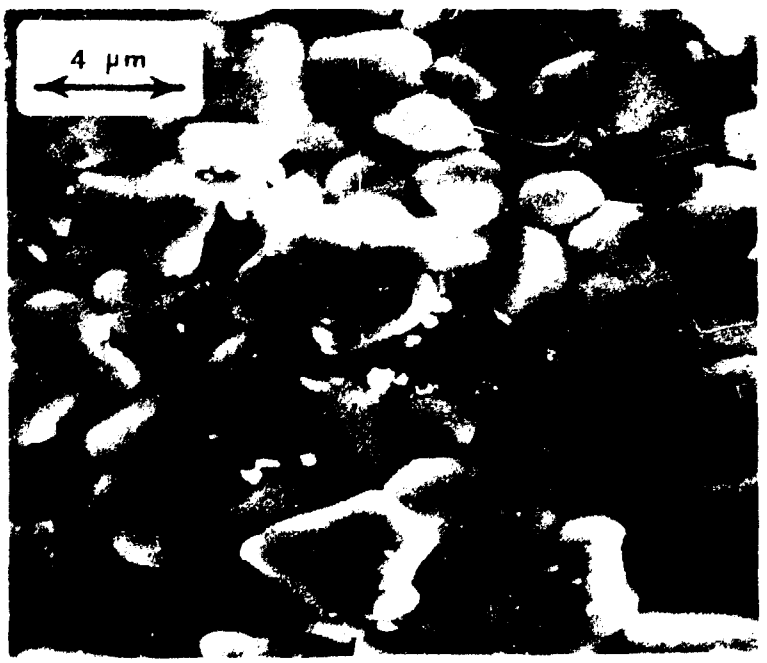

Figure 78 – Microstructures of UO_2 type M-1 sintered in H_2 + He

Figure 79 – Grain-morphology and columnar grain-growth in neck formed during sintering of microspheres.

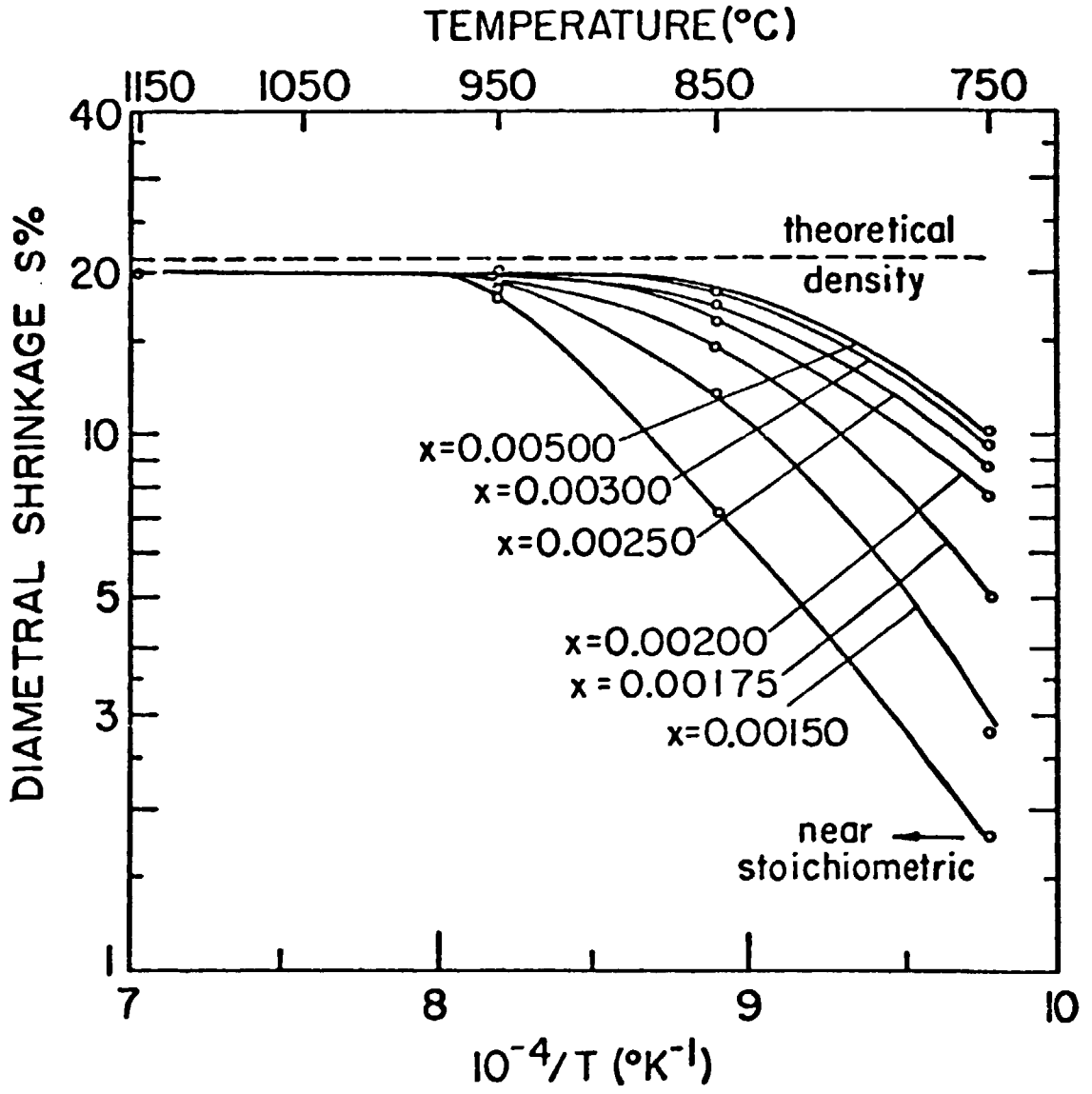

Figure 80 – Shrinkage vs. 1/T for UO_{2+x} microspheres sintered in argon + O_2 for 30 minutes

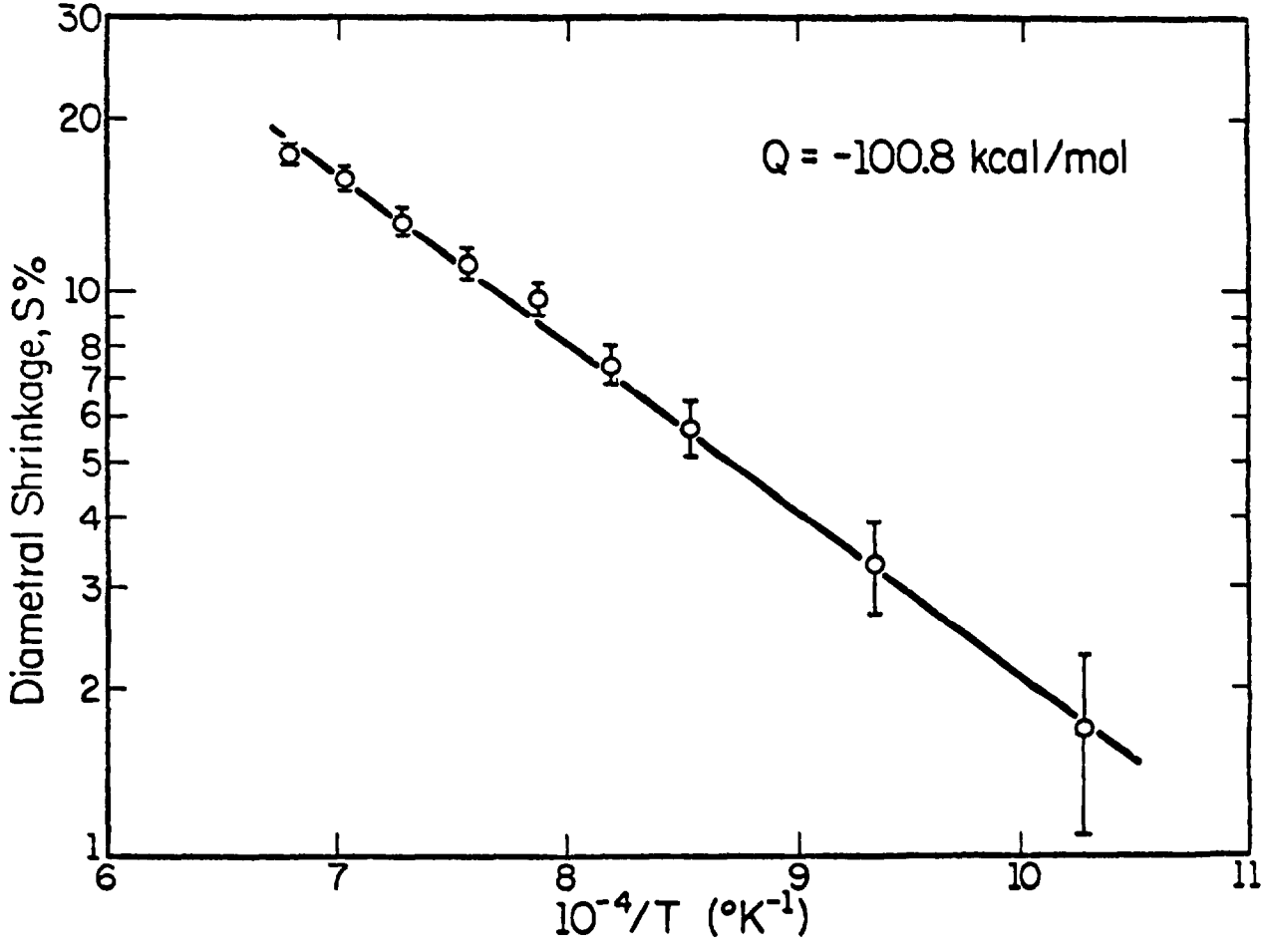

Figure 81 – Shrinkage vs. $\frac{1}{T}$ for UO_2 microspheres sintered in H_2

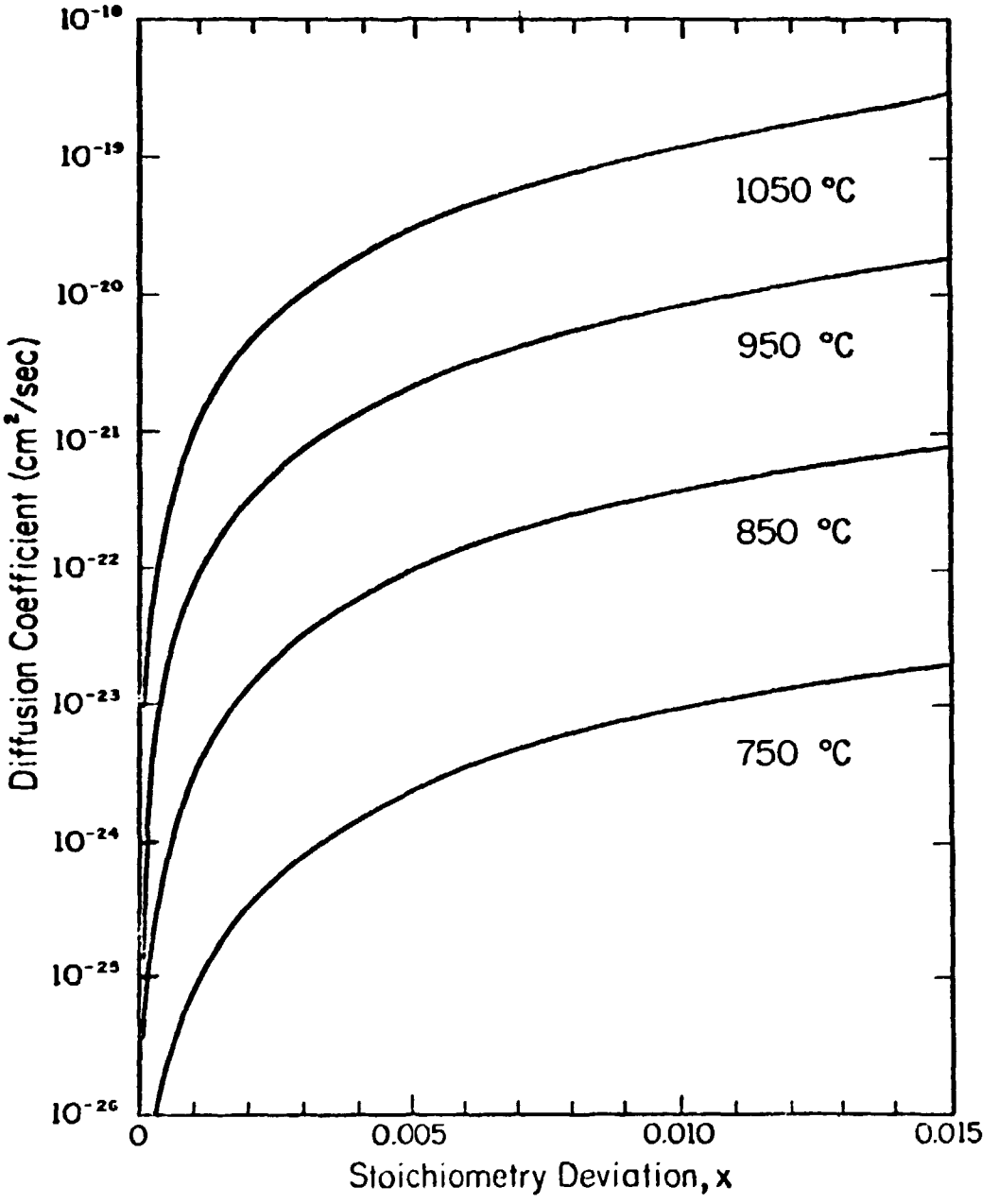

Figure 82 – The variation of the uranium self-diffusion coefficient in UO_{2+x} with x and T

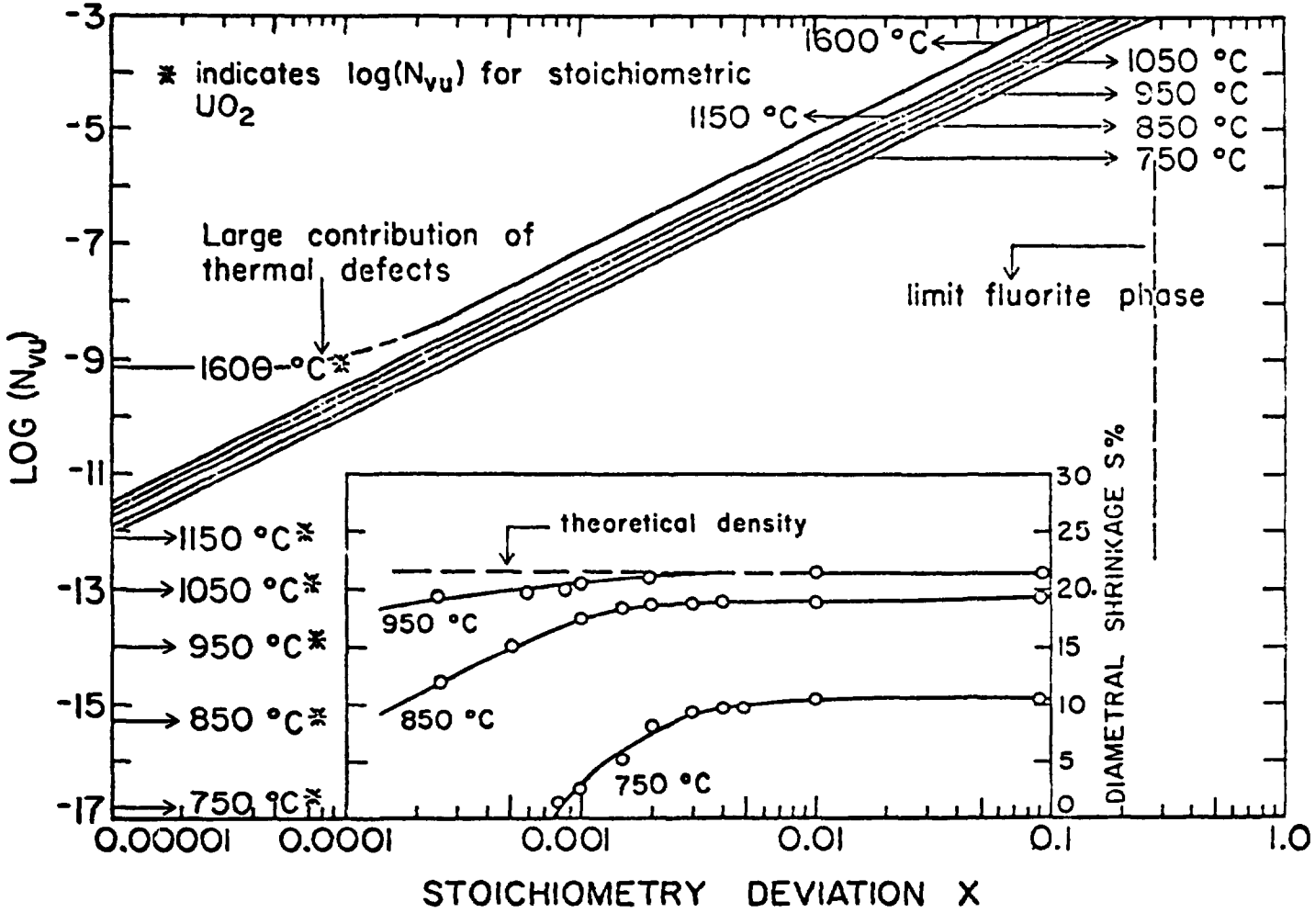

Figure 83 — Influence of stoichiometry deviation on uranium vacancy concentration in UO_{2+x}. The insert indicates the variation of UO_{2+x} microsphere diametral shrinkages with stoichiometry deviations.

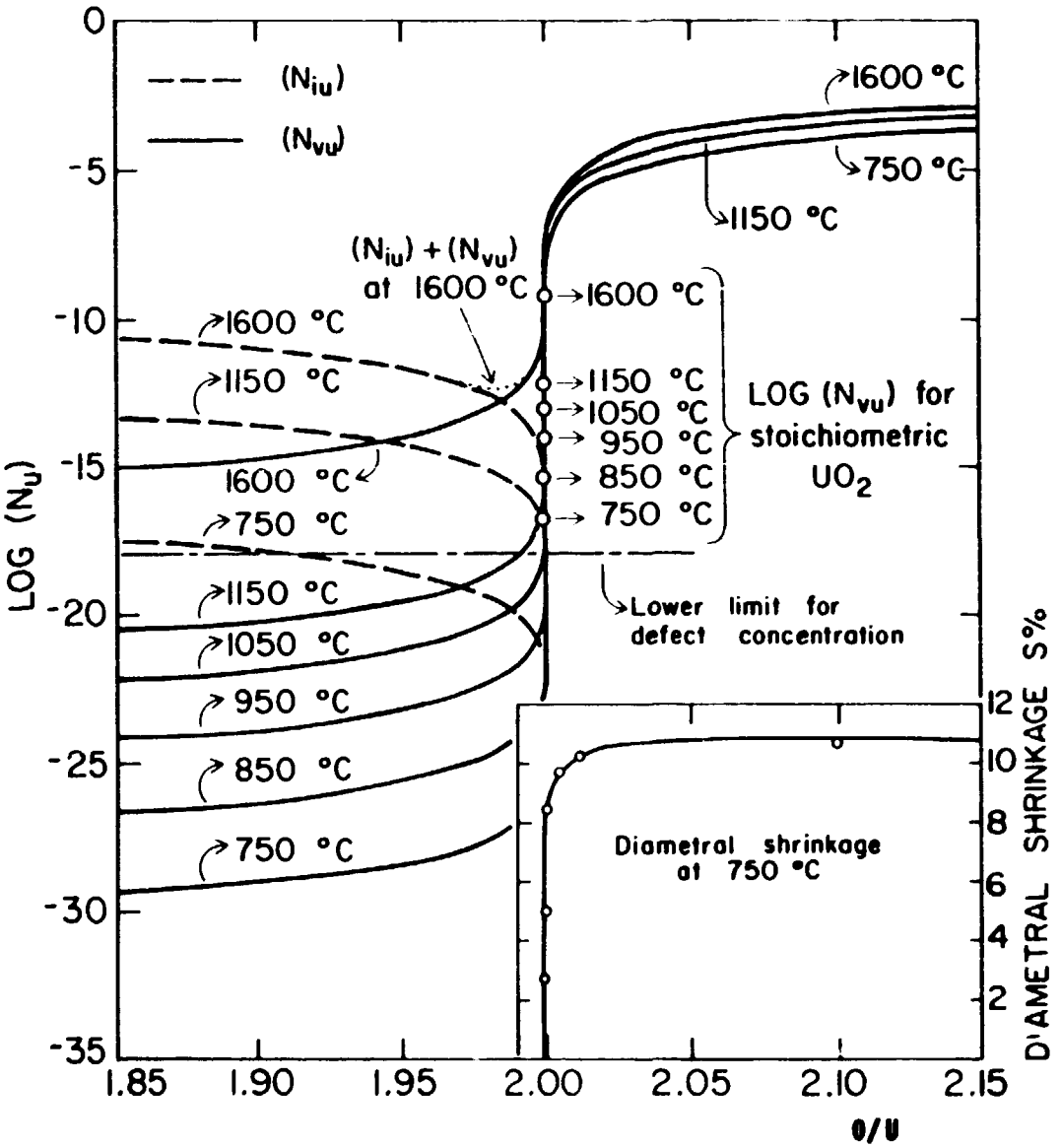

Figure 84 – Concentrations (N_{iu}) and (N_{vu}) respectively of interstitial and vacancy cation defects in UO_{2+x} in function of stoichiometry deviation. The insert indicates the variation of UO_{2+x} microsphere diametral shrinkages with stoichiometry deviations, during sintering in argon + O_2 at 750°C for 30 minutes.

For $\frac{O}{U} < 2.00$, Figure 84 indicates that $(N_{iu}) > (N_{vu})$, at temperatures in the 750 to 1150°C range. At 1150°C the concentration of defects $(N_{iu}) + (N_{vu})$, in the hypostoichiometric range $1.85 \leqslant \frac{O}{U} \leqslant 2$, is many orders of magnitude smaller than (N_{vu}) for $\frac{O}{U} > 2.01$.

In Figure 84 a low limit for values of defect concentrations is shown.* The indicated smaller or slightly higher values of $\log(N_u)$ are only physically meaningful as suggesting trends in the variation of defect concentration with stoichiometry deviations. The curves for $\log(N_{iu})$ in the hyperstoichiometric range were not presented, since they correspond to defect concentrations significantly lower than the above mentioned limit.

5.7 – Discussion

Sintering in reducing atmospheres for both microspheres and pellets obtained respectively from gels and ceramic grade UO_2 powder, led to final densities comparable to those mentioned in the literature (cf. references(1,148) and appendix 2 of this work).

For UO_2 microspheres sintered in hydrogen at 1061°C, Figure 56 shows that 8% diametral shrinkage was reached in 11 minutes. For UO_2 pellets sintered in hydrogen at 1300°C, the same shrinkage was attained in 36 minutes. For these conditions the Kingery and Berg initial stage equation (5.1) is applicable. The ratio S_P/S_M of diametral shrinkages is given by

$$1 = S_p/S_M = \left(\frac{T_P}{T_M}\right)^{-2/5} \left(\frac{a_P}{a_M}\right)^{-6/5} \left(\frac{t_P}{t_M}\right)^{2/5} \tag{5.4}$$

where the subscripts P and M refer respectively to pellets and microspheres. Therefore $\frac{a_P}{a_M} = 1.41$.

The value of a_p can be derived from the UO_2 powder surface area S_a using the formula**

$$2ap = \frac{0.5474}{S_a} \ (\mu m) \tag{5.5}$$

with S_a in m^2/g.

For $a_p = 380A$ and $S_a = 5\ m^2/g$ from (5.5)

$$\frac{a_P}{a_M} = 1.44$$

This excellent agreement suggests that under reducing conditions, sintering both of microspheres and pellets is controlled by uranium volume diffusion, for which Kingery and Berg's equation (5.4) is valid. Under these conditions, the better sinterability of the microspheres is explained by its smaller initial particle size.

The sintering kinetics is similar to that described by Haas[49], for UO_2 and thoria gels. The data fit a power curve $S\% = kt^n$, for shrinkages up to about 13% at 1050°C, as shown in Figure 64.

---

* It corresponds roughly to only one defect in the mass of the smallest sample utilized in the experiments.

** Derived based on the assumption that all the particles are spheres.

Lay[88] and Bacmann[14] also related their initial stage sintering data by power curve fits, with n equal to 0.40 and 0.31 respectively. The values 0.13 (microspheres) and 0.20 (pellets) determined in this investigation, are significantly smaller, but they agree with results referred to by Thümmler[138].

It is necessary to mention that in the investigations of Lay and Bacmann, ceramic grade powder were used, with surface areas smaller than 5 m^2/g. It was also noted in section 3.13 that Lay[87] himself recognized that the analysis of his data was affected by an erroneous assumption[18], regarding the application of a sintering model for very small shrinkage values. It is thought here that the same restriction can be applied to the Bacmann data evaluation, that led to the conclusion uranium grain-boundary diffusion is the dominant sintering mechanism. Consequently, it is not possible to accept these authors' conclusions that their measured n values imply grain boundary and volume diffusion to be the controlling mechanisms during the initial stage of hydrogen sintering of UO_2.

In the present work the values of n were used for the calculation of activation energies. The same value Q = 101 kcal/mole was found for sintering of either microspheres or pellets. It is in good agreement with the values determined by Reimann and Lundy[120] (98,300 ± 9,700 kcal/mole) and Lindner and Schmitz[94] (104,500 kcal/mole) for uranium volume diffusion in UO_2.

Considering the above result and the excellent agreement in the calculation of $\frac{S_P}{S_M}$ by two different methods, one applying Kingery and Berg's model for sintering controlled by volume diffusion, it was concluded that the initial stage of UO_2 sintering, in reducing atmosphere, is controlled by uranium volume diffusion. For the pellets, made from ceramic grade powder, this result agrees with those presented in references 88 and 7. For microspheres no confirmation was found in the literature.

The above results suggested that sintering in reducing conditions of microspheres previously reduced to UO_2 in hydrogen, would not differ in the intermediate and final stages from behavior already described in the literature for ceramic grade powder. The work of Coleman and Beere[34] suggested uranium volume diffusion as the controlling mechanism for the intermediate stage. Figure 81 shows that in the present investigation the activation energy corresponding to the intermediate sintering stage of microspheres is 100.8 kcal/mole, also implying uranium volume diffusion as the controlling mechanism. The kinetics data in the final stage being approximately the same for both microspheres and pellets, it seems reasonable to conclude that in this phase the same mechanism predominates that is, grain-boundary diffusion.

From the above considerations we see that the relatively samll particle size of the microspheres **per se** does not introduce any anomalous effect during sintering.

The direct sintering of gels, without prior low-temperature reduction to UO_2, constituted an entirely different approach that was plainly successful. It was thought to use better the initially very small particle size of the gel as a factor of sinterability enhancement. The solution of the gel breakage problem during initial shrinkage, by hot-stage microscopy optimization of the sintering cycle, is illustrative of the technique power. Up to 600°C a heating-rate of 55°C/min was necessary to avoid sample rupture. After this initial treatment very fast temperature increases permitted the attainment of higher densities than in the previously described microsphere sintering cycle.

The application of the rate equations (2.2) to (2.15), led to the construction of the sintering diagram shown in Figure 3, corresponding to an UO_2 gel with an initial particle size of 58Å. In this case the extremely small initial particle size is responsible for a change of dominant sintering mechanism, during the initial stage. Now uranium grain-boundary diffusion controls, except for a narrow range in which uranium surface diffusion from surface sources becomes dominant. For the intermediate and final stages Figure 3 shows uranium grain-boundary diffusion as the dominant mechanism. The total shrinkage shown in Figure 55 is considerably greater than in the case of previously reduced microspheres, due to the much smaller density of the UO_2 gels (3.1 and 5.3 $g\,cm^{-3}$, respectively).

The interpretation of the reactive sintering data is complicated by the fact that chemical composition gradients might be considerable during initial shrinkage, originating an additional process driving force[27] that could significantly influence the kinetics. However it is felt that this sintering cycle presents considerable technological interest, due to its rapid densification characteristics.

The observed neck growth between microspheres allows the determination of the controlling sintering mechanism. However, for sintering under reducing conditions, the necessary temperatures proved to be too high for the application of hot-stage microscopy. At 1850°C the temperature gradients were very severe. That could explain long dendritic structures originated at the sample surface, and be the cause of a complete loss of the initially spherical geometry. The same effect was observed for microspheres sintered in the hot-stage at 1500-1600°C in argon + O_2. The lower temperature in which the effect occurs was explained by the higher vapor pressure of the resulting hyperstoichiometric material. All the microsphere necks mentioned here were obtained in the relatively tempereture gradient-free hot-zone of the sintering furnace shown in Figure 49.

The value of the uranium volume diffusion coefficient calculated from the Kingery and Berg equation (5.1) applied to necks formed at 1850°C in H_2 + 10v/o He, was too high. It is thought that volume diffusion is not the main sintering mechanism at 1850°C. The sintering diagram shown in Figure 1 indicates that vapor transport is the dominant mechanism at 1850°C and $\log \frac{x}{a} = -0.517$. This last value being derived from neck measurements in the present work. The columnar grain-growth observed in the neck regions shown in Figure 79, also suggests evaporation-condensation as an active mechanism. Therefore it was concluded that vapor transport is the dominant sintering mechanism for microsphres, in the 1850 to 1950°C temperature range, where neck growth was carried out.

UO_2 microspheres sintered in argon + O_2 according to the sintering cycle indicated in Figure 62, resulted in shrinkage kinetics not substantially different from those obtained under reducing conditions. The values of n in $S\% = kt^n$ were the same (0.13). It is remarked that in this case sample equilibration with the sintering atmosphere was expected to occur, which manitained $p(O_2)$ constant during the entire sintering experiment. This approach simplified considerably control of the oxygen partial pressure. However it caused sample oxidation during pre-sintering of the microspheres at 600°C (as indicated in Figure 62). This pre-sintering proved to be necessary to prevent microsphere rupture prior to the final isothermal heat tratment. It is now thought thar equilibartion of the sample with the atmosphere was not always attained when this particular sintering cycel was used. For instance, for $p(O_2)$ = constant = 10^{-10} atm, Figure 65 indicates the UO_{2+x} reached $x > 0.2$ at 600°C, which is out of the fluorite-phase range. At 1050°C, x would be 0.0075, but a strong reducing action would be necessary to assure equilibration of the oxidized sample with the atmosphere. Sample weight loss measurements indicated that for $10^{-16} \leqslant p(O_2) \leqslant 10^{-18}$ atm, equilibration had occured. The main significance of the results presented in Figure 62 consists in showing that very small amounts of oxygen in a sintering atmosphere, indeed much lower than those normally present in commercial gases, can drastically affect the kinetics of the sintering process.

If the Kurnakov school of thought that all crystalline inorganic compounds are inherently nonstoichiometric (cf. section 3.1 of this work) is accepted, then traces of oxygen in sintering atmospheres may also affect substantially the sintering kinetics of the other ceramic compounds besides UO_{2+x}. For uranium oxide, this reasoning could explain the large diversity of sintering data found in the literature. It is believed that this explanation also applies to other property determinations carried out on compounds with the potential for large stoichiometry deviations.

The sintering cycle shown in Figure 46 was developed to give a better assurance that sample-atmosphere equilibrium would be reached in acceptable times, with durations samaller than those of the heating transients involved. Again in this situation hot-stage microscopy was very helpful to suggest the adopted procedure, since slight oxidation was immediately detectable by the darkening of the sample surface.

In this sintering cycle, equilibration was attained by oxidation of the initially stoichiometric sample. This oxidation was very rapid, as seen through the microscope. It was thought to occur without any significant shrinkage, since the volume diffusivity of oxygen is many orders of magnitude faster than that of uranium. In the previous sintering cycle equilibration had to be reached by reduction, in this case a thermodynamically less favorable approach.

The results obtained with this new sintering cycle were significantly different from those using other cycles, either in reducing or oxidizing atmospheres. Theoretical densities were attained in less than 45 seconds, in the 1050 to 1150°C temperature range. The values of n, in $S\% = kt^n$, went from 0.13 (typical of sintering under reducing conditions) to 3 or higher, for shrinkages under 10%. The activation energy for the process was under 96 kcal/mole (vs. 101 kcal/mole for sintering under reducing conditions). The difference in sintering kinetics was even more striking when regular ceramic grade UO_2 was compared with UO_2 prepared from gels, as shown in Figure 85. To reach 93% of theoretical density, 100 minutes at 1600°C were necessary for pellets prepared with regular ceramic grade powder. The same density was reached by the UO_2 prepared from gels in 23 seconds at 1150°C. Therefore the time decreased by more than 2 orders of magnitude (261 X) at a temperature that was 450°C lower.

As previously mentioned in this discussion, the smaller initial particicle size of the UO_2 prepared from gels cannot, **per se** explain its better sinterability. The considerable influence of the oxygen potential on sintering, shown in Figure 66 to 70 and 80 was judged to account for the extraordinary sintering kinetics mentioned above.

As was shown in chapter 3 of this work, the defect concentrations in the fluorite structure of UO_{2+x} are strongly dependent on the oxygen activity of the atmosphere. Figures 83 and 84 indicate the variation of cation defect concentration with stoichiometry deviation, while the relationship between x and $p(O_2)$ is given in Figure 65. When initially stoichiometric samples, for instance at 750°C, are oxidized to about the middle range of hyperstoichiometry indicated in Figure 84, the concentration of uranium vacancies increases by 13 orders of magnitude. It was shown in section 3.10 how significantly defects affect diffusion coefficients and therefore sintering kinetics. The good correlation between sintering kinetics and $\log (N_{vu})$, presented in the Figure 84 is obvious. It is due to the rapid increase of the uranium volume diffusion coefficient with $\log (N_{vu})$ from the initial stoichiometric value, up to a saturation point, which is reached at about $x = 0.05$. This direct relationship between defect concentrations and the sintering kinetics of UO_2 prepared from gels, is thought to be a novel description of the exceptional sintering behavior of the material.

The author believes that some of the currently adopted sintering models used in the description of the process kinetics can also be used in the situation discussed above. However it became readily apparent, when such models were tried, that modifications are necessary. In the construction of sintering diagrams for instance, Kingery and Berg's equation (5.1) cannot be applied, since the time exponents are too different ($\simeq 3.5$ experimentally, vs. 0.4 theoretically). The development of the necessary modifications to those models was considered beyond the scope of the present investigation.

The very low activation energies for sintering of UO_{2+x} microspheres in argon + O_2, after the equilibration of the initially stoichiometric material, is attributed to the increase of available diffusional paths for defect complex movement introduced by the creation of defects upon equilibration. The much lower sinterability of the hypostoichiometric microspheres sintered in hydrogen is attributed to the smaller defect concentrations in the hypostoichiometric range, as shown in Figure 84. The author believes that there is no need to attribute the lower sinterability to adsorbate effects, that are not well understood[132].

Unquestionably proper sample-atmosphere equilibration is essential for the detection of the full influence of oxygen potential on sintering. The atmosphre effect phenomenon is suggested from investigations with poorly equilibrated material, as discussed for the previously reported works, but then the beneficial effects of large defect concentrations on sintering is partially masked by undesirable oxidation.

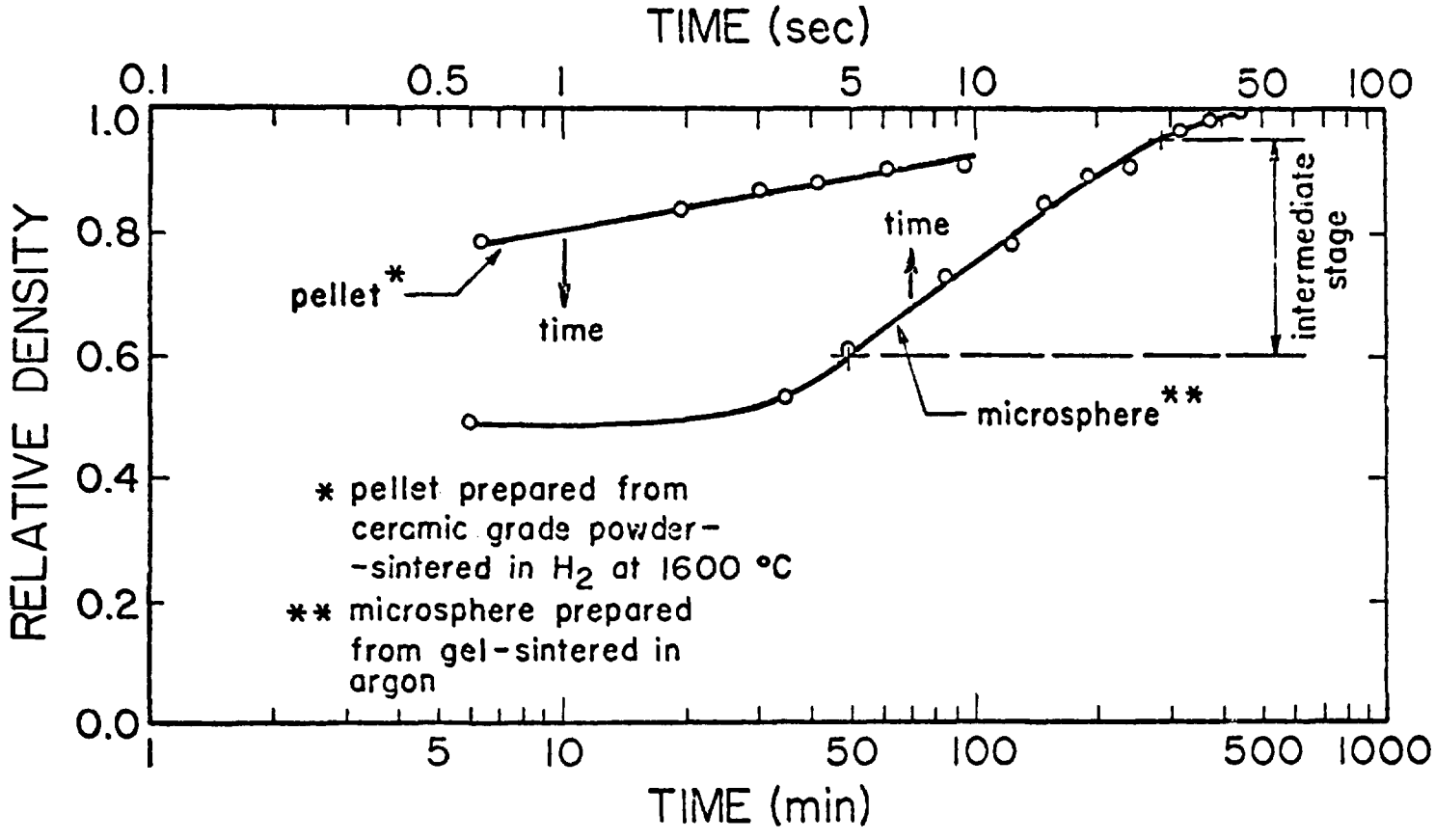

Figure 85 — Sintering kinetics of specimens prepared using gels and ceramic-grade powders. The temperature was 1600°C for pellets and 1150°C for microspheres.

The author believes the importance of correct equilibration cannot be overemphasized. The full potential of large defect concentrations for sinterability enhancement is only evidenced by adequate equilibration. Improperly done it can lead to scientifically meaningless results.

Equilibration procedures are therefore of major significance for the correct evaluation of nonstoichiometric UO_2 behavior on theoretical or technical* grounds.

CHAPTER 6

CONCLUSIONS

1 – For sample prepared using both gels and ceramic grade powder, the initial sintering stage kinetics can be described by a power-law curve of the form $S\% = At^n$.

2 – The exponent n in the above formula is equal to 0.13 ± 0.01, for both microspheres sintered in hydrogen and in argon $+O_2$, if in the latter case equilibration had been reached maintaining $p(O_2)$ constant during the entire sintering experiment.

3 – $n = 0.20 \pm 0.1$ for pellets prepared from ceramic grade powder and sintered in hydrogen.

4 – n varies between 3.5 and 4.5 as a function of stoichiometry, for microspheres sintered in argon + O_2 and equilibrated by previous reduction to stoichiometric UO_2 and subsequent oxidation to the desired oxygen potential.

5 – Activation energies calculared for the initial stage of sintering using the above values of n and slopes of $\log S\% = f \log(t)$, are the following:

a) microspheres sintered in argon + O_2, equilibrated without previous reduction to stoichiometry

$Q = 101 \pm 2$ kcal/mole

b) microspheres sintered in H_2

$Q = 99 \pm 2$ kcal/mole

c) pellets sintered in H_2

$Q = 101 \pm 2$ kcal/mole

*It is useful to observe that the sintering cycle shown in Figure 46 can be applied to the industrial sintering of nonstoichiometric ceramics. In the case of UO_2 pellets, even a continuous sintering process would be feasible, using flowing hydrogen as sintering atmosphere (as in the regular industrial process), but with the injection of a slightly oxidizing atmosphere in the low temperature zone of the furnace. For instance $N_2 + O_2$ could be introduced via inconel tubing to the 600°C zone, where the initially stoichiometric UO_2 would be slightly oxidized. A further discussion of potential industrial application of controlled atmosphere sintering is outside of the scope of this work.

d) microspheres sintered in argon + O_2, equilibrated with previous reduction to stoichiometry: $61 \leqslant Q \leqslant 96$ kcal/mole; the value of Q is variable with stoichiometry.

6 – The activation energies for cases a, b, c in the previous item are equal to that corresponding to uranium lattice diffusion in UO_2. The activation energy for case d can be associated with uranium volume diffusion in UO_{2+x}.

7 – A sintering diagram indicates grain boundary diffusion to be the dominant mechanism for the intermediate and final stages of UO_2 microspheres sintered in argon + 10 v/o H_2.

8 – Studies of neck growth between pairs or triplets of 500 μm diameter microspheres, sintered in slightly reducing atmospheres, led to the determination of uranium lattice volume diffusion coefficients substantially higher than those in the literature, corresponding to UO_2 crystals or samples prepared from ceramic grade powder. D was found to be 4.8×10^{-7} cm^2/sec, at 1850°C. At this temperature vapor transport was concluded to be the dominant sintering mechanism.

9 – For H_2 sintering of UO_2 pellets (prepared from ceramic grade powder), $S\% = At^n$ for the intermediate sintering stage, with the same n and Q values mentioned in conclusion 3. Therefore uranium lattice diffusion was found to be the dominant mechanism.

10 – The influence of oxygen-potential on sintering rate is a dominant factor, affecting all the sintering stages. For stoichiometry deviations under 0.050 it is possible to go from initial to final sintering stage at constant temperature, varying only the atmosphere oxygen potential.

11 – The crystallite size of UO_2 gels was found to be 110 A, by transmission electron microscopy. The size increased to 760 A during reduction to UO_2 in hydrogen, attaining 2200 A and 4 μm during sintering at 1050 and 1850°C, respectively.

12 – For the initial sintering stage the functions f and F in $S\% = f(x)$ and $\log(N_{vu}) = F(x)$ can be described by parametrically equal expressions.

13 – The final stage of UO_2 sintering in dry hydrogen, either for microspheres produced from gels or pellets made with ceramic grade powder, is controlled by grain-boundary diffusion.

14 – The exceptional behavior of UO_2 microspheres produced from gels, reduced in hydrogen immediately prior to sintering and thereafter equilibrated with the argon + O_2 sintering atmosphere, is explained by the sintering cycle characteristics, that permit full utilization of the diffusional paths corresponding to the defects created during a very rapid sample-atmosphere equilibration.

CHAPTER 7

SUGGESTIONS FOR FUTURE WORK

1 – The influence of atmosphere equilibration on sintering kinetics is felt to deserve systematic evaluation, since its results can lead to the definition of sintering cycles of high effectivity, for ceramic compounds affected by large stoichiometry deviations. Different rates to equilibration can be achieved simply by varying heating transients during sintering, or by changing the sintering atmosphere oxygen potential during these transients.

2 – The microstructure evaluation of gels during sintering, as a function of oxygen potential, deserves further investigation. A knowledge of microstructure is essential for the aplication of many sintering models.

3 – The application of sintering diagrams to materials for which grain-growth is considerable at small shrinkages, requires the development of special computer programs. At present there are no means available for an acceptable processing time of sintering kinetics data, essential for the construction of the above diagrams. Regular iteration procedures demand many hours of mini-computer assisted work for the elaboration of a single sintering diagram.

The mathematical boundary conditions assumed to be valid by Ashby, for the transitions between different sintering stages, are felt to deserve further attention. Simple continuity assumptions for the transitions are felt to be elegant and expediting, but physically there is a significant discontinuity in the passage for instance from the initial to the intermediate stage, when major grain growth might occur. More elaborated and realistic boundary conditions allowing for discontinuities, could better describe the behavior of materials such as the gels studied in this experiment.

4 – A main characteristc of the high temperature hot stage microscope usde in this investigation was not fully exploited. Heating rates of up to 6000°C per minute are easily attained. It is felt that the temperature transients are of major importance in the rate of defect formation in materials with large deviations from stoichiometry. The high temperature hot stage would permit the development of systematic studies of the influence of heating rates in sintering kinetics.

5 – It is believed that neck formation between microspheres is possible at temperatures lower than 1550°C, in argon + O_2 with the correct oxygen potential. Such line of work was not followed in this investigation due to the difficulty of equilibrating the samples with the sintering atmosphere in the short-muffle furnace available. However it could be carried out in a longer furnace with a 2" diameter muffle, for which thermal segregation of the argon + O_2 mixture components would be minimized at acceptable levels of gas flow. With such a furnace, systematic studies of UO_{2+x} pellets sintered in controlled oxygen potential would also be practical.

APPENDIX I

A.1.1 – A Definition of Sintering Proposed by Thümmler[138]

Thümmler[138] proposed the following definition for sintering: "It is the heat-treatment of a system of individual particles or of a porous body, with or without the application of external pressure, in which some or all of the properties of the system are changed with the reduction of the free enthalpy in the direction of those of the porosity-free system; in this connection, at least enough solid phases remain to ensure shape stability".

A.1.2 – The Sintering Stages Accoruing to Coble[32]

It is possible to describe a sintering stage as an interval of geometric transience in which the pore shape modification is completely defined (for instance the rounding of pores in the initial stage of the process), or a time interval for which the pore decreases in size while remaining constant in shape (as in the final stage where shrinkage of spherical pores occurs).

a) Initial stage

The initial stage is that in which interparticle contact area increases from zero to approximately 0.2 of the cross-sectional area of the particle. This initial stage is frequently referred to as neck growth. Interparticle shrinkage of several percent accompanies neck growth; values for the increasing relative density vary between 0.5 and 0.6, for a typical powder compact.

During the initial stage grain growth cannot occur due to the fact the solid-vapour surfaces diverge at an acute angle from the particle-particle contact area. It would require a significant increase in grain boundary contact areas and energies in order to allow grain growth. In this manner the grain boundaries are restricted to the neck areas. This restriction decreases after the neck surface has become blunted by neck growth and grain growth becomes possible. The initial stage terminates when grain growth first takes place.

b) Transition stage

In this stage grain growth and pore shape changes cause a transition to a grain boundary and pore condition that closely approaches a continuous matrix.

c) Intermediate stage

The intermediate stage is that in which the pore phase can be approximately described by continuous channels coincident with theree-grain edges throughout the matrix.

d) Final stage

In the final stage the pore phase become discontinuous. The microstructure is formed by nearly spherical closed pores occupying four-grain corners.

An alternate final stage is defined. It occurs when discontinuous graiw growth (secondary recrystallization) takes place. The alternate final stage is that for which closed pores are mostly isolated from grain boundaries.

APPENDIX 2

A.2.1 – Sintering Behavior of Nonstoichiometric Uranium Oxides – Data of Williams et al., Webster and Bright.

The following five tables summarize results presented by Williams et al. in Ref. 145.

Table A-1

The sintering behavior of nonstoichiometric uranium oxides. Sintering atmospheres: argon, nitrogen and carbon dioxide[145]

Sintering temperature (°C)	Atmosphere	O:U ratio		Density (g/cm³)		Measured weight loss (wt o/o)	Calculated oxygen loss (wt o/o)
		Initial	Final	Initial	Final		
1410		2.08	2.05		10.40	0.24	0.18
1260		2.08	2.05		10.37	0.22	0.18
1160	argon	2.08	2.05	5.4	10.29	0.23	0.18
1060		2.08	2.05		9.87	0.20	0.18
1410		2.24	2.14		10.17	0.62	0.58
1260		2.24	2.15		10.07	0.64	0.53
1160	argon	2.24	2.14	4.6	10.17	0.60	0.58
1060		2.24	2.15		9.84	0.54	0.53
960		2.24	2.15		9.49	0.54	0.53
1300		2.18	not determined		10.3		
1200		2.18			10.0		
1100		2.18			9.8		
1000	nitrogen	2.18		4.6	9.3	not determined	
900		2.18			7.8		
800		2.18			6.1		
1300		2.18	2.15	4.6	10.3		
	carbon-dioxide	2.08	2.10	5.4	10.3	not determined	
1410		2.40	2.20		9.93	1.37	1.16
1260		2.40	2.23		9.79	1.19	0.99
1160	argon	2.40	2.25	4.6	9.70	1.12	0.87
1060		2.40	2.22		9.65	1.13	1.04
960		2.40	2.22		9.11	1.13	1.04

Table A-2

The influence of oxidation treatment on the sintering behavior of a nonstoichiometric uranium oxide[145]

Oxidation temperature (°C)	O:U ratio		Final density (g/cm^3)	Atmosphere	Sintering temperature (°C)
	Initial	Final			
200	2.40	2.19	10.2	argon	1410
300	2.59	2.22	10.7		1410
400	2.66	2.26	10.8		1410
500	2.67	2.26	10.8		1410
500	2.67	2.0	10.4	hydrogen	1410
500	2.67	2.0	9.8		1300
500	2.67	2.0	7.7		1200

Table A-3

The sintering behavior of nonstoichiometric uranium oxides in vacuo[145]

Sintering temperature (°C)	O:U ratio		Density (g/cm³)		Measured weight loss (wt o/o)	Calculated oxygen loss (wt o/o)
	Initial	Final	Initial	Final		
1410		2.04		10.3	1.58	0.24
1260		2.05		10.2	0.32	0.18
1160	2.08	2.06	5.4	10.3	0.22	0.12
1060		2.05		9.8	0.2	0.18
1410		2.06		10.2	6.0 to 8.0	0.05
1260	2.24	2.13	4.6	10.0	1.38	0.53
1160		2.13		10.0	0.88	0.53
1410	2.33	2.06	4.6	9.5	10.0	1.3
1410 (effusion cell)	2.21	2.08	4.6	10.13	cell 0.78 pellet 1.00	0.75
1410	2.21	2.03	4.6	10.15		

Table A-4

The sintering behavior of uranium oxides in hydrogen[145]

Sintering temperature (°C)	Atmosphere	O:U ratio		Density (g/cm³)		Measured weight loss (wt o/o)	Calculated oxygen loss (wt o/o)
		Initial	Final	Initial	Final		
1400	dry		2.0		9.43	0.48	0.47
1410	hydrogen		2.0		9.07	0.49	0.47
1260	"	2.08	2.02	5.4	6.75	0.37	0.36
1160	"		2.03		6.0	0.32	0.29
1460	"		2.01		8.56	1.3	1.29
1260	"	2.24	2.01	4.6	7.6	1.27	1.29
1160	"		2.04		6.19	1.27	1.18
1410	"		2.02		8.24	2.03	2.01
1260	"		2.07		6.03		
1160	"	2.4	2.09	4.6	5.54	not	not
1060	"		2.15		4.96	determined	calculated
960	"		2.17		4.84		
1550	partialiy		2.0		9.93		
1450	dried		2.0		9.75	not	not
1400	hydrogen	2.18	2.0	4.6	9.65	determined	calculated
1300	"		2.0		8.95		
1200	"		2.0		7.35		
1300	dry hydrogen	2.18	2.0	4.6	7.2	not determined	not calculated

Table A-5

The sintering behavior of nonstoichiometric uranium oxides in combination of atmospheres[145]

Sintering Cycle	$UO_{2.08}$		$UO_{2.18}$	
	Sintered density (g/cm^3)	Sintered O:U ratio	Sintered density (g/cm^3)	Sintered O:U ratio
Heated to 750°C in hydrogen, evacuated, heated to 1400°C in argon and held for 1 hour	9.05 9.15 9.15	2.0 2.0 2.0	8.9 8.94 8.97	2.0 2.0 2.0
Heated to 750°C in hydrogen, evacuated, heated to 1400°C in vacuo and held for 1 hour	9.5 9.4	2.0	9.55 9.49	2.0 2.0
Heated to 1400°C in argon and held for 1 hour	10.46 10.63 10.64	2.09 2.09	10.52 10.45 10.45	2.16 2.16
Heated to 1400°C in vacuo and held for 1 hour	10.42 10.32	2.06 2.06	10.29 10.25	2.12

The following 7 tables summarize results obtained by Webster and Wright in Ref. 142.

Table A-6

Sintering in undiluted hydrogen atmosphere[142]

Soaking Temp. (°C)	Green Density, g/cm^3	Sintered Density, g/cm^3	O/U atomic ratio	Uranium Content** of Sintered Compacts Calculated as $UO_{2.00}$ g/cm^3
1200	5.50	6.95	2.034	6.92**
1300	5.48	7.22*	2.043	7.20
1400	5.56	8.06	2.012	8.05
1500	5.55	8.81	2.003	8.81
1700	5.55	9.47	1.999	9.47

* Mean for three compacts

** In this and succeeding Appendix 2 tables, this final column of data gives the amount of uranium dioxide that would be present, in g/cm^3, if all the nonstoichiometric oxygen were removed without any concurrent crystallographic changes.

Table A-7

Sintering in nitrogen + hydrogen atmospheres[142] N_2:H_2 = 4:1 by volume

Soaking Temp. (°C)	Green Density, g/cm^3	Sintered Density, g/cm^3	O/U atomic ratio	Uranium Content of Sintered Compacts Calculated as $UO_{2.00}$ g/cm^3
1200	5.45	6.45	2.080	6.42*
1400	5.45	8.15	2.016	8.14

* Phase present: α-UO_2.

Table A-8

Sintering in undiluted argon atmospheres[142]

Soaking Temp. (°C)	Green Density, g/cm³	Sintered Density, g/cm³	O/U atomic ratio	Uranium Content of Sintered Compacts Calculated as $UO_{2.00}$ g/cm³
1200	5.56	9.44	2.070	9.40
1300	5.52	10.04	2.189**	9.93
1400	5.52	10.24	2.182**	10.13
1500	5.46	10.21	2.167**	10.11*

* Phases present after firing: α-UO_2 + U_4O_9

** This retention of nonstoichiometric oxygen at increasing temperatures is probably due to a small partial pressure of oxygen impurity in the argon supply.

Table A-9

Sintering in argon + 0.6% water vapor atmospheres[142]

Soaking Temp. (°C)	Green Density, g/cm³	Sintered Density, g/cm³	O/U atomic ratio	Uranium Content of Sintered Compacts Calculated as $UO_{2.00}$ g/cm³
1200	5.47	9.83	2.163	9.74
	5.66	9.32	2.068	9.28
	5.45	8.77	2.030	8.75
1300	5.67	9.61	2.053	9.58
1400	5.46	9.61	2.090	9.56
	5.60	9.68	2.062	9.64
1500	5.58	9.69	2.071	9.65*

* Phases present after firing: α-UO_2 -- U_4O_9

Table A-10

Sintering in argon + oxygen atmospheres[142]

Soaking Temp. (°C)	Green Density, g/cm³	Sintered Density, g/cm³	O/U atomic ratio	Uranium Content of Sintered Compacts Calculated as $UO_{2.00}$ g/cm³
1200	5.56	9.54**	2.089	9.49*
1300	5.68	9.88**	2.177	9.78
1400	5.68	9.60	2.151	9.51
	5.48	10.00	2.184	9.89
1500	5.63	10.22	2.212	10.09*

* Phases present after firing α-UO_2 + U_4O_9

** Out of 5 compacts fired to 1200°C, 1 disintegrated
Out of 5 compacts fired to 1300°C, 2 disintegrated

Table A-11

Sintering in undiluted nitrogen atmospheres[142]

Soaking Temp. (°C)	Green Density, g/cm³	Sintered Density, g/cm³	O/U atomic ratio	Uranium Content of Sintered Compacts Calculated as $UO_{2.00}$ g/cm³
1200	5.50	8.99	2.049	8.96*
1300	5.59	9.57	2.076	9.53
1400	5.65	9.75	2.053	9.72
1500	5.58	9.90	2.074	9.86

* Phase present after firing: α-UO_2

Table A-12

Sintering in nitrogen + 0.6% water vapor atmospheres[142]
Heating, soaking, and cooling in N_2 containing 0.6% water vapor

Soaking Temp. (°C)	Green Density, g/cm³	Sintered Density, g/cm³	O/U atomic ratio	Uranium Content of Sintered Compacts Calculated as $UO_{2.00}$ g/cm³
1200	5.46	9.37	2.099	9.32*
1300	5.58	9.47	2.054	9.44
1400	5.57	9.69	2.070	9.65
1500	5.57	10.00	2.093	9.95

* Phases present after firing: α-UO_2 + U_4O_9

A.2.2 – Summary of Uranium Dioxide Characteristics, Sample Preparation and Sintering Time-Temperature Relationships in the Work of Webster and Br...t[142]

The basic material had an oxygen-to-uranium ratio of 2.19 and reached a density of 9.47 g/cm^3 (86% T.D) when fired in a hydrogen atmosphere at 1700°C for thirty minutes.

Compacts of 5g weight and 12.7 mm diameter were prepared by cold pressing at 2.8 t/cm^2 using kerosene as binder and stearic acid as a mold lubricant. The heating rates to the desired peak temperature varied between 90 and 150°C/hour, soaking for thirty minutes and cooling at rates of 400 to 900°C/hour. The slower heating and faster cooling rates corresponded to the higher temperature experiments. In the case of steam atmosphere sintering, heating to 750°C and cooling below 750°C were done in argon, to avoid condensation in the cooler parts of the furnace.

APPENDIX 3

A.3.1 – Chemical Analysis of Material Utilized in the Production of M-1 Type Microsphere.

The semi-quantitative spectrographic analysis presented in Table A-13 was made in the Chemistry Division of the "Instituto de Energia Atômica"*. The results are presented in μg of each element per gram of uranium.

* São Paulo, Brazil.

Table A-13

Chemical Analysis of Material M-1

elementos amostras	DUAN 74	DUAN 75	DUAN 76	DUAN 77	elementos amostras	DUAN 74	DUAN 75	DUAN 76	DUAN 77	elementos amostras	
Fe	≪14	< 14,0	< 14,0	≪14,0	Mo	< 2	< 2,0	< 2,0	< 2,0		
Si	> 260	∿ 110	∿ 60	∿ 10,0	V	< 11	< 11,0	< 11,0	< 11,0		
Mn	≪ 1	< 1,0	< 1,0	< 1,0	Cu	∿ 4	∿ 5,0	< 0,5	< 0,5		
B	< 0,1	⩽ 0,1	⩽ 0,1	⩽ 0,1	Cd	< 0,3	< 0,3	< 0,3	< 0,3		
Mg	< 2	< 2,0	< 2,0	< 2,0	Zn	< 50	< 50,0	< 50,0	< 50,0		
Pb	< 1	∿ 1,0	∿ 2,0	∿ 20,0	Ti						
Ag	∿ 0,1	∿ 0,2	∿ 0,7	< 0,1	Co						
Cr	< 3	< 3,0	< 3,0	< 3,0	Ca						
Sn	∿ 2	< 1,0	5,0	< 1,0	P	< 55	< 55,0	< 55,0	< 55,0		
Al	< 4	< 4,0	< 4,0	< 4,0							
Ni	< 2	< 2,0	< 2,0	< 2,0							
Bi	< 1	< 1,0	< 1,0	< 1,0							

amostra	nº Lab.	material	observações
			Análise espectrográfica semiquantitativa.
			Resultados apresentados em μg EI/gU

06/01/1977
data

visto

APPENDIX 4

A.4.1 – Microscopy Heating-Stage Power Supply

The power supply for the hot-stage had to provide output up to approximately 175W, maintaining current stability. Typically the maximum current variation should be smaller than 0.2A, in the 30 to 110A range. The current had to be regulated, monitored continuously, adjustable and capable of being switched to full power on or off instantly. The original Leitz power supply could not satisfy these requirements, and was substituted by that shown in Figures A4-1 and A4-2, built by the Electronics Shop of the University of Illinois Nuclear Engineering Program. The following description of the power controller, regulator and monitor board was taken from the system design report*.

(1) Power Controller and Regulator (Figure A-1). Line voltage (117 VAC) is stepped down to 42.5 VAC with a powerstat. This low voltage/high current appears across either the series transistor (2N6258) or the output transformer. The amount of base current, hence accordingly, the ac voltage appearing across the series transistor, is determined by the power adjust potentiometer. The greater the base current, the less the ac voltage that appears across the transistor and the greater the ac voltage appears across the transformer.

A voltage signal across the heater element is the feedback to the regulator circuit on the bottom. This voltage is amplified (gain 1) and rectified by the first two 741s respectively IC3 (741) is used as a comparator and its output is fed to IC4 and then to the 2N3866 transistor. Currents up to approximately 100 mA are provided to the base of the 2N6258 when the DC voltage from the emitter of the 2N3866 is raised continuously.

For this system, an ON/OFF switch, SW1, controls the powerstat separately. A second switch, SW2, does three operations:

a) allows the stepped-down ac voltage to be fed to the controller,

b) turns on the power to the ± 15 VDC power supply module, and,

c) turns on the power for the fan of the 2N6258.

(2) Power Monitor Board (Figure A-2). The voltage signal (approximately 1 Vrms) across the secondary of the transformer is fed into the top 741 OP AMP, 1C1, which has a gain of 2. IC2 rectifies the ac signal and introduces it to the X port of the multiplier. The current signal (approximately 1 Vrms) from the Simpson Model 150 AC Clamp, although distorted, is fed into the bottom 741, IC3, which is set at a gain of approximately 1.5. IC4 rectifies the amplified current signal and introduces it to the Y port of the multiplier.

The multiplied signal, -XY/10, represents the power and is fed into one of two 741s. The bottom 741, IC6, is a DC amplifier with gain of approximately 4.5 so that full scale on the ammeter 50 μA, represents 200 W. The top 741, IC5, has a gain of approximately 4.5 and provides a DC voltage which is proportional to the power level, to the LINE PRINTER. The 22 k Ω resistor provides a load for the 741 and the 200 μF capacitor reduces the oscillations present at the load.

No measurement of the transition from zero power to full power can be made using this circuit. The capacitor at the load determines the time constant of the recorder response. Its value is a compromise between two considerations, namely, (i) minimum oscillations of the recorder pen, i.e., large capacitance value, (ii) quickness of transient response, i.e., small capacitance value. Outputs to the line printer range from 0 to approximately 10 volts.

---

* By Eric H. Iwamoto, December 1975.

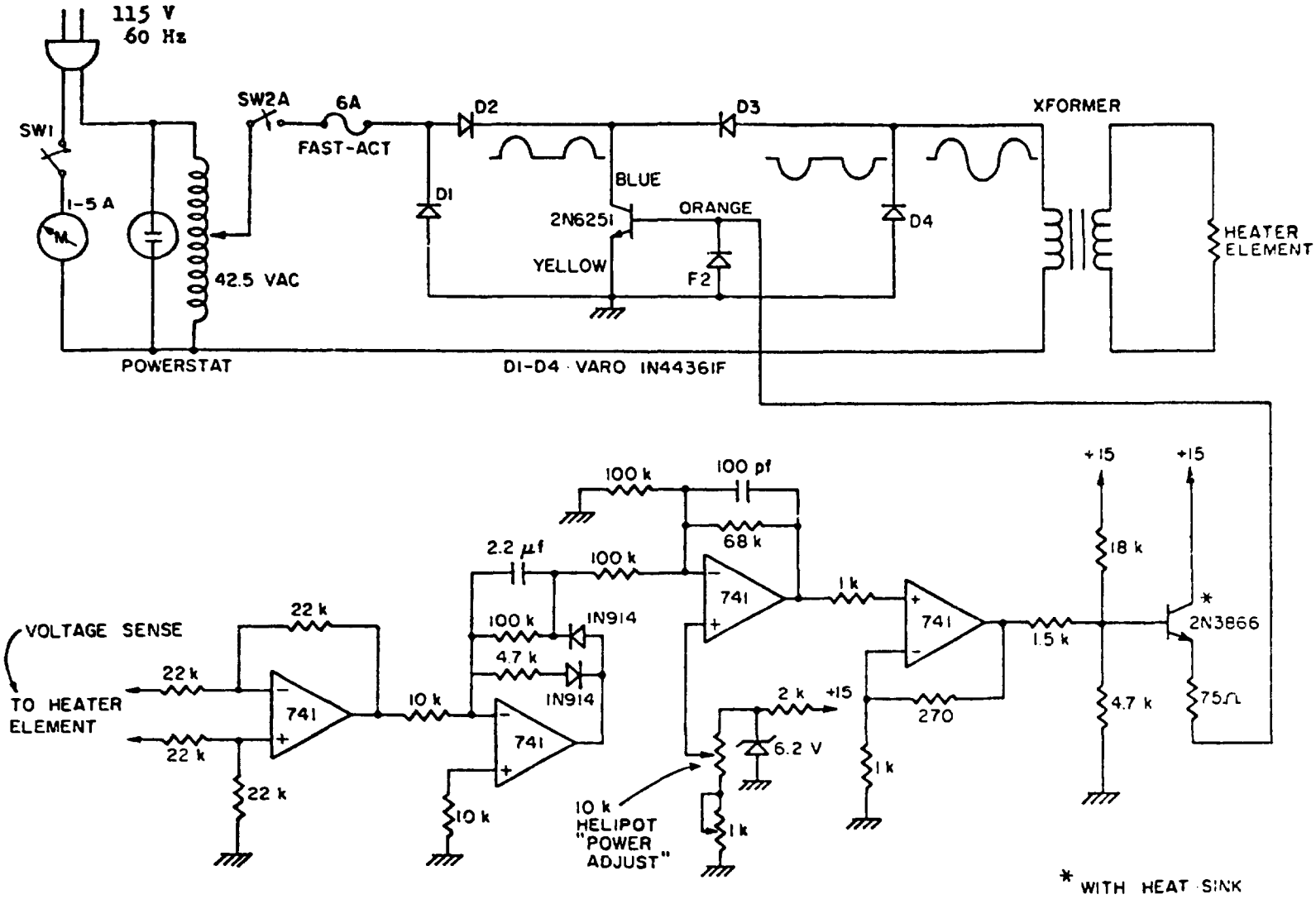

Figure A-1 — Hot-Stage Power Controller and Regulator

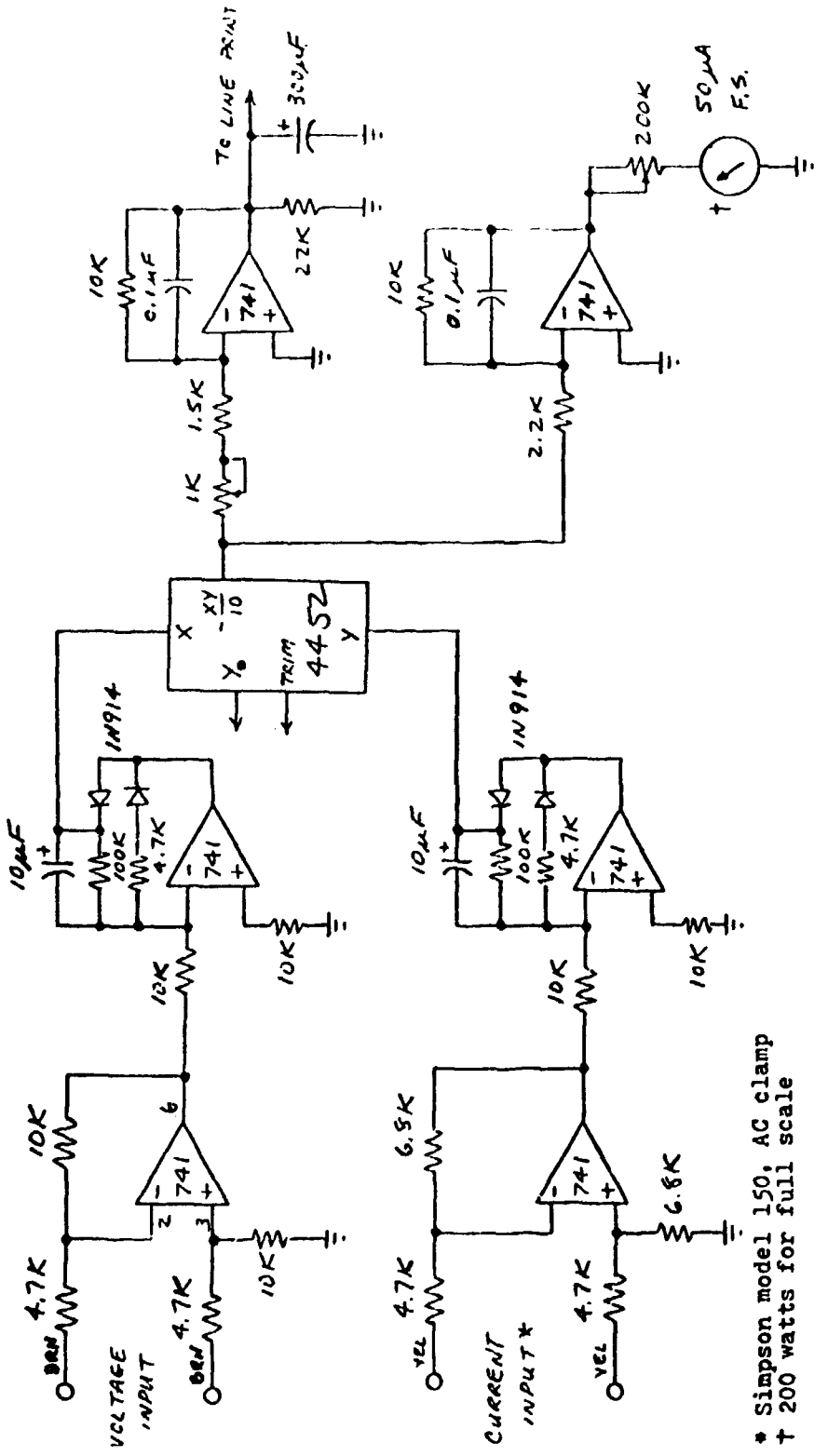

Figure A-2 — Hot Stage Power Monitor Board

APPENDIX 5

A.5.1 – Error in Shrinkage Determination as a Function of Error in the Measurement of Sample Diameter.

The following error propagation formulas* will be used:

$$\text{For } u = x \pm y \pm \ldots, \quad \sigma_u^2 = \sigma_x^2 + \sigma^2 + \ldots \tag{A5.1}$$

$$\text{For } v = x^a y^b, \quad (\text{fr } \sigma_v)^2 = \frac{a^2 \sigma_x^2}{x^2} + \frac{b^2 \sigma_y^2}{y^2} \tag{A5.2}$$

For a = b, from (A5.2):

$$(\text{fr } \sigma_v)^2 = (\text{fr } \sigma_x)^2 + (\text{fr } \sigma_y)^2 \tag{A5.3}$$

In the above formulas σ and (fr σ) are respectively standard and fractional standard deviations.

From (A5.3):

$$(\text{fr } \sigma_{\phi_S/\phi_R}) = [(\text{fr } \sigma_{\phi_S})^2 + (\text{fr } \sigma_{\phi_R})^2] \tag{A5.4}$$

with

ϕ_S= diameter of sintered sample

ϕ_R= diameter of microsphere after reduction to UO_2, or pellet diameter before sintering.

The subscripted symbols correspond to the variables being considered.

The percent shrinkage S% is defined by:

$$S\% = \left(1 - \frac{\phi_S}{\phi_R}\right) 100 \tag{A5.5}$$

From (A5.3):

$$(\text{fr } \sigma_{S\%}) = (\text{fr } \sigma_{[1 - \phi_S/\phi_R]}) \tag{A5.6}$$

By definition:

* Presented for instance by L. G. Parratt, in Probability and Experimental Errors in Science, Dover Public., Inc., New York, pp. 116-118 (1971).

$$(\text{fr } \sigma_{[1-\phi_S/\phi_R]}) = \frac{\sigma(1-\phi_S/\phi_R)}{1-\phi_S/\phi_R} \tag{A5.7}$$

$$(\text{fr } \sigma_{\phi_S/\phi_R}) = \frac{\sigma_{\phi_S/\phi_R}}{\phi_S/\phi_R} \tag{A5.8}$$

The experimental data showed that:

$$\text{fr } \sigma_{\phi_s} \simeq \text{fr } \sigma_{\phi_r} = \text{fr } \sigma_{\phi} \tag{A5.9}$$

From (A5.4), (A5.9) and (A5.8):

$$(\text{fr } \sigma_{\phi_S/\phi_R}) = (\text{fr } \sigma_{\phi})\sqrt{2} = \frac{\sigma_{\phi_S/\phi_R}}{\phi_S/\phi_R} \tag{A5.10}$$

$$\text{or } \sigma_{\phi_S/\phi_R} = \phi_S/\phi_R\,(\text{fr } \sigma_{\phi})\sqrt{2} \tag{A5.11}$$

From (A5.1):

$$\sigma_{(1-\phi_S/\phi_R)} = \sigma_{\phi_S/\phi_R} \tag{A5.12}$$

Therefore from (A5.6) and (A5.7)

$$(\text{fr } \sigma_{S\%}) = \frac{\sigma_{\phi_S/\phi_R}}{1-\phi_S/\phi_R} \tag{A5.13}$$

From (A5.11), (A5.13) and (A5.5)

$$(\text{fr } \sigma_{S\%}) = \frac{\phi_S/\phi_R\,(\text{fr } \sigma_{\phi})\sqrt{2}}{1-\phi_S/\phi_R} = \frac{(1-\frac{S\%}{100})\,(\text{fr } \sigma_{\phi})\sqrt{2}}{\frac{S\%}{100}} \tag{A5.14}$$

$$\text{or } (\%\text{ fr } \sigma_{S\%}) = (\frac{100}{S\%} - 1)\,(\%\text{ fr } \sigma_{\phi})\sqrt{2} \tag{A5.15}$$

where % fr σ indicates percent fractional standard deviation.

From (A5.14):

$$\frac{\sigma_{S\%}}{S\%} = (\frac{100}{S\%} - 1)\,(\text{fr } \sigma_{\phi})\sqrt{2}, \text{ or}$$

$$\sigma_{S\%} = (1 - \frac{S\%}{100})\,(\%\text{ fr } \sigma_{\phi})\sqrt{2} \tag{A5.16}$$

RESUMO

Os estágios inicial, intermediário e final de sinterização de dióxido de urânio foram investigados em função de desvios de composição estequiométrica e de temperatura, mediante o estudo da cinética de reação de sinterização. Os desvios de composição estequiométrica foram controlados por meio do potencial de oxigênio da atmosfera de sinterização, medido continuamente por sensores (eletrólitos sólidos) de oxigênio. Incluidas no estudo de cinética estavam tanto microesferas originadas de gels de UO_2 como pastilhas desse óxido produzidas por compactação isostática de pós com boas qualidades cerâmicas.

O comportamento na sinterização das microesferas foi examinado usando microscopia com platina aquecedora e um forno especialmente construido, dotado de atmosfera controlada. Este mesmo forno foi empregado como parte de um dilatômetro ótico, o qual se utilizou nas investigações de sinterização de pastilhas de UO_2.

Para controlar os desvios de composição estequiométrica durante o tratamento térmico, a pressão parcial de oxigênio na atmosfera de sinterização foi variada pela passagem do gás através de um retentor de oxigênio constituido por cobre e titanio. A temperatura do retentor determinou a pressão parcial de oxigênio na mistura gasosa proveniente do aparelho. Hidrogênio seco foi utilizado em algumas das experiências de sinterização de UO_{2+x}.

A determinação de retrações diametrais e índices de sinterização foi feita por meio de microcinematografia de alta velocidade e de técnicas de pesagem em ultra-microbalança.

Foi observado que o potencial de oxigênio tem influência substancial na cinética dos três estágios de sinterização. O controle de pressão parcial de oxigênio na atmosfera de sinterização resultou em densificação bastante rápida de UO_{2+x}. Valores no intervalo de 95,0 a 99,5% da densidade teórica foram atingidos em menos de um minuto.

A difusão em volume de urânio é o mecanismo dominante nos estágios inicial e intermediário da sinterização. Para o estágio final, a difusão de urânio pelos contornos de grão foi determinada como sendo o principal mecanismo de sinterização.

REFERENCES*

1. ALCOCK, C. B.; HAWKINS, R. J.; HILLS, A. W. D.; McNAMARA, P. A study of cation diffusion in stoichiometric UO_2 using α-ray spectrometry. In: INTERNATIONAL ATOMIC ENERGY AGENCY. *Thermodynamics: proceedings of the symposium on . . . held in Vienna, 22-27 July 1965, v.2.* Vienna, 1966. p.57-62. (Proceedings series).

2. AMATO, I.; COLOMBO, R. L.; PROTTI, A. M. On the activation energy of sintering non-stoichiometric uranium oxide. *J. nucl. Mater.*, 11(2):229-35, 1964.

3. AMATO, I.; COLOMBO, R. L.; PROTTI, A. M. Sintering of UO_2 in carbon dioxide atmosphere. *Nucl. Sci. Engng*, 16(2):137-40, 1963.

4. AMATO, I. et alii. Influence of stoichiometry on the rate of grain growth of UO_2. *J. Am. Ceram. Soc.*, 46(8):407, 1963.

5. AMELINCKX, S. et alii. *Physical properties of UO_2 single crystals.* Brussels, Commission of the European Communities, 1965. (EUR-2042 e).

6. ANDERSON, J. S. The thermodynamics and theory of nonstoichiometric compounds. In: RABENAU, A., editor. *Problems of non-stoichiometry.* Amsterdam, North-Holland, 1970. p.1-76.

(*) As referências bibliográficas relativas a documentos localizados pelo IEA foram revistas e enquadradas na NB-66 da ABNT.

7. ARAOZ, C. *Sintering mechanism in stoichiometric and nonstoichiometric UO_2*. Argonne, Ill., Argone National Lab., 1963. (Internal report). (ANL-FGP-472).

8. ARENBERG, A. C. & JAHN, P. Steam sintering of uranium dioxide. *J. Am. Ceram. Soc.*, 41(5):179-83, 1958.

9. ARIYA, S. M. & MOROZOVA, M. P. The properties of salt-form compounds of variable composition and views on their chemical structure. *J. gen. Chem. U.S.S.R.*, 28(10):2647-52, 1958.

10. ARONSON, S & BELLE, J. Nonstoichiometry in uranium dioxide. *J. chem. Phys.*, 29(1):151-8, 1958.

11. ASHBY, M. F. A first report on sintering diagrams. *Acta metall.*, 22(3):275-89, 1974.

12. AUSKERN, A. B. & BELLE, J. Oxygen ion self-diffusion in uranium dioxide. *J. nucl. Mater.*, 3(3):267-76, 1961.

13. AUSKERN, A. B. & BELLE, J. Uranium ion self-diffusion in UO_2. *J. nucl. Mater.*, 3(3):311-9, 1961.

14. BACMANN, J. J. & CIZERON, G. Contribution a l'etude des mecanismes du debut de frittage du bioxyde d'uranium. *J. nucl. Mater.*, 33(4):271-85, 1969.

15. BACMANN, J. J. & CIZERON, G. Dorn method in the study of initial phase of uranium dioxide sintering. *J. Am. Ceram. Soc.*, 51(4):209-12, 1968.

16. BAILY, W. E.; DANKO, J. C.; FERRARI, H. M.; COLOMBO, H. M. Steam sintering of uranium dioxide. *Bull. Am. Ceram. Soc.*, 41:768-72, Nov. 1962.

17. BANNISTER, M. J. Crystallite size measurements in thoria gel. *J. Am. Ceram. Soc.*, 50(11):619-23, 1967.

18. BANNISTER, M. J. & WOOLFREY, J. L. Discussion of time and length corrections in analysis of initial stages of diffusion-controlled sintering. *J. Am. Ceram. Soc.*, 53(2):114, 1970.

19. BAZIN, J. & ACCARY, A. Contribution to the study of the U-C-O system. *Br. Ceram Soc. Proc.* (8):175-91, 1967.

20. BEERE, W. B. The second stage sitering kinetics of powder compacts. *Acta metall.*, 23(1):139-45, 1975.

21. BEERE, W. B. The sintering and morphology of interconnected porosity in UO_2 powder compacts. *J. Mater. Sci.*, 8(12):1717-24, 1973.

22. BELLE, J. Oxygen and uranium in uranium dioxide (A review). *J. nucl. Mater.*, 30(1):3-15, 1969.

23. BELLE, J. & TENNERY, V. J. Debye temperature. In: BELLE J., editor. *Uranium dioxide: properties and nuclear applications*. Washington, D. C., U. S. Atomic Energy Commission, 1961. p.190-2.

24. BEVAN, D. J. M. Non-stoichiometric compounds. In: TROTMAN, A. F., editor. *Comprehensive inorganic chemistry, V.4: lanthanide and transition compounds*. Oxford, Pergamon, 1973. p.453.

25. BROOK, R. J. Controlled grain growth. In: WANG, F. Y., editor. *Treatise on materials science and technology, V.9: ceramic fabrication processes.* New York, N. Y., Academic, 1976. p.331-64.

26. BROWN, S. D. Private communication. 1975.

27. BURKE, J. E. & ROSOLWSKI, J. H. Sintering. In: HANNAY, N. B., editor. *Treatise on solid state chemistry, v.4.* New York, N. Y., Plenum, 1976. p.621-58.

28. BURTON, B. & REYNOLDS, G. L. The sintering of grain boundary cavities in uranium dioxide. *J. nucl. Mater.*, 45(1):10-4, 1972.

29. CAHOON, H. P. & CHRISTENSEN, C. J. Sintering and grain growth of alpha alumina. *J. Am. Ceram. Soc.*, 39(10):337-43, 1956.

30. COBLE, R. L. Diffusion sintering in the solid state. In: KINGERY, W. D., editor. *Kinetics of high temperature processes.* Cambridge, Mass., Massachusetts Institute of Technology, 1959. p.147-63.

31. COBLE, R. L. Intermediate-stage sintering: modifications and correction of a lattice-diffusion model. *J. appl. Phys.*, 36(7):2327, 1965.

32. COBLE, R. L. Sintering crystalline solids I. Intermediate and final state diffusion models. *J. appl. Phys.*, 32(5):787-92, 1961.

33. COBLE, R. L. & BURKE, J. E. Sintering in ceramics. In: BURKE, J. E., editor. *Progress in ceramic science, v.3.* New York, N. Y., Pergamon, 1963. p.199-251.

34. COLEMAN, S. C. & BEERE', W. B. The sintering of open and closed porosity in UO_2. *Phil. Mag.*, 31(Ser. 8) 6):1403-13, 1975.

35. CONDIT, R. H. The behaviour of oxygen in oxides during sintering. In: GRAY, T. J. & FRECHETTE, V. D., editores. *Kinetics of reactions in ionic systems.* New York, N. Y., Plenum, 1969. p.362-74.

36. CONTAMIN, P. & SLODZIAN, G. Application de l'emission ionique secondaire a l'etude de l'autodiffusion de l'oxygene dans le bioxyde d'uranium. *C. r. Acad. Sci. Paris, C,* 267(9):805-8, 1968.

37. CONTAMIN, P. & SLODZIAN, G. Oxygen isotopic concentration gradient determination with the Caneca ion mass analyzer. *Appl. Phys. Lett.*, 13(12):416-7, 1968.

38. DOLLING, G.; COWLEY, R. A.; WOODS, A. D. B. The crystal dynamics of uranium dioxide. *Can. J. Phys.*, 43(8):1397-413, Aug. 1965.

39. DORNELAS, W. & LACOMBE, P. Diffusion sous champ electrique de l'oxygene aux temperatures de 900° a 1000°C dans l'oxide d'uranium UO_2. *J. nucl. Mater.*, 21(1):100-4, 1967.

40. EGGERDING, C. L. *Desorption from alumina powder surfaces as it relates to compaction and sintering.* Urbana, Ill., 1976. (Ph D. thesis, University of Illinois).

41. FEDORCHENKO, I. M. & SKOROKHATL, V. V. Theory and practice of sintering. *Poroshk. Metall.*, 58(10):29-50, 1967.

42. FREITAS, C. T. de *Hot pressing of actinides oxides.* Urbana, Ill., 1970. (M. Sc. thesis, University of Illinois).

43. FRENKEL, J. Viscous flow of crystalline bodies under the action of surface tension. *J. Phys. (Moscow)*, 9(5):385, 1945.

44. GOETZEL, C. G. *Treatise on powder metallurgy, V.1-3.* New York, N. Y., Interscience, 1949-1952.

45. GRAY, T. J. Defect nature of solids. In: GRAY, T. J.; DETWILER, D. P.; RASE, D. E.; LAWRENCE, W. G.; WEST, R. R.; JENNINGS, T. J. *The defect solid state.* New York, N. Y., Interscience, 1957. p.1-24.

46. GRAY, T. J. Diffusion in ionic lattices, sintering and reactions in the solid state. In: GRAY, T. J.; DETWILLER, D. P.; RASE, D. E.; LAWRENCE, W. G.; WEST, R. R.; JENNINGS, T. J. *The defect solid state.* New York, N. Y., Interscience, 1957. p.77-137.

47. GREENWOOD, N. N. *Ionic crystals, lattice deffects and nonstoichiometry.* New York, N. Y., Chemical Pub. Co., 1970. p.37-61; 62-86; 87-110; 111-47.

48. HAAS, P. A.; CLINTON, S. D.; KLEINSTEUBER, A. T. Preparation of urania and urania-zirconia microspheres by a sol-gel process. *Can. J. chem. Engng*, 44:348-53, 1966.

49. HAAS, P. A.; KITTS, F. G.; BEUTLER, H. Preparation of reactor fuels by sol-gel processes. *Chem. Engng Prog. Symp. Ser.*, 63(80):16-27, 1967.

50. HAGMARK, K. & BROLI, M. Equlibrium oxygen pressures over the nonstoichiometric uranium oxides UO_{2+x} and U_3O_{8-x} at higher temperatures. *J. inorg. nucl. Chem.*, 28(12):2837-50, 1966.

51. HARMER, R. S. *Effects of water vapour on the dehydroxylation. sintering and grain growth in active alumina powders.* Urbana, Ill., 1971. (PhD. thesis, University of Illinois).

52. HAWKINS, R. J. & ALCOCK, C. B. A study of cation diffusion in UO_{2+x} and ThO_2 using α-ray spectrometry. *J. nucl. Mater.*, 26(1):112-22, 1968.

53. HENNEY, J. & JONES, J. W. S. Surface-diffusion studies on UO_2 and MgO. *J. Mater. Sci.*, 3(2):158-64, 1968.

54. HIRTH, J. P. & LOTHE, J. *Theory of dislocations.* New York, N. Y., McGraw-Hill, 1968. p.764.

55. HOEKSTRA, H. R. Phase relationships in the uranium-oxygen and binary oxide system. In: BELLE, J., editor. *Uranium dioxide: properties and nuclear applications.* Washington, D. C., U. S. Atomic Energy Commission, 1961. p.234-8.

56. HONEYCOMBE, R. W. K. *The plastic deformation of metals.* London, Edward Arnold, 1968. p.219.

57. HULL, D. & RIMER, D. The growth of grain-boundary voids under stress. *Phil. Mag.*, 4(6):673-87, 1959.

58. INTERNATIONAL ATOMIC ENERGY AGENCY. *Sol-gel process for ceramic nuclear fuels: proceedings of a panel on... held in Vienna, 6-10 May 1968.* Vienna, 1968. p.175. (Panel proceedings series).

59. JAKESHOVA, L. The sintering behavior of uranium dioxide under controlled oxygen potential. *Phys. Sintering*, 2(1):33-46, 1970.

60. JOHNSON, D. L. General model for the intermediate stage of sintering. *J. Am. Ceram. Soc.*, 53(10):574-7, 1970.

61. JOHNSON, D. L. New method of obtaining volume, grain boundary and surface diffusion coefficients from sintering data. *J. appl. Phys.*, 40(1):192-200, 1969.

62. JOHNSON, D. L. Nonstoichiometry and doping in the sintering of oxides. In: SELTZER, M. S. & JAFFEE, R. I., editores. *Defects and transport in oxides.* New York, N. Y., Plenum, 1974. p.365-78.

63. JOHNSON, D. L. Powder compact studies of initial sintering. In: GRAY, T. J. & FRECHETTE, V. D., editores. *Kinetics of reactions in ionic systems, v.4.* New York, N. Y., Plenum, 1969. p.331-48.

64. JOHNSON, D. L. Sintering kinetics for combined volume grain boundary and surface diffusion. *Phys. Sintering*, 1(1):B1-B22, 1969.

65. JOHNSON, D. J. & CLARKE, T. M. Grain boundary and volume diffusion in the sintering of Silver. *Acta metall.*, 12(10):1173-9, 1964.

66. JOHNSON, D. L. & CUTLER, I. B. Diffusion sintering. I. Initial stage sintering models and their application to shrinkage of powder compacts. *J. Am. Ceram. Soc.*, 46(11):541-5, 1963.

67. JONES, W. D. *Fundamental principles of powder metallurgy.* London, Edward Arnold, 1960.

68. JORGENSEN, P. J. Modification of sintering kinetics by solute segregation in Al_2O_3. *J. Am. Ceram. Soc.*, 48(4):207-10, 1965.

69. JORGENSEN, P. J. & ANDERSON, R. C. Grain-boundary segregation and final stage sintering of Y_2O_3. *J. Am. Ceram. Soc.*, 50(11):553-8, 1967.

70. JORGENSEN, P. J. & WESTBROOK, J. W. Role of solute segragation at grain boundaries during final-stage sintering of alumina. *J. Am. Ceram. Soc.*, 47(7):332-8, 1964.

71. KINGERY, W. D. & BERG, M. Study of the initial stages of sintering solids by viscous flow, evaporation-condensation, and self-diffusion. *J. appl. Phys.*, 26(10):1205-12, 1955.

72. KINGERY, W. D.; BOWEN, H. K.; UHLMAN, R. *Introduction to ceramics.* 2. ed. New York, N. Y., Wiley, 1976. p. 865-6.

73. KOFSTAD, P. *Nonstoichiometry, diffusion and electrical conductivity in binary metal oxides.* New York, N. Y., Wiley, 1972. p.17.

74. KOFSTAD, P. *Nonstoichiometry, diffusion and electrical conductivity in binary metal oxides.* New York, N. Y., Wiley, 1972. p.23.

75. KOFSTAD, P. *Nonstoichiometry, diffusion and electrical conductivity in binary metal oxides.* New York, N. Y., Wiley, 1972. p.26-46.

76. KOFSTAD, P. *Nonstoichiometry, diffusion and electrical conductivity in binary metal oxides.* New York, N. Y., Wiley, 1972. p.300-17.

77. KROGER, F. A. *The chemistry of imperfect crystals.* Amesterdam, Nort-Holland, 1964.

78. KROGER, F. A. & VINK, H. J. Relations between the concentrations of imperfections in crystalline solids. IN: SEITZ, F. & TURNBULL, D., editores. *Solid state physics, v.3.* New York, N. Y., Academic, 1956. p.307-435.

79. KUCZYNSKI, G. C. Self-diffusion in sintering of metallic particles. *Trans. Am. Inst. Min. metall. Engrs,* 185(2):169-78, 1949.

80. KUCZYNSKI, G. C., editor. *Sintering and catalysis.* New York, N. Y., Plenum, 1975. (Materials science research, V.10).

81. KUCZYNSKI, G. C.; ABERNETHY, L.; ALLAN, J. Sintering mechanism of aluminium oxide. In: KINGERY, W. D., editor. *Kinetics of high-temperature processes.* Cambridge, Mass., Massachusetts Institute of Technology, 1959. p.163-72.

82. KUMAR, P. & JOHNSON, D. L. Sintering of CoO. I. Initial stage. *J. Am. Cera. Soc.,* 57(2):62-64, 1974.

83. KUMAR, P. & JOHNSON, D. L. Sintering of CoO:II. Intermediate stage. *J. Am. Ceram. Soc.,* 57(2):65-8, 1974.

84. KURNAKOV, N. S. Verbindung und Chemisches Individuum. *Z. anorg. allg. Chem.,* 88(H.2):109-27, 1914.

85. KURNAKOV, N. S. & PUSCHIN, N. A. Die Legierungen des Bleies mit Thallium und Indium. *Z. anorg. allg. Chem.,* 52(H.4):430-51, 1907.

86. LANGROD, K. Sintering of uranium oxide in the range of 1200-1300°C. *Bull. Am. Ceram. Soc.,* 39(7):366-9, 1960.

87. LAY, K. W. Initial sintering kinetics of hyperstoichiometric uranium dioxide. *J. Am. Ceram. Soc.,* 54(1):18-21, 1971.

88. LAY, K. W. & CARTER, R. E. Role of the O/U ratio on the sintering of UO_2. *J. nucl. Mater.,* 30(1):74-87, 1969.

89. LENEL, F. V. The early stages of the mechanism of sintering. *Phys. Sintering,* 4(1):1-20, 1972.

90. LEE, H. M. & ALCOOK, C. B. Cation diffusion in UO_2-based solid solutions as a function of stoichiometry. *Proc. Br. Ceram. Soc.,* 19(3):85-93, 1971.

91. LEONARD, R. O. The electromagnetic microbalance. In: WHAM, W. N., editor. *Laboratory instrumentation, V.4, ser.2.* Fairfield, Conn., International Scientific Communications, 1977. p.472-7.

92. LIBOWITZ, G. G. Nonstoichiometry in chemical compounds. In: RLISS, H., editor. *Progress in solid state chemistry, V.2.* Oxford, Pergamon, 1965. p.216, 218.

93. LIDIARD, A. B. Self-diffusion of uranium in UO_2. *J. nucl. Mater.,* 19(1):106-8, 1966.

94. LINDNER, R. & SCHMITZ, F. Diffusion of uranium 233 in uranium dioxide. *Z. Naturf.,* 16a(12):1373-8, 1961.

95. MAcEWAN, J. R. & HAYASKI, J. Grain growth in UO_2. *Proc. Br. Ceram. Soc.,* 7:245-72, 1967.

96. MARIN, J. F. Estimation des energies d'activation de diffusion intergranularire de l'uranium dans de dioxide surstoechiometrique UO_{2+x}. *J. nucl. Mater.,* 34(3):348-50, 1970.

97. MARIN, J. F. & CONTAMIN, P. Uranium and oxygen self-diffusion in UO_2. *J. nucl. Mater.*, 30(1):16-25, 1969.

98. MARKIN, T. L.; WHEELER, V. J.; BONES, R. J. High temperature thermodynamic data for $UO_{2\pm x}$. *J. inorg. nucl. Chem.*, 30(3):807-17, 1968.

99. MATZKE, H. *On the effect of TiO_2 additions on defect structure, sintering and gas release of UO_2*. Chalk River, Atomic Energy of Canada, May, 1966. (AECL-2585).

100. MATZKE, H. Lattice disorder and metal self-diffusion in nonstoichiometric UO_2 and $(U, Pu)O_2$. *J. Phys. (Paris)*, 34(11-12):C9-317, 1973.

101. MATZKE, H. Lattice disorder and metal self-diffusion in nonstoichiometric UO_2 and $(U, Pu)O_2$. *J. Phys. (Paris)*, 34(11-12):317-25, 1973.

102. MATZKE, H. On uranium self-diffusion in UO_2 and UO_{2+x}. *J. nucl. Mater.*, 30(1):26-35, 1969.

103. MICROSCOPE heating stage 1750. Ernst Leitz GMBH Wetzlar introductions ref. list 513-67a/Engl. R. 1965.

104. MORGAN, C. S. Densification kinetics during nonisothermal sintering of oxides. In: GRAY, T. J. & FRECHETTE, V. D., editores. *Kinetics of reaction in ionic systems*. New York, N. Y., Plenum, 1969. p.349-61.

105. MORGAN, C. S. Material transport by dislocation motion in sintering. *Phys. Sintering*, 5(1):31-9, 1973.

106. MUAN, A. & OSBORN, E. F. *Phase equilibria among oxides in steel making*. Reading, Mass., Addison-Wesley, 1965. p.26.

107. MULLER, N. Sintern von UO_2. *Ber. Dtsch. Keram. Ges.*, 40(2):140-5, 1963.

108. MURRAY, P. & THACKRAY, R. W. 1950. (MIR-614)

109. MURRAY, P.; PUGH, S. F.; WILLIAMS, J. Uranium dioxide as a reactor fuel. In: COMMISSARIAT A L'ENERGIE ATOMIQUE. *Fuel elements conference, Paris, November 18-23, 1957*. Paris, 1958. p.432-41. (TID-7546(Book 1&2)).

110. NAFZIGER, R. H. et alii. Gaseous buffering for the control of oxygen fugacity at one atmosphere. In: ULMER, G. C., editor. *Research techniques for high pressure and high temperature*. New York, N. Y., Springer, 1971. p.9-41.

111. NELSON, G. O. *Controlled test atmospheres: principles and techniques*. Ann Arbor, Mich., Ann Arbor Science, 1971. p.39-42.

112. NICKEL, H. *Development of coated fuel particles*. Jülich, Kernforschungsanlage, 1970. (JUL-687-RW).

113. NIKLEWSKI, J. B. *Measurement of adsorbate evaluation temperatures and of adsorbate effects in processing and fired properties of submicron alumina*. Urbana, Ill., 1974, (PhD. thesis, University of Illinois).

114. NORRIS, F. L. & PARRAVANO, G. Sintering of zinc oxide. *J. Am. Ceram. Soc.*, 46(9):449-52, 1963.

115. OLANDER, D. R. *Fundamental aspects of nuclear reactor fuel elements.* sem local, U. S. Energy Research and Development Administration, 1976.

116. PERIO, P. Oxidation of uranic oxide at low temperatures. *Bull. Soc. chim. Fr.*, 20:256-63, 1953.

117. PERRON, P. O. *Thermodynamics of non-stoichiometric uranium dioxide.* Chalk River, Atomic Energy of Canada Ltd., May 1968. (AECL-3072).

118. REED-HILL, R. E. *Physical metallurgy principles.* 2.ed. New York, N. Y., Van Nostrand, 1973. p.418-22.

119. REIJNEN, P. J. L. Nonstoichiometry and sintering in ionic solids. In: RABENAU, A., editor. *Problems of nonstoichiometry.* Amsterdan, Nort-Holland, 1970. p.219-38.

120. REIMANN, D. K. & LUNDY, T. S. Diffusion of ^{233}U in UO_2. *J. Am. Ceram. Soc.*, 28(9):511-12, 1969.

121. RICHARDSON, F. D. & ALCOCK, C. B. Chemical equilibria. In: BOCKRIS, J., et alii, editores. *Physico-chemical measurements at high temperatures.* London, Butterworths, 1959. p.135-70.

122. ROBERTSON, W, M. Surface diffusion of oxides. *J. nucl. Mater.*, 30(1):36-49, 1969.

123. ROCKLAND, J. G. R. The determination of the mechanism of sintering. *Acta metall.*, 15(2):277-86, 1967.

124. ROTHMAN, S. J. Diffusion in UO_2. *Adv. Nucl. Sci. Technol.*, 1:160-71, 1962.

125. SAITO, Y. Nonstoichiometry in uranium dioxide. *J. nucl. Mater.*, 51(5):118, 1974.

126. SAITO, Y. Nonstoichiometry in uranium dioxide. *J. nucl. Mater.*, 51(5):123, 1974.

127. SATO, M. Electrochemical measurements and control of oxygen fugacity and other gaseous fugacities with solid electrolyte sensors. In: ULMER, G. C., editor. *Research techniques for high pressure and high temperature.* New York, N. Y., Springer, 1971. p.43-99.

128. SCHWARZKOPF, P.; GOETZEL, C. G.; STERN, G.; STEINITZ, R.; LESZYNSKI, W. *Powder metallurgy.* New York, N. Y., MacMillan, 1947.

129. SCOTT, R.; HALL, A., WILLIAMS, J. The plastic deformation of uranium oxides above 800°C. *J. nucl. Mater.*, 1(1):39-48, 1959.

130. SHEWMON, P. G. *Diffusion in solids.* New York, N. Y., MacGraw-Hill, 1963.

131. SMOTHERS, N. J. & REYNOLDS, H. J. Sintering and grain growth of alumina. *J. Am. Ceram. Soc.*, 37(12):588-94, 1954.

132. STUART, W. J. & ADAMS, R. B. Effects of sintering atmoshere on the density of uranium dioxide pellets. *J. nucl. Mater.*, 58(11):201-4, 1975.

133. STURGIS, D. H. *Effects of absorbed gases on the compaction and initial sintering of an active alumina powder.* Urbana, Ill., 1968.

134. SWALIN, R. A. *Thermodynamics of solids.* 2.ed. New York, N. Y., Wiley, 1972. p.107.

135. TETENBAUM, M. & HUNT, P. D. High-temperature thermodynamic properties of oxygen-defficient urania. *J. chem. Phys.*, 49(11):4739-44, 1968.

136. THORN, R. J. & WINSLOW, G. H. Nonstoichiometry in uranium dioxide. *J. chem. Phys.*, 44(7):2632-43, 1966.

137. THORN, R. J. & WINSLOW, G. H. Oxygen self-diffusion in uranium dioxide. *J. chem. Phys.*, 44(7):2822-3, 1966.

138. THUMMLER, F. & THOMMA, W. The sintering process. *Metall. Rev.*, 12:69-108, 1967.

139. WADSLEY, A. D. Inorganic non-stoichiometric compounds. In: MANDELCORN, L., editor. *Non-stoichiometric compounds.* New York, N. Y., Academic, 1964. p.39-209.

140. WADSLEY, A. D. & ANDERSON, S. Crystallographic shear, and the niobium oxides and oxide fluorides in the composition region MXx, $2.4 < X < 2.7$. In: DUNSTY, J. D. & IBERS, J. A., editores. *Perspectives in structural chemistry, V.3.* New York, N. Y., Wiley, 1969. p.1-58.

141. WAGNER, C. & SCHOTTKY, W. Theories der Geodneten Mischphasen. *Z. phys. Chem.*, B11(H.2-3):163-210, 1931.

142. WEBSTER, A. H. & BRIGHT, N. F. H. *The effects of furnace atmospheres on the sintering behavior of uranium dioxide.* Ottawa, Dept. of Mines and Technical Surveys, 1958. (Mines Branch Research Report, R2).

143. WHEELER, V. J. & JONES, I. G. Thermodinamic and composition changes in UO_{2+x} ($x < 0.005$) at 1950K. *J. nucl. Mater.*, 42(1):117-21, 1972.

144. WHITE, J. Basic phenomena in sintering. In: STEWART, G. H., editor. *Science of ceramics: proceedings of a conference held at Oxford, 26-30 June, 1961, V.1.* London, Academic, 1962. p.1-19.

145. WILLIAMS, J.; BARNES, E.; SCOOT, R.; HALL, A. Sintering of uranium oxides of composition UO_2 to U_3O_8 in various atmospheres. *J. nucl. Mater.*, 1(1):28-38, 1959.

146. WILLIAMS, R. J. *A solid ceramic electrolyte system for measuring redox conditions in high-temperature gas mixing studies.* sem local, National Aeronautics and Space Administration, 1972. (NASA-TM-X-58105).

147. WILLIS, B. T. M. Positions of the oxygen atoms in UO_2.13. *Nature (London)*, 197(2):755-6, 1963.

148. WIRTH, D. G. *The sintering kinetics of a ultra-fine calcia stabilized zirconia.* Urbana, Ill., 1967. (Ph.D. thesis University of Illinois).

149. YAJIMA, S.; FURUYA, H.; HIRAI, T. Lattice and grain-boundary diffusion of uranium in UO_2. *J. nucl. Mater.*, 20:162-70, 1966.

INSTITUTO DE PESQUISAS ENERGÉTICAS E NUCLEARES
Caixa Postal, 11 049 – Pinheiros
CEP 05508
01000 – São Paulo – SP

Telefone: 211-6011
Endereço Telegráfico – IPENUCLEAR
Telex – (011) 23592 - IPEN - BR